



HAL
open science

ARBITRARY ORDER HILBERT SPECTRAL ANALYSIS DEFINITION AND APPLICATION TO FULLY DEVELOPED TURBULENCE AND ENVIRONMENTAL TIME SERIES

Yongxiang Huang

► **To cite this version:**

Yongxiang Huang. ARBITRARY ORDER HILBERT SPECTRAL ANALYSIS DEFINITION AND APPLICATION TO FULLY DEVELOPED TURBULENCE AND ENVIRONMENTAL TIME SERIES. Fluid Dynamics [physics.flu-dyn]. Université des Sciences et Technologie de Lille - Lille I; Shanghai University, 2009. English. NNT: . tel-00439605

HAL Id: tel-00439605

<https://theses.hal.science/tel-00439605>

Submitted on 8 Dec 2009

HAL is a multi-disciplinary open access archive for the deposit and dissemination of scientific research documents, whether they are published or not. The documents may come from teaching and research institutions in France or abroad, or from public or private research centers.

L'archive ouverte pluridisciplinaire **HAL**, est destinée au dépôt et à la diffusion de documents scientifiques de niveau recherche, publiés ou non, émanant des établissements d'enseignement et de recherche français ou étrangers, des laboratoires publics ou privés.

Doctoral Dissertation in Fluid Mechanics
SIAMM, SHU & LOG, USTL – CNRS

1

2

ARBITRARY ORDER HILBERT SPECTRAL ANALYSIS
DEFINITION AND APPLICATION TO FULLY
DEVELOPED TURBULENCE AND ENVIRONMENTAL
TIME SERIES

3

4

5

6

By

7

Yongxiang HUANG (黄永祥)

8

TO OBTAIN THE GRADE OF DOCTEUR DE L'UNIVERSITÉ DE LILLE 1 -
SCIENCES ET TECHNOLOGIES
AND
DOCTOR OF SHANGHAI UNIVERSITY
JULY 2009

9

10

11

12

13

In front of the jury composed of:

14

Prof. Shiqiang DAI	member
Prof. Patrick FLANDRIN	reviewer
Prof. Song FU	member
Prof. Norden E. HUANG	reviewer
Prof. Yulu LIU	supervisor
Prof. Gilmar MOMPEAN	member
Prof. Yuehong QIAN	member
Prof. François G. SCHMITT	supervisor
Prof. Heng ZHOU	member

15

To My Mother and Father.

17

My Best Memory in Wimereux.

18

Table of Contents

19

Table of Contents	v	20
List of Tables	viii	21
List of Figures	x	22
摘要	xvii	23
Abstract	xix	24
Résumé	xxiii	25
Acknowledgements	xxvii	26
I Methodology: Empirical Mode Decomposition and Hilbert Spectral Analysis		27
	1	28
1 An Informal Introduction to Time-Frequency Analysis	3	29
1.1 Decomposition and representation	3	30
1.2 Characteristic scale	5	31
1.3 Nonstationary and nonlinear effects	9	32
1.4 Alternative Approach?	15	33
2 Norden Huang's 1998 Proposal: Hilbert-Huang Transform	19	34
2.1 Empirical mode decomposition	20	35
2.2 Hilbert spectral analysis	25	36
2.3 Intrawave frequency modulation and nonlinear mechanism	27	37
2.4 Summary	29	38

39	3 Our Generalization: Arbitrary Order HSA	31
40	3.1 Definition	31
41	3.2 Calibration and validation	33
42	3.2.1 Fractional Brownian motion and multifractal time series	33
43	3.2.2 Calibration and validation	39
44	3.3 Marginal pdf of the Instantaneous Frequency ω	48
45	3.4 Summary	50
46	II Application to Fully Developed Turbulence	53
47	4 Homogeneous Turbulence and Intermittency	55
48	4.1 Kolmogorov's 1941 theory	57
49	4.2 Intermittency and Kolmogorov's 1962 theory	59
50	4.3 Multifractality	61
51	4.4 Intermittency models	64
52	4.5 Passive scalar	66
53	4.6 Summary	68
54	5 Structure Functions and Autocorrelation Functions	71
55	5.1 Second order structure function	72
56	5.2 Autocorrelation function of velocity increments	85
57	5.3 Summary	97
58	6 Experimental Homogeneous and Isotropic Turbulence	99
59	6.1 Experimental data	100
60	6.2 EMD decomposition of turbulent data	105
61	6.3 Joint pdf and dimensional analysis	108
62	6.4 Intermittency	115
63	6.5 Isotropy ratio and isotropy scaling exponent	117
64	6.6 Summary	130
65	7 Passive Scalar Turbulence	133
66	7.1 Temperature data	135
67	7.2 EMD results	137
68	7.3 HSA results	138
69	7.4 Structure function analysis	141
70	7.5 Summary	143

8	Extended Self-Similarity and Hierarchy Model	145	71
8.1	Extended-Self similarity	147	72
8.2	Hierarchy Model	150	73
8.3	Generalized Extended-Self similarity	155	74
8.4	Summary	161	75
III	Application to Environmental Time Series	165	76
9	Analysis of River Flow Fluctuation	167	77
9.1	Introduction	168	78
9.2	Seine River and Wimereux River	169	79
9.3	EMD Results	172	80
9.4	HSA Results	177	81
9.5	Discussion	180	82
9.6	Summary	183	83
10	Marine Turbulence in the Surf Zone	187	84
10.1	Characterization of intermittency using cumulants	188	85
10.2	Presentation of the experimental database	192	86
10.3	EMD and HSA results	194	87
10.4	Non analytic cumulant generating function	198	88
10.5	Summary	202	89
IV	Conclusion and Discussion	205	90
A	List of Publications	213	91
	Bibliography	216	92

List of Tables

93

1.1	Main properties of FFT, WT and HHT	9	94
5.1	A numerical solution of cumulative function $\mathcal{P}(f, \ell)$	77	95
6.1	Some parameters of turbulent flow	100	96
6.2	Dimension of several quantities	111	97
8.1	Scaling exponents $\zeta(q)$ from different approaches	163	98
9.1	Mean period of the Seine river and Wimereux river	173	99

List of Figures

100

1.1	Demonstration of the characteristic scale	5	101
1.2	Characteristic scale in frequency-time and amplitude-time space . . .	6	102
1.3	Example of a nonstationary event	10	103
1.4	IMF modes from a nonstationary event	11	104
1.5	Instantaneous frequency for nonstationary events	11	105
1.6	Comparison of the Hilbert and Fourier spectra for nonstationary event	12	106
1.7	Numerical solution of Duffing equation	13	107
1.8	IMF modes from EMD for Duffing equation	14	108
1.9	Instantaneous frequency for Duffing equation	14	109
1.10	Comparison of the HMS and PSD for Duffing equation	15	110
2.1	Illustration of the basic idea of EMD	20	111
2.2	An example of IMF from EMD decomposition	21	112
2.3	The flowchart of the EMD algorithm	22	113
2.4	Illustration of the sifting process	23	114
2.5	Intrawave frequency modulation	27	115
2.6	Interwave frequency modulation	28	116
2.7	Comparison of the wave profiles	29	117
3.1	Fractional Brownian motion with various Hurst number H	34	118
3.2	Illustration of the discrete cascade process	36	119
3.3	A sample for one realization 2^{17} points with $\mu = 0.25$	37	120

121	3.4	Synthesized multifractal nonstationary time series with various inter-	
122		mittent parameters μ	38
123	3.5	Hilbert marginal spectra for fBm, $H = 0.4$ and 0.6	40
124	3.6	Scaling exponents $\xi_H(q)$ for fBm	41
125	3.7	Comparison of the Hurst number	42
126	3.8	Structure functions and Hilbert marginal spectra for a realization . .	43
127	3.9	The n dependent of mean normalized scaling exponent $\tilde{\zeta}_n(q)$	44
128	3.10	pdf of scaling exponents $\zeta(q)$ (resp. $\xi_n(q) - 1$)	45
129	3.11	Representation of scaling exponents $\zeta(q)$ (resp. $\xi(q) - 1$)	46
130	3.12	Representation of μ^*	47
131	3.13	Marginal pdf $\mathcal{L}_{H,0}(\omega)$ of the instantaneous frequency ω	48
132	3.14	Scaling exponent $\xi(0)$ for different types data	49
133	4.1	Illustration of the energy cascade process	57
134	4.2	Illustration of the discrete cascade process	62
135	4.3	Comparison of the scaling exponents $\zeta(q)$ and $\zeta_\theta(q)$	67
136	5.1	Nonstationary effects on velocity increments	73
137	5.2	Nonstationary effects on statistical moments	74
138	5.3	Compensated spectrum $E(f)f^\beta$ at $x/M = 20$	77
139	5.4	Cumulative function $\mathcal{P}(f, \ell)$	78
140	5.5	Cumulative function $\mathcal{P}_1(f)$	79
141	5.6	A portion of fBm data and its Fourier power spectrum	80
142	5.7	A single scale influence on the structure function and Hilbert spectrum	81
143	5.8	One portion of the temperature time series	83
144	5.9	Compensated spectrum of transverse velocity	84
145	5.10	Scaling exponents for temperature time series	85
146	5.11	Autocorrelation function $\Gamma_\ell(\tau)$ of the velocity increment $\Delta u(\ell)$	86
147	5.12	Location $\tau_o(\ell)$ of the minimum value of the autocorrelation function .	87
148	5.13	Numerical solution of the rescaled autocorrelation function $\Upsilon(\varsigma)$. . .	88

5.14	Comparison of the autocorrelation function	89	149
5.15	Minima value $\Gamma_o(\ell)$ of the autocorrelation function	92	150
5.16	Cumulative function $\mathcal{Q}(f, \ell, \tau)$	94	151
5.17	Cumulative function $\mathcal{Q}_1(f)$	95	152
5.18	Compensated spectrum of turbulent transverse velocity	96	153
6.1	Schematic representation of the wind tunnel	101	154
6.2	Schematic representation of the active grid	102	155
6.3	One 1s portion of longitudinal velocity	103	156
6.4	Comparison of the spectrum for longitudinal velocity	104	157
6.5	IMF modes of one 2^{14} points segment from EMD	105	158
6.6	Representation of the mean frequency for IMF modes	106	159
6.7	Fourier spectra for IMF modes	107	160
6.8	Fourier spectra for sum of IMF modes	108	161
6.9	Joint pdf $p(\omega, \mathcal{A})$ for longitudinal velocity	109	162
6.10	The skeleton of the joint pdf $p(\omega, \mathcal{A})$	110	163
6.11	Representation of $\mathcal{A}_{\max}(\omega)$ and $p(\mathcal{A}_{\max}(\omega))$	113	164
6.12	Rescaled pdf $p_1(\mathcal{A}, \omega)$	114	165
6.13	Arbitrary order Hilbert marginal spectra for longitudinal velocity	116	166
6.14	Comparison of the scaling exponents for longitudinal velocity	117	167
6.15	Scale dependent isotropy ratio $I(\omega) = \mathcal{L}_{u,2}(\omega)/\mathcal{L}_{v,2}(\omega)$	118	168
6.16	Scale dependent generalized isotropy ratio $I_q(\omega)$	121	169
6.17	Scale dependent generalized isotropy ratio $I_q(\omega)$	122	170
6.18	Representation of generalized isotropy ratio $\tilde{I}(q)$	123	171
6.19	Representation of the isotropy test of $\mathcal{L}_{u,q}(\omega)$ vs $\mathcal{L}_{v,q}(\omega)$	125	172
6.20	Representation of the isotropy test of $S_{v,q}(\omega)$ vs $S_{u,q}(\omega)$	126	173
6.21	Representation of the isotropy scaling exponent $\Gamma(q)$	127	174
6.22	Spatial evolution of the isotropy ratio $\mathcal{I}(\omega)$	128	175
6.23	Spatial evolution of the isotropy ratio $\tilde{\mathcal{I}}(q)$ and isotropy scaling exponent $\Gamma(q)$	129	177

178	6.24 Slope of the isotropy ratio and isotropy scaling exponent	130
179	7.1 Illustration of the “ramp-cliff” structure	134
180	7.2 Sketch of the experiment	135
181	7.3 A 0.3 s portion of temperature time series	135
182	7.4 Comparison of the HMS and PSD for temperature	136
183	7.5 The mean frequency of IMF modes for temperature fluctuations . . .	137
184	7.6 Joint pdf $p(\omega, \mathcal{A})$ for temperature	139
185	7.7 Arbitrary order Hilbert marginal spectrum for temperature	140
186	7.8 The scaling exponent for passive scalar turbulence	141
187	7.9 Structure function of $\Delta\theta(\tau)$	142
188	8.1 A test of ESS for $\mathcal{L}_q(\omega)$ vs $\mathcal{L}_0(\omega)$	148
189	8.2 A test of ESS for $\mathcal{L}_q(\omega)$ vs $\mathcal{L}_3(\omega)$	149
190	8.3 Comparison of the scaling exponent $\xi_0(q)$ and $\xi_3(q)$	150
191	8.4 Representation of the hierarchical spectral function $\mathcal{L}^{(q)}$	153
192	8.5 Representation of the scaling exponents $\pi(q)$	154
193	8.6 The dimensionless arbitrary order Hilbert marginal spectra $\mathcal{Z}_q(\omega)$. .	156
194	8.7 Scaling exponent $\sigma(q)$	157
195	8.8 Representation of GESS $\mathcal{Z}_q(\omega)$ vs $\mathcal{Z}_0(\omega)$	158
196	8.9 Representation of the scaling ratio $\rho(q, p)$ of GESS	159
197	8.10 Representation of the GESS $\mathcal{Z}_{(q)}$ vs $\mathcal{Z}_{(q-1)}$	160
198	8.11 Scaling exponent ratio $\rho(q, q - 1)$ from GESS	161
199	8.12 Comparison of the scaling exponents $\zeta(q)$ from GESS	162
200	8.13 Absolute and relative error from $\zeta(q)$ (Benzi <i>et al.</i> , 1993b)	162
201	9.1 Seine and Wimereux river flow discharge	170
202	9.2 A map showing the location of the Seine river and Wimereux river . .	171
203	9.3 IMF modes for the Seine river	173
204	9.4 IMF modes for Wimereux river	174
205	9.5 Mean frequency of IMF modes for the Seine and Wimereux river . . .	175

9.6	Cross-correlation between the Seine and Wimereux rivers	176	206
9.7	Most correlated IMF modes between the Seine and Wimereux rivers .	177	207
9.8	Energy spectrum for the Seine river and Wimereux river	178	208
9.9	Arbitrary order Hilbert marginal spectrum for the Seine river	179	209
9.10	Scaling exponents $\xi(q) - 1$ for the Seine river	180	210
9.11	Structure function for the Seine river and Wimereux river	181	211
9.12	ESS test of the Seine river	182	212
9.13	ESS test of the Wimereux river	182	213
9.14	Comparison of the relative scaling exponents	183	214
10.1	Location of the measurements	192	215
10.2	ADV measuring device	193	216
10.3	A portion of surf zone data	194	217
10.4	IMF modes from one segment	195	218
10.5	Mean time scales of each mode	196	219
10.6	Spectrum of surf zone data	197	220
10.7	Joint pdf of surf zone velocity	198	221
10.8	The skeleton of the joint pdf	199	222
10.9	Estimation of the first cumulant c_1	200	223
10.10	Cumulant function $\Phi(q)$	201	224
10.11	Comparison of log-stable index $\alpha(\ell)$	202	225
10.12	Comparison of $c_\alpha(\ell)$	203	226

摘要

227

经验模态分解(Empirical Mode Decomposition-EMD,又被称作Hilbert-Huang变换 (Hilbert-Huang Transform)-HHT) 是由黄锷等人 (Huang *et al.*, 1998, 1999)于十年前提出的一种新的分析非平稳和非线性数据的时频分析方法。在过去的十余年中, 有超过1000篇文献报道在工程应用及科学研究的不同领域中使用该方法。本论文首次使用该方法分析湍流数据以及环境观测数据。在对湍流的数据分析中发现EMD类似于一类二分滤波器(dyadic filter bank)。为了能使之刻画所分析信号中的间歇性, 我们将经典的Hilbert谱分析(Hilbert Spectral Analysis-HSA) 方法推广为任意阶Hilbert谱分析。对HSA方法提供的联合概率密度分布函数 $p(\omega, \mathcal{A})$ 对幅值 \mathcal{A} 进行边际积分, 就为我们提供了在幅值-频率空间中对尺度不变特性刻画的新框架, 其中 ω 是瞬时频率, \mathcal{A} 为幅值。我们首先对构造的分形布朗运动时间序列以及多分形非平稳时间序列进行分析, 从而来验证该方法的可行性和有效性。通过和结构函数的结果相对比, 我们发现新方法对间歇性参数提供了更加有效的预测。

通过统计平稳假设, 我们提出了速度增量时间序列 $\Delta u_\ell(t)$ 自相关函数的解析模型, 速度增量定义为 $\Delta u_\ell(t) = u(t + \ell) - u(t)$ 。通过这个模型, 我们解析证明了当原始变量具有标度行为时, 其速度增量的自相关函数将在相应的时间分隔 ℓ 位置取得最小值。同时该模型还表明该最小值存在标度行为, 并被分形布朗运动以及湍流实验数据所证明。通过定义自相关的累积函数, 在傅立叶谱空间里对不同的尺度贡献进行了刻画。我们发现对于自相关函数的主要贡献来自于大尺度部分。同样的分析过程被应用于二阶结构函数。分析结果表明二阶结构函数强烈受到大尺度部分影响, 这表明结构函数并不适合用来提取标度指数, 特别是当所分析的数据中含有大尺度的含能结构的时候。

我们然后将该方法应用于均匀、近似各向同性的湍流实验数据来刻画湍流的间

250 歇性，发现速度的联合概率密度分布函数 $p(\omega, \mathcal{A})$ 本身具有标度趋势，相应的标度
251 值很接近Kolmogorov值。我们随后在幅值-频率空间里对结果函数所提供的标度指
252 数进行了重复。我们对局部各向同性假设在幅值-频率空间里进行检验，发现拓展
253 的各向同性比值随着统计阶数 q 线性减小。

254 我们还使用该方法分析了射流实验中的一段温度数据，该数据有着较强的峭壁
255 结构(ramp-cliff)。对于该数据，传统的结构函数方法不再适用。但是新方法在统计
256 阶数高达8的时候仍然给出了清晰的标度行为，相应的标度指数 $\xi_\theta(q) - 1$ 非常接近
257 充分发展湍流中的流向速度的标度指数。

258 最后，我们用该方法分析了河流数据以及近海海洋湍流数据，在Hilbert框架下
259 刻画了其中的尺度不变特性。

Abstract

260

Empirical Mode Decomposition (EMD), or Hilbert-Huang Transform (HHT) is a novel 261
general time-frequency analysis method for nonstationary and nonlinear time series, 262
which was proposed by Huang *et al.* (1998, 1999) more than ten years ago. During 263
the last ten years, there have been more than 1000 papers applying this new method 264
to various applications and research fields. In this thesis we apply this method to 265
turbulence time series for the first time, and to environmental time series. It is found 266
that the EMD acts a dyadic filter bank for fully developed turbulence. To characterize 267
the intermittent properties of a scaling time series, we generalize the classical Hilbert 268
spectral analysis to arbitrary order q , performing what we denoted “arbitrary order 269
Hilbert spectral analysis”. This provides a new frame to characterize scale invariance 270
directly in an amplitude-frequency space, by taking a marginal integral of a joint pdf 271
 $p(\omega, \mathcal{A})$ of instantaneous frequency ω and amplitude \mathcal{A} . We first validate the method 272
by analyzing a simulated fractional Brownian motion time series, and by analyzing 273
a synthesized multifractal nonstationary time series respectively for monofractal and 274
multifractal processes. Compared with the classical structure function approach, it 275
is found numerically that the Hilbert-based methodology provides a more precise 276
estimator for the intermittency parameter. 277

Assuming statistical stationarity, we propose an analytical model for the au- 278
tocorrelation function of velocity increments time series $\Delta u_\ell(t)$, where $\Delta u_\ell(t) =$ 279
 $u(t + \ell) - u(t)$, and ℓ is the time increment. With this model, we prove analyti- 280
cally that, if a power law behaviour holds for the original variable, the location of the 281
minimum values of the autocorrelation function is equal exactly to the time separation 282

283 ℓ when ℓ belongs to scaling range. A power law behaviour for the minimum values
 284 is suggested by this model, and verified by a fractional Brownian motion simulation
 285 and a turbulent database. By defining a cumulative function for the autocorrelation
 286 function, the scale contribution is then characterized in the Fourier frequency space.
 287 It is found that the main contribution to the autocorrelation function comes from the
 288 large scale part. The same idea is applied to the second order structure function. It
 289 is found the second order structure function is strongly influenced by the large scale
 290 part, showing that it is not a good approach to extract the scaling exponent from a
 291 given scaling time series when the data possess energetic large scales.

292 We then apply this Hilbert-based methodology to an experimental homogeneous
 293 and nearly isotropic turbulent database to characterize multifractal scaling properties
 294 of the velocity time series in fully developed turbulence. We obtain a scaling trend
 295 in the joint pdf $p(\omega, \mathcal{A})$ with a scaling exponent close to the Kolmogorov value. We
 296 recover the structure function scaling exponents $\zeta(q)$ in amplitude-frequency space
 297 for the first time. The isotropy hypothesis is then checked scale by scale in amplitude-
 298 frequency space. It is found that the generalized isotropy ratio decreases linearly with
 299 the order q .

300 We also perform the analysis on a temperature (passive scalar) time series with
 301 strong ramp-cliff structures. For these data, the traditional structure function fails.
 302 However, the new method extracts a clear power law up to $q = 8$. The scaling
 303 exponents $\xi_\theta(q) - 1$ is quite close to the scaling exponents $\zeta(q)$ of the longitudinal
 304 velocity in fully developed turbulence.

305 We then consider the traditional Extended Self-Similarity (ESS) (Benzi *et al.*,
 306 1993b) and the hierarchy model (She & Lévéque, 1994) under the Hilbert frame. For
 307 the case of ESS, we have here two special cases $q = 0$ and $q = 3$ to define the ESS in
 308 the Hilbert frame. Both of them work for the fully developed turbulence providing the
 309 same scaling exponents. Based on the turbulent database we have, it seems that the
 310 lognormal model with a proper chosen intermittency parameter μ provides a better
 311 prediction of the scaling exponents.

We finally apply the new method to daily river flow discharge and surf zone marine	312
turbulence to characterize the scale invariance under the Hilbert frame.	313

Résumé

314

La Décomposition Modale Empirique (Empirical Mode Decomposition - EMD) ou la 315
Transformation de Hilbert-Huang (HHT) est une nouvelle méthode d'analyse temps- 316
fréquence qui est particulièrement adaptée pour des séries temporelles nonlinéaires 317
et non stationnaires. Cette méthode a été proposée par [Huang *et al.* \(1998, 1999\)](#) il 318
y a plus de dix ans. Pendant les dix dernières années, plus de 1000 articles ont ap- 319
pliqué cette méthode dans le cadre de diverses applications ou domaines de recherche. 320
Dans cette thèse, nous appliquons cette méthode à des séries temporelles de turbu- 321
lence, pour la première fois, et à des séries temporelles environnementales. Nous 322
avons obtenu comme résultat le fait que la méthode EMD correspond à un banc de 323
filtre dyadique (ou quasi-dyadique) pour la turbulence pleinement développée. Pour 324
caractériser les propriétés intermittentes d'une série temporelle invariante d'échelle, 325
nous avons généralisé l'analyse spectrale de Hilbert-Huang classique à des moments 326
d'ordre arbitraire q , pour effectuer ce que nous avons appelé "analyse spectrale de 327
Hilbert d'ordre arbitraire". Ceci fournit un nouveau cadre pour analyser l'invariance 328
d'échelle directement dans un espace amplitude-fréquence, en estimant une intégrale 329
marginale d'une pdf jointe $p(\omega, \mathcal{A})$ de la fréquence instantanée ω et de l'amplitude \mathcal{A} . 330
Nous validons tout d'abord la méthode en analysant des séries temporelles de mou- 331
vement Brownien fractionnaire, et en analysant des séries temporelles multifractales 332
synthétiques, en tant que modèle respectivement de processus monofractals et multi- 333
fractals. Nous comparons les résultats obtenus avec la nouvelle méthode, à l'analyse 334
classique utilisant les fonctions de structure: nous trouvons numériquement que la 335
méthodologie utilisant l'approche de Hilbert fournit un estimateur plus précis pour 336

337 le paramètre d'intermittence.

338 Avec une hypothèse de stationarité, nous proposons un modèle analytique pour la
 339 fonction d'autocorrélation des incréments de séries temporelles de vitesse $\Delta u_\ell(t)$, où
 340 $\Delta u_\ell(t) = u(t + \ell) - u(t)$, et ℓ est l'incrément temporel. Dans le cadre de ce modèle,
 341 nous prouvons analytiquement que, si une loi de puissance est valide pour la série
 342 d'origine, la position minimisant la fonction d'autocorrélation de la variable d'origine
 343 est égale exactement au temps de séparation ℓ lorsque ℓ appartient à la zone invariante
 344 d'échelle. Ce modèle prédit une loi de puissance pour la valeur minimum, comporte-
 345 ment vérifié par une simulation de mouvement Brownien fractionnaire et à partir
 346 de données expérimentales de turbulence. En introduisant une fonction cumulative
 347 pour la fonction d'autocorrélation, la contribution en échelle est alors caractérisée
 348 dans l'espace de fréquence de Fourier. Nous observons que la contribution principale
 349 à la fonction d'autocorrélation provient des grandes échelles. La même idée est ap-
 350 pliquée à la fonction de structure d'ordre 2. Nous obtenons que celle-ci est également
 351 fortement influencée par les grandes échelles, ce qui montre que ceci n'est pas une
 352 bonne approche pour extraire les exposants invariants d'échelle d'une série temporelle
 353 lorsque les données sont caractérisées par des grandes échelles énergétiques.

354 Nous appliquons ensuite cette méthodologie Hilbert-Huang à une base de données
 355 de turbulence homogène et presque isotrope, pour caractériser les propriétés multi-
 356 fractales invariantes d'échelle des série temporelles de vitesse en turbulence pleinement
 357 développée. Nous obtenons un comportement invariant d'échelle pour la pdf jointe
 358 $p(\omega, \mathcal{A})$ avec un exposant proche de la valeur de Kolmogorov. Nous estimons les ex-
 359 posants $\zeta(q)$ dans un espace amplitude-fréquence, pour la première fois. L'hypothèse
 360 d'isotropie est testée échelle par échelle dans l'espace amplitude-fréquence. Nous
 361 obtenons que le rapport d'isotropie généralisé décroît linéairement avec le moment q .

362 Nous effectuons également l'analyse d'une série temporelle de température (scalaire
 363 passif) possédant un effet de rampe marqué (ramp-cliff). Pour ces données, l'approche
 364 traditionnelle utilisant les fonctions de structure ne fonctionne pas. Mais la nouvelle
 365 méthode développée dans cette thèse fournit un net régime invariant d'échelle jusqu'au

moment $q = 8$. Les exposants $\xi_\theta(q) - 1$ sont très proches des exposants $\zeta(q)$ obtenus 366
 par l'approche des fonctions de structure pour la vitesse longitudinale. 367

Nous nous intéressons ensuite à l'auto-similarité étendue (Extended Self Similarity 368
 - ESS) (Benzi *et al.*, 1993b) dans le cadre Hilbert-Huang. En ce qui concerne la 369
 méthode ESS, qui est devenue classique en turbulence, nous adaptons l'approche 370
 pour le cas Hilbert-Huang dans un espace de fréquence, et nous constatons que le 371
 modèle lognormal, avec un coefficient adéquat, fournit une très bonne estimation des 372
 exposants invariants d'échelle. 373

Finalement nous appliquons la nouvelle méthodologie à des données environ- 374
 nementales: des débits de rivières, et des données de turbulence marine dans la zone 375
 de surf. Dans ce dernier cas, la méthode ESS permet de séparer les ondes de vent de 376
 la turbulence à petite échelle. 377

Acknowledgements

378

I would like to thank my two supervisors, Prof. François G. Schmitt from CNRS 379
and Prof. Yulu Liu in Shanghai University, for their many suggestions and constant 380
support during my Ph.D research. I also thank to Prof. Zhiming Lu for useful 381
discussion. I thank Prof. Y. Gagne in Joseph Fourier University for providing the 382
experimental temperature data. I appreciate Prof. P. Flandrin in Lyon to share 383
his EMD MATLAB[®] codes, which are available at web page: [http://perso.ens-
lyon.fr/patrick. flandrin/emd.html](http://perso.ens-lyon.fr/patrick.flan-384
drin/emd.html). I appreciate Prof. C. Meneveau in Johns Hopkins 385
University to share the experimental data. The data are available for download at 386
his web page: <http://www.me.jhu.edu/~meneveau/datasets.html>. 387

During my whole three years Ph.D research, I was financed in part by a Ph.D 388
grant from the French Ministry of Foreign Affairs, by part from Lille 1 University and 389
Shanghai University. 390

Finally, I want to thank my supervisor, Prof. François G. Schmitt, again for his 391
very valuable comments on this thesis. 392

Yongxiang HUANG (黄永祥) Laboratory of Oceanology and Geosciences 393

May 8, 2009 Wimereux, France 394

395

Part I

396

Methodology

397

Empirical Mode Decomposition

398

and Hilbert Spectral Analysis

Chapter 1

An Informal Introduction to Time-Frequency Analysis

In this chapter, we recall some general ideas of the time-frequency analysis, such as decomposition and representation, characteristic scale, nonlinear and nonstationary effects, etc.

1.1 Decomposition and representation

There are plenty of time-frequency analysis methods (Cohen, 1995; Flandrin, 1998). Their basic idea can be interpreted as representing a given signal/function, $f(x)$, by a given basis

$$f(x) = \int_{-\infty}^{+\infty} \psi(\nu, x') \varphi(x, x', \nu) d\nu dx' \quad (1.1.1)$$

where φ is a given basis (function), and ψ is the coefficient (function) which can be determined by

$$\psi(x, \nu) = \int_{-\infty}^{+\infty} f(x) \varphi(x, x', \nu) dx' \quad (1.1.2)$$

Here the basis function φ also can be interpreted as an integral kernel of the above equation (Cohen, 1995). It is an asymptotic approximation: the signal is asymptotically approximated by the chosen basis (function) φ . The property of the chosen

basis are usually well known. Then we check φ to see how the given signal looks like 414
 with the chosen basis (function) φ . For example, when the trigonometric function is 415
 chosen, we obtain the classical Fourier transform 416

$$\psi(f) = \int_{-\infty}^{+\infty} f(x)e^{i2\pi fx} dx \quad (1.1.3)$$

Another example is the Wavelet transform 417

$$\psi(a, x) = |a|^{-1/2} \int_{R^n} f(x')\varphi\left(\frac{x' - x}{a}\right) dx' \quad (1.1.4)$$

where n is the dimension of the space, $\varphi(x)$ is the so-called mother wavelet and a is 418
 a dilatation parameter¹. This is the traditional approach for time-frequency analysis: 419
 the basis are chosen before the decomposition. Therefore once we choose a basis 420
 (function), the information that can be extracted from the data is determined. They 421
 are also energy based approaches: only when the component contains enough energy, 422
 it then can be detected by such methods (Huang *et al.*, 1998; Huang, 2005). 423

Moreover, most *a priori* basis are defined in the global sense and they require 424
 that the signal satisfies stationary and linearity assumptions (Cohen, 1995; Flandrin, 425
 1998; Huang *et al.*, 1998). Here the stationarity means that the statistical properties 426
 are identical for different samples². Many modifications, such as short-time Fourier 427
 transform with various windows, Wigner-Ville distribution, have been designed to 428
 overcome these obstacles (Cohen, 1995; Flandrin, 1998). However, they inherit more 429
 or less the shortcoming of the Fourier transform (Huang *et al.*, 1998, 1999). 430

¹To be a mother wavelet, $\varphi(x)$ should satisfy some conditions. For details on wavelet theory see Daubechies (1992). We may also consider the wavelet transform approach as an adaptive-windows Fourier transform (Huang *et al.*, 1998).

²The mathematical definition of stationarity is more rigorous. In practice, if some statistical quantities of a given time series do not change beyond a certain size of sample and are identical for different samples, then the time series is called stationary process.

431 1.2 Characteristic scale

432 The power of a time-frequency analysis method is determined by the chosen basis φ .
 433 Indeed, for a certain time-frequency analysis method, a characteristic scale (CS) is al-
 434 ways defined explicitly or implicitly. Once we choose a definition of the characteristic
 435 scale for a certain method, then the ability and property of this method is deter-
 436 mined/fixed. We compare here three different definitions of the CS, corresponding
 437 to Fourier transform, Wavelet transform and Hilbert-Huang transform (HHT) (see
 chapter 2 for more details of HHT).

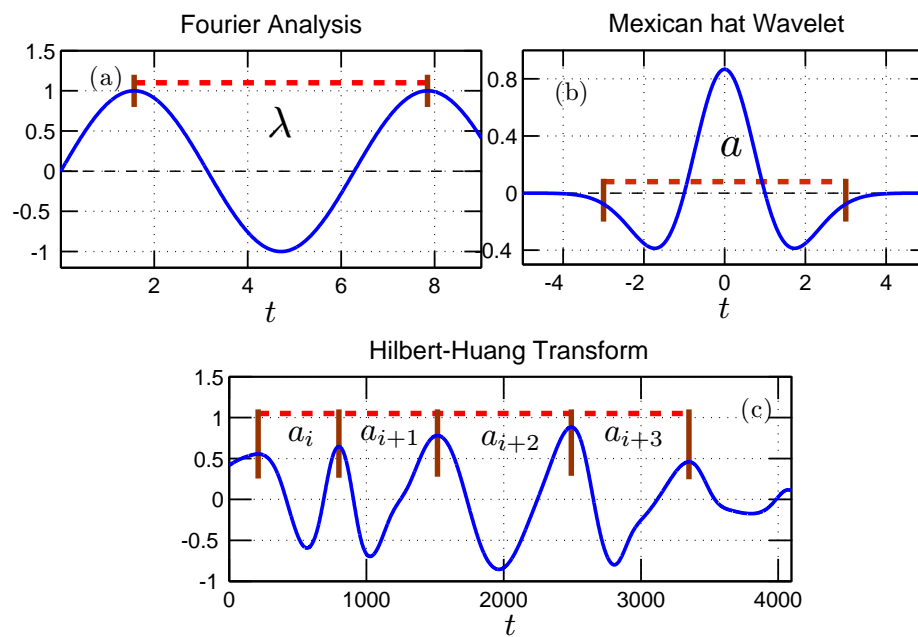


Figure 1.1: Demonstration of the characteristic scale of (a) Fourier analysis, (b) Wavelet transform and (c) Hilbert-Huang transform, respectively.

438

439 • Fourier Transform:

440 The length of one period of sine or cosine wave.

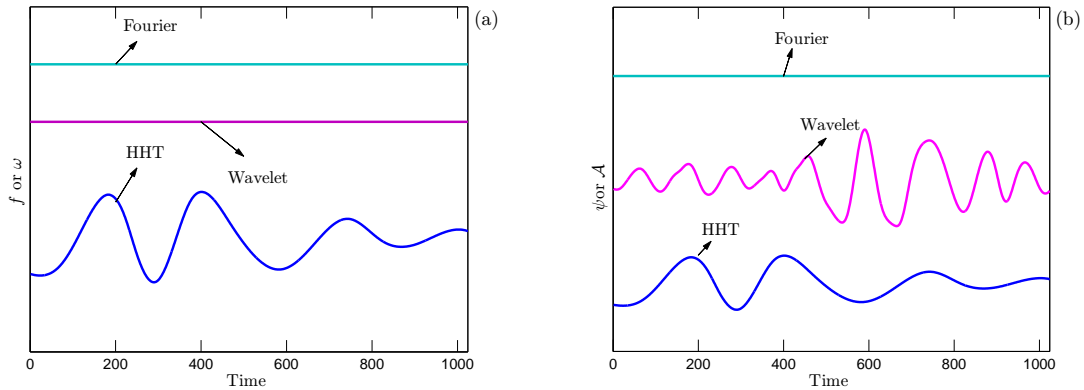


Figure 1.2: The characteristic scale in (a) frequency-time space, and (b) amplitude-time space.

- Wavelet Transform: 441
 The shape of the mother wavelet together with the dilation factor. 442
- Hilbert-Huang Transform: 443
 The distance between successive local extrema maxima (resp. minima) points. 444

We illustrate the corresponding CS in Fig. 1.1: (a) Fourier analysis, (b) Mexican hat wavelet, and (c) Hilbert-Huang transform (HHT). As we have mentioned above, for an *a priori* approach, once the basis (function) φ is chosen, the shape of CS is then fixed. We illustrate here two examples for *a priori* approach: the Fourier transform and Mexican hat wavelet. However, the shape of the CS of HHT can be varied from time to time. In other words, these three time frequency analysis methods describe the characteristic scale globally, regionally, and locally, respectively (Huang, 2005).

Frequency-Modulation

Figure 1.2 shows the CS in both frequency-time view and amplitude-time view. The difference among them are clear. For further discussion convenience, we introduce

455 here the concepts of frequency-modulation and amplitude-modulation. Let us con-
 456 sider here a monochromatic wave

$$x(t) = a \cos 2\pi\nu_o t \quad (1.2.1)$$

457 where the constants a and ν_o are the amplitude and the frequency. It is natural to
 458 extend this point of view to evolutionary situations

$$x(t) = a(t) \cos 2\pi\nu_o(t)t \quad (1.2.2)$$

459 where the amplitude a and the frequency ν_o now may vary in time. Let us first keep
 460 the amplitude a as a constant, and let the frequency ν_o vary in time. We call this
 461 “frequency modulation”.

462 **Definition 1.2.1** (Frequency-Modulation). Frequency ν_o may vary in time.

463 Both the Fourier analysis and Wavelet transform³ do not allow the frequency
 464 modulation, since the frequency for each component is fixed, see Fig. 1.2 (a). On
 465 the contrary, the HHT does allow frequency-modulation, since the idea of the in-
 466 stantaneous frequency (Cohen, 1995; Flandrin, 1998) is employed to describe the
 467 frequency. We will see this point in chapter 2, the fact that frequency modulation
 468 may be further termed into two different types: interwave-frequency-modulation and
 469 intrawave-frequency-modulation. The latter one can be associated to a nonlinear
 470 mechanism (Huang *et al.*, 1998, 1999).

471 Amplitude-Modulation

472 Now we consider another situation, the so-called amplitude-modulation. Let us keep
 473 the frequency ν_o constant, and let the amplitude a vary in time. It is then called

³In fact, Wavelet may detect the so-called interwave-frequency-modulation (Huang *et al.*, 1998, 1999). However, this ability comes from the amplitude-modulation: the wavelet coefficient $\varphi(x, a)$ may be zero at some locations and scales.

amplitude-modulation. 474

Definition 1.2.2 (Amplitude Modulation). Amplitude a may vary in time. 475

Figure 1.2 (b) shows the amplitude of the above mentioned three approaches 476
in amplitude-time view. Here again, the Fourier representation does not allow the 477
amplitude-modulation, since it describes the scale in a global sense. Due to a com- 478
pact support property of the wavelet in physical domain, it allows the amplitude- 479
modulation (Daubechies, 1992). HHT allows the amplitude-modulation mechanism. 480
Therefore, it allows the frequency-modulation and amplitude-modulation simultane- 481
ously (Huang *et al.*, 1998, 1999; Huang, 2005). 482

Potential Shortcoming of Fourier-Based Approach 483

We then reproduce the main properties of the Fourier analysis, Wavelet transform 484
and HHT in Table 1.1 from Huang (2005). These properties determine the power of 485
each method and also the potential shortcoming of each one. We then list the main 486
potential shortcoming of the Fourier-based approach here 487

- *a priori* 488
The basis φ are given before decomposition. 489
- Stationary 490
They require that the data satisfy the stationarity assumption. 491
- Asymptotical approximation 492
They are a linear asymptotical approximation to the original data. 493
- Global uncertainty 494

495 They are limited by the so-called Heisenberg-Gabor uncertainty principle⁴.

496 Due to the above mentioned properties of the Fourier-based time-frequency analysis
 497 methods, they require high order harmonic component to mimic a transit signal, in
 498 which both the amplitude and the frequency may vary in time.

499 For more details on the time-frequency analysis and potential shortcomings of the
 500 Fourier-based approach, we suggest [Cohen \(1995\)](#) and [Flandrin \(1998\)](#).

Table 1.1: Comparison of the main properties of the Fourier analysis, Wavelet transform and Hilbert-Huang transform.

	Frequency-Modulation		Amplitude-Modulation
	Interwave	Intrawave	
Fourier analysis	No	No	No
Wavelet transform	Yes	No	Yes
Hilbert-Huang transform	Yes	Yes	Yes

501 1.3 Nonstationary and nonlinear effects

502 In the real world, most data are nonlinear, nonstationary and noisy. A general method
 503 to deal with nonlinear and nonstationary time series is required. The terminology
 504 ‘nonlinear’ here means that the underling mechanism is nonlinear. Below, we il-
 505 lustrate the nonstationary and nonlinear effects on both the Fourier analysis and
 506 Hilbert-Huang transform.

⁴The Heisenberg-Gabor uncertainty principle ([Cohen, 1995](#); [Flandrin, 1998](#)) means that the time resolution δt and the frequency resolution δf are restricted by the following relation

$$\delta t \delta f \geq \frac{1}{4\pi} \tag{1.2.3}$$

Nonstationary Effect

507

Definition 1.3.1 (Stationarity). A time series $x(t)$ is stationary in the weak sense, if, for all t

508

$$E(|x(t)|^2) < \infty \tag{1.3.1a}$$

509

$$E(x(t)) = m \tag{1.3.1b}$$

510

$$C(x(t_1), x(t_2)) = C(x(t_1) + \tau, x(t_2) + \tau) = C(t_1 - t_2) \tag{1.3.1c}$$

511

where $E(\cdot)$ is the expected value, and $C(\cdot)$ is the covariance function.

512

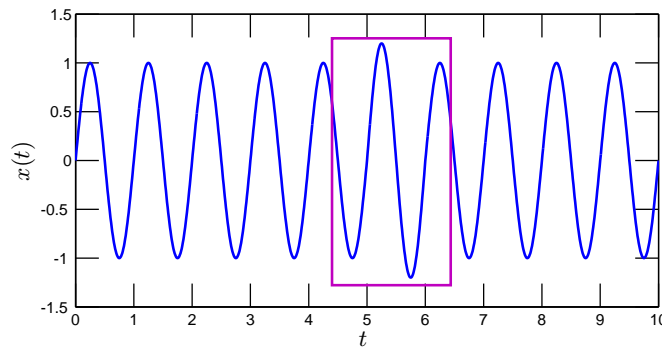


Figure 1.3: Example of a nonstationary event $x(t)$: the amplitude on range $5 \leq t \leq 6$ is 20% higher, which is marked by a rectangle.

In practice, we only have a finite size sample. Obviously, the data we have may not satisfy the above condition, which means it is nonstationary. We give an example of a nonstationary effect here. We produce a sine wave $x(t)$ on the range $0 < t < 10$

513

514

515

$$x(t) = \begin{cases} \sin(2\pi t) & t < 5 \\ 1.2 \sin(2\pi t) & 5 \leq t \leq 6 \\ \sin(2\pi t) & 6 < t < 10 \end{cases} \tag{1.3.2}$$

where a nonstationary event with 20% higher amplitude is superposed on range $5 \leq t \leq 6$, see Fig. 1.3, in which the nonstationary event is marked by a rectangle. The sampling frequency is set as 100 Hz. Figure 1.4 shows the intrinsic mode

516

517

518

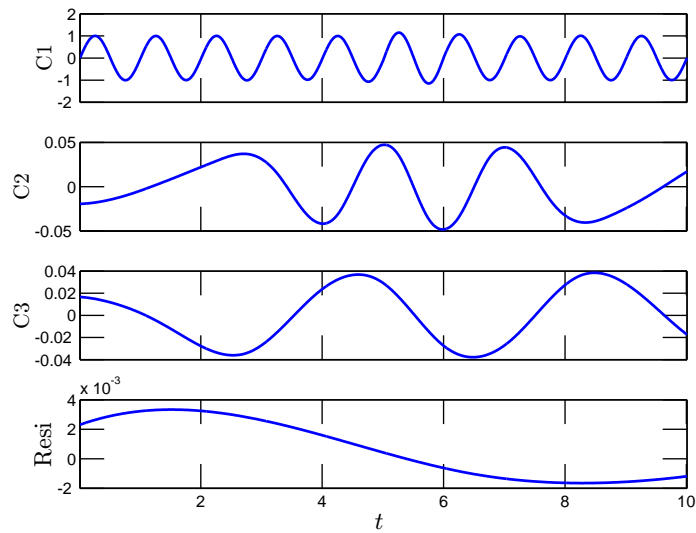


Figure 1.4: Intrinsic mode functions from empirical mode decomposition.

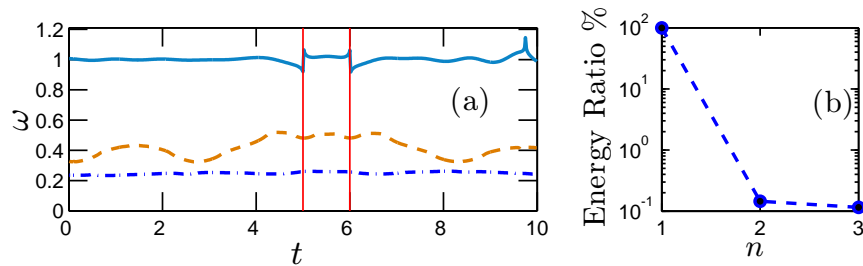


Figure 1.5: Instantaneous frequency of each mode: (a) instantaneous frequency, (b) the relative energy. The vertical solid lines indicate the location of the nonstationary event.

519 functions (IMF) from the empirical mode decomposition (EMD)⁵. Figure 1.5 shows
 520 the corresponding (a) instantaneous frequency, and (b) energy ratio, where the verti-
 521 cal solid lines indicate the location of nonstationary event. The nonstationary event
 522 is well captured by HHT in a very local level. We compare the Hilbert marginal spec-
 523 trum with the Fourier spectrum in Fig. 1.6, where the thin solid line is the Fourier
 524 power spectrum of the signal without perturbation. The Fourier power spectrum is

⁵The concept of intrinsic mode function and the empirical mode decomposition methodology will be presented in chapter 2.

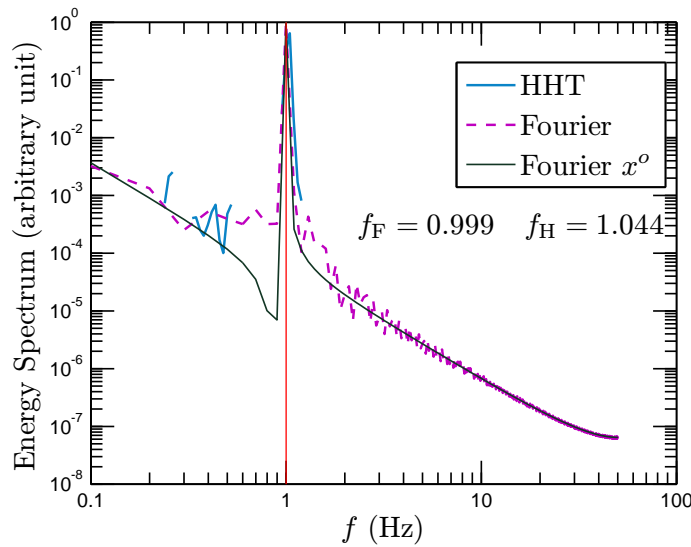


Figure 1.6: Comparison of the Hilbert marginal spectrum and Fourier spectra.

directly estimated by a Fourier transform without any window. All these three curves 525
 detect the domain frequency. For the Fourier power spectrum, there are some fluc- 526
 tuation on the high frequency range, indicating the presence of high order harmonic 527
 component. For the Hilbert marginal spectrum, we note that it does not require 528
 any high order harmonic component to mimic the nonstationary effect, since it allows 529
 amplitude-modulation. We also note some energy leakage on the low frequency, which 530
 may be the end-point effect in the empirical mode decomposition. 531

Nonlinear Effect 532

We turn to nonlinear effect. There is no general definition of nonlinearity for a discrete 533
 time series, since we may represent it by a linear asymptotical approximation way. 534
 Therefore, we propose here a definition of the nonlinearity for a discrete time series: 535

Definition 1.3.2 (Nonlinearity). If the underlying mechanism behind a time series 536
 is nonlinear, we then call the dataset itself nonlinear. 537

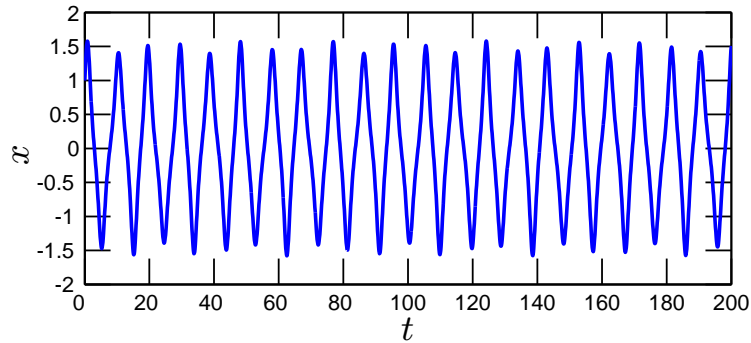


Figure 1.7: A 5th order Runge-Kutta numerical solution of the Duffing equation.

538 Here we consider the classical Duffing equation with a periodic forcing. The
 539 Duffing equation is written as

$$\frac{d^2x}{dt^2} + x(1 - \varepsilon x^2) = b \cos \omega t \quad (1.3.3)$$

540 where ε is a nonlinear parameter, $b \cos \omega t$ is a periodic forcing. It can be considered
 541 as a nonlinear spring system with a nonlinear spring $(1 - \varepsilon x^2)$, and a periodic forcing
 542 $b \cos(\omega t)$. The parameter and inertial condition are taken as $b = 0.1$, $\varepsilon = 1$, $\omega =$
 543 $2\pi/25$, and $[x(0), x'(0)] = [1, 1]$. A 5th order Runge-Kutta scheme is performed to
 544 integrate the equation numerically with $\Delta t = 0.1$. Figure 1.7 shows the corresponding
 545 numerical solution. Due to the nonlinear mechanism, the wave profile of the numeri-
 546 cal solution departs from a sine wave. We show the corresponding intrinsic mode
 547 functions from EMD decomposition in Fig. 1.8. The original time series is separated
 548 into five modes with one residual. Figure 1.9 shows the corresponding instantaneous
 549 frequency for each mode. A frequency-modulation is clearly observed for the first
 550 mode. As we will show in chapter 2, it belongs to the intrawave frequency-modulation
 551 family. We compare the corresponding Hilbert marginal spectrum and the Fourier

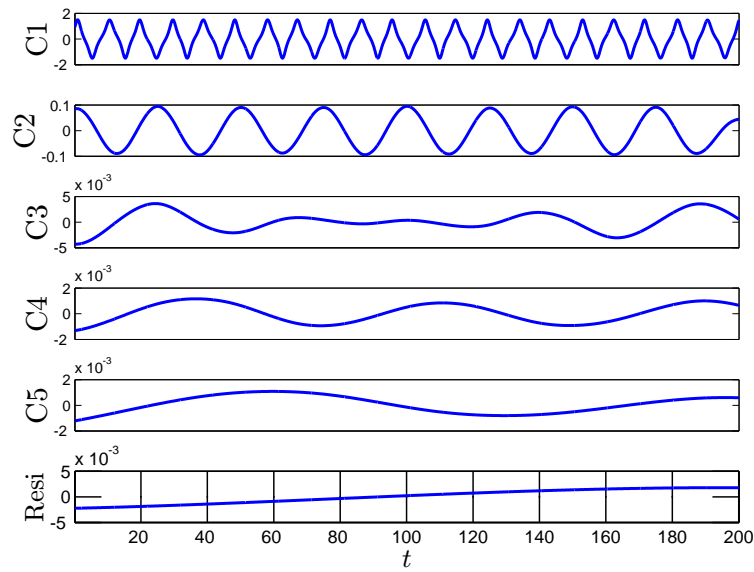


Figure 1.8: Intrinsic mode functions from empirical mode decomposition for numerical solution of the Duffing equation.

power spectrum in Fig. 1.10. They are significantly different. Both approaches capture the domain frequency and the periodic forcing. However, the Fourier analysis needs high order harmonic components to mimic the nonlinear process, which is indeed a requirement of mathematics without physics sense. It stems from the linear asymptotic representation of the nonlinear process. As we already have pointed out previously, due to the nonlinear mechanism, the wave profile of the Duffing equation

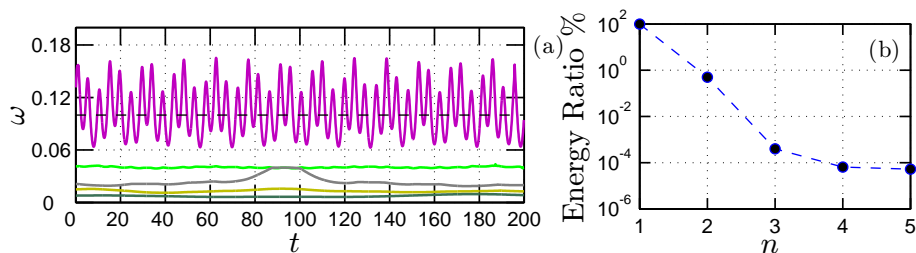


Figure 1.9: Instantaneous frequency for the Duffing equation: (a) instantaneous frequency, (b) the relative energy. Frequency modulation is observed for the first IMF mode.

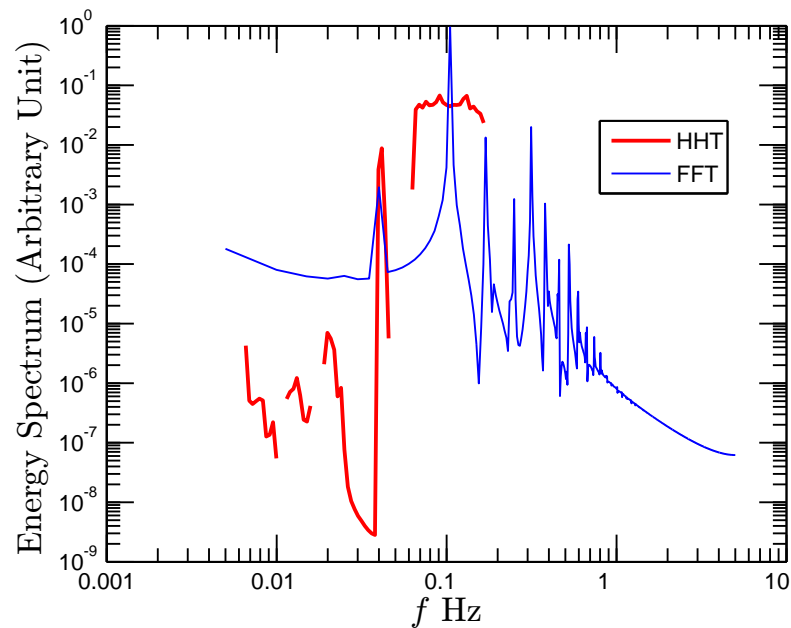


Figure 1.10: Comparison of the Hilbert marginal spectrum and Fourier power spectrum for Duffing equation. High order harmonic components are required by Fourier analysis to mimic the nonlinear distortion of the nonlinear wave.

558 solution is in far deviation from a pure sine wave. High order harmonic components
 559 are thus required by the Fourier analysis to mimic this deviation, namely nonlinear
 560 distortion. For HHT, since it allows frequency- and amplitude-modulation simulta-
 561 neously, it does not need the high order harmonic component any more to describe
 562 the nonlinear distortion (Huang *et al.*, 1998, 1999).

563 1.4 Alternative Approach?

564 About ten year ago, Huang *et al.* (1998, 1999) introduced a novel time-frequency anal-
 565 ysis method, the Hilbert-Huang transform, or Empirical Mode Decomposition called
 566 by some authors⁶, to deal with general nonstationary and nonlinear time series. This

⁶In fact, a complete Hilbert-Huang transform has two steps. They are the empirical mode decomposition and Hilbert spectral analysis. However, we note that some authors call the empirical

method has a very local level ability both in physical domain and spectral domain. 567
It also possesses fully self-adaptiveness ability, since there is no basis assumption *a* 568
priori (Huang *et al.*, 1998, 1999; Flandrin & Gonçalves, 2004). As an alternative 569
method to the Fourier-based approach, we will apply this methodology on turbulent 570
and environmental time series in this thesis. 571

* * * * *

This thesis is organized as follows. In chapter 2, we present more details on the 573
traditional Hilbert-Huang transform, including Empirical Mode Decomposition, the 574
classical Hilbert Spectral Analysis. We generalize the latter one into arbitrary order 575
to consider the scale invariant properties of intermittent multifractal time series in 576
an amplitude-frequency space with validation in chapter 3. 577

In chapter 4, we recall the classical Kolmogorov's 1941 theory on local homogenous 578
and isotropic turbulence together with intermittency and multifractal cascade ideas. 579
In chapter 5, we present an analytical model of the classical structure function analysis 580
to show its potential shortcoming. A similar analytical model is proposed to the 581
autocorrelation function of the velocity increment time series. It is found that the 582
autocorrelation function is a better inertial range indicator than structure functions. 583
In chapter 6, we apply the new Hilbert-based methodology to a turbulent database 584
from an experimental homogeneous and nearly isotropic turbulence experiment. We 585
recover the classical structure function scaling exponents $\zeta(q)$ in spectral space for the 586
first time. In chapter 7, we analyze a passive scalar (temperature) turbulence data 587
with very strong ramp-cliff structure, in which the classical structure function analysis 588
mode decomposition as Hilbert-Huang transform.

589 fails. In chapter 8, we generalize the Extended-Self-Similarity (ESS) into Hilbert
590 frame to compare the scaling property of turbulent velocity with various turbulent
591 intermittency models. We finally apply the new methodology to environmental time
592 series: river flow discharge data in chapter 9, and surf zone marine turbulence data
593 in chapter 10, to characterize the scale invariant properties in amplitude-frequency
594 space. In chapter IV, we draw the main conclusions of this thesis.

595 Chapter 2

596 Norden Huang's 1998 Proposal: 597 Hilbert-Huang Transform

598 About ten year ago, [Huang *et al.* \(1998, 1999\)](#) introduced a new method, namely
599 Hilbert-Huang transform or Empirical Mode Decomposition, to deal with time se-
600 ries analysis that was claimed to be well adapted for nonlinear and nonstationary
601 data. During the last ten years, there have been more than 1000 papers devoted to
602 apply this new method to various engineering applications and many different sci-
603 ence research fields. For example, waves ([Hwang *et al.*, 2003](#); [Veltcheva & Soares,
604 2004](#); [Schmitt *et al.*, 2009](#)), biological applications ([Echeverria *et al.*, 2001](#); [Baloc-
605 chi *et al.*, 2004](#); [Ponomarenko *et al.*, 2005](#)), financial studies ([Huang *et al.*, 2003b](#)),
606 meteorology and climate studies ([Coughlin & Tung, 2004](#); [Jánosi & Müller, 2005](#);
607 [Molla *et al.*, 2006](#); [Solé *et al.*, 2007](#); [Wu *et al.*, 2007](#); [Huang *et al.*, 2009b](#)), mechanical
608 engineering ([Loh *et al.*, 2001](#); [Chen *et al.*, 2004](#)), acoustics ([Loutridis, 2005](#)), aquatic
609 environment ([Schmitt *et al.*, 2007](#)), and turbulence ([Huang *et al.*, 2008](#)), to quote a
610 few. In this chapter, we introduce this method in detail.

2.1 Empirical mode decomposition

611

The most innovative part of the HHT is the Empirical Mode Decomposition. The starting point of the EMD is that most of the signal are multi-component, which means that there exist different scales simultaneously (Cohen, 1995; Huang *et al.*, 1998, 1999). This may be considered as faster oscillations superposed to slower ones at very local levels (Rilling *et al.*, 2003; Flandrin & Gonçalvès, 2004). We illustrate this idea in Fig. 2.1. The characteristic scale is taken, for EMD method, as the distance between two successive maxima positions. This idea was at the original of the introduction of Intrinsic Mode Function (IMF in the following). The definition of an IMF is: (i) the difference between the number of local extrema and the number of zero-crossings must be zero or at most one; (ii) the running mean value of the envelope defined by the local maxima and the envelope defined by the local minima is zero. Figure 2.2 shows an example of IMF. The next step is to consider how IMFs can be extracted from time series.

624

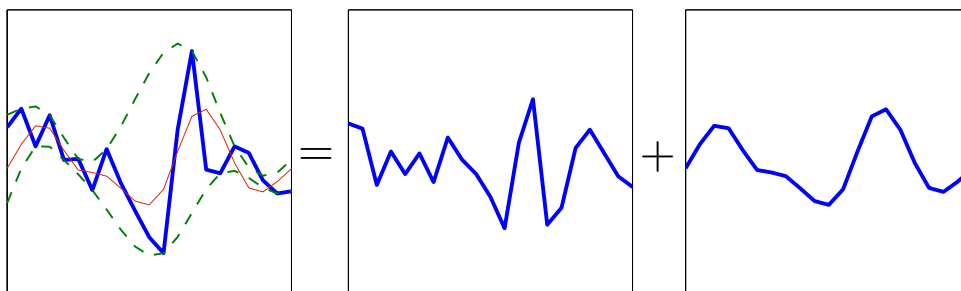


Figure 2.1: A schematic illustration of the basic idea of EMD. The original signal (thick line in the left diagram) is considered as the superposition of a faster oscillation (middle diagram) on a slower oscillation (right diagram).

Norden Huang *et al.* (1998, 1999) introduced the Empirical Mode Decomposition algorithm, called by himself “sifting process”, to decompose a given signal into several

625

626

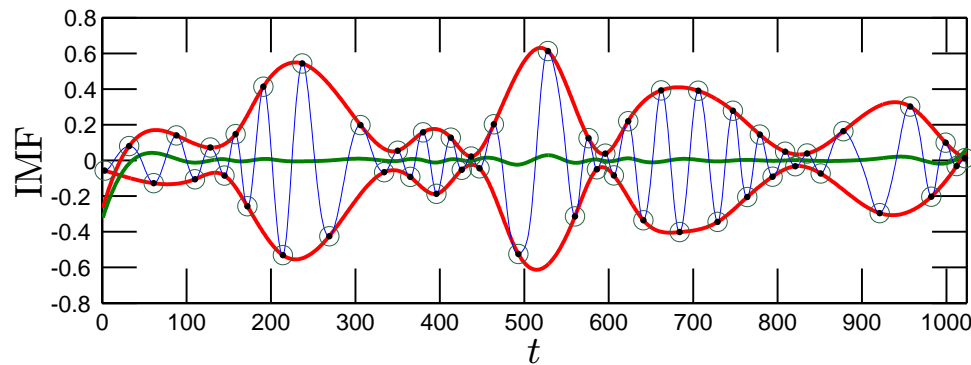


Figure 2.2: An example of IMF from EMD decomposition.

627 IMF modes (Flandrin *et al.*, 2004). The corresponding flow chart of this sifting process
 628 is shown in Fig. 2.3.

629 The first step of sifting process is to identify all the local extrema maxima (resp.
 630 minima) points for a given time series $x(t)$. Once all the local extrema maxima
 631 points are identified, the upper envelope $e_{\max}(t)$ is constructed by a cubic spline. The
 632 the procedure is repeated for the local extrema minima points to produce the lower
 633 envelope $e_{\min}(t)$. Then the mean between these two envelope is defined as

$$m_1(t) = \frac{e_{\max}(t) + e_{\min}(t)}{2} \quad (2.1.1)$$

634 The first component is then estimated by

$$h_1(t) = x(t) - m_1(t) \quad (2.1.2)$$

635 The procedure is illustrated in Fig. 2.4, where the the original data $x(t)$ are shown
 636 as thin solid line. Ideally, $h_1(t)$ should be an IMF as expected. In reality, however,
 637 $h_1(t)$ may not satisfy the condition to be an IMF. We thus take $h_1(t)$ as a new time
 638 series and repeat the sifting process j times, until $h_{1j}(t)$ is an IMF

$$h_{1j}(t) = h_{1(j-1)}(t) - m_{1j}(t) \quad (2.1.3)$$

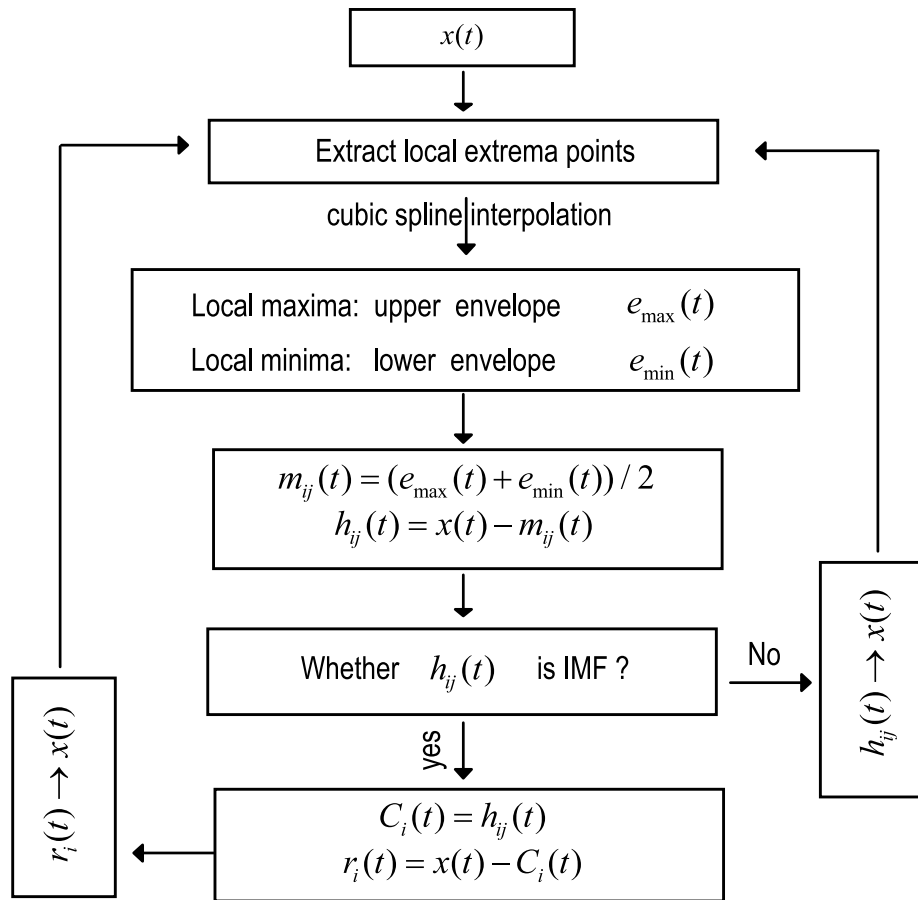


Figure 2.3: The flowchart of sifting process for EMD algorithm.

We thus extract the first IMF component $C_1(t)$

639

$$C_1(t) = h_{1j}(t) \quad (2.1.4)$$

and the residual $r_1(t)$

640

$$r_1(t) = x(t) - C_1(t) \quad (2.1.5)$$

from the data $x(t)$. An illustration of the first sifting process for a real time series

641

is shown in Fig. 2.4. The sifting procedure is then repeated on residual until $r_n(t)$

642

becomes monotonic function or at most has one local extreme point. This means no

643

more IMF can be extracted from $r_n(t)$. We finally have $n - 1$ IMF modes with one

644

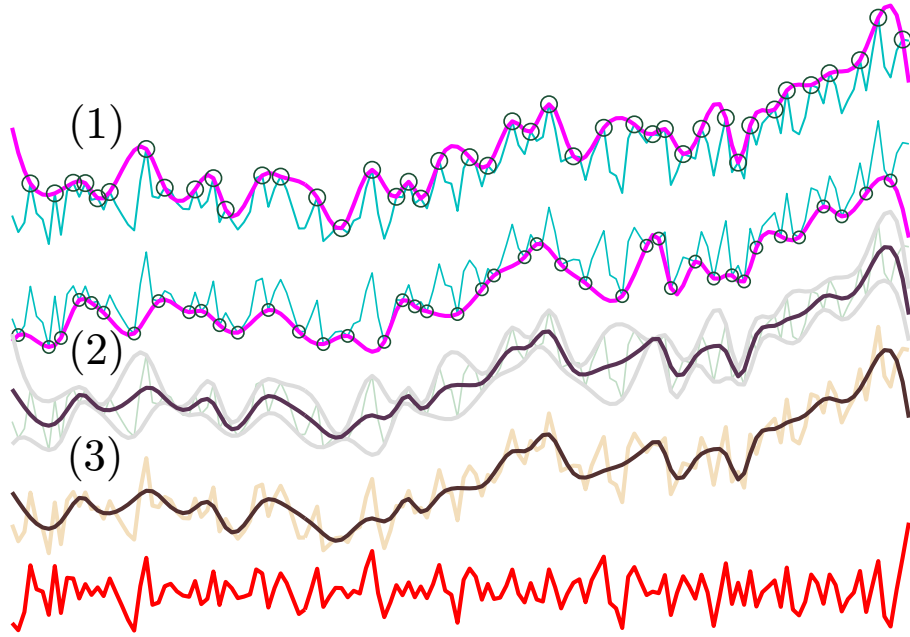


Figure 2.4: Illustration of the sifting process of EMD algorithm: (1) identify all the local extrema points (\circ), and construct the upper envelop $e_{\max}(t)$, and the lower envelop $e_{\min}(t)$, (2) calculate the running average $m_1(t)$, and (3) get the local detail $h_1(t)$ after 1st sifting. The original time series $x(t)$ is shown as thin solid line.

645 residual $r_n(t)$. The original data $x(t)$ is then rewritten as

$$x(t) = \sum_{i=1}^{n-1} C_i(t) + r_n(t) \quad (2.1.6)$$

646 Due to a dyadic filter bank property of the EMD algorithm (Wu & Huang, 2004;
647 Flandrin *et al.*, 2004; Huang *et al.*, 2008), usually in practice, the number of IMF
648 modes is less than $\log_2(N)$, where N is the length of the data set.

649 The above sifting process serves as two purposes: (i) to eliminate the riding wave,
650 (ii) to make the wave profiles more symmetric. Therefore, the sifting process should
651 be repeated enough times. However, if too many times sifting are performed, the
652 amplitude of the IMF modes will become constant, and the nonlinear wave profiles
653 is then distorted, which means the modes lose their physical meaning (Huang *et al.*,

1998, 1999). To guarantee that the IMF modes retain enough physical sense for both 654
 amplitude and frequency modulations, a stopping criterion has to be introduced to 655
 stop the sifting process. Different types of stopping criteria have been introduced by 656
 several authors (Huang *et al.*, 1998, 1999; Rilling *et al.*, 2003; Huang *et al.*, 2003a; 657
 Huang, 2005). We only describe here what we used in this thesis. The first stop 658
 criterion is a Cauchy-type convergence criterion. In this we introduce the standard 659
 deviation (SD), which is defined for two successive sifting process as 660

$$\text{SD} = \frac{\sum_{t=0}^T |h_{i(j-1)}(t) - h_j(t)|^2}{\sum_{t=0}^T h_{i(j-1)}^2(t)} \quad (2.1.7)$$

If a calculated SD is smaller than a given value, then the sifting stops and gives an 661
 IMF. A typical value proposed by Huang *et al.* (1998) is $0.2 \sim 0.3$, proposed based 662
 on their experience (Huang *et al.*, 1998). Another widely used criterion is based on 3 663
 thresholds α , θ_1 and θ_2 , which are designed to guarantee globally small fluctuations 664
 in the mean while taking into account locally large excursions (Rilling *et al.*, 2003). 665
 Mode amplitude and evaluation functions are then given by 666

$$a(t) = \frac{e_{\max}(t) - e_{\min}(t)}{2} \quad (2.1.8)$$

and 667

$$\sigma(t) = |m(t)/a(t)| \quad (2.1.9)$$

The sifting is iterated until $\sigma(t) < \theta_1$ for some prescribed fraction $1 - \alpha$ of the total 668
 duration, while $\sigma(t) < \theta_2$ for the remaining fraction. The typical values proposed by 669
 Rilling *et al.* (2003) are $\alpha \approx 0.05$, $\theta_1 \approx 0.05$ and $\theta_2 \approx 10 \theta_1$, respectively based on their 670
 experience. We also set the maximal iteration number, for example 300, to avoid to 671
 over-decompose the time series. In practice, if one of these criteria is satisfied, then 672
 the sifting process stops to give an IMF. 673

674 The above described EMD algorithm does the decomposition in a very local level
 675 in physical domain without *a priori* basis. It also means that it is an *a posteriori*
 676 method, since the basis (function) is induced by the data itself (Huang *et al.*, 1998,
 677 1999; Flandrin & Gonçalvès, 2004). The fully adaptiveness ability of this method
 678 explains that it can be considered to be well adapted for nonlinear and nonstationary
 679 data. However, the main drawback of this method is that it is not mathemati-
 680 cally proved (Huang, 2005). More detail about the EMD algorithm can be found in
 681 Refs. Huang *et al.* (1998, 1999); Rilling *et al.* (2003); Flandrin *et al.* (2004); Flandrin
 682 & Gonçalvès (2004); Huang (2005).

683 2.2 Hilbert spectral analysis

684 After having extracted the IMF modes, one can apply the associated Hilbert spectral
 685 analysis to each IMF component C_i in order to extract the energy-time-frequency
 686 information from the data (Long *et al.*, 1995; Huang *et al.*, 1998, 1999). The Hilbert
 687 transform of a function $C(t)$ is written as

$$\tilde{C}(t) = \frac{1}{\pi} P \int_0^{+\infty} \frac{C(t')}{t-t'} dt' \quad (2.2.1)$$

688 where ‘ P ’ means the Cauchy principle value (Cohen, 1995; Long *et al.*, 1995; Huang
 689 *et al.*, 1998). It is a singularity integration, which means that it should have a very
 690 local ability to denoting fluctuations. For each IMF mode, one can construct the
 691 analytic signal (Cohen, 1995), $\mathbb{C}_i(t)$, as

$$\mathbb{C}_i(t) = C_i(t) + j\tilde{C}_i(t) = \mathcal{A}_i(t)e^{j\theta_i(t)} \quad (2.2.2)$$

692 where

$$\mathcal{A}_i(t) = |\mathbb{C}_i(t)| = [C_i(t)^2 + \tilde{C}_i^2(t)]^{1/2}, \quad \theta_i(t) = \arctan \left(\frac{\tilde{C}_i(t)}{C_i(t)} \right) \quad (2.2.3)$$

26 Chapter 2. Norden Huang's 1998 Proposal: Hilbert-Huang Transform

Hence the instantaneous frequency can be defined by using the information of phase function $\theta_i(t)$, which is written as

$$\omega_i = \frac{d\theta_i(t)}{dt} \quad (2.2.4)$$

The original signal is finally represented (excluding the residual $r_n(t)$) as

$$x(t) = \text{RP} \sum_{i=1}^N \mathcal{A}_i(t) e^{j\theta_i(t)} = \text{RP} \sum_{i=1}^N \mathcal{A}_i(t) e^{j \int \omega_i(t) dt} \quad (2.2.5)$$

where 'RP' means real part. The Hilbert-Huang transform can be taken as a generalization of Fourier transform, see Eq. (1.1.3): it allows a frequency-modulation and amplitude-modulation simultaneously. A Hilbert spectrum, $H(\omega, t) = \mathcal{A}^2(\omega, t)$, is thus designed to represent the energy in time-frequency representation (Long *et al.*, 1995; Huang *et al.*, 1998). We further can define the Hilbert marginal spectrum as

$$h(\omega) = \int_0^{+\infty} H(\omega, t) dt \quad (2.2.6)$$

This is similar with the Fourier spectrum, and can be interpreted as the energy associated to each frequency. We however underline the fact that the definition of frequency here is different from the definition in the Fourier frame (Huang *et al.*, 1998, 1999).

We do not give the validation and calibration detail of the Hilbert-Huang transform here. For details of the validation and calibration, we suggest Refs. Huang *et al.* (1998, 1999).

708 2.3 Intrawave frequency modulation and nonlinear 709 mechanism

710 We have mentioned in chapter 1 that the the frequency modulation can be further
711 termed into two different types, intrawave frequency modulation and interwave fre-
712 quency modulation. Indeed, the former one may be linked to the nonlinear distortion.
713 More precisely, it may be considered as a signature of nonlinear mechanism. We show
714 this by an example.

715 Intrawave Frequency Modulation

716 We have taken Duffing equation as an example to show the nonlinear distortion of
Fourier representation. Figure 2.5 (a) reproduces the instantaneous frequency ω of the

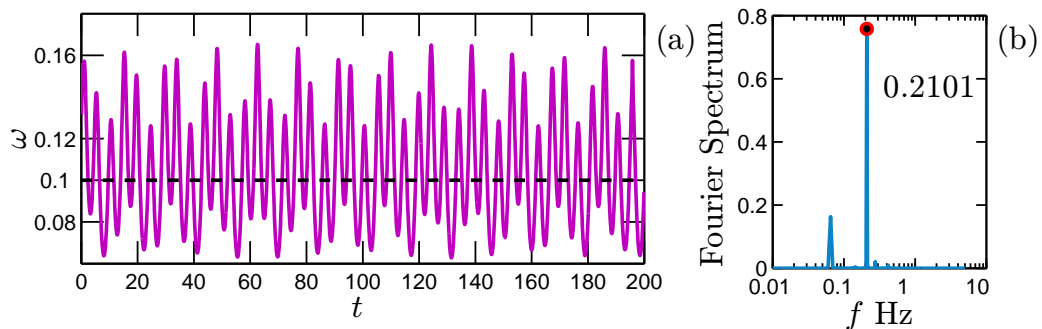


Figure 2.5: Illustration of the Intrawave Frequency Modulation by using Duffing equation: (a) instantaneous frequency of the 1st mode, (b) the Fourier energy spectrum of the instantaneous frequency of 1st mode, respectively.

717

718 first IMF mode of the numerical solution of the Duffing equation. One can find that
719 the instantaneous frequency ω itself varies with the time t between 0.05 ~ 0.15 Hz,
720 with a mean value of 0.1 Hz. This corresponds to frequency-modulation. We take ω as
721 a new time series and calculate its Fourier power spectrum. The corresponding Fourier
722 power spectrum is shown Fig. 2.5 (b). The dominant frequency is 0.21 Hz, twice of the

mean frequency of the 1st IMF mode. This means that the instantaneous frequency 723
 does vary within one period. This is an intrawave type of frequency modulation. We 724
 argue that it corresponds to a nonlinear mechanism behind the time series. 725

Interwave Frequency Modulation 726

We consider another type of FM here, interwave frequency modulation. We construct 727
 a linear chirp signal as (Flandrin, 1998): 728

$$x(t) = \sin\left(\frac{\pi}{20}t + \frac{\pi}{100}t^2\right), \quad 0 \leq t \leq 50 \tag{2.3.1}$$

The corresponding instantaneous frequency is written 729

$$\omega(t) = \frac{1}{40} + \frac{1}{200}t \tag{2.3.2}$$

Figure 2.6 shows (a) the constructed chirp signal and (b) the corresponding instan- 730
 tantaneous frequency. As a comparison with Fig. 2.5, one can immediately find the 731
 difference between them: the instantaneous frequency ω here is linearly increasing 732
 with time t .

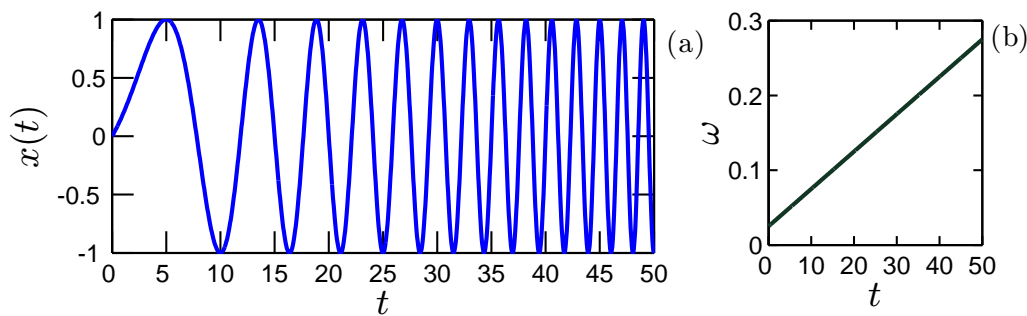


Figure 2.6: Illustration of the Interwave Frequency Modulation: (a) a chirp $x(t) = \sin(\frac{\pi}{20}t + \frac{\pi}{100}t^2)$, (b) the instantaneous frequency $\omega(t) = \frac{1}{40} + \frac{1}{200}t$, respectively.

734 **Nonlinear Mechanism**

735 For comparison convenience, we replot the first IMF mode of Duffing equation (top)
736 and the chirp signal (bottom) in Fig. 2.7. This illustrates the difference between
737 them. The former one provides a departure from the sine wave due to a nonlinear
738 mechanism. The latter still keeps sine wave profile from period to period. Thus,
739 any nonlinear distorted waveform has been referred to as “harmonic distortions for
Fourier based methods”.

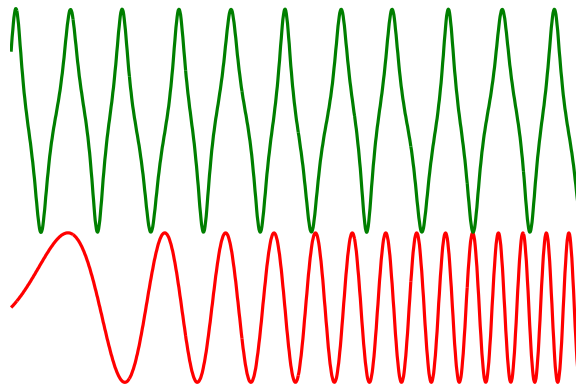


Figure 2.7: Comparison of the wave profiles of the first IMF mode of Duffing equation (top) and the chirp signal (bottom). The former one deviates from a pure sine wave profile with nonlinear distortion. The latter still keeps sine wave profile.

740

741 **2.4 Summary**

742 We introduced the Hilbert-Huang transform above, including the empirical mode
743 decomposition and the Hilbert spectral analysis. The combination of EMD and HSA
744 also is called Hilbert-Huang transform (HHT). It has been shown that the HHT has
745 fully self-adaptiveness and very local ability in both physical and spectral domains.
746 It is particularly suitable for nonstationary time series analysis.

30 Chapter 2. Norden Huang's 1998 Proposal: Hilbert-Huang Transform

The main drawback of the HHT is its lack of solid theoretical ground, since the 747
EMD part is almost empirical (Huang, 2005). Recently, Flandrin *et al.* have obtained 748
new theoretical results on the EMD method (Flandrin & Gonçalves, 2004; Rilling & 749
Flandrin, 2006, 2008, 2009). However, more theoretical work is still needed to fully 750
mathematically understand this method. 751

752 Chapter 3

753 Our Generalization: Arbitrary 754 Order Hilbert Spectral Analysis

755 We consider here the main contribution of our work: the generalization of the classical
756 Hilbert-Huang approach for arbitrary order moments, in order to deal with scaling
757 intermittent multifractal time series. The results presented in this chapter are pub-
758 lished in [Huang *et al.* \(2008, 2009a,d\)](#) [Y. Huang, *et al. Europhy. Lett.*, 84, 40010, 2008.;
759 Y. Huang, *et al. Traitement du Signal*, 25, 481-492, 2008; Y. Huang, *et al. Phys. Rev. E*,
760 2009 (submitted).]

761 3.1 Definition

762 The Hilbert marginal spectrum is defined as a marginal integration of the Hilbert
763 spectrum $H(\omega, t)$ over t , which is written as

$$h(\omega) = \int_0^{+\infty} H(\omega, t) dt \quad (3.1.1)$$

764 where $H(\omega, \mathcal{A})$ is the Hilbert spectrum. There is another equivalent definition, which
765 is based on the joint probability density function $p(\omega, \mathcal{A})$ of the instantaneous fre-
766 quency ω and the amplitude \mathcal{A} ([Long *et al.*, 1995](#); [Huang *et al.*, 2008, 2009a](#)). The

Hilbert marginal spectrum is thus rewritten as the marginal integral of the joint pdf $p(\omega, \mathcal{A})$ over \mathcal{A}^2

$$h(\omega) = \int_0^{+\infty} p(\omega, \mathcal{A}) \mathcal{A}^2 d\mathcal{A} \quad (3.1.2)$$

One can find that the above definition is no more than a second order statistical moment. This constatation leads us to generalize this approach to arbitrary order moment

$$\mathcal{L}_q(\omega) = \int_0^{+\infty} p(\omega, \mathcal{A}) \mathcal{A}^q d\mathcal{A} \quad (3.1.3)$$

where $q \geq 0^1$ (Huang *et al.*, 2008, 2009a). In case of scale invariance, we expect a power law of the form

$$\mathcal{L}_q(\omega) \sim \omega^{-\xi(q)} \quad (3.1.4)$$

where $\xi(q)$ is the corresponding Hilbert-based scaling exponent. Due to the integration operator, $\xi(q) - 1$ can be associated to the classical $\zeta(q)$ from structure function analysis: $\langle \Delta x_\ell^q \rangle \sim \ell^{\zeta(q)}$. Therefore, the generalized Hilbert spectral analysis provides a new methodology to characterize the scale invariance in an amplitude-frequency space (Huang *et al.*, 2008, 2009d,a).

In the following context, we validate and calibrate the idea of the arbitrary order HSA methodology by fractional Brownian motion simulations and a synthesized multifractal nonstationary time series.

¹In fact here q can be take as $q \geq -1$. However, we only consider the case $q \geq 0$ in this thesis.

782 3.2 Calibration and validation

783 3.2.1 Fractional Brownian motion and multifractal time series 784

785 Fractional Brownian Motion

786 Fractional Brownian motion (fBm) is a continuous-time random process proposed
787 by Kolmogorov (1940) in the 1940s and Yaglom (1957) and later named ‘fractional
788 Brownian motion’ by Mandelbrot & Van Ness (1968). It consists in a fractional in-
789 tegration of a white Gaussian process and is therefore a generalization of Brownian
790 motion, which consists simply in a standard integration of a white Gaussian pro-
791 cess (Mandelbrot & Van Ness, 1968; Flandrin, 1992; Samorodnitsky & Taqqu, 1994;
792 Beran, 1994; Rogers, 1997; Doukhan *et al.*, 2003; Gardiner, 2004; Biagini *et al.*, 2008).
793 Because it presents deep connections with the concepts of self-similarity, fractal, long-
794 range dependence or $1/f$ -process, fBm quickly became a major tool for various fields
795 where such concepts are relevant, such as in geophysics, hydrology, turbulence, eco-
796 nomics, communications, etc (Samorodnitsky & Taqqu, 1994; Gardiner, 2004; Biagini
797 *et al.*, 2008).

798 For a fBm $X(t)$ process, the autocorrelation is well known to be the following

$$R_H(t, t') = \frac{\sigma^2}{2} (|t|^{2H} + |t'|^{2H} - |t - t'|^{2H}) \quad (3.2.1)$$

799 where σ is the variance of $X(t)$, and H is the so-called Hurst number (Samorodnitsky
800 & Taqqu, 1994; Beran, 1994; Gardiner, 2004; Biagini *et al.*, 2008). The process is said
801 to be self-similar, since in terms of distributions for any real a

$$X(at) \sim |a|^H X(t) \quad (3.2.2)$$

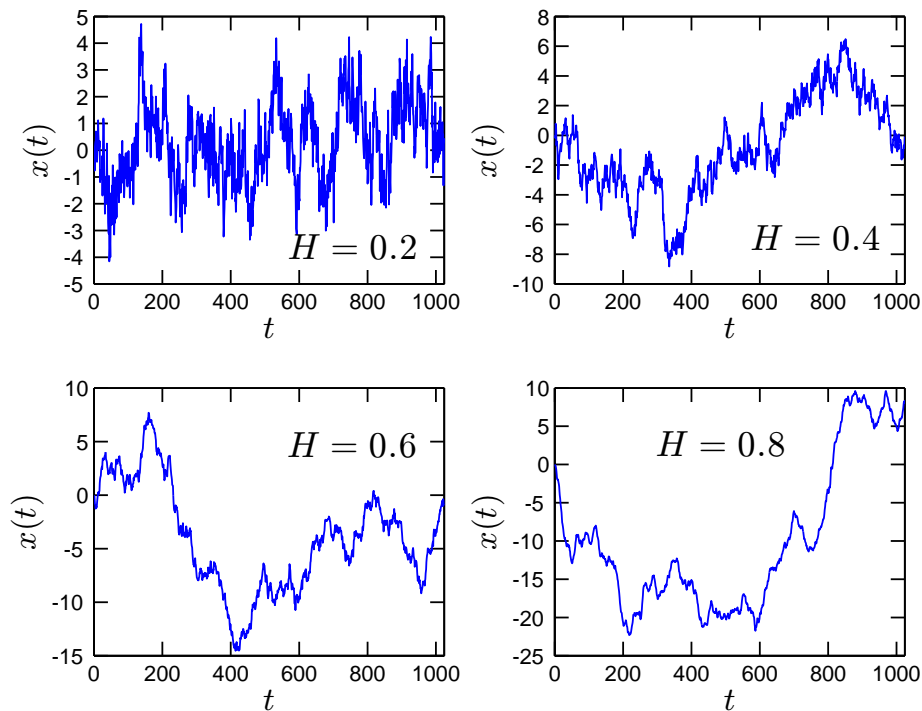


Figure 3.1: Illustration of fractional Brownian motion with various Hurst number H .

It is also well known for its stationary increments

802

$$X(t) - X(\tau) \sim X(t - \tau) \quad (3.2.3)$$

For the case $H > 1/2$, the process exhibits long-range dependence, which means that

803

$$\int_0^{+\infty} C(\tau) d\tau = \infty \quad (3.2.4)$$

where the autocorrelation function is written as

804

$$C(\tau) = \langle X(t)X(t + \tau) \rangle \quad (3.2.5)$$

in which $\langle \rangle$ means ensemble average.

805

The fBm is a classical monofractal process. It requires only one parameter, the

806

807 Hurst number H , to characterize the stochastic process. For structure function anal-
 808 ysis, the scaling exponents is well known to be the following

$$\langle |X(t + \tau) - X(t)|^q \rangle \sim \tau^{\zeta_H(q)}, \zeta_H(q) = qH \quad (3.2.6)$$

809 where $\zeta_H(q)$ is the scaling exponent from structure functions. We thus expect for the
 810 HSA approach the corresponding scaling exponents $\xi_H(q)$ to be the following

$$\mathcal{L}_{q,H}(\omega) \sim \omega^{-\xi_H(q)}, \xi_H(q) = qH + 1 \quad (3.2.7)$$

811 where the '+1' corresponds to the integration operator in Eq. (3.1.3).

812 We consider here a Wavelet based algorithm to simulate the fBm process, which
 813 was first proposed by Meyer (n.d.) and Sellan (1995), then developed by Abry &
 814 Sellan (1996). Starting from the expression of the fBm process as a integral of the
 815 fractional Gaussian noise process, the idea of the algorithm is to build a biorthogonal
 816 wavelet depending on a given orthogonal one and adapted to the parameter H . Then
 817 the generated sample path is obtained by the reconstruction using the new wavelet
 818 starting from a wavelet decomposition at a given level designed as follows: details
 819 coefficients are independent random Gaussian realizations and approximation coeffi-
 820 cients come from a fractional Autoregressive Integrated Moving Average (ARIMA)
 821 process. A MATLAB[®] code, namely wfbm, to realize this algorithm can be found
 822 in the Wavelet toolbox of MATLAB[®].

823 Figure 3.1 illustrates a 2^{12} data points portion of fBm with various Hurst numbers
 824 H by using above mentioned algorithm with db2 wavelet. One can find that for the
 825 long-range dependence case, $H > 1/2$, an increasing pattern in the previous steps is
 826 likely to be followed by the current increasing step as well.

The validation of the new arbitrary order Hilbert spectral analysis using this data series will be considered below.

Nonstationary Multifractal Time Series

Since the introduction of multifractal concepts in the 1980s (Parisi & Frisch, 1985; Grassberger & Procaccia, 1983; Benzi *et al.*, 1984; Grassberger, 1986) in the field of turbulence and chaos, this approach has met huge success.

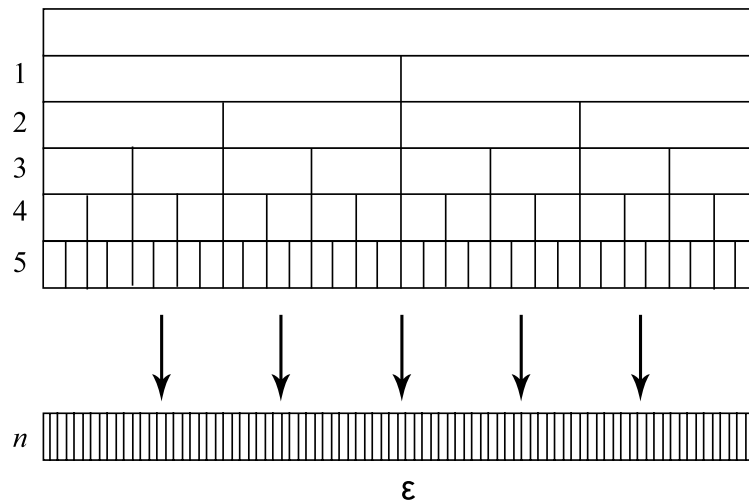


Figure 3.2: Illustration of the discrete cascade process. Each step is associated to a scale ratio of 2. After n steps, the total scale ratio is 2^n .

Multifractal properties have been found in many fields, such as, turbulence (Anselmet *et al.*, 1984; Frisch, 1995), financial time series (Ghashghaie & Dodge, 1996; Schmitt *et al.*, 1999; Lux, 2001; Calvet & Fisher, 2002), physiology (Ivanov *et al.*, 1999), rainfall (Schertzer & Lovejoy, 1987; Schmitt *et al.*, 1998; De Lima & Grassman, 1999; Venugopal *et al.*, 2006), etc. A multifractal process is a generalization of monofractal process, in which a single exponent, such as Hurst number H , is not enough to describe its dynamics; instead, a continuous spectrum of exponents is

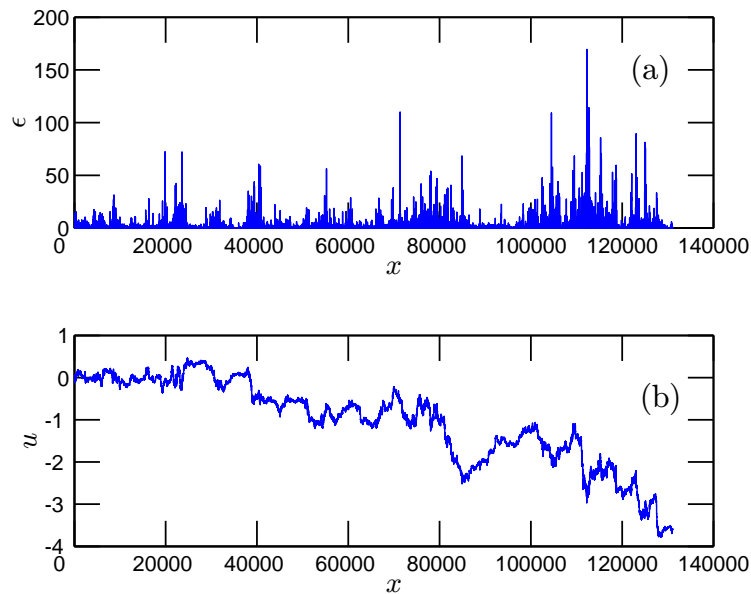


Figure 3.3: A sample for one realization 2^{17} points with $\mu = 0.25$: (a) the multifractal measure (b) the constructed multifractal nonstationary process.

840 needed.

841 For a few years now, new methods to generate nonstationary multifractal time se-
 842 ries mimicking turbulent velocity or passive scalar time series have been proposed (Muzy
 843 & Bacry, 2002). Here we adapt the idea of multifractal random walks using discrete
 844 multiplicative cascades (Schmitt, 2003).

845 We consider here a synthesized multifractal nonstationary time series, which is
 846 constructed based on a multiplicative discrete cascades (Schmitt, 2003). Figure 3.2
 847 illustrates the cascade process algorithm. The larger scale corresponds to a unique
 848 cell of size $L = \ell_0 \lambda_1^n$, where ℓ_0 is a fixed scale and $\lambda_1 > 1$ is dimensional scale ratio.
 849 For discrete model, this ratio is often taken as $\lambda_1 = 2$. The model being discrete,
 850 the next scale involved corresponds to λ_1 cells, each of size $L/\lambda_1 = \ell_0 \lambda_1^{n-1}$. This is
 851 iterated and at step p ($1 \leq p \leq n$) there are λ_1^p cells, each of size $L/\lambda_1^p = \ell_0 \lambda_1^{n-p}$.

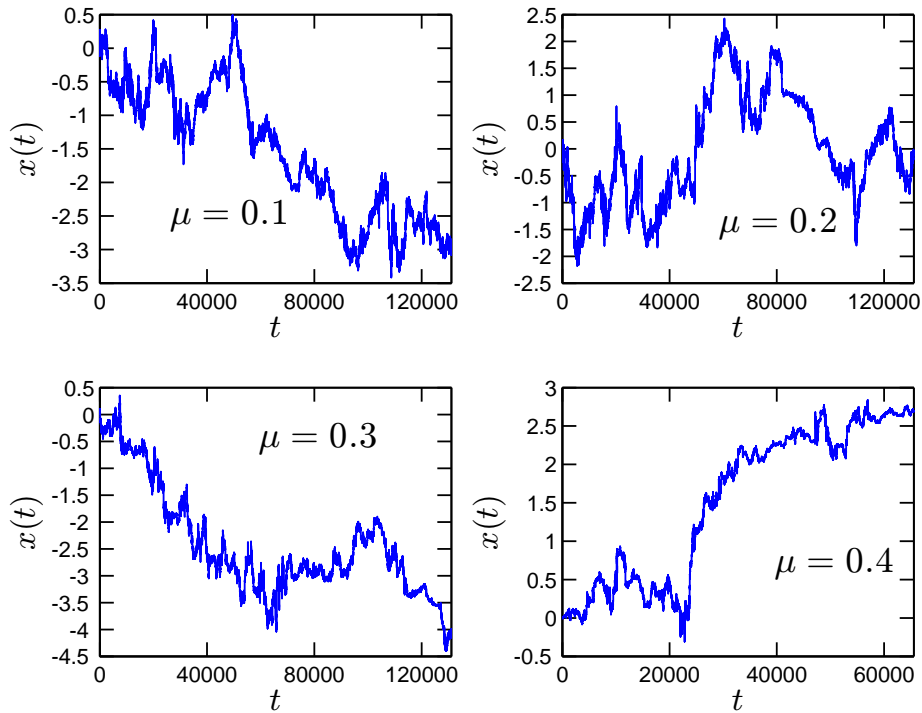


Figure 3.4: Illustration of synthesized nonstationary multifractal time series with various intermittent parameters μ .

There are n cascade steps, and at step n there are λ_1^n cells, each of size ℓ_0 , which 852
is the smallest scale of the cascade. To reach this scale, all intermediate scales have 853
been involved. Finally, at each point the multifractal measure writes as the product 854
of n cascade random variables 855

$$\epsilon(x) = \prod_{p=1}^n W_{p,x} \quad (3.2.8)$$

where $W_{p,x}$ is the random variable corresponding to position x and level p in the 856
cascade (Schmitt, 2003). Following multifractal random walk ideas (Bacry *et al.*, 857
2001; Muzy & Bacry, 2002), we generate a nonstationary multifractal time series as 858

$$u(x) = \int_0^x \epsilon(x')^{1/2} dB(x') \quad (3.2.9)$$

where $B(x)$ is Brownian motion. Taking lognormal statistic for ϵ , the scaling exponent 859

860 $\zeta(q)$ such as $\langle |\Delta u_\tau(t)|^q \rangle \sim \tau^{\zeta(q)}$ is written as

$$\zeta(q) = \frac{q}{2} - \frac{\mu}{2} \left(\frac{q^2}{4} - \frac{q}{2} \right) \quad (3.2.10)$$

861 where μ is the intermittency parameter ($0 \leq \mu \leq 1$) characterizing the lognormal
862 multifractal cascade (Huang *et al.*, 2009d).

863 A sample for one realization is shown in Fig. 3.3 (a) the multifractal measure, and
864 (b) the nonstationary multifractal time series, with $\mu = 0.25$, and $n = 17$ levels, cor-
865 responding to data sets with data length 2^{17} points. Figure 3.4 shows the synthesized
866 nonstationary multifractal time series with various intermittent parameters μ .

867 As for fBm time series, these multifractal synthetic time series are analyzed below
868 using our new method.

869 3.2.2 Calibration and validation

870 Monofractal Processes: Fractional Brownian Motions

871 For the fBm process, we simulate 500 segments of length 2^{12} data points each, using
872 above mentioned wavelet based algorithm (Abry & Sellan, 1996), with db2 wavelet
873 and various Hurst values from 0.1 to 0.9. The Hilbert transform is numerically esti-
874 mated by using a FFT based method (Marple Jr, 1999). Figure 3.5 shows the first six
875 order Hilbert marginal spectrum for $H = 0.4$ and 0.6 . Power law is observed for each
876 curve as expected. The scaling exponent $\xi(q)$ is then estimated on the corresponding
877 power law range by a first order least square fitting algorithm. We then represent the
878 corresponding scaling exponents $\xi(q)$ for various value of q from 0 to 6 in Fig. 3.6,
879 in which perfect straight lines of equation $1 + qH$ confirms the usefulness of the new
880 method to estimate $\xi(q)$.

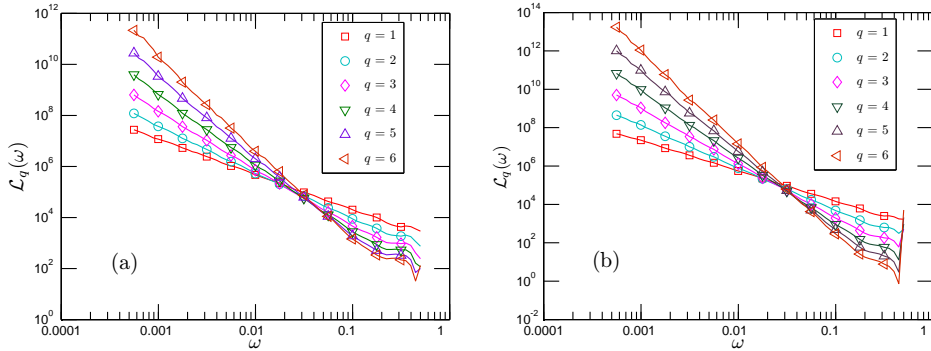


Figure 3.5: The first six order Hilbert marginal amplitude spectra of fractional Brownian motion with Hurst number (a) $H = 0.4$, and (b) $H = 0.6$. Power law behaviour is observed for each curve as expected.

We then consider estimation of the H value. For this, we consider different estimators. They involve the first and second order moment. These estimators are

$$H^\dagger = \xi(1) - 1 \quad (3.2.11a)$$

$$H^\star = (\xi(2) - 1)/2 \quad (3.2.11b)$$

and using the least square fitting for all q

$$H^\diamond = (\xi(q) - 1)/q \quad (3.2.11c)$$

The estimated H_{est} are shown in Fig. 3.7 for H^\dagger (\triangleright), H^\star (\circ) and H^\diamond (\square). They are in good agreement with the theoretical H . The mean error for each estimator are 5.3%, 3.1% and 9.4%. For comparison, we reproduce the estimated value H from Ref. Rilling *et al.* (2005), in which two estimators \hat{H}_1 (∇), \hat{H}_2 (\triangle) based on IMF modes and one estimator based on discrete wavelet transform H_W (\diamond) are presented. We also show the absolute error $|H_{\text{est}} - H|$, the estimated values departure from the given Hurst number H as inset, where the gray patch indicates the deviation less than 5%. We underline that Rilling *et al.* (2005) simulated the fractional Gaussian

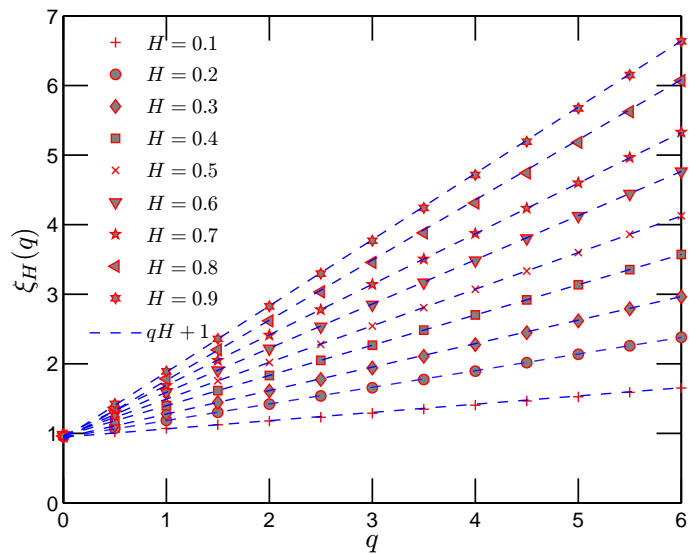


Figure 3.6: Scaling exponents $\xi_H(q)$ for fractional Brownian motion simulations with H from 0.1 to 0.9.

894 noise by using the algorithm proposed by Wood & Chan (1994). Their proposed
 895 estimators \hat{H}_1 and \hat{H}_2 are based on the assumption of a dyadic filter bank for the
 896 EMD method (Rilling *et al.*, 2005). If the absolute error is less than 5%, then there
 897 is no significant difference between estimators. Their results show two different range
 898 for $H < 1/2$ and $1/2 < H$, see Fig. 3.7, in which it is indicated by the vertical dashed
 899 line. They argued that for the case where $H < 1/2$, the dyadic filter bank property
 900 which underlies the EMD approach is only an approximation that has to be refined
 901 further (Rilling *et al.*, 2005). The estimators H^\dagger , H^* and H^\diamond we proposed here may
 902 provide more precise estimators, since they do not require the dyadic property.

903 The above numerical experiment confirms the usefulness of the arbitrary order
 904 Hilbert spectral analysis methodology for the monofractal case.

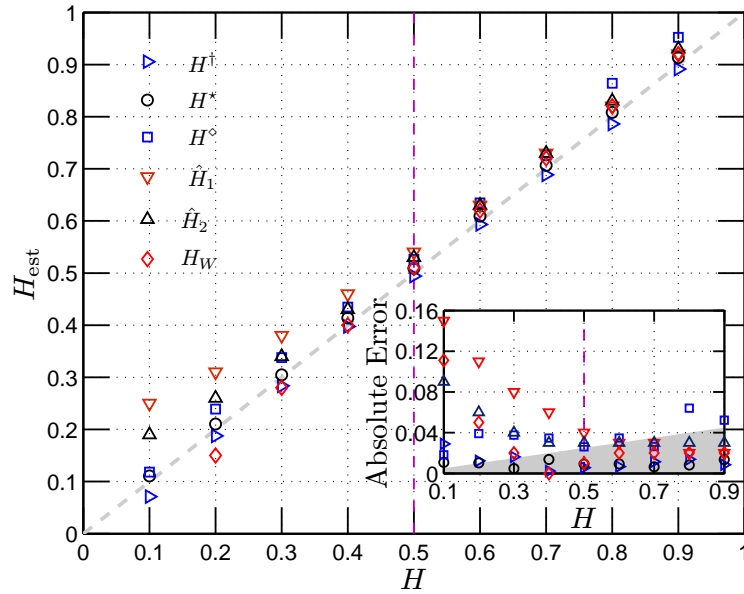


Figure 3.7: Representation of the estimation Hurst number H^\dagger (\triangleright), H^* (\circ) and H^\diamond (\square) with the theoretical values H used for simulations. For comparison, the values from Ref. [Rilling *et al.* \(2005\)](#) are also presented, using the estimator \hat{H}_1 (∇), \hat{H}_2 (\triangle) and discrete wavelet transform H_W (\diamond). The inset shows the absolute error for each estimator. The gray patch indicates when the absolute error $|H_{\text{est}} - H|$ is less than 5%.

Multifractal Process: Nonstationary Multifractal Time Series

905

We then validate the Hilbert-based methodology for intermittent time series by con- 906
 sidering the synthesized nonstationary multifractal time series, and quantify the error 907
 parameter estimation. For each realization, we choose $n = 17$ levels with data length 908
 2^{17} points each. We estimated the structure function on the range $2 < \tau < 10000$. The 909
 corresponding scaling exponents $\zeta(q)$ are then estimated on the range $10 < \tau < 1000$. 910
 For the HSA approach, the 2^{17} points are divided into several segments, each one 911
 with 2^{14} points. This averaged Hilbert marginal spectrum is taken for each realiza- 912
 tion. Power law behaviour is found on the range $0.0002 < \omega < 0.3$, corresponding to 913
 $3 < \tau < 5000$. The corresponding scaling exponents $\xi(q)$ are then estimated on this 914

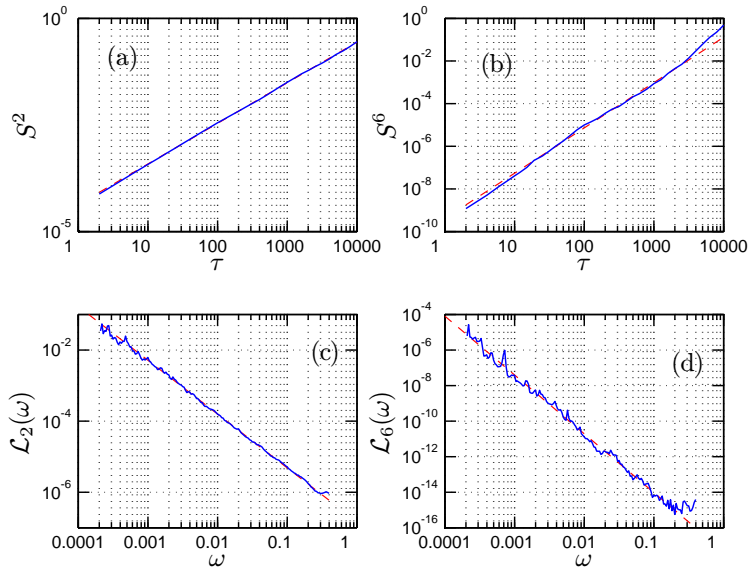


Figure 3.8: Structure function and Hilbert marginal spectra for one 2^{17} points realization (a) the second order structure function, (b) the six order structure function, (c) the second order Hilbert marginal spectrum and (d) the six order Hilbert marginal spectrum, where the dashed line in each figure is the best fit in least square sense.

915 range. Figure 3.8 shows the second and the sixth order structure functions and the
 916 corresponding Hilbert marginal spectra for one realization, where the dashed line is
 917 the least square fitting of the power law. For comparison convenience, we consider in
 918 the following $\xi(q) - 1$.

919 We then consider the convergence of the scaling exponents. For this we consider
 920 the number of realization n and for each n , for $i \in [1, n]$, we estimate separately each
 921 value ζ_i (or ξ_i). We also take

$$\bar{\zeta}(q) = \lim_{n \rightarrow \infty} \frac{1}{n} \sum_{i=1}^n \zeta_i(q) \quad (3.2.12)$$

922 Then the convergence is characterized by the ratio

$$\mathcal{R}_n(q) = \frac{1}{n} \frac{\sum_{i=1}^n \zeta_i(q)}{\bar{\zeta}(q)} \quad (3.2.13)$$

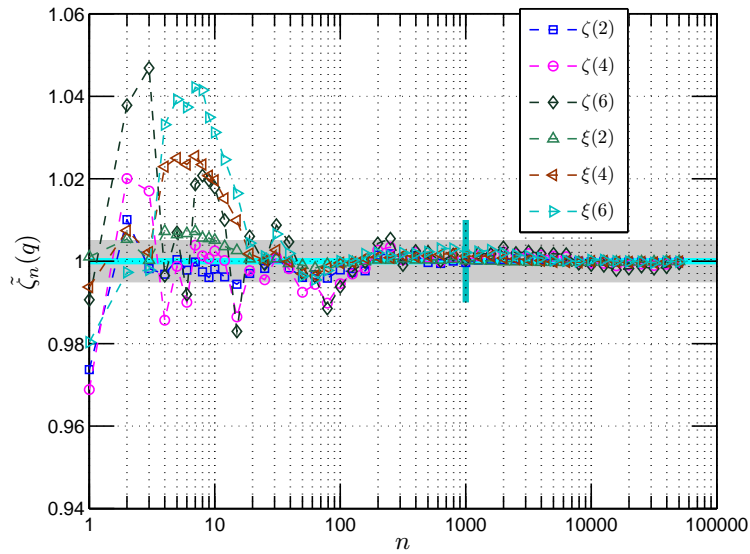


Figure 3.9: The n -dependence of the average estimator $\tilde{\zeta}_n(q)$ for various q , where n is the number of realization. The vertical solid line indicates the number $n = 1000$.

where $\lim_{n \rightarrow \infty} \mathcal{R}_n(q) = 1$. Figure 3.9 shows the convergence of this ratio for n between 923
 1 and 70,000 for the case $\mu = 0.25$. It shows that if one wants an error of 1% in the 924
 estimation of ζ , $n = 100$ realizations are enough. In the following we consider 70,000 925
 realizations corresponding in average to an error $100 \times |1 - \mathcal{R}_n|$ in the estimation of 926
 $\bar{\zeta}(q)$ (resp. $\bar{\xi}(q)$) of 0.02% for $q = 2$, 0.07% for $q = 4$ and 0.13% for $q = 6$ for structure 927
 functions, and 0.03% for $q = 2$, 0.04% for $q = 4$ and 0.05% for $q = 6$ for HSA. This 928
 shows that we obtain very precise estimates of $\bar{\zeta}(q)$ (resp. $\bar{\xi}(q)$). 929

Fig. 3.10 shows the pdf of the scaling exponents provided by structure functions 930
 and the HSA approach for $q = 2$ and 6 estimated for individual realizations, where 931
 the solid line is the Gaussian distribution fitting. These graphics show the spreading 932
 of the scaling exponents estimates. The number $n = 70,000$ of realizations considered 933
 here is rather huge compared to other multifractal studies, and represents a rather 934
 consequent numerical effort. Graphically, for small values of q , the variability in the 935

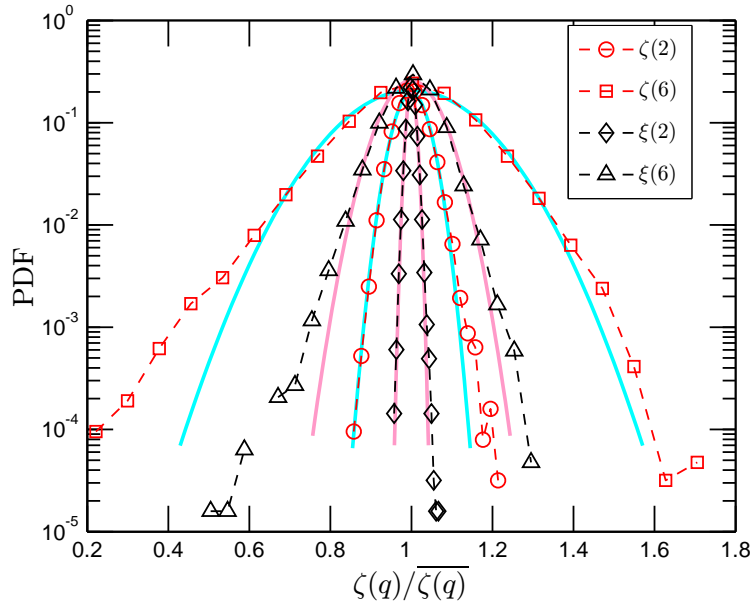


Figure 3.10: pdf of scaling exponents $\zeta(q)$ (resp. $\xi_n(q) - 1$) for 70,000 realizations with $\mu = 0.25$. The solid line is the Gaussian fitting.

936 estimation of scaling exponents provided by both approaches are quite close to the
 937 Gaussian distribution. We also note that the shape of the pdf corresponding to the
 938 HSA approach is narrower, which indicates that this approach provides a more precise
 939 estimator of multifractal parameters.

940 We show the scaling exponents predicted by the structure functions (\square) and the
 941 HSA approach (\circ) in Fig. 3.11 for the cases $\mu = 0.25$ with $n = 70,000$, where the
 942 inset shows the departure from $q/2$. The curves provided by the two methods are in
 943 good agreement with each other.

944 We synthesized the multifractal time series with various intermittent parameter
 945 μ from 0.1 to 0.5, and 1000 realizations for each case (except the case $\mu = 0.25$). We
 946 estimate μ by considering the first order derivative of Eq. (3.2.10). We then have the

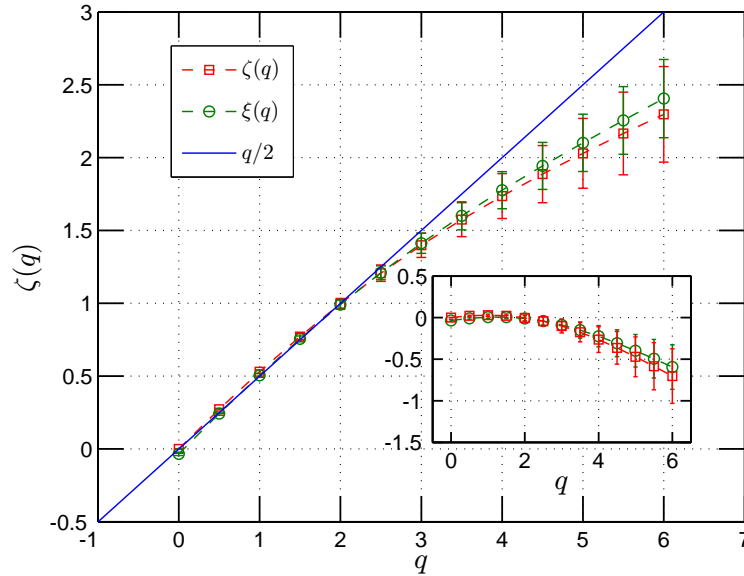


Figure 3.11: Representation of scaling exponents $\zeta(q)$ (resp. $\xi(q) - 1$) for 70000 realizations with $\mu = 0.25$.

estimator μ^* given by

$$\mu^* = \frac{2 - 4\zeta'(q)}{q - 1} \quad (3.2.14)$$

where $\zeta'(q)$ is the first derivative of $\zeta(q)$. The first order derivative can be estimated by the central finite difference algorithm with a second order accuracy

$$\zeta'(q) \simeq \frac{\zeta(q + \delta q) - \zeta(q - \delta q)}{2\delta q} \quad (3.2.15)$$

where δq is the increment of the order q . To estimate the first order derivative more accurately, we may firstly fit the scaling exponents $\zeta(q)$ by a quadratic polynomial, which is suggested by Eq. (3.2.10)

$$\zeta(q) \simeq p_1 q^2 + p_2 q + p_3 \quad (3.2.16)$$

where p_1 , p_2 and p_3 are fitting coefficients in least square sense. We thus have

$$\zeta'(q) \simeq 2p_1 q + p_2 \quad (3.2.17)$$

954 We show the estimated μ^* with $q = 2$ in Fig. 3.12, where the inset shows the relative
 955 error (in %) from the theoretical μ values. It seems that both methods slightly overes-
 956 timate μ ; however, the HSA provides a better estimation of μ , which may be linked to
 957 the local ability of the method both in the physical and frequency domains (Huang
 958 *et al.*, 1998, 2008). We thus have shown above the usefulness of the present new
 959 methodology to extract multifractal exponents with values consistent with structure
 functions.

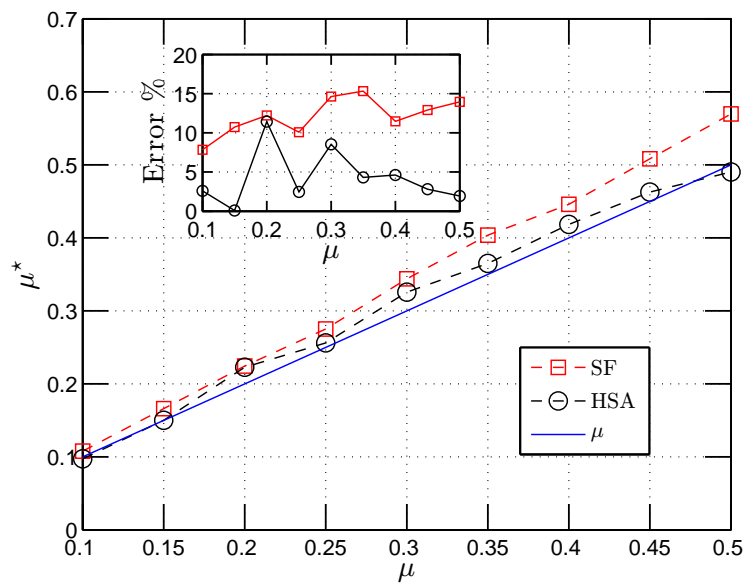


Figure 3.12: Representation μ^* , which is estimated by $\mu^* = 2 - 4\zeta'(2)$. We first fit the corresponding scaling exponent by a quadratic polynomial. Then the first order derivative is estimated by Eq. (3.2.17).

3.3 Marginal pdf of the Instantaneous Frequency

We consider here a special case, the zeroth order Hilbert marginal spectrum, which is written as

$$\mathcal{L}_0(\omega) = \int_0^{+\infty} p(\omega, \mathcal{A}) d\mathcal{A} \quad (3.3.1)$$

a marginal integration over \mathcal{A} . More precisely, it is the marginal pdf of the instan-

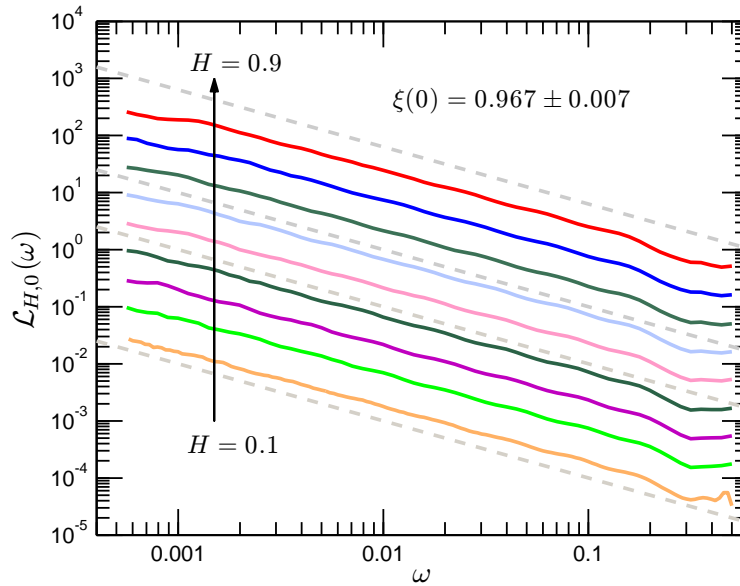


Figure 3.13: The zeroth order Hilbert marginal spectrum $\mathcal{L}_{H,0}(\omega)$ for various H . It is also the marginal pdf for the instantaneous frequency ω . The value of the scaling exponent is found as $\xi_H(0) = 0.967 \pm 0.007$. The slope of the dashed line is -1.

taneous frequency ω . We note that the scaling exponent $\xi(0) \simeq 1$ for all H and μ , for example, see Fig. 3.6 and Fig. 3.11². Figure 3.13 shows the corresponding zeroth order Hilbert marginal spectra $\mathcal{L}_{H,0}(\omega)$ for various H , where the dashed line indicates the line with slope -1. The scaling exponents are then estimated on each power law range. The mean scaling exponent is calculated as $\xi_H(0) = 0.967 \pm 0.007$. A ‘-1’ like

²For the other μ , the zeroth scaling exponents are also quite close to 1.

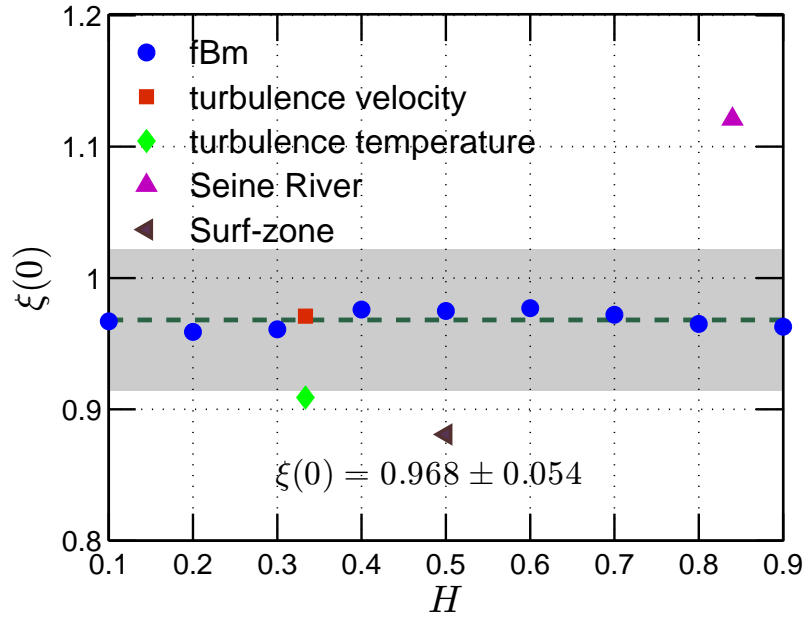


Figure 3.14: The scaling exponent $\xi(0)$ of the zeroth order Hilbert marginal spectrum $\mathcal{L}_0(\omega)$ for different types data: fractional Brownian motion (\bullet), velocity turbulence (\blacksquare), temperature turbulence (\blacklozenge), the Seine river discharge (\blacktriangle), and marine surf-zone (\blacktriangleleft). The value $\xi(q)$ is found to be close to 1: 0.968 ± 0.054 , which is marked as the gray patch. The dashed line indicates the mean value of $\xi(0)$.

970 power law for the zeroth order Hilbert marginal spectrum is also found in various
 971 experimental data, for example, turbulence velocity (Huang *et al.*, 2008) (\blacksquare), turbu-
 972 lence temperature (\blacklozenge), Seine river flow discharge (Huang *et al.*, 2009b) (\blacktriangle), surf-zone
 973 fluctuation (\blacktriangleleft), etc. Figure 3.14 represents the corresponding $\xi(0)$ for different types
 974 data. A mean scaling exponent is then estimated as

$$\langle \xi(0) \rangle = 0.968 \pm 0.054 \quad (3.3.2)$$

975 It seems that the zeroth order scaling exponent $\xi(0) \simeq 1$ is a quite general property
 976 of the present Hilbert-based methodology (Huang *et al.*, 2008). This brings us a
 977 question: whether this exponent $\xi(0) = 1$ for the zeroth order Hilbert marginal
 978 spectral $\mathcal{L}_0(\omega)$ is physically meaningful? If yes, what does it really mean? It should

be a subject of further studies for future work.

979

3.4 Summary

980

In this chapter we have proposed a new methodology, namely arbitrary order Hilbert spectral analysis, to characterize the scale invariance directly in amplitude-frequency space (Huang *et al.*, 2008, 2009d,a). We have calibrated and validated the new method by fractional Brownian motion simulation for the monofractal case and by synthesized multifractal time series for the multifractal intermittent case. We found that the Hilbert-based methodology provides a better Hurst estimator for $0 < H < 1$. The numerical experiments, performed for $n = 70,000$ realizations each of size 2^{17} for multifractal time series, have shown that the HSA approach provides a better estimator than structure function. We have also found that the scaling exponent for the zeroth order Hilbert marginal spectrum or the marginal pdf of the instantaneous frequency is quite close to 1. It seems that it is a general property of the present method, still to be further understood.

992

We provide some comments on the present methodology, that we called “Arbitrary Order Hilbert Spectral Analysis”. The arbitrary order Hilbert spectral analysis is an extended version of the Hilbert-Huang transform. Therefore, it inherits all the advantages and shortcomings of the HHT. The main drawback of the HHT method is its lack of solid mathematical ground, since the EMD part is almost empirical (Huang, 2005). It has been found experimentally that the method, especially for the HSA, is statistically stable with different stopping criteria (Huang *et al.*, 2003a). Furthermore, the present method measures the scale invariant properties directly in an amplitude-frequency space (Huang *et al.*, 2008, 2009d,a). For the joint pdf, it seems that it

1000

1001

1002 requires a large sample size to get a good statistical quantities. We find that the joint
1003 pdf itself may be scattered, but the Hilbert marginal spectrum may converge ([Huang](#)
1004 *et al.*, 2008). However, we need more theoretical/experimental work to help us to
1005 fully understand the present Hilbert-based method.

1006

Part II

1007

Application to Fully Developed

1008

Turbulence

1009 Chapter 4

1010 Homogeneous Turbulence and 1011 Intermittency: Velocity and 1012 Passive Scalar

1013 It is well-known that turbulence is the “last great unsolved problem of the classical
1014 physics” (Feynman, 1964). Let us recall the problem of turbulence here.

1015 Since Reynolds’ very famous experiment and seminal paper of 1894 (Reynolds,
1016 1883, 1894), turbulence has attracted many researchers interest. However, even after
1017 long time studies (Navier-Stokes equations date back to 1821), the problem of tur-
1018 bulence is still open. It is often believed that turbulence researches are still in their
1019 infancy (Lumley, 1992; L’vov & Procaccia, 1997; Yaglom, 2001; Lumley & Yaglom,
1020 2001; Tsinober, 2001). Let us quote Sir Lamb’s famous story here (L’vov & Procac-
1021 cia, 1997). In 1932, in an address to the British Association for the Advancement of
1022 Science, he wittily expressed the difficulty of explaining and studying turbulence in
1023 fluids. He said

1024 “ I am an old man now, and when I die and go to Heaven there are two
1025 matters on which I hope enlightenment. One is quantum electro-dynamics
1026 and the other is turbulence of fluids. About the former, I am really rather

optimistic. ”

1027

Soon after this Kolmogorov's 1941 (K41) phenomenological theory of turbulence was one of the main successful phenomenological theories to help us quantitatively understanding the turbulence. In this chapter, we will recall the classical framework of K41 and its continuation dealing with intermittency and multifraction cascade

1028

1029

1030

1031

The Navier-Stokes equations for the velocity field u of an incompressible fluid are

1032

$$\partial_t u + (u \cdot \nabla)u = \frac{\nabla p}{\rho} + \nu \Delta u + f, \quad \nabla \cdot u = 0 \quad (4.0.1)$$

where p is the pressure, ρ the density, f an external force and ν the kinematic viscosity.

1033

The flow is controlled by the Reynolds number

1034

$$Re = \frac{UL}{\nu} \quad (4.0.2)$$

where U and L are the characteristic velocity and length scale of the fluid. It measures

1035

the ratio between the inertial forces and the viscous forces. The number of degrees of

1036

freedom may link to the Reynolds number as $Re^{9/4}$ by a dynamical arguments (Bohr

1037

et al., 1998). As a consequence, for high Reynolds number turbulent flows, it is im-

1038

possible to produce a direct numerical analysis/simulation of Navier-stokes equations.

1039

Furthermore, a numerical simulation just reproduces the turbulent flow phenomena

1040

numerically. It does not reveal the underlying mechanisms. The difficulties also come

1041

from the fact that the Navier-Stokes equations are nonlinear, nonintegrable and non-

1042

local simultaneously (Tsinober, 2001). We still need a statistical theory to describe

1043

the turbulent flows, and more experiments to accumulate knowledge about the turbu-

1044

lent flows (Lumley & Yaglom, 2001; Yaglom, 2001; Tsinober, 2001). Here we consider

1045

the homogeneous and locally isotropic turbulence and focus on 1D turbulent time

1046

series.

1047

1048 **4.1 Kolmogorov's 1941 theory**1049 **Richardson Cascade**1050 We quote Richardson's famous words here ([Richardson, 1922](#)):

Big whirls have little whirls
 that feed on their velocity
 and little whirls have lesser whirls
 and so on to viscosity in the molecule sense.

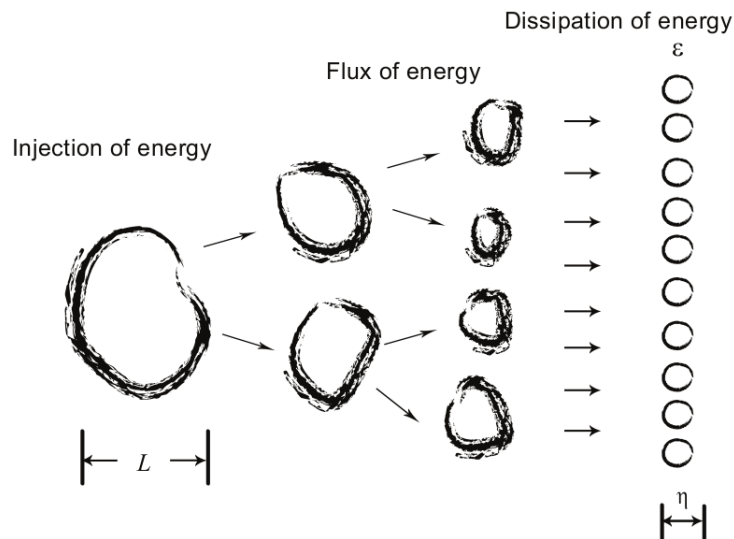


Figure 4.1: Illustration of the cascade process: the eddy is broken from integral scale L , where the energy injects into turbulent flow, to Kolmogorov scale η , where energy converts into heat.

1052 It describes qualitatively a picture of an energy flux from large vortices to small ones.

1053 It is often believed that the energy injects into the flow from large forcing scale L ,

1054 called integral scale. The energy transforms the energy from a large scale to a small

1055 scale on the inertial subrange, $\eta \ll \ell \ll L$, until one reaches the finest scale η , namely

Kolmogorov scale. Due to the fluid viscosity, the energy is then converted into heat at this finest scale. Figure 4.1 demonstrates this procedure.

Kolmogorov's 1941 Phenomenological Theory

In 1935, Sir G.I. Taylor postulated the concept of homogeneous and isotropic turbulence behind a grid, which is an ideal model of turbulence (Taylor, 1935). In the same time, he introduced the powerful Fourier analysis into turbulence research (Taylor, 1935, 1938). In 1941, Kolmogorov proposed a different version of homogeneous and locally isotropic turbulence (Kolmogorov, 1941a), in which the statistical properties of turbulent quantities of the velocity field are independent of the position and rotation of the axes. Based on the Richardson cascade, he postulated the famous two universality hypotheses (Kolmogorov, 1941a; Monin & Yaglom, 1971; Frisch, 1995):

Hypothesis 4.1.1 (Kolmogorov's First Universality Hypothesis). At very high, but not infinite Reynolds numbers, all the small scale statistical properties are uniquely and universally determined by the scale ℓ , the mean energy dissipation rate ϵ and the viscosity ν .

Hypothesis 4.1.2 (Kolmogorov's Second Universality Hypothesis). At very high, but not infinite Reynolds numbers, if $\eta \ll \ell \ll L$, then the statistical properties at scale ℓ are uniquely and universally determined by the scale ℓ , and the mean energy dissipation rate ϵ .

In his original paper Kolmogorov considered only the second order structure function

$$B_{dd}(r) = \langle \Delta u(r)^2 \rangle \quad (4.1.1)$$

1076 where $\Delta u(r) = u(x+r) - u(x)$ is the velocity increment and r is the separation scale.
 1077 Kolmogorov's second universality hypothesis together with dimensional consideration
 1078 gives

$$B_{dd}(r) \sim c\bar{\epsilon}^{2/3}r^{2/3} \quad (4.1.2)$$

1079 where c is the Kolmogorov constant and is believed to be universal (Kolmogorov,
 1080 1941a; Monin & Yaglom, 1971; Frisch, 1995). Independently from Kolmogorov,
 1081 Obukhov (1941) used the power spectrum of the velocity field and obtained the -
 1082 5/3 power law

$$E_{11}(k) = C_0\bar{\epsilon}^{2/3}k^{-5/3} \quad (4.1.3)$$

1083 where C_0 is the Kolmogorov constant and k is the wavenumber. These two 2/3
 1084 and -5/3 laws are mathematically equivalent and have since been verified by many
 1085 experiments (Grant *et al.*, 1962; Anselmet *et al.*, 1984).

1086 4.2 Intermittency and Kolmogorov's 1962 theory

1087 Energy Dissipation and Intermittency

1088 In his original postulation, Kolmogorov assumed that the energy dissipation rate of
 1089 each unite ϵ is almost constant. The energy dissipation ratio ϵ is defined as

$$\epsilon = \frac{\nu}{2} \sum_{i,j} \left(\frac{\partial u_i}{x_j} + \frac{\partial u_j}{x_i} \right)^2 \quad (4.2.1)$$

1090 where ν is the kinematic viscosity. Soon after Kolmogorov's K41 theory, Landau
 1091 gave his famous remark that the energy dissipation can not be a constant¹ (Landau

¹The Russian edition of the book on Fluid Mechanics was published in 1944. In the later versions, the footnote was moved to the main text.

& Lifshitz, 1987). Batchelor & Townsend (1949) also found by experiments that the energy dissipation is intermittent.

Kolmogorov's 1962 (K62) Theory

In order to take into account intermittency, K41 theory had to be revised. This was done in 1962 by Obukhov and Kolmogorov. Concerning intermittent of the energy dissipation, Obukhov (1962) suggested to replace the mean energy dissipation rate $\bar{\epsilon}$ by a local space averaged energy dissipation rate

$$\epsilon_\ell(x) = \frac{6}{\pi\ell^3} \int_{r' < \ell/2} \epsilon(x + r') dr' \quad (4.2.2)$$

where ℓ is radius of the sphere. Following Obukhov (1962), Kolmogorov (1962) further proposed the hypothesis that fluctuations of the energy dissipation rate $\epsilon(x)$ satisfy a lognormal distribution or have a scaling representation. Denoting σ_ℓ^2 the variance of $\log \epsilon_\ell$, he assumed

$$\sigma_\ell^2 = A + \mu \ln(\ell_0/\ell) \quad (4.2.3)$$

where A and μ are constants (μ is often called the intermittency exponent). He then postulated two refined hypotheses² (Kolmogorov, 1962; Monin & Yaglom, 1971; Stolovitzky & Sreenivasan, 1994; Frisch, 1995; Sreenivasan & Antonia, 1997).

Hypothesis 4.2.1 (Kolmogorov's First Refined Hypothesis). If $r \ll L$ then the conditional probability distribution function for the dimensionless relative velocities

$$V = \frac{\Delta u(\ell)}{(\ell\epsilon_\ell)^{1/3}} \quad (4.2.4)$$

depends only on the local Reynolds number $Re_\ell = \ell(\ell\epsilon_\ell)^{1/3}/\nu$.

²In fact, in Kolmogorov's 1962 paper, there are three hypotheses. We only consider the first two here. The third hypothesis is "Two subsets of values in the set (11) (the first hypothesis) are stochastically independent, if in the first set $|X^{(k)} - X| \geq r_1$, in the second $|X^{(k)} - X| \leq r_2$, and $r_1 \gg r_2$ ".

1109 **Hypothesis 4.2.2** (Kolmogorov’s Second Refined Hypothesis). If $Re_\ell \gg 1$ then the
 1110 conditional probability distribution function indicated in the first hypothesis of V
 1111 does not depend on Re_ℓ , i.e., it is universal.

1112 Following the above two refined hypotheses, the structure function is then rewritten
 1113 as

$$S^q(\ell) = \langle \Delta u_\ell(x)^q \rangle = C_q \langle \epsilon_\ell^{q/3} \rangle \ell^{q/3} \quad (4.2.5)$$

1114 where $\Delta u_\ell(x) = u(x + \ell) - u(x)$ is the velocity increment with separation scale ℓ .
 1115 Assuming the lognormal distribution of the energy dissipation ϵ , one can obtain the
 1116 scaling exponent $\zeta(q)$ of the lognormal model

$$\zeta(q) = \frac{q}{3} - \frac{\mu}{18} (q^2 - 3q) \quad (4.2.6)$$

1117 4.3 Multifractality

1118 A few years after K62 theory, [Gurvich & Zubkovskii \(1963\)](#); [Pond & Stewart \(1965\)](#)
 1119 shown that the dissipation field possesses long-range power-law correlations

$$\langle \epsilon(x)\epsilon(x + \ell) \rangle \sim \ell^{-\mu} \quad (4.3.1)$$

1120 This was not included in the K62 proposal. It leads [Yaglom \(1966\)](#) to attempt to con-
 1121 ciliate his “Master” Kolmogorov and experiment results: the lognormal distribution
 1122 of the energy dissipation ϵ and the long-range correlations of the energy dissipation,
 1123 by building a recursively nested cascade model, see also [Schmitt \(2003\)](#).

1124 Let us consider a multiplicative discrete cascades process to simulate a multifractal
 1125 measure $\epsilon(x)$. [Fig. 4.2](#) illustrates the multiplicative discrete cascade process. The
 1126 larger scale corresponds to a unique cell of size $L = \ell_0 \lambda_1^n$, where ℓ_0 is a fixed scale

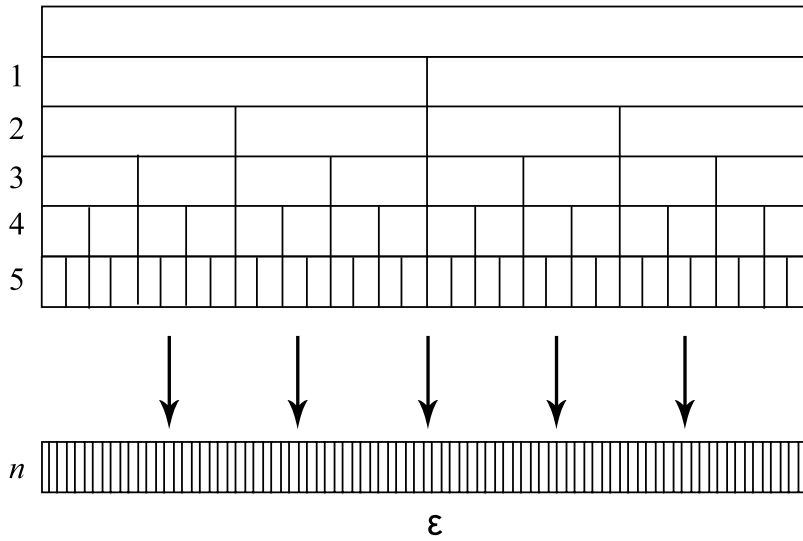


Figure 4.2: Illustration of the discrete cascade process. Each step is associated to a scale ratio of 2. After n steps, the total scale ratio is 2^n .

and $\lambda_1 > 1$ is dimensional scale ratio. For discrete models, this ratio is often taken 1127
as $\lambda_1 = 2$. The model being discrete, the next scale involved corresponds to λ_1 cells, 1128
each of size $L/\lambda_1 = \ell_0 \lambda_1^{n-1}$. This is iterated and at step p ($1 \leq p \leq n$) there are λ_1^p 1129
cells, each of size $L/\lambda_1^p = \ell_0 \lambda_1^{n-p}$. There are n cascade steps, and at step n there are 1130
 λ_1^n cells, each of size ℓ_0 , which is the smallest scale of the cascade. To reach this scale, 1131
all intermediate scales have been involved. Finally, at each point the multifractal 1132
measure writes as the product of n cascade random variables 1133

$$\epsilon(x) = \prod_{p=1}^n W_{p,x} \quad (4.3.2)$$

where $W_{p,x}$ is the random variable corresponding to position x and level p in the 1134
cascade (Schmitt, 2003). Since each $W_{p,x}$ for different cells are assumed independent, 1135
their moment of order $q > 0$ can be estimated as 1136

$$\langle \epsilon(x)^q \rangle = \prod_{i=0}^n \langle W_{p,x}^q \rangle = \langle W^q \rangle^n \quad (4.3.3)$$

1137 This gives

$$\langle \epsilon_\lambda^q \rangle \sim \lambda^{K(q)} \quad (4.3.4)$$

1138 where $\lambda = L/\ell = 2^n$ is the scale ratio, $K(q) = \log_2 \langle W^q \rangle$. The conservative property
 1139 $\langle W \rangle = 1$ gives $K(1) = 0$ and also $\langle \epsilon \rangle = 1$. One can obtain finally for the scaling
 1140 exponents $\zeta(q)$

$$\zeta(q) = \frac{q}{3} - K\left(\frac{q}{3}\right) \quad (4.3.5)$$

1141 where $K(q) = \frac{\mu}{2}(q^2 - q)$ for lognormal model.

1142 Later, to explain Anselmet *et al.* (1984) results, Parisi & Frisch (1985) proposed
 1143 a multifractal formalism. The multifractal idea have been proposed in parallel by
 1144 several authors in turbulence (Parisi & Frisch, 1985; Benzi *et al.*, 1984) and chaos
 1145 (Hentschel & Procaccia, 1983; Halsey *et al.*, 1986). The early Yaglom (1966) pa-
 1146 per, together with Mandelbrot (1974) cascades, were recognized as belonging to the
 1147 multifractal framework.

1148 These papers also gave a link between fractal singularities, their dimensions, and
 1149 the moment functions through a Legendre transform (Parisi & Frisch, 1985; Benzi
 1150 *et al.*, 1984; Halsey *et al.*, 1986).

1151 Now, the accepted approach for multifractal cascades using singularities can be
 1152 written as (Schertzer & Lovejoy, 1987)

$$\epsilon_\ell \sim \ell^{-\gamma}, \quad p(\gamma) \sim \ell^{c(\gamma)}, \quad c(\gamma) = d - d(\gamma) \quad (4.3.6)$$

1153 where γ is a singularity, $d(\gamma)$ its dimension, $c(\gamma)$ the codimension. Singularities and
 1154 codimensions can be related to moments through a Legendre transform

$$\langle \epsilon_\ell^q \rangle \sim \ell^{-K(q)}, \quad K(q) = \max_\gamma (q\gamma - c(\gamma)) \quad (4.3.7)$$

This expresses a one-to-one relation between singularities $(\gamma, c(\gamma))$ and moments $(\zeta(q), K(q))$. This is for the cascading quantity ϵ representing the flux, becoming the dissipation ϵ at small scales. For the velocity fluctuations, the framework is the same: locally, velocity are singular, $\Delta u(\ell) \sim \ell^h$ (where h can be < 0 , but is most of the time > 0) with codimension on the form

$$p(h) \sim \ell^{c(h)} \quad (4.3.8)$$

and moments

$$\langle \Delta u(\ell)^q \rangle \sim \ell^{\zeta(q)} \quad (4.3.9)$$

where $\zeta(q) = \min \{qh + c(h)\}$. In the multifractal framework, one usually considers the scaling properties of fluctuations using the dimension or codimension, or more frequently, the moment functions $K(q)$ or $\zeta(q)$.

4.4 Intermittency models

Many statistical models have been proposed since the introduction of the multifractal formalism or even before. Let us only recall the most well known here. The debate still exists to know which one is the closest to the data for turbulent fluctuations.

- The β model: This model was introduced by Frisch *et al.* (1978) but already presented by Mandelbrot (1974) or Novikov (1969)

$$K(q) = \mu(q - 1), \quad \zeta(q) = \frac{q}{3} - \mu\left(\frac{q}{3} - 1\right) \quad (4.4.1)$$

This model is monofractal $K(q)$ or $\zeta(q)$ are linear and there is only one fractal dimension.

- 1172 • The lognormal model: This model is introduced by [Kolmogorov \(1962\)](#) and
1173 [Obukhov \(1962\)](#)

$$K(q) = \frac{\mu}{2}(q^2 - q), \quad \zeta(q) = \frac{q}{3} - \frac{\mu}{18}(q^2 - 3q) \quad (4.4.2)$$

1174 where μ is the intermittent exponent. For this model, the most famous multi-
1175 fractal model, the moment functions are quadratic.

- 1176 • The log-Poisson model: This model was introduced by [She & L ev eque \(1994\)](#),
1177 [Dubrulle \(1994\)](#) and [She & Waymire \(1995\)](#)

$$K(q) = c[(1 - \gamma)q - 1 + \gamma^q], \quad \zeta(q) = \frac{q}{3} - c \left[(1 - \gamma)\frac{q}{3} - 1 + \gamma^{q/3} \right] \quad (4.4.3)$$

1178 where c is the codimension and γ is linked to the maximum singularity events.
1179 [She & L ev eque \(1994\)](#) original proposed $c = 2$ and $\gamma = 2/3$ providing a relation
1180 without adjustable parameters

$$\zeta(q) = \frac{q}{9} + 2 - 2(2/3)^{q/3} \quad (4.4.4)$$

1181 For this model, the nonlinear part is exponential.

- 1182 • The log-stable model: This model was proposed [Schertzer & Lovejoy \(1987\)](#)
1183 and [Kida \(1991\)](#); see also [Schertzer *et al.* \(1997\)](#)

$$K(q) = \frac{C_1}{\alpha - 1}(q^\alpha - q), \quad \zeta(q) = \frac{q}{3} - \frac{C_1}{\alpha - 1} \left[\left(\frac{q}{3} \right)^\alpha - \frac{q}{3} \right] \quad (4.4.5)$$

1184 where C_1 is the codimension of the mean events ($0 \leq C_1 \leq d$, where d is the
1185 dimension of the observation space), and α is the L evy index, bounded between
1186 0 and 2. When $\alpha = 2$ one recovers the lognormal model and when $\alpha = 0$ the
1187 β model. For $\alpha = 1$ one has a log-Cauchy model. For this model the nonlinear
1188 term is a power law.

The log-Poisson and log-stable (including lognormal) belong to the log-1D (in- 1189
 finitely divisible) models, whereas the log-stable is based on a stable property. Let us 1190
 note that the $\zeta(q)$ is concave and has two fixed points $\zeta(0) = 0$ by its definition and 1191
 $\zeta(3) = 1$ (Kolmogorov, 1941c), but there are no more result on $\zeta(q)$, and the precise 1192
 analytical form depend on the model. The best model for turbulence intermittency 1193
 is still a matter of debate. 1194

4.5 Passive scalar 1195

Another important topic in turbulence research is the passive scalar turbulence (Sreeni- 1196
 vasan, 1991; Shraiman & Siggia, 2000; Warhaft, 2000). We recall the Kolmogorov- 1197
 Obukhov-Corrsin theory here. 1198

Governing Equation 1199

The advection/diffusion equation for a scalar Θ reads as 1200

$$\partial_t \Theta(x, t) + u(x, t) \cdot \nabla \Theta(x, t) = \kappa \nabla^2 \Theta(x, t) \quad (4.5.1)$$

where Θ is the scalar field (for example, temperature or dye concentration), $u(x, t)$ 1201
 is the velocity field, and κ is molecular diffusivity. We consider here only the case of 1202
 passive scalar, in which it has a negligible back effect on the flow (Shraiman & Siggia, 1203
 2000; Warhaft, 2000). 1204

1205 **Kolmogorov-Obukhov-Corrsin Theory**

1206 Following Kolmogorov's argument (Kolmogorov, 1941a), Obukhov (1949); Corrsin
 1207 (1951) extended the K41 theory for passive scalar. It is well-known now as Kolmogorov-
 1208 Obukhov-Corrsin (KOC) theory. The KOC theory prediction of 1D spectrum of scalar
 1209 is

$$F_\theta(k) = C_\theta \langle \epsilon \rangle^{-1/3} \langle \epsilon_\theta \rangle k^{-5/3} \quad (4.5.2)$$

where ϵ is the energy dissipation rate, and

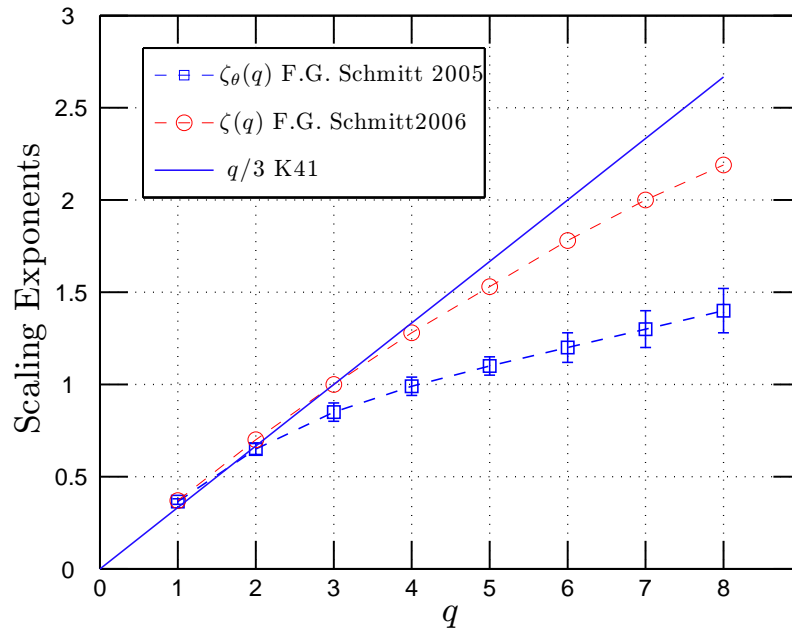


Figure 4.3: Comparison of the scaling exponents $\zeta(q)$ and $\zeta_\theta(q)$. It is notable that $\zeta(q) > \zeta_\theta(q)$ for $q > 2$. The data are compiled by Schmitt (2005) and Schmitt (2006).

1210

$$\epsilon_\theta = 2\kappa(\partial\Theta/\partial x_i)(\partial\Theta/\partial x_i) \quad (4.5.3)$$

1211 is the scalar dissipation rate. It also implies for the structure functions

$$S_\theta^q(r) = \langle \Delta\Theta(r)^q \rangle \sim \langle \epsilon^{-1/6} \epsilon_\theta^{1/3} \rangle^q r^{q/3} \sim r^{\zeta_\theta(q)} \quad (4.5.4)$$

where $\Delta\Theta(r) = \Theta(x+r) - \Theta(x)$ is the scalar increment with scale separation r , and $\zeta_\theta(q)$ is the corresponding scaling exponent. Let us note that we have the only fixed point $\zeta_\theta(0) = 0$ but we do not have $\zeta_\theta(3) = 1$ as in velocity because of the nonlinear mixing of the two fluxes (or dissipations) ϵ and ϵ_θ . We should note that structure functions for velocity and passive scalar are quite stable experimentally and seem to such $\zeta(q) > \zeta_\theta(q)$ for $q > 2$, see Fig. 4.3.

Intermittency and Ramp-cliff Structures

For a time, people thought that the passive scalar field is just a complementary of the velocity field (Shraiman & Siggia, 2000; Warhaft, 2000). Thus the statistical properties of the passive scalar field should be determined by the velocity field. However, experimental and numerical experiments indicate a more intermittent field than the velocity field (Celani *et al.*, 2000; Shraiman & Siggia, 2000; Warhaft, 2000; Moisy *et al.*, 2001; Gylfason & Warhaft, 2004). It is usually believed that the so-called ramp-cliff structures play an important role in the passive scalar field. Ramp-cliffs are large scale structures with sharp frontiers. Thus there is a coupling with the small scales by this frontier (Shraiman & Siggia, 2000; Warhaft, 2000), see more discussion in chapter 5 and chapter 7.

4.6 Summary

In this chapter, we recalled the classical Kolmogorov's 1941 and 1962 phenomenological theories of turbulence. Historically, Kolmogorov 1941 theory is the first successful phenomenological theories about the turbulence, and provides a quantitative description of the turbulent phenomena. In his theory, the structure functions play an

1234 important role to characterize the scale invariant properties of intermittency in the
1235 physical domain. We will emphasize on the structure functions analysis in chapter 5.

1236 Chapter 5

1237 Structure Functions and 1238 Autocorrelation Functions of 1239 Increments

1240 Since Kolmogorov's 1941 milestone work, the structure function analysis is widely
1241 used to extract scaling exponents in turbulent research (Monin & Yaglom, 1971;
1242 Anselmet *et al.*, 1984; Frisch, 1995). In his original proposal, Kolmogorov considered
1243 a tensor $\Delta V_{\alpha\beta}$ in space, whereas we consider here a 1D process: we do not consider
1244 the tensor and analyze time series. For this, we implicitly involve Taylor's hypothesis
1245 to consider scaling 1/3 properties of turbulent time series (Taylor, 1938; Frisch, 1995).

1246 The structure function itself is seldom investigated (Nichols Pagel *et al.*, 2008;
1247 Podesta *et al.*, 2009). In this chapter, based on statistical stationary assumption,
1248 we present an analytical analysis of the structure function to characterize the scale
1249 contribution and the influence of a single scale (Huang *et al.*, 2009d,a,e). The re-
1250 sults presented in this chapter are for most of them are published in Huang *et al.*
1251 (2009a,d,e). [Y. Huang, *et al. Traitement du Signal*, 25, 481-492, 2008 ; Y. Huang, *et al.*
1252 *Phys. Rev. E*, 2009 (submitted); Y. Huang, *et al. Phys. Rev. Lett.*, 2009 (in preparation).]

5.1 Second order structure function

1253

We investigate here the second order structure function of velocity increments in fully developed turbulence. For this, we use some properties of the Fourier transform. We will obtain results about the scale contribution and an influence of single scale to the second order structure function.

1257

Statistical Stationary Assumption

1258

Considering the statistical stationarity assumption (Monin & Yaglom, 1971; Frisch, 1995), the velocity $u(t)$ may represent in Fourier space as

1260

$$\hat{U}(f) = \mathcal{F}(u(t)) = \int_{-\infty}^{+\infty} u(t)e^{-i2\pi ft} dt \quad (5.1.1)$$

where \mathcal{F} means Fourier transform. Then the velocity $u(t)$ may be reconstructed by

1261

$$u(t) = \mathcal{F}^{-1}(\hat{U}_t(f)) = \int_{-\infty}^{+\infty} \hat{U}(f)e^{i2\pi ft} df \quad (5.1.2)$$

and $u(t + \ell)$ as

1262

$$u(t + \ell) = \mathcal{F}^{-1}(\hat{U}_{t+\ell}(f)) = \int_{-\infty}^{+\infty} \hat{U}(f)e^{i2\pi f(t+\ell)} df \quad (5.1.3)$$

where \mathcal{F}^{-1} means inverse Fourier transform, and ℓ is a separation time scale. There-

1263

fore the velocity increment $\Delta u_\ell(t) = u(t + \ell) - u(t)$ in structure functions may be

1264

represent as

1265

$$\Delta u_\ell(t) = \int_{-\infty}^{\infty} \hat{U}(f)(e^{i2\pi f(t+\ell)} - e^{i2\pi ft}) df \quad (5.1.4)$$

This means that $\hat{U}(f)(e^{i2\pi f\ell} - 1)$ is the inverse Fourier transform of $\Delta u_\ell(t)$. The

1266

Fourier transform of the velocity increment is thus written as

1267

$$S_\ell(f) = \mathcal{F}(\Delta u_\ell(t)) = \hat{U}(f)(e^{i2\pi f\ell} - 1) \quad (5.1.5)$$

1268 The corresponding Fourier power spectrum is expressed as

$$E_{\Delta}(f) = |S_{\ell}(f)|^2 = E_v(f)(1 - \cos(2\pi f\ell)) \quad (5.1.6)$$

1269 where $E_v(f) = 2|\hat{U}(f)|^2$ is the Fourier power spectrum of original velocity (Frisch,
1270 1995; Hou *et al.*, 1998; Huang *et al.*, 2009c,e). When $f_{\Delta} = n/\ell$, where $n = 0, 1, 2, \dots$,
1271 we have

$$1 - \cos(2\pi f_{\Delta}\ell) \equiv 0 \quad (5.1.7)$$

showing that the contributions of frequency sequences f_{Δ} are cancelled. In other

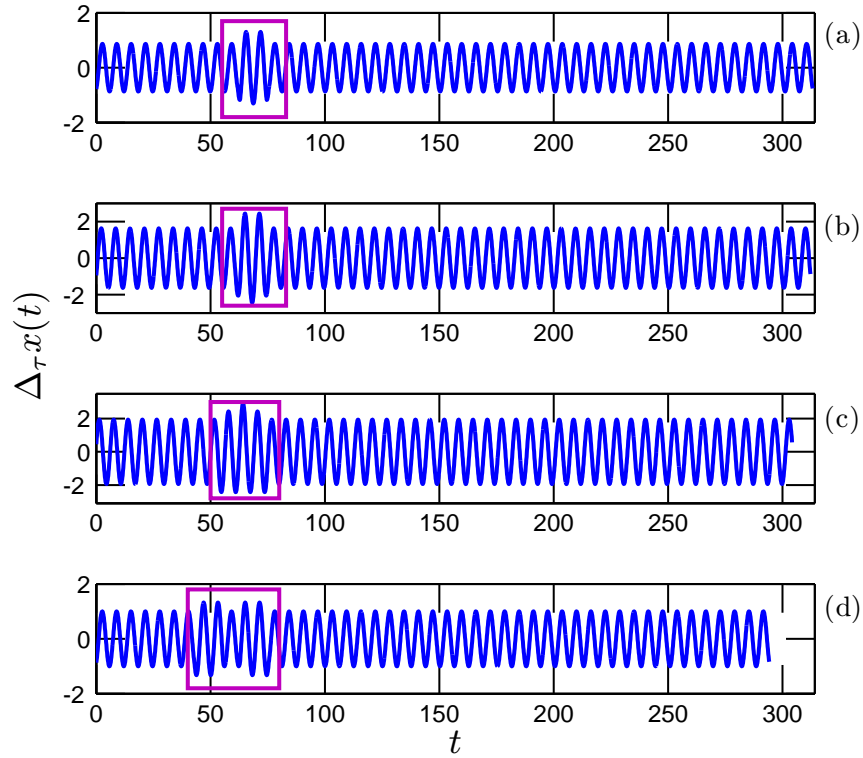


Figure 5.1: Illustration of the nonstationary effect on velocity increments: the velocity increment $\Delta x(\tau) = x(t) - x(t + \tau)$ with different time delay, (a) $\tau = 1$, (b) $\tau = 2$, (c) $\tau = 10$, and (d) $\tau = 20$ points, respectively. The nonstationary effect is marked as a rectangle. Here $x(t)$ is taken from Eq. (5.1.8).

1272

1273 words, the difference operator acts as a kind of filter operator, where the corresponding

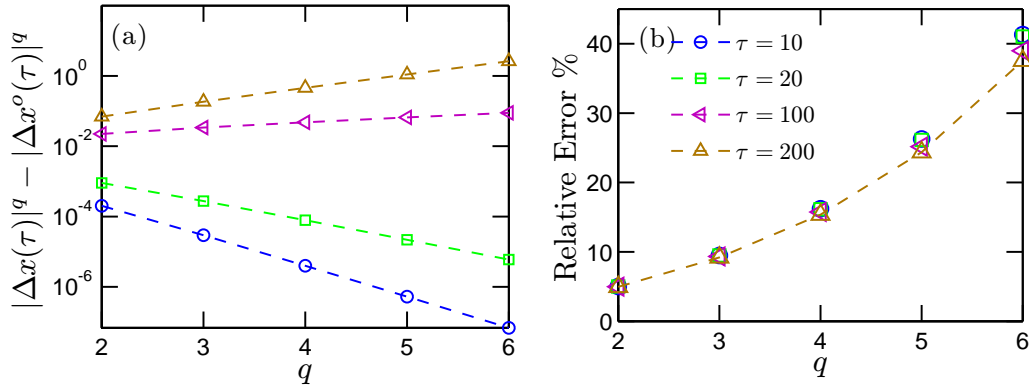


Figure 5.2: Estimation of the statistical moments for $q = 2, 3, 4, 5$ and 6 : (a) the absolute error $|\Delta x(\tau)|^q - |\Delta x^o(\tau)|^q$, (b) the relative error $(|\Delta x(\tau)|^q - |\Delta x^o(\tau)|^q)/|\Delta x^o(\tau)|^q$, respectively. The time delay τ is taken as 10 (o), 20 (□), 100 (◁) and 200 (△) points.

frequencies f_Δ are filtered. This means that the structure function analysis provides 1274
a statistical information without taking into account the corresponding scales $1/f_\Delta$. 1275
The scale invariance properties are indirectly measured. Furthermore, the structure 1276
function analysis is a global operator in physical space, since the difference operator 1277
is manipulated on the same data for each separation scale (Huang *et al.*, 2009d,e). 1278

We illustrate the nonstationary effect on structure functions by constructing a 1279
signal $x(t)$ with a nonstationary perturbation as following 1280

$$x(t) = \begin{cases} \sin(t) & 0 \leq t < 20\pi \\ 1.5 \sin(t) & 20\pi \leq t \leq 24\pi \\ \sin(t) & 24\pi < t < 100\pi \end{cases} \quad (5.1.8)$$

where the sampling frequency is set as 10 Hz. Figure 5.1 shows the increments for 1281
various time delay (a) $\tau = 1$ point, (b) $\tau = 2$ points, (c) $\tau = 10$ points, and (d) $\tau = 20$ 1282
points, where the nonstationary effect is marked by the rectangle. Graphically, the 1283
nonstationary event does have influence on all scales, since the increment operator is 1284
manipulated on the same data for each time delay. We then compare the statistical 1285

1286 moments with non-perturbation case

$$x^o(t) = \sin(t), \quad 0 \leq t \leq 100\pi \quad (5.1.9)$$

1287 Figure 5.2 shows (a) the absolute error $\langle |\Delta x(\tau)|^q \rangle - \langle |\Delta x^o(\tau)|^q \rangle$, (b) the relative
 1288 error $\langle |\Delta x(\tau)|^q \rangle / \langle |\Delta x^o(\tau)|^q \rangle - 1$ for various time lag τ . The influence increases with
 1289 the order q . The relative error shows the same evolution trend with q . This shows
 1290 experimentally that the difference operator is still a global operator in the physical
 1291 domain.

1292 Cumulative function

1293 The mean kinetic energy (one-half of the variance of the random function) is the
 1294 integral of the energy spectrum over all frequencies

$$\frac{1}{2} \langle u^2 \rangle = \int_0^{+\infty} E_v(f) \, df \quad (5.1.10)$$

1295 where $E_v(f)$ is the Fourier power spectrum of the velocity u (Frisch, 1995). Assuming
 1296 statistical stationarity, the second order is thus rewritten as

$$\langle \Delta u_\ell(t)^2 \rangle = 2 \langle u^2 \rangle - 2 \langle u(t)u(t+\ell) \rangle = 2 \langle u^2 \rangle - 2\Gamma(\ell) \quad (5.1.11)$$

1297 where $\Gamma(\ell)$ is the autocorrelation function of the velocity u . The Wiener-Khinchin
 1298 theorem shows that (Percival & Walden, 1993; Frisch, 1995),

$$\Gamma(\ell) = \int_{-\infty}^{+\infty} E_v(f) e^{2i\pi f\ell} \, df \quad (5.1.12)$$

1299 Here, $E(f)$ is extended to negative frequencies by $E(-f) = E(f)$. Thus the the
 1300 second order structure function is finally rewritten as (Monin & Yaglom, 1971; Frisch,
 1301 1995)

$$\langle \Delta u_\ell(t)^2 \rangle = 4 \int_0^{+\infty} E_v(f) (1 - e^{i2\pi f\ell}) \, df \quad (5.1.13)$$

Let us introduce here a cumulative function for the second order structure function 1302

$$\mathcal{P}(f, \ell) = \frac{\int_0^f E_\Delta(f') \, df'}{\int_0^{+\infty} E_\Delta(f') \, df'} \quad (5.1.14)$$

where $E_\Delta(f) = E_v(f)(1 - \cos(2\pi f\ell))$. It is increasing 0 and 1, and measures the relative contribution to the second order structure function from 0 to f . When $f = 1/\ell$, the cumulative function $\mathcal{P}_1(f) = \mathcal{P}(1/\ell, \ell)$ thus characterizes the contribution from the large scale part for frequencies larger than the one associated to the increment time scale ℓ . We further assume a pure power law for the original velocity Fourier power spectrum 1308

$$E_v(f) = cf^{-\beta}, \quad c > 0 \quad (5.1.15)$$

where the value of β will be specified later. When substituted into Eq. (5.1.13), this gives an integral which is divergent for some values of β . The convergence condition requires $1 < \beta < 3$ (Frisch, 1995; Hou *et al.*, 1998; Huang *et al.*, 2009e). A scaling calculation (Frisch, 1995; Huang *et al.*, 2009e) leads to 1312

$$\langle \Delta u_\ell(t)^2 \rangle \sim \ell^{\beta-1} \quad (5.1.16)$$

For fully developed turbulence, the Kolmogorov spectrum corresponds to $\beta = 5/3$. 1313

Experimental Results 1314

We apply here the above arguments to an homogeneous and nearly isotropic turbulent flow¹ at downstream $x/M = 20$, where M is the mesh size. The flow is characterized by the Taylor microscale based Reynolds number $Re_\lambda = 720$ (Kang *et al.*, 2003). Details about the experiment can be found in chapter 6. Let us note here $T_s = 1/f_s$ the time resolution of these measurements, where $f_s = 40000$ Hz is the sampling 1319

¹We will present more analysis results using these data in chapter 6 and chapter 8.

1320 frequency. Figure 5.3 shows the compensated spectra $E(f)f^\beta$ for both longitudinal
 1321 (thick line, $\beta \simeq 1.63$) and transverse (thin line, $\beta \simeq 1.62$) velocity components,
 1322 showing a more than two decades inertial range. The Fourier spectra are taken from
 1323 Ref. Kang *et al.* (2003), which are estimated by a window Fourier transform, see Kang
 1324 *et al.* (2003) for more information. The scaling exponent β is estimated from each
 1325 spectrum by a least square fitting algorithm.

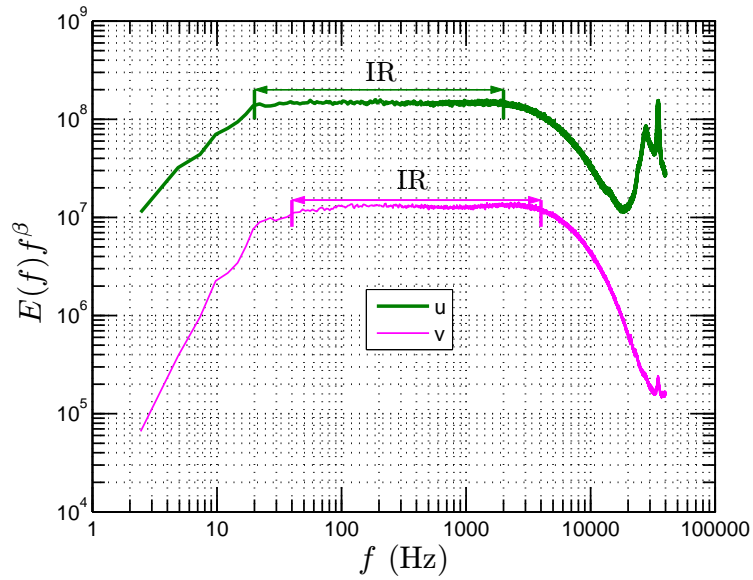


Figure 5.3: Compensated spectrum $E(f)f^\beta$ of longitudinal ($\beta \simeq 1.63$) and transverse ($\beta \simeq 1.62$) velocity at $x/M = 20$, where β is the corresponding power law estimated from the power spectrum. The plateau is observed on the range $20 < f < 2000$ Hz and $40 < f < 4000$ Hz for longitudinal and transverse velocity, respectively.

f	0.01	0.04	0.1	0.2	0.5	1	10	100
\mathcal{P} (%)	0.5	3.0	10.0	24.1	62.9	78.8	95	99

Table 5.1: A numerical solution of cumulative function $\mathcal{P}(f, \ell)$ with $\beta = 5/3$ and $\ell = 1$, which corresponds to the Kolmogorov scaling.

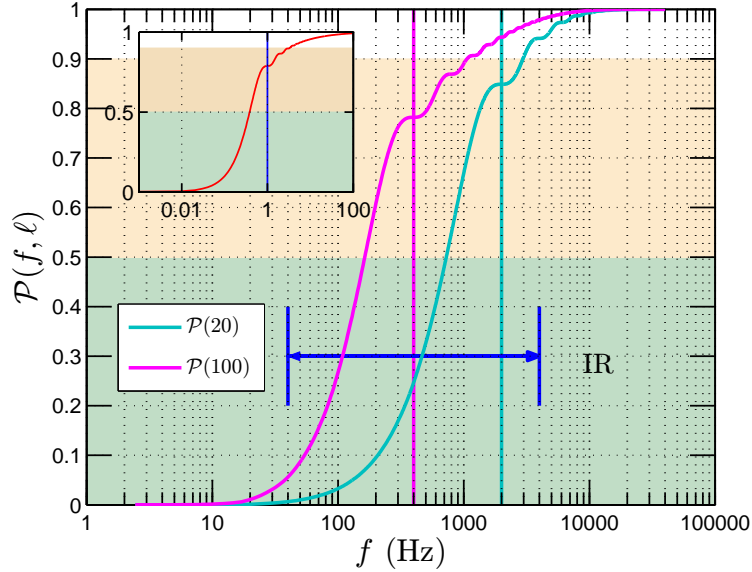


Figure 5.4: Cumulative function $\mathcal{P}(f, \ell)$ estimated from turbulent experimental data for transverse velocity with ℓ in the inertial range, where the numerical solution is shown as inset with $\ell = 1$. The inertial range is denoted as IR. Vertical solid lines demonstrate the corresponding scale in spectral space.

To avoid the effect of measurement noise, see Fig. 5.3, we only consider the trans- 1326
 verse velocity here. Figure 5.4 shows the cumulative function \mathcal{P} estimated from the 1327
 transverse velocity data, in which the spectrum $E_v(f)$ is directly estimated from the 1328
 data. The inertial range is marked as IR. We choose two time scales $\ell/T_s = 20$ and 1329
 $\ell/T_s = 100$ in the inertial range. The large scale contribution range is more than 1330
 1.4 decades wide. A numerical solution of Eq. (5.1.14) for a pure power law by tak- 1331
 ing $E_v(f) = f^{-5/3}$ is performed on range $10^{-4} < f < 10^4$ with $\ell = 1$ and the step 1332
 $\Delta f = 10^{-6}$ by using a fourth order accurate Simpson rule. The numerical solution 1333
 is shown as inset in Fig. 5.4, where the vertical solid line indicates the location of 1334
 1. The shape of the numerical solution is the same as the experimental one. We list 1335
 various value of \mathcal{P} in Tab. 5.1. Not surprisingly, the large scale contribution $\mathcal{P}_1(1)$ 1336

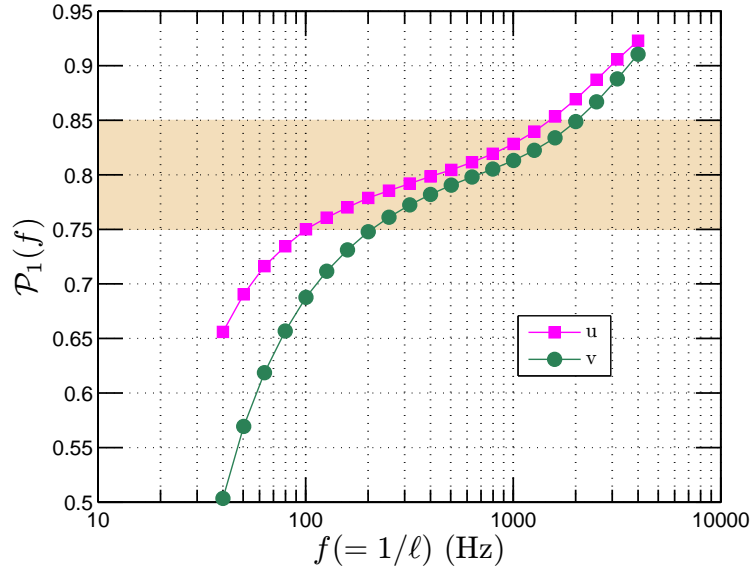


Figure 5.5: Cumulative function $\mathcal{P}_1(f)$ estimated from turbulent experimental data for both longitudinal and transverse velocity with various ℓ .

1337 is about 79%, which is consistent with experimental result, see Fig. 5.5. One can
 1338 find that the contribution from the first decade large scale, $0.1 < f < 1$, is about
 1339 69%. Even for the second decade part, $0.01 < f < 0.1$, the contribution is about
 1340 9.5%. These results show the important contribution of the large scales to the second
 1341 order structure function statistic. Figure 5.5 shows the corresponding $\mathcal{P}_1(f)$ directly
 1342 estimated from turbulent experimental data for longitudinal (■) and transverse (●)
 1343 velocity on range $40 < f(= 1/\ell) < 4000$ Hz, where the spectrum $E_v(f)$ is taken the
 1344 Fourier power spectrum of each velocity component. Both curves have a similar evo-
 1345 lution trend, which may be termed into three terms: i) near forcing scale range, in
 1346 which the large scale contribution is less than 0.75, ii) unaffected inertial range, in
 1347 which the large scale contribution is on range $0.75 < \mathcal{P}_1(f) < 0.85$, close to the value
 1348 0.79 indicated by the numerical solution, and iii) near dissipation range, in which the
 1349 large scale contribution is larger than 0.85. Taking the transverse velocity as example,

the unaffected range is found around 1 decade, on range $200 < f < 2000$ Hz. It is 1350
 good agreement with the observation in Fig. 5.18, see next section. In the first and 1351
 the third terms of the cumulative function $\mathcal{P}_1(f)$, the large scale contribution signif- 1352
 icantly deviates from the pure power law value 0.79. This indicates that these two 1353
 range are strongly influenced by either the large forcing scales or dissipation scales. 1354
 Furthermore, we note that the deviation may come from the following reasons: (i) 1355
 the finite power law range (Hou *et al.*, 1998), (ii) the spectrum of the original velocity 1356
 is not a pure power law (Nelkin, 1994; Frisch, 1995) and (iii) the violation of the sta- 1357
 tistical stationary assumption. In any case, the above results indicate that structure 1358
 functions are strongly influenced by the large scales. 1359

Influence by a Single Scale: Deterministic Forcing 1360

We then consider the influence of a single scale both on the structure function and 1361
 the arbitrary order Hilbert spectral analysis. 1362

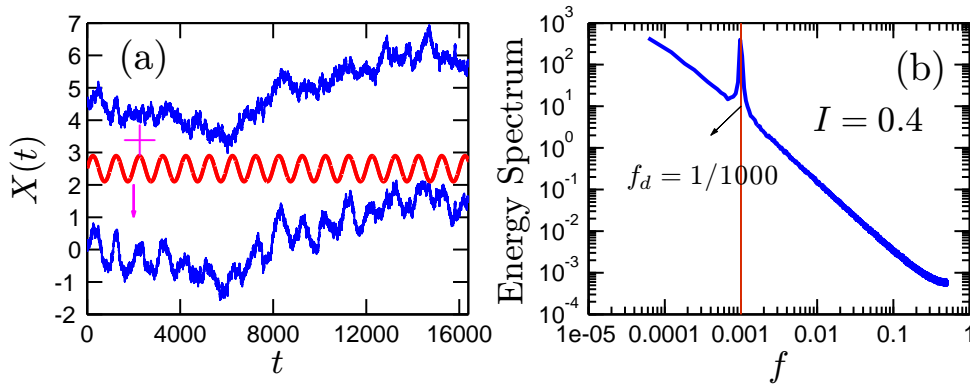


Figure 5.6: (a) A portion of fBm data with (bottom) and without (top) a sine wave 1363
 perturbation (middle), and (b) the corresponding Fourier power spectrum. 1364

We simulate a fBm time series $X(t)$ with Hurst number $H = 1/3$, corresponding 1363
 to the Hurst value of turbulent velocity. We first normalize the time series by its 1364

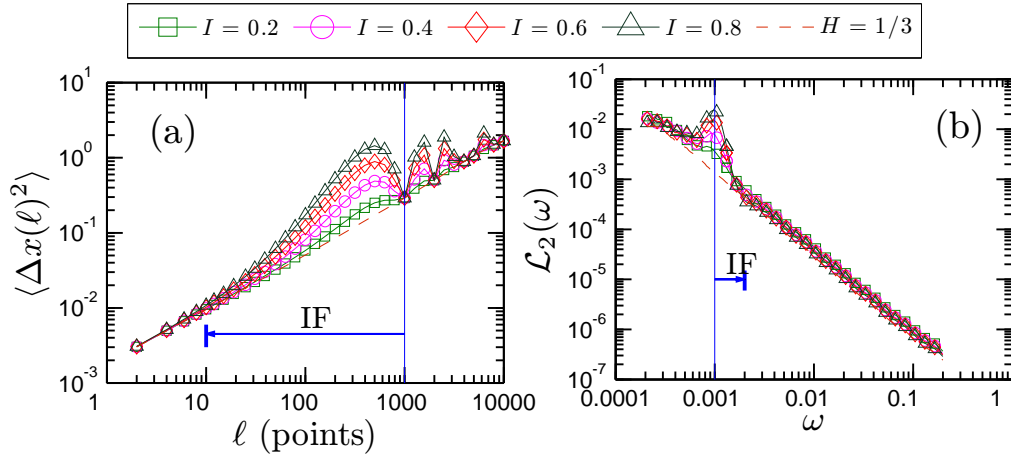


Figure 5.7: Influence of a single scale on (a) the second order structure function, and (b) the second order Hilbert marginal spectrum with various intensities I . The vertical solid line indicates location of disturbance.

1365 variance and then add on these data a pure sine wave with a disturbance frequency
 1366 $f_0 = 0.001$ and various intensities I . This is written as

$$X(t) = X(t)/\sigma + I \sin(2\pi f_0 t) \quad (5.1.17)$$

1367 where σ is the variance of $X(t)$. We show a 2^{14} points portion of the simulated
 1368 fBm data in Fig. 5.6 (a) fBm data with (bottom) and without (top) a sine wave
 1369 perturbation (middle) with intensity $I = 0.4$, and (b) its corresponding Fourier power
 1370 spectrum. We then apply the structure function analysis and the arbitrary order
 1371 Hilbert spectral analysis on these data with various intensities I . For the former
 1372 approach, we consider time lags on the range $0 < \tau < 10000$ points. For the original
 1373 fBm data, a power law behaviour is found on the range $5 < \tau < 10000$ points.
 1374 The latter methodology is performed on each realization and the ensemble averaged
 1375 spectrum is taken as final spectrum. For the original fBm data, we find that a power
 1376 law behaviour holds on the range $0.0002 < \omega < 0.2$, corresponding to $5 < \tau < 5000$
 1377 points. Figure 5.7 shows (a) the second order structure function, and (b) the second

order Hilbert marginal spectrum, where the solid vertical line indicates the location 1378
of the disturbance frequency f_0 . The second order structure function is strongly 1379
influenced by the single scale. An influence range down to the small scale is found 1380
to be as large as 2 decades, which is marked by IF in Fig. 5.7. However, for the 1381
Hilbert-based method, the influence range down to the small scale is constrained to 1382
0.3 decades, which might be link to the fact that the EMD acts a dyadic filter bank 1383
for several types of time series (Wu & Huang, 2004; Flandrin *et al.*, 2004; Flandrin & 1384
Gonçalvès, 2004; Huang *et al.*, 2008). 1385

We may also consider here the single scale as a periodic component (Huang *et al.*, 1386
2009d). A quite general common property of multifractal time series (turbulent-like 1387
stochastic dynamics) in the nature and geophysical sciences is superposed to a de- 1388
terministic forcing associated to astronomical events (tide, daily cycle, annual cycle, 1389
etc). This may pose a problem for the estimation of scaling exponents. This is the 1390
case, for example, for river flow time series (Tessier *et al.*, 1996; Kantelhardt *et al.*, 1391
2003; Huang *et al.*, 2009b), oceanic monitoring time series (Dur *et al.*, 2007; Schmitt 1392
et al., 2008), etc, also see chapter 9. As already noticed by several authors, the struc- 1393
ture function may fail when a periodic component is present in the data (Kantelhardt 1394
et al., 2003, 2006). Thus, we show here numerically that this influence on the struc- 1395
ture function. We also show that the Hilbert-based methodology can constrain this 1396
effect in an amplitude-frequency space (Huang *et al.*, 2009d). 1397

Passive Scalar: An Example of Ramp-Cliff Structures 1398

The above arguments and results indicate that the structure function may not con- 1399
sidered a proper tool for scaling exponent extraction when the data possess energetic 1400

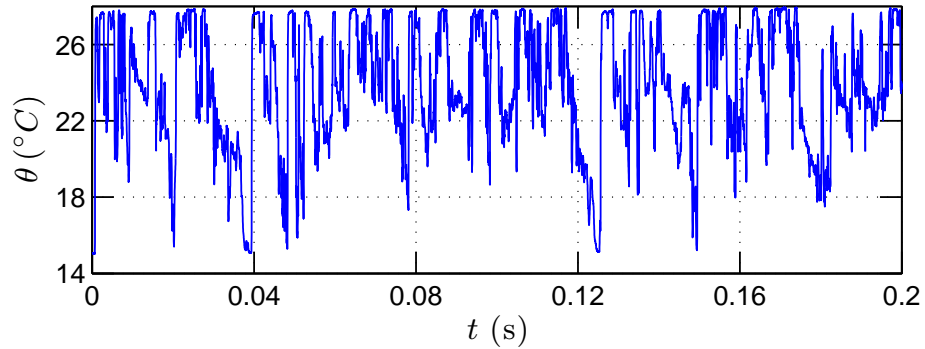


Figure 5.8: One 0.2s portion of the temperature time series, showing strong ramp-cliff structure.

1401 large scales. This is the case of ramp-cliff structure in scalar turbulence (Sreeni-
 1402 vasan, 1991; Shraiman & Siggia, 2000; Warhaft, 2000; Celani *et al.*, 2000): the struc-
 1403 ture induced by shear effect (Staicu & van de Water, 2003; Xia *et al.*, 2008). To
 1404 show this experimentally, we consider a temperature time series with strong ramp-
 1405 cliff structure. The data is obtained in a shear layer of the mixing between a jet
 1406 flow and a cross flow, provided by Prof. Y. Gagne. The bulk Reynolds number is
 1407 about $Re = 60000$. The initial temperature of the two flows are $T_J = 27.8^\circ C$ and
 1408 $T = 14.8^\circ C$. The measurement location is close to the nozzle of the jet. For more
 1409 detail about this experiment, see chapter 7. Figure 5.8 shows a 0.2s portion temper-
 1410 ature data, showing strong ramp-cliff structures. Figure. 5.9 shows the compensated
 1411 spectra directly estimated by the Fourier analysis (solid line), the second order struc-
 1412 ture function (\square), the Hilbert spectral analysis (\circ) and the autocorrelation function
 1413 (\diamond) (see Eq. (5.2.10) in next section). Both the structure function and the auto-
 1414 correlation function are converted from from physical domain to spectral domain by
 1415 taking $f = 1/\ell$. Except for the structure function, the others show a clear plateau,
 1416 on the range $100 < f < 2000$ Hz. For the structure function, an ambiguous plateau is

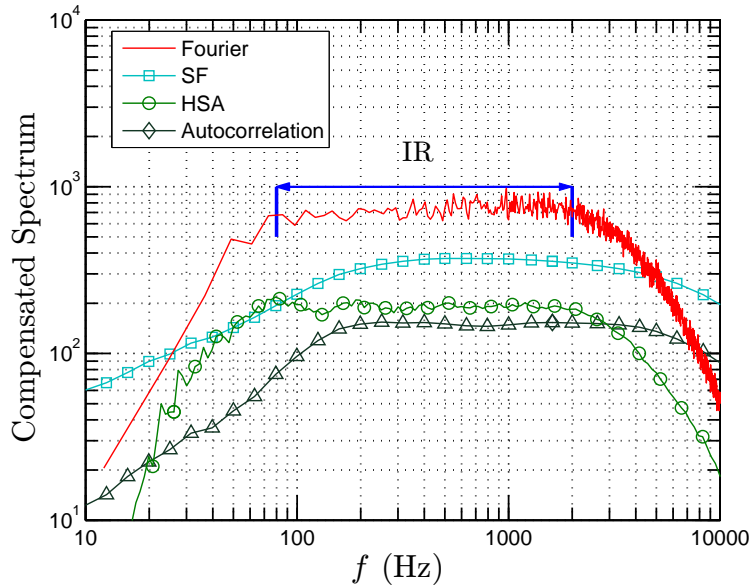


Figure 5.9: Compensated spectrum of transverse velocity. Plateau is observed on range $80 < f < 2000$ Hz for both Fourier spectrum (solid line) and Hilbert spectrum (\square). For comparison, the compensated spectra estimated from the second order structure function (\circ) and the autocorrelation function (\diamond) are also shown.

found on the range $300 < f < 2000$ Hz; for higher order structure function, we even 1417
cannot find an ambiguous inertial range, see chapter 7. However, the Hilbert spectral 1418
analysis shows a clear inertial range even for q up to 8. We reproduce the scaling 1419
exponent estimated by the Hilbert methodology (\circ) in Fig. 5.10. It seems that the 1420
scaling exponent $\xi(q) - 1$ is quite close to the scaling exponent $\zeta(q)$ for the velocity by 1421
using the extended self-similarity approach (dash line) (Arneodo *et al.*, 1996). The 1422
scaling exponent provided directly by the structure function (\diamond) seems to saturate 1423
when $q > 3$. 1424

The comparison between scaling exponents for temperature and velocity shows 1425
that for $q > 2$ 1426

$$\zeta_\theta(q) < \zeta_v(q) \quad (5.1.18)$$

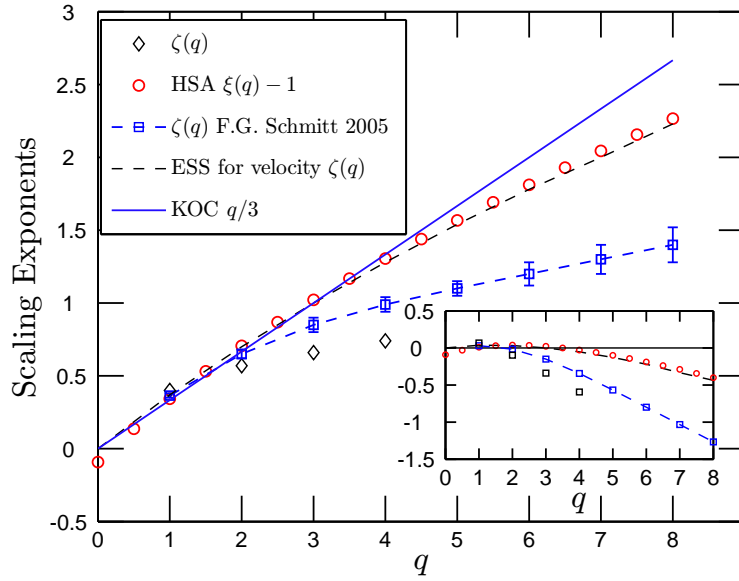


Figure 5.10: Representation of the scaling exponents, which is estimated by HSA (\circ), and structure function (\diamond). For comparison, the scaling exponent from Ref. Schmitt (2005) (\square) for passive scalar and from Ref. Arneodo *et al.* (1996) for the velocity (dashed-line) are also shown.

1427 this is interpreted as an evidence that the scalar turbulence is more intermittent than
 1428 the velocity field (Frisch, 1995; Warhaft, 2000). The experimental results shown here
 1429 indicate that the effect of ramp-cliff structures for passive turbulence may be given
 1430 more attention. The passive turbulent field may be less intermittent than what we
 1431 believed before. We will present more detail and discussion in chapter 7.

1432 5.2 Autocorrelation function of velocity increments

1433 We consider in this section the autocorrelation of velocity increments (without abso-
 1434 lute value), inspired by a remark found in Anselmet *et al.* (1984). In this reference,
 1435 it is found that the location of the minimum value of the autocorrelation function

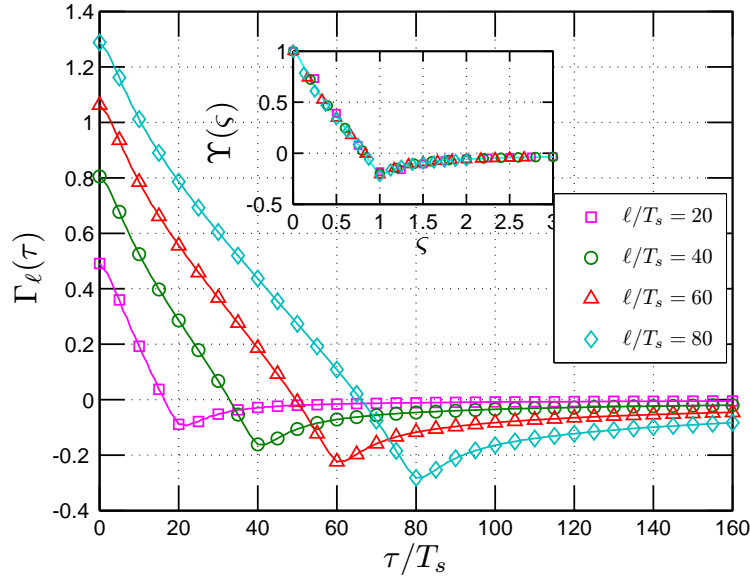


Figure 5.11: Autocorrelation function $\Gamma_\ell(\tau)$ of the velocity increment $\Delta u(\ell)$ estimated from an experimental homogeneous and nearly isotropy turbulence time series with various increments ℓ . The location of the minimum value is very close to the separation time ℓ . The inset shows the rescaled autocorrelation function $\Upsilon(\zeta)$.

$\Gamma(\tau)$ of velocity increment $\Delta u_\ell(t)$ of fully developed turbulence with time separation ℓ is approximately equal to ℓ . The autocorrelation function of the increment $V_\ell(t) = \Delta u_\ell(t)$ time series is defined as

$$\Gamma_\ell(\tau) = \langle (V_\ell(t + \tau) - \bar{\mu})(V_\ell(t) - \bar{\mu}) \rangle \quad (5.2.1)$$

where $\bar{\mu}$ is the mean value of $V_\ell(t)$, and $\tau \geq 0$ is the time lag.

We show the autocorrelation function $\Gamma_\ell(\tau)$ of the velocity increments $\Delta u_\ell(t)$ for the longitudinal velocity in Fig. 5.11, where the rescaled autocorrelation function is shown as inset. The location τ_o of the minimum value of each curve is graphically very close to ℓ , which confirms Anselmet's observation (Anselmet *et al.*, 1984).

Let us define the minimum value of an autocorrelation function

$$\Gamma_o(\ell) = \min_{\tau} \{\Gamma_\ell(\tau)\} \quad (5.2.2)$$

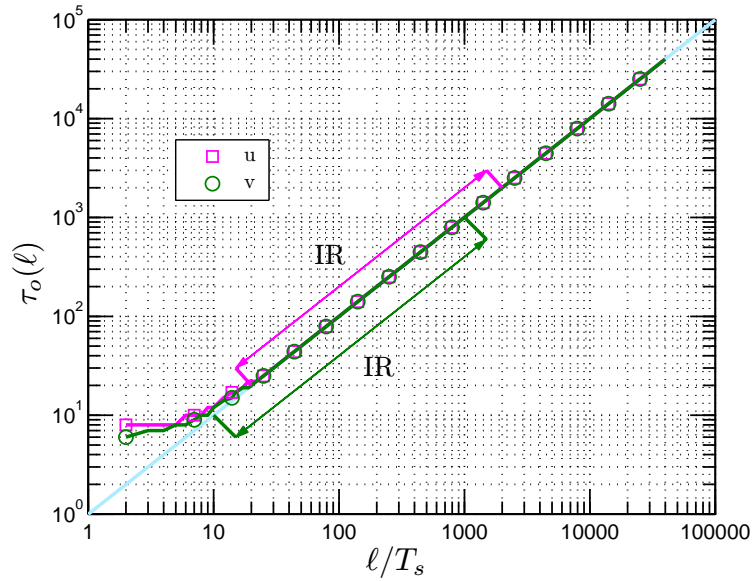


Figure 5.12: Location $\tau_o(\ell)$ of the minimum value of the autocorrelation function estimated from experimental data, where the inertial range is marked as IR. The solid line indicates $\tau_o(\ell) = \ell$.

1445 and τ_o the location of the minimum value

$$\Gamma_o(\ell) = \Gamma_\ell(\tau_o(\ell)) \quad (5.2.3)$$

1446 We show the estimated $\tau_o(\ell)$ for both longitudinal and transverse velocity on the
 1447 range $2 < \ell/T_s < 40000$ in Fig. 5.12, where the inertial range is indicated by IR. The
 1448 solid line illustrates $\tau_o(\ell) = \ell$. When ℓ is larger than $20T_s$, τ_o is very close to ℓ even
 1449 when ℓ is in the large forcing scale range, in agreement with the remark of Anselmet
 1450 *et al.* (1984). We prove this observation analytically in the following.

1451 An Analytical Model

1452 We have shown previously that the Fourier transform of the velocity increment $\Delta u(\ell)$
 1453 is written as

$$S_\ell(f) = \mathcal{F}(\Delta u(\ell)) = \hat{U}(f)(e^{2\pi i f \ell} - 1)$$

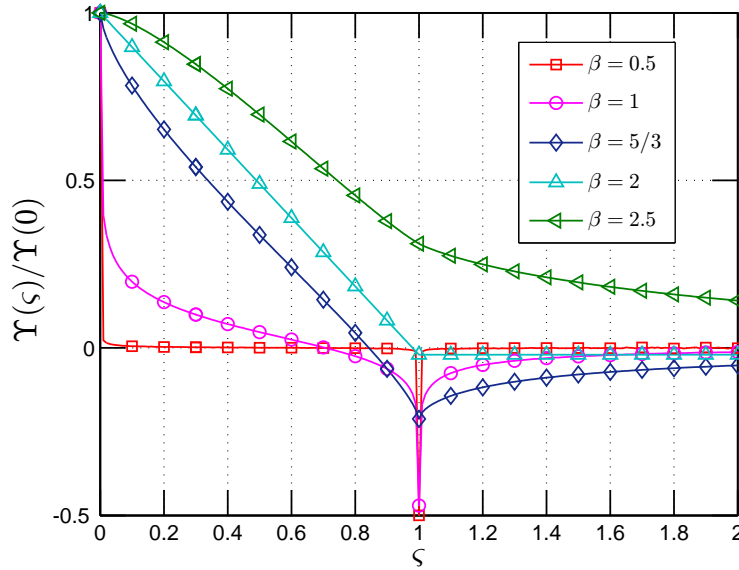


Figure 5.13: Numerical solution of the rescaled autocorrelation function $\Upsilon(\varsigma)$ with various β from 0.5 to 2.5 estimated from Eq. (5.2.8).

where $\Delta u(\ell) = u(x + \ell) - u(x)$ and $\hat{U}(f)$ is the Fourier transform of the original 1454
velocity. Hence, the 1D power spectral density function of velocity increments $E_{\Delta}(f)$ 1455
is expressed as 1456

$$E_{\Delta}(f) = |S_{\ell}(f)|^2 = E_v(f)(1 - \cos(2\pi f\ell)) \quad (5.2.4)$$

where $E_v(f) = 2|\hat{U}(f)|^2$ is the velocity power spectrum (Frisch, 1995). 1457

Let us consider now the autocorrelation function of the increment. The Wiener- 1458
Khinchin theorem relates the autocorrelation function to the power spectral density 1459
via the Fourier transform (Percival & Walden, 1993; Frisch, 1995) 1460

$$\Gamma_{\ell}(\tau) = \int_0^{+\infty} E_{\Delta}(f) \cos(2\pi f\tau) df \quad (5.2.5)$$

The theorem can be applied to wide-sense-stationary random processes, signals whose 1461
Fourier transforms may not exist, using the definition of autocorrelation function in 1462
terms of expected value rather than an infinite integral (Percival & Walden, 1993). 1463

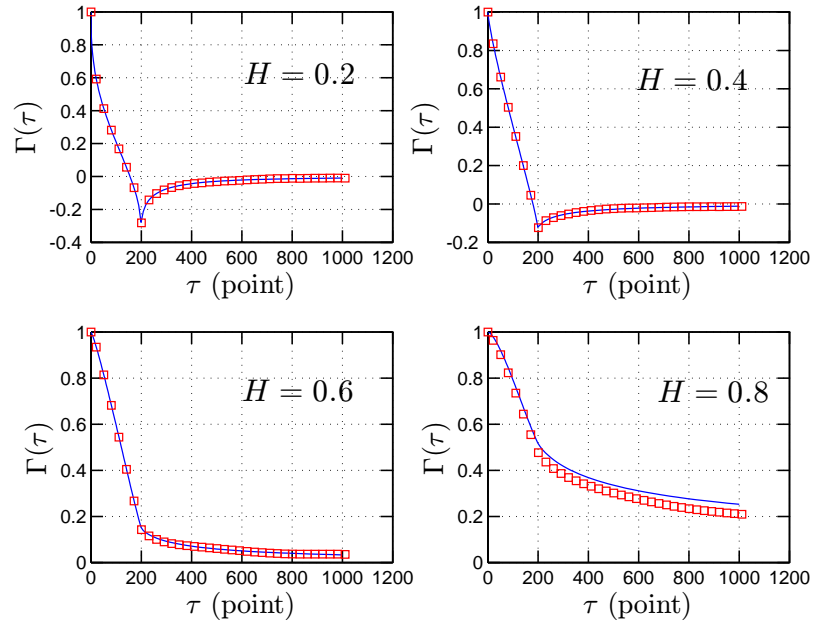


Figure 5.14: Comparison of the autocorrelation function, which is predicted by Eq. (5.2.19) (solid line) and estimated from fBm simulation (\square) with $\ell = 200$ points.

1464 Substituting Eq. (5.2.4) into the above equation, we thus have

$$\Gamma_{\ell}(\tau) = \int_0^{+\infty} E_v(f)(1 - \cos(2\pi f\ell)) \cos(2\pi f\tau) df \quad (5.2.6)$$

1465 Assuming a power law for 1D velocity spectrum (a hypothesis of similarity)

$$E_v(f) = cf^{-\beta}, \quad c > 0 \quad (5.2.7)$$

1466 we obtain

$$\Gamma_{\ell}(\tau) = c \int_0^{+\infty} f^{-\beta}(1 - \cos(2\pi f\ell)) \cos(2\pi f\tau) df \quad (5.2.8)$$

1467 The convergence condition requires $0 < \beta < 3$. It implies a rescaled relation, using

1468 scaling transformation inside the integral. This can be estimated by taking $\ell' = \lambda\ell$,

1469 $f' = f\lambda$, $\tau' = \tau/\lambda$ for $\lambda > 0$, providing the identity directly from Eq. (5.2.8)

$$\Gamma_{\lambda\ell}(\tau) = \Gamma_{\ell}(\tau/\lambda)\lambda^{\beta-1} \quad (5.2.9)$$

If we take $\ell = 1$ and replace λ by ℓ , we then have

1470

$$\Gamma_\ell(\tau) = \Gamma_1(\tau/\ell)\ell^{\beta-1} \quad (5.2.10)$$

Thus, we have a universal autocorrelation function for each ℓ

1471

$$\Gamma_\ell(\ell\zeta)\ell^{1-\beta} = \Upsilon(\zeta) = \Gamma_1(\zeta) \quad (5.2.11)$$

This universal autocorrelation function is shown as inset in Fig. 5.11. A derivative of

1472

Eq. (5.2.9) gives $\Gamma'_{\lambda\ell}(\tau) = \Gamma'_\ell(\tau/\lambda)\lambda^{\beta-2}$. The minimum value of the left-hand side is

1473

$\tau = \tau_o(\lambda\ell)$, verifying $\Gamma'_{\lambda\ell}(\tau_o(\lambda\ell)) = 0$ and for this value we have also $\Gamma'_\ell(\tau_o(\lambda\ell)/\lambda) = 0$.

1474

This shows that $\tau_o(\ell) = \tau_o(\lambda\ell)/\lambda$. Taking again $\ell = 1$ and $\lambda = \ell$, we have

1475

$$\tau_o(\ell) = \ell\tau_o(1) \quad (5.2.12)$$

Showing that $\tau_o(\ell)$ is proportional to ℓ in the scaling range (when ℓ belongs to the

1476

inertial range). With the definition of $\Gamma_o(\ell) = \Gamma_\ell(\tau_o(\ell))$ we have, also using Eq. (5.2.9),

1477

for $\tau = \tau_o(\lambda\ell)$:

1478

$$\begin{aligned} \Gamma_{\lambda\ell}(\tau_o(\lambda\ell)) &= \Gamma_\ell(\tau_o(\lambda\ell)/\lambda)\lambda^{\beta-1} \\ &= \Gamma_\ell(\tau_o(\ell))\lambda^{\beta-1} \end{aligned} \quad (5.2.13)$$

Hence $\Gamma_o(\lambda\ell) = \lambda^{\beta-1}\Gamma_o(\ell)$ or

1479

$$\Gamma_o(\ell) = \Gamma_o(1)\ell^{\beta-1} \quad (5.2.14)$$

We consider the location $\tau_o(1)$ of the autocorrelation function for $\ell = 1$. We take

1480

the first derivative of Eq. (5.2.8), written for $\ell = 1$

1481

$$\mathcal{R}(\tau) = \frac{d\Gamma_1(\tau)}{d\tau} = - \int_0^{+\infty} f^{1-\beta}(1 - \cos(2\pi f)) \sin(2\pi f\tau) df \quad (5.2.15)$$

where we left out the constant in the integral. The same rescaling calculation leads

1482

to the following expression

1483

$$\begin{aligned} \mathcal{R}(\tau) &= [(1 + 1/\tau)^{\beta-2} + (1 - 1/\tau)^{\beta-2} - 2] M/2, \tau \neq 1 \\ \mathcal{R}(\tau) &= (2^{\beta-3} - 1) M, \quad \tau = 1 \end{aligned} \quad (5.2.16)$$

1484 where $M = \int_0^{+\infty} x^{1-\beta}(1 - \cos(2\pi x)) \sin(2\pi x\tau) dx$ and $M > 0$ (Samorodnitsky &
 1485 Taqqu, 1994). The convergence condition requires $1 < \beta < 4$. When $\beta < 2$, one
 1486 can find that both left and right limits of $\mathcal{R}(1)$ are infinite, but the definition of
 1487 $\mathcal{R}(1)$ in Eq. (5.2.15) is finite. Thus $\tau = 1$ is a second type discontinuity point of
 1488 Eq. (5.2.15) (Malik & Arora, 1992). It is easy to show that

$$\begin{cases} \mathcal{R}(\tau) < 0, \tau \leq 1 \\ \mathcal{R}(\tau) > 0, \tau > 1 \end{cases} \quad (5.2.17)$$

1489 It means that $\mathcal{R}(\tau)$ changes its sign from negative to positive when τ is increasing
 1490 from $\tau < 1$ to $\tau > 1$. In other words the autocorrelation function will take its
 1491 minimum value at location where τ is exactly equal to 1. We thus see that $\tau_o(1) = 1$
 1492 and hence from Eq. (5.2.12) we proved that

$$\tau_o(\ell) = \ell \quad (5.2.18)$$

1493 For the fBm, the autocorrelation function of the increments is known to be the
 1494 following (Biagini *et al.*, 2008)

$$\Gamma_\ell(\tau) = \frac{1}{2} \{(\tau + \ell)^{2H} + |\tau - \ell|^{2H} - \tau^{2H}\} \quad (5.2.19)$$

1495 where H is Hurst number, and $\tau \geq 0$. We compare the autocorrelation (coefficient)
 1496 function estimated from fBm simulation (\square) with Eq. (5.2.19) (solid line) in Fig. 5.14,
 1497 where $\ell = 200$ points. Eq. (5.2.19) provides a very good agreement with numerical
 1498 simulation. Based on this model, it is not difficult to find that $\Gamma_o(\ell) \sim \ell^{2H}$ when
 1499 $0 < H < 1$, corresponding to $1 < \beta < 3$, and $\tau_o(\ell) = \ell$ when $0 < H < 0.5$,
 1500 corresponding to $1 < \beta < 2$. One can find that the validity range found here for
 1501 the scaling exponent β is only a subset of the validity range for Wiener-Khinchin
 1502 theorem.

Experimental Results

1503

There is no analytical solution for Eq. (5.2.8). Above we could only give a rescaling 1504
property of this function, and also give its explicit form for the fBm. It can also be 1505
solved by a proper numerical algorithm. We perform this here using a fourth order 1506
accurate Simpson rule of Eq. (5.2.8) on range $10^{-4} < f < 10^4$ with $\ell = 1$ for various β 1507
with $\Delta f = 10^{-6}$. We show the rescaled numerical solutions for various β values $\Upsilon(\zeta)$ 1508
in Fig. 5.13. We can verify that the location $\tau_o(1)$ of the minimum autocorrelation 1509
function is exactly equal to 1 when $0 < \beta < 2$. 1510

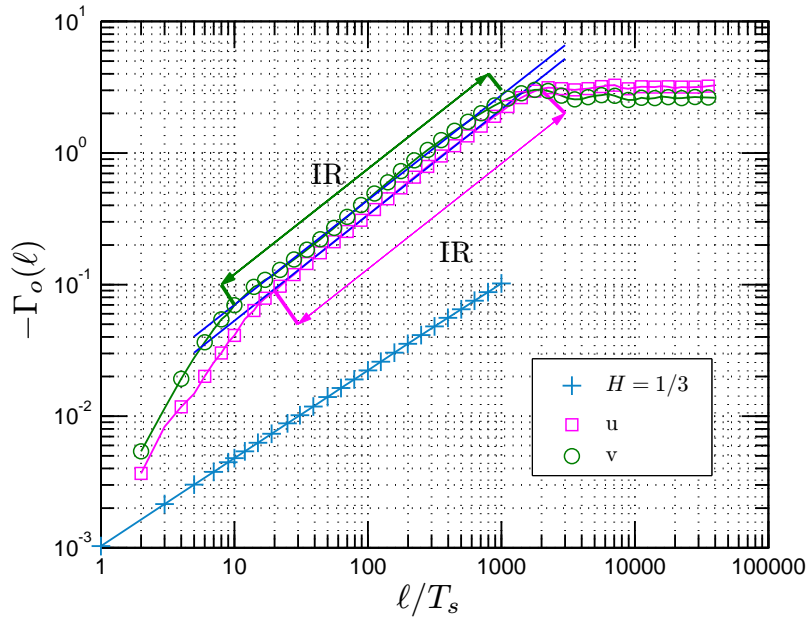


Figure 5.15: Representation of the minima value $\Gamma_o(\ell)$ of the autocorrelation function estimated from synthesized fBm time series with $H = 1/3$ (+), and the experimental data for longitudinal (\square) and transverse (\circ) turbulent velocity components, where the corresponding inertial range is denoted as IR. Power law behaviour is observed with scaling exponent $\beta - 1 = 2/3$ and $\beta - 1 = 0.78 \pm 0.04$ for fBm and turbulent velocity, respectively.

We then check the power law for the minimum value of autocorrelation function 1511

1512 given in Eq. (5.2.10). We simulate 100 segments of fBm with length 10^6 data points
 1513 each, by performing a Wavelet based algorithm (Abry & Sellan, 1996). We take db2
 1514 wavelet with $H = 1/3$ (corresponding to the Hurst number of turbulent velocity). We
 1515 plot the estimated minima value $\Gamma_o(\ell)$ (+) of the autocorrelation function in Fig. 5.15,
 1516 where the solid line demonstrates $\Gamma_o(\ell) \sim \ell^{2/3}$. A power law behaviour is observed
 1517 with the scaling exponent $\beta - 1 = 2/3$ as expected. It confirms Eq. (5.2.10) for fBm,
 1518 the monofractal case. We also plot $\Gamma_o(\ell)$ estimated from turbulent experimental data
 1519 for both longitudinal (\square) and transverse (\circ) velocity component in Fig. 5.15, where
 1520 the inertial range is marked by IR, which is provided by the Fourier power spectrum
 1521 of the original velocity. Power law behaviour is observed on the corresponding inertial
 1522 range, with scaling exponent $\beta - 1 = 0.78 \pm 0.04$. This scaling exponent is larger
 1523 than $2/3$, which may be an effect of intermittency. The exact relation between this
 1524 scaling exponent with intermittent parameter should be investigated in future work.
 1525 The power law range is almost the same as the inertial range estimated by Fourier
 1526 power spectrum. It indicates that autocorrelation function can be used to determine
 1527 the inertial range. Indeed, as we show later, it seems to be a better inertial range
 1528 indicator than structure function.

1529 Cumulative function

1530 As we have done for the second order structure function, we define here a cumulative
 1531 function

$$\mathcal{Q}(f, \ell, \tau) = \frac{\int_0^f K(f', \ell, \tau) df'}{\int_0^{+\infty} K(f', \ell, \tau) df'} \quad (5.2.20)$$

1532 where

$$K(f, \ell, \tau) = E_v(f)(1 - \cos(2\pi f\ell)) \cos(2\pi f\tau) \quad (5.2.21)$$

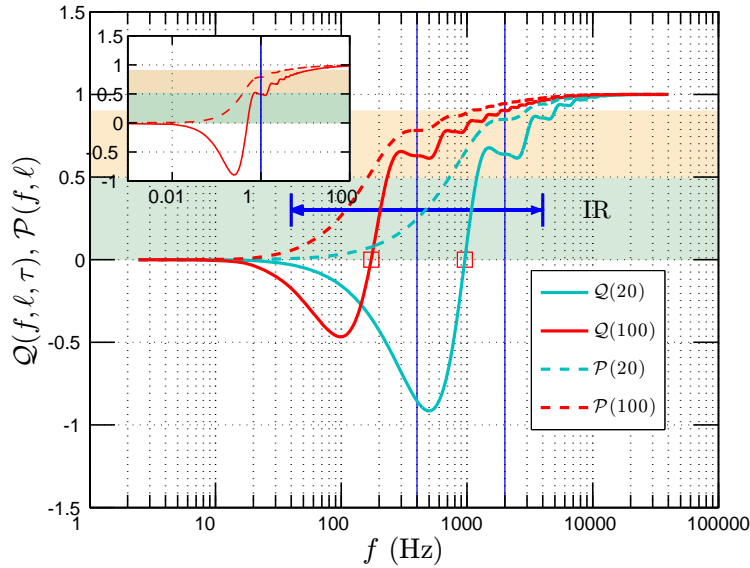


Figure 5.16: Cumulative function $\mathcal{Q}(f, \ell, \tau)$ estimated from turbulent experimental data for transverse velocity with $\tau = \ell$ in the inertial range, where the numerical solution is shown as inset with $\ell = 1$. The inertial range is denoted as IR. Vertical solid lines demonstrate the corresponding scale in spectral space. For comparison, we also show the cumulative function $\mathcal{P}(f, \ell)$ for the second order structure function.

is the integration kernel of Eq. (5.2.6). It measures the contribution of the frequency 1533
from 0 to f at a given time scale ℓ and time delay τ . We are particularly concerned 1534
by the case $\tau = \ell$. To avoid the measurement noise, we only consider here the 1535
transverse velocity. We show the estimated \mathcal{Q} in Fig. 5.16 for two scales $\ell/T_s = 20$ 1536
and $\ell/T_s = 100$ (solid line) in the inertial range, in which the spectrum $E_v(f)$ in 1537
Eq. (5.2.21) is directly estimated for the transverse velocity from the experimental 1538
turbulent data. The vertical solid line illustrates the location of the corresponding 1539
time scale in spectral space by taking $f = 1/\ell$. The corresponding inertial range is 1540
denoted by IR. We show the numerical solution of Eq. (5.2.20) for a pure power law 1541
with $\ell = 1$ (solid line) as inset, in which the spectrum $E_v(f)$ in Eq. (5.2.21) is taken 1542
as $E_v(f) = f^{-5/3}$ for a pure Kolmogorov power law. We notice that both curves cross 1543

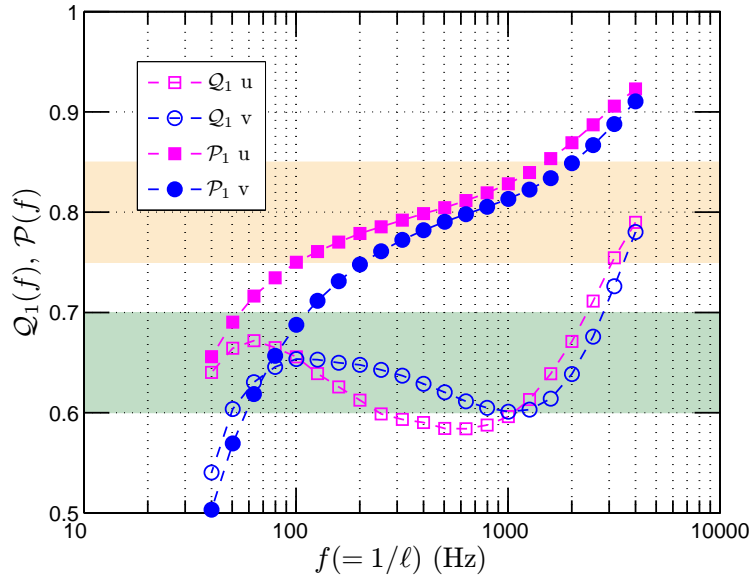


Figure 5.17: Cumulative function $\mathcal{Q}_1(f)$ estimated from turbulent experimental data for both longitudinal and transverse velocity with various ℓ . The numerical solution shows $\mathcal{Q}_1 \simeq 0.49$. For comparison, we reproduce the cumulative function $\mathcal{P}_1(f)$ for the second order structure function.

1544 the line $\mathcal{Q} = 0$, which is marked by \square . We denote f_o such as $\mathcal{Q}(f_o) = 0$. It has the
 1545 advantage that the contribution from the large scale part, $\ell > 1/f_o$, is canceled by
 1546 itself, and the small-scale and large-scale contributions are equal (Huang *et al.*, 2009c).
 1547 In the inertial range, the distance between f_o and the corresponding scale ℓ is less than
 1548 0.3 decade. The numerical solution indicates that this distance is about 0.3 decade.
 1549 We then separate the contribution into a large scale part and a small scale part.
 1550 We denote the contribution from the large scale part as $\mathcal{Q}_1(f) = \mathcal{Q}(1/\ell, \ell, \ell)$. The
 1551 experimental result is shown in Fig. 5.17 for both longitudinal (\square) and transverse (\circ)
 1552 velocity components. The mean contribution from the large scale is found graphically
 1553 to be 0.64. It is significantly larger than 0.5, the value indicated by the numerical
 1554 solution. It means that the autocorrelation function is influenced more by large scales

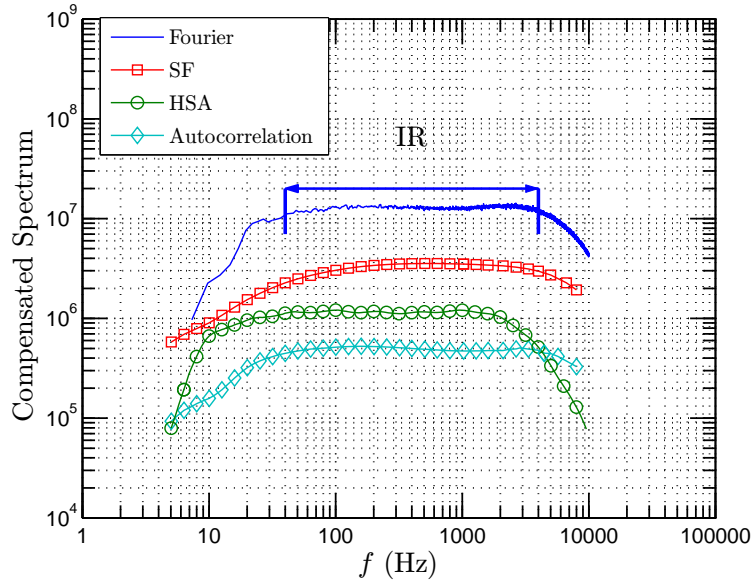


Figure 5.18: Compensated spectrum of transverse velocity. A plateau is observed on the range $40 < f < 4000$ Hz and $20 < f < 2000$ Hz for Fourier spectrum (solid line) and Hilbert spectrum (\circ), respectively. For comparison, the compensated spectra for the second order structure function (\square) and the autocorrelation function (\diamond) are also shown.

than by small scales. 1555

For comparison, we reproduce the cumulative function $\mathcal{P}(f, \ell)$ and $\mathcal{P}_1(f)$ for the 1556
second order structure function in Fig. 5.16 (dash line) and Fig. 5.17 (filled symbol). 1557
The contribution range from the large scale part to the second order structure 1558
function is much larger than the contribution range of the autocorrelation function. It is also 1559
confirmed by Fig. 5.17 that the large scale contribution of the second order structure 1560
function is larger than the large scale contribution of the autocorrelation function, 1561
which can be linked to the cancellation property of the large scale part $f < f_o$ of the 1562
autocorrelation function. This explains that the autocorrelation function is a **better** 1563
inertial range indicator than the second order structure function (Huang 1564
et al., 2009c). 1565

1566 We now consider the inertial range provided by the different methods. We replot
1567 the corresponding compensated spectra estimated directly by Fourier power spectrum
1568 (solid line), the second order structure function (\square), the Hilbert spectral analysis (\circ)
1569 and the autocorrelation function (\diamond) in Fig. 5.18 for transverse velocity. For compar-
1570 ison convenience, both the second order structure function and the autocorrelation
1571 function are converted from physical space into spectral space by taking $f = 1/\ell$.
1572 Graphically, except for the second order structure function, the others show a clear
1573 plateau more than two decades wide. The similar shape for the compensated sec-
1574 ond order structure function can be found in Refs. Anselmet *et al.* (1984, Figure 10
1575 and Figure 11) and Frisch (1995, P128, Figure 8.6). We have focused here on the
1576 existence of the power law, not the value of the scaling exponent or the range of the
1577 plateau. Thus we do not compare the scaling exponents here. Based on this obser-
1578 vation, we state that the autocorrelation function is a better inertial range indicator
1579 than structure functions (Huang *et al.*, 2009c).

1580 5.3 Summary

1581 In this chapter, we considered the second order structure function and the autocor-
1582 relation function of the velocity increment time series $\Delta u_\ell(t)$, where ℓ is a time scale.
1583 Taking statistical stationary assumption, we proposed an analytical model of the sec-
1584 ond order structure function and the autocorrelation function. Within this model,
1585 for the second order structure function, we found that it is strongly influenced by the
1586 large scale part. Furthermore, the influence range down to the small scale part is as
1587 large as two decades. However, the Hilbert-based methodology seems to constrain
1588 the periodic effect in 0.3 decade, which may be linked to the fact that EMD acts a

dyadic filter bank. We thus argued that the widely used structure function method 1589
is not a good method to extract the scaling exponents from a given time series when 1590
the data possess energetic large scales. We showed this experimentally by analyzing 1591
a passive turbulence data, a temperature time series obtained from a jet experiment. 1592

For the autocorrelation function, we proved analytically that the location of the 1593
minimum autocorrelation function is exactly equal to the separation time scale ℓ 1594
when the scaling of power spectrum of the original variable belongs to the range 1595
 $0 < \beta < 2$. In fact, this property was found experimentally to be valid outside 1596
the scaling range, but our demonstration here concerns only the scaling range. This 1597
model also suggests a power law expression for the minimum autocorrelation $\Gamma_o(\ell)$. 1598
Considering the cumulative integration of the autocorrelation function, it was shown 1599
that the autocorrelation function is influenced more by the large scale part. We thus 1600
argued that the autocorrelation function is a better indicator of the inertial range 1601
than second order structure function. These results have been illustrated using fully 1602
developed turbulence data; however, they are of more general validity since we only 1603
assumed that the considered time series is stationary and possesses scaling statistics. 1604

1605 Chapter 6

1606 Experimental Homogeneous and 1607 Locally Isotropic Turbulence

1608 Since Kolmogorov (1941c,a,b) proposed his very famous K41 turbulence theory, the
1609 studies to extract the scaling exponents from various turbulent flows becomes one
1610 central problem in turbulent research (Monin & Yaglom, 1971; Anselmet *et al.*, 1984;
1611 Antonia *et al.*, 1984; Kraichnan, 1991; Frisch, 1995; Kahalerras *et al.*, 1998; van de
1612 Water & Herwijer, 1999; Sreenivasan & Antonia, 1997; Tsinober, 2001; Moisy *et al.*,
1613 2001; Tsuji, 2004; Chevillard *et al.*, 2005). The structure function scaling exponent
1614 $\zeta(q)$ extracted from various turbulent flows are well documented (Frisch, 1995; Sreeni-
1615 vasan & Antonia, 1997). In this chapter, we apply the arbitrary order Hilbert spectral
1616 analysis on an experimental homogeneous and nearly isotropy turbulent data to char-
1617 acterize the scale invariant properties in amplitude-frequency space for the first time.
1618 The results presented in this chapter are for part of them published in Huang *et al.*
1619 (2008) [Y. Huang, *et al. Europhy. Lett.*, 84, 40010, 2008.].

6.1 Experimental data

1620

The database we consider here is the same database we used in chapter 5. Here we present it on more details.

1622

Conventional passive grid wind tunnels of normal laboratory size allow to generate only moderate Reynolds number turbulent flow, with Taylor microscale based Reynolds numbers typically less than 150. The main reason is that the root-mean-square (r.m.s.) velocity downstream of a passive grid is relatively low (Kang *et al.*, 2003). As an alternative, the ‘active grid’ technique, which allows to achieve higher Reynolds number turbulent flow, has been studied by several authors (Makita, 1991; Mydlarski & Warhaft, 1996, 1998; Kang *et al.*, 2003).

1623

1624

1625

1626

1627

1628

1629

Table 6.1: Some parameters of the turbulent flow consider here at four different locations: mean velocity $\langle u \rangle$, r.m.s velocity $u_{\text{r.m.s.}}(\langle (u - \langle u \rangle)^2 \rangle^{1/2})$, isotropy ratio I , turbulence intensity (%), Kolmogorov scale η ($(\nu^3/\epsilon)^{1/4}$), Taylor microscale λ ($(15u_{\text{r.m.s.}}^2\nu/\epsilon)^{1/2}$) and corresponding Reynolds number Re_λ . The details about this experiment and data can be found in Kang *et al.* (2003).

	$x_1/M = 20$	$x_1/M = 30$	$x_1/M = 40$	$x_1/M = 48$
$\langle u_1 \rangle$ (ms ⁻¹)	12.0	11.2	11.0	10.8
$u_{1\text{r.m.s.}}$ (ms ⁻¹)	1.85	1.43	1.19	1.08
$u_{2\text{r.m.s.}}$ (ms ⁻¹)	1.64	1.25	1.04	0.932
$I = u_{1\text{r.m.s.}}/u_{2\text{r.m.s.}}$	1.13	1.14	1.14	1.16
$u_{1\text{r.m.s.}}/\langle u_1 \rangle$ (%)	15.4	12.8	10.8	10.0
η (mm)	0.11	0.14	0.16	0.18
λ (mm)	5.84	7.13	8.25	8.78
$Re_\lambda = u_{1\text{r.m.s.}}\lambda/\nu$	716	676	650	626

Experiments are performed downstream of an active grid in the return-type Corrsin wind tunnel (Comte-Bellot & Corrsin, 1966, 1971) in the Johns Hopkins University’s Corrsin wind tunnel (Kang *et al.*, 2003). The wind tunnel has primary and secondary

1630

1631

1632

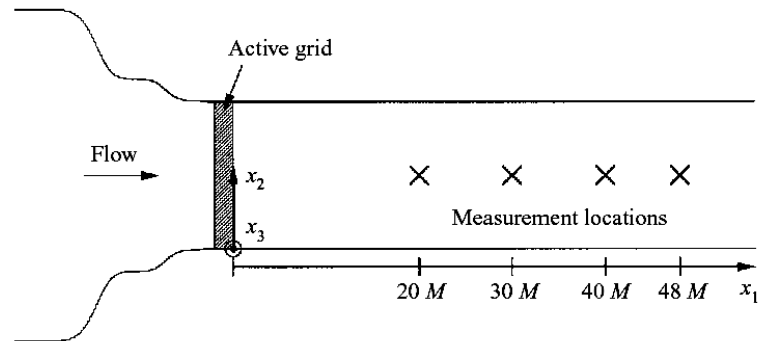


Figure 6.1: Schematic representation of the wind tunnel. Taken from Ref. [Kang *et al.* \(2003\)](#).

1633 contraction ratios of 25:1 and 1.27:1, respectively. The active grid is placed down-
 1634 stream of the secondary contraction, see the schematic of the wind tunnel in Fig. 6.1.
 1635 The test section length is 10 m and the cross-section is 1.22 m by 0.91 m. The span-
 1636 wise width of the wind tunnel gradually increases along the test section to account for
 1637 boundary layer growth. Figure 6.1 demonstrates the schematic of the wind tunnel,
 1638 where the measurement locations are marked by \times .

1639 The design of the active grid follows that of [Makita \(1991\)](#) and [Mydlarski &](#)
 1640 [Warhaft \(1996, 1998\)](#). The active grid is composed of five horizontal and seven vertical
 1641 rotating shafts to which diamond-shaped winglets are attached. The shafts are made
 1642 of 19.05 mm square aluminium channel with 3.18 mm-thick walls. The horizontal and
 1643 vertical shafts have eight and six winglets, respectively, so that the grid size, M , is
 1644 0.152 m. The $0.102 \times 0.102 \text{ m}^2$ square winglets are made of 3.18 mm-thick aluminium
 1645 plate. Along each shaft, the winglets are attached to opposite sides in an alternating
 1646 fashion to help reduce vibrations ([Kang *et al.*, 2003](#)). A schematic diagram of the
 1647 active grid is shown in Fig. 6.2. Each shaft is independently driven by a 1/4 hp
 1648 AC motor (Baldor Industrial Motor, CNM20252) and each motor is controlled by an

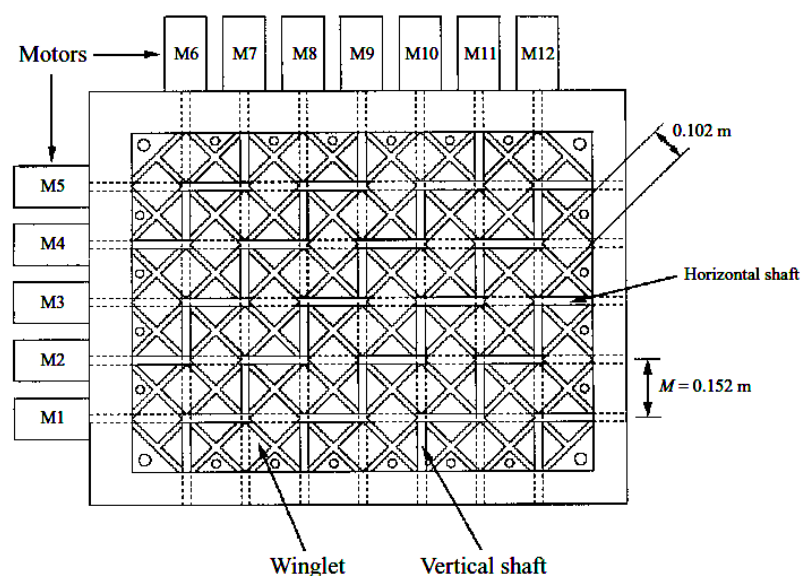


Figure 6.2: Schematic representation of the active grid. Taken from Ref. Kang *et al.* (2003).

inverter (ABB Industrial Systems Inc., ACS 140). The control signal is generated by 1649
 a PC and sent to the twelve inverters through two six-node RS-485 serial networks, 1650
 using a National Instruments AT-485 card. Each motor is set to randomly change 1651
 rotational speed and direction once every second. The speed is selected from a uniform 1652
 distribution in the range of about 210-420 r.p.m., in both directions. 1653

Figure 6.1 shows the schematic of the experimental wind-tunnel setup, in which the 1654
 active grid is located at the beginning of the test section. The measurement locations 1655
 in the streamwise (longitudinal) direction (x_1) are at $x_1/M = 20, 30, 40$ and 48 and 1656
 marked by \times . An X-wire probe array described in Kang & Meneveau (2001) is used 1657
 for measuring two velocity components in the (x_1, x_2) -plane. The probe array is 1658
 composed of four custom-made miniature X-type hot-wire probes. The signals are 1659
 sampled at $f_s = 40$ kHz, low-pass filtered at a frequency of 20 kHz and digitized with 1660

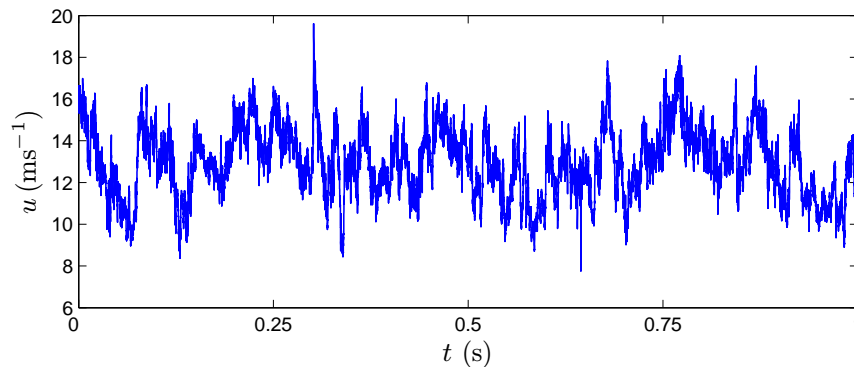


Figure 6.3: One 1s portion of longitudinal velocity at location $x/M = 48$, showing the intermittency nature of turbulent velocity field.

1661 a 12-bit simultaneous sample and hold A/D converter (United Electronic Industries,
 1662 WIN-30DS). The sampling time is 30×30 s, so the total number of data points per
 1663 channel for each measurement location is 36×10^6 . The array is located at the centre
 1664 of the wind tunnel and is moved manually to various downstream locations. The data
 1665 are recorded in the central core region ($0.25 \text{ m} < x_2 < 0.65 \text{ m}$ and $0.25 \text{ m} < x_3 < 0.95 \text{ m}$).
 1666 To obtain the spatial quantities in the streamwise direction from the temporal data,
 1667 Taylor's hypothesis is invoked.

1668 Table 6.1 shows the main parameters of each experimental data set, including the
 1669 mean longitudinal velocity $\langle u_1 \rangle$, the r.m.s. velocities $u_{1\text{r.m.s.}}$ and $u_{2\text{r.m.s.}}$, the isotropy
 1670 ratio $I = u_{1\text{r.m.s.}}/u_{2\text{r.m.s.}}$, the turbulence intensity $u_{1\text{r.m.s.}}/\langle u_1 \rangle$, the Kolmogorov scale
 1671 $\eta = (\nu^3/\epsilon)^{1/4}$, the Taylor microscale $\lambda = (15u_{1\text{r.m.s.}}^2\nu/\epsilon)^{1/2}$, and the Taylor microscale
 1672 based Reynolds number $Re_\lambda = u_{1\text{r.m.s.}}\lambda/\nu$. A 1s portion of velocity at downstream
 1673 $x/M = 48$, where M is the mesh size, is displayed in Fig. 6.3 to demonstrate the
 1674 intermittency and stochastic nature of the turbulent velocity field. We then show
 1675 the Fourier spectrum and the corresponding second order Hilbert marginal spectrum
 1676 at the downstream $x/M = 48$ in Fig. 6.4, where the compensated spectrum $E(f)f^{5/3}$

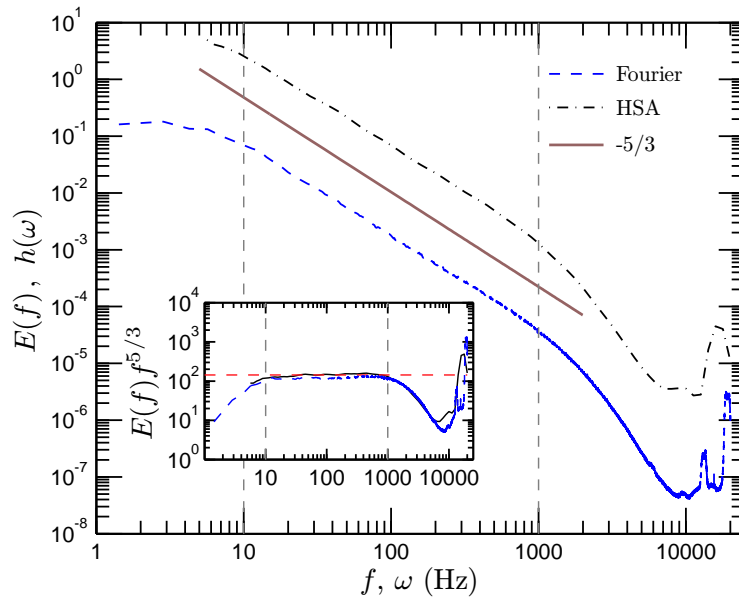


Figure 6.4: Comparison of the Hilbert marginal spectrum (dashed-dotted line) and Fourier spectrum (dashed line) at downstream $x/M = 48$. Both of them predict the inertial subrange on the range $10 \leq \omega \leq 1000$ Hz. The inset shows the corresponding compensated spectra $E(f) f^{5/3}$.

is shown as inset. The Hilbert marginal spectrum which is shown here is the first 1677
 experimental estimate of a Kolmogorov 5/3 spectrum in Hilbert spectral frame that 1678
 we published in a recent work (Huang *et al.*, 2008). We can find that both spectra 1679
 predict an almost two decades inertial subrange on the range $10 \leq f(\text{or } \omega) \leq 1000$ Hz, 1680
 which is illustrated as vertical dashed line. Therefore, the data we have chosen here 1681
 have a sufficient inertial subrange to test our new Hilbert-based methodology. For 1682
 more details about the experiment and the data see Kang *et al.* (2003); the data can 1683
 be found at <http://www.me.jhu.edu/~meneveau/datasets.html>. 1684

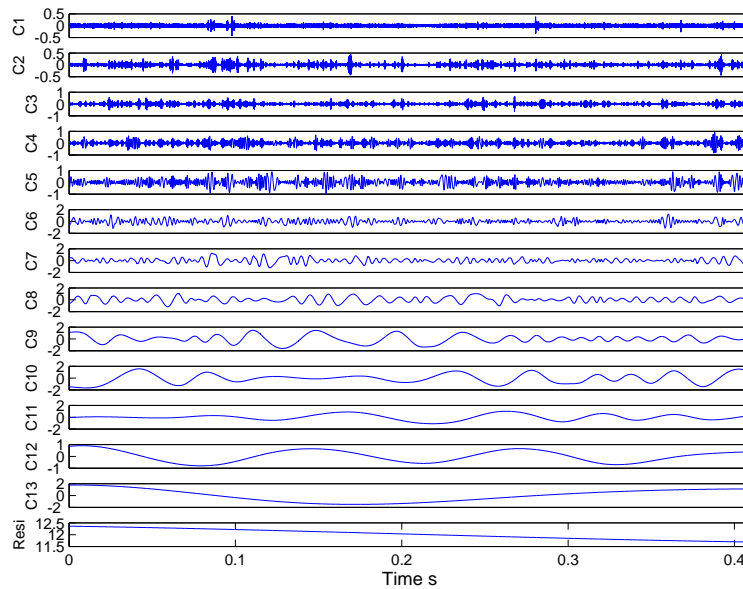


Figure 6.5: IMF modes of one 2^{14} points segment from EMD.

1685 6.2 EMD decomposition of turbulent data

1686 The original velocity time series is divided into 73 segments (without overlapping)
 1687 of 2^{14} points each. After decomposition, the original velocity series is decomposed
 1688 into several IMFs, from 11 to 13 modes with one residual. Figure 6.5 shows the IMF
 1689 modes of one segment from EMD algorithm. The time scale increases with the mode
 1690 index n . We note that the number of IMF modes is deduced by the data themselves,
 1691 and depends on the length and the complexity of the data. In practice, based on
 1692 the dyadic filter bank property of the EMD algorithm, this number is usually less
 1693 than $\log_2(N)$, where N is the length of the database (Flandrin & Gonçalves, 2004;
 1694 Flandrin *et al.*, 2004; Wu & Huang, 2004; Huang *et al.*, 2008).

1695 The time scale is increasing with the mode index n ; and each mode can be char-
 1696 acterized by its mean frequency, which is estimated by considering the Fourier energy

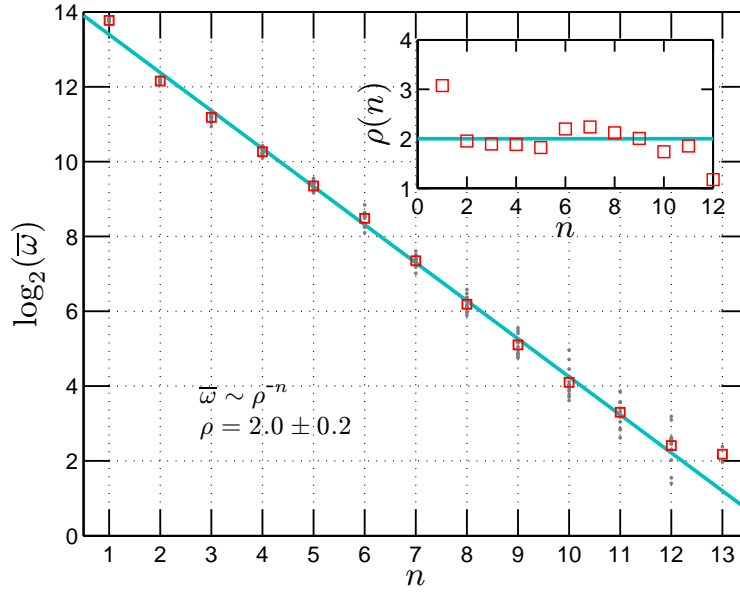


Figure 6.6: Mean frequency $\bar{\omega}$ vs mode index n for the longitude velocity time series. There is an exponential decrease with a slope very close to 1, which indicates that EMD acts as a dyadic filter bank. The inset shows the local slope $\rho(n)$.

weighted mean frequency, $\bar{\omega}$. The mean frequency $\bar{\omega}$ is defined as

1697

$$\bar{\omega}_i = \frac{\int f |S_i(f)|^2 df}{\int |S_i(f)|^2 df} \quad (6.2.1)$$

where $S_i(f)$ is the Fourier power spectrum of each IMF mode $C_i(t)$. Figure 6.6 shows the mean frequency $\bar{\omega}(n)$, where the inset shows local slope. The straight line in log-linear plot suggests the following relation

1698

1699

1700

$$\bar{\omega}(n) = \omega_o \rho^{-n} \quad (6.2.2)$$

where $\omega_o \simeq 22000$, and $\rho = 2.0 \pm 0.1$, very close to 2. This implies that the EMD algorithm acts as a dyadic filter bank in the frequency domain. An analogous property was obtained using stochastic simulations of Gaussian noise and fractional Gaussian noise (Wu & Huang, 2004; Flandrin & Gonçalvès, 2004), and it is interesting to note here that the same result holds for fully developed turbulence time series.

1701

1702

1703

1704

1705

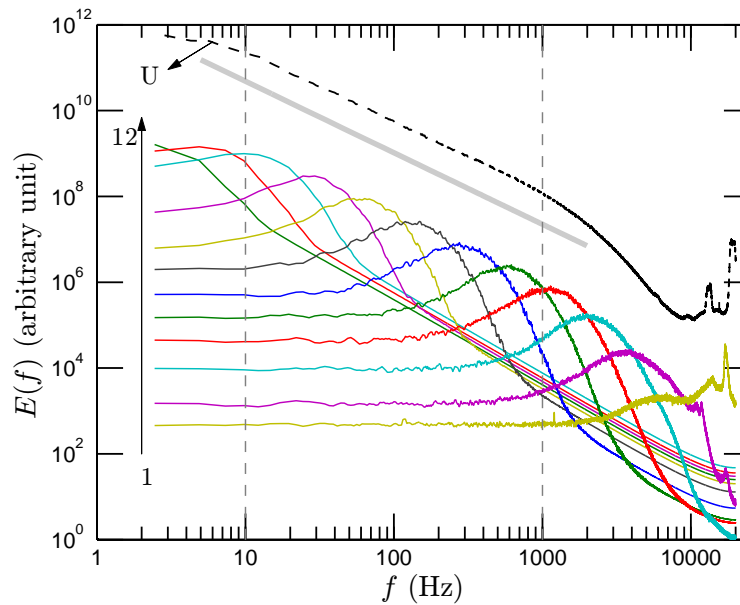


Figure 6.7: Fourier spectra for IMF modes. The vertical dashed lines indicate the inertial subrange $10 \leq f \leq 1000$ Hz. One can find that the modes belonging to the inertial range have a similar shape.

1706 We then interpret each mode according to their characteristic time scale. When
 1707 compared with the original Fourier spectrum of the turbulent time series, see Fig. 6.7,
 1708 these modes can be termed as follows: the first mode, which has the smallest time
 1709 scale, corresponds to the measurement noise; modes 2 and 3 are associated with the
 1710 dissipation range of turbulence. Mode 4 corresponds to the Kolmogorov scale, which
 1711 is the scale below which dissipation becomes important; it is a transition scale between
 1712 inertial range and dissipation range. Modes 5 to 10 all belong to the inertial range,
 1713 corresponding to the scale-invariant Richardson-Kolmogorov energy cascade (Frisch,
 1714 1995); larger modes belong to the large forcing scales. Figure 6.7 represents the
 1715 Fourier power spectra of each mode. It shows that each mode in the inertial range is
 1716 narrow-banded. This confirms that the EMD approach acts as a filter bank for turbu-
 1717 lence time series and that each mode can be associated to a given part of the different

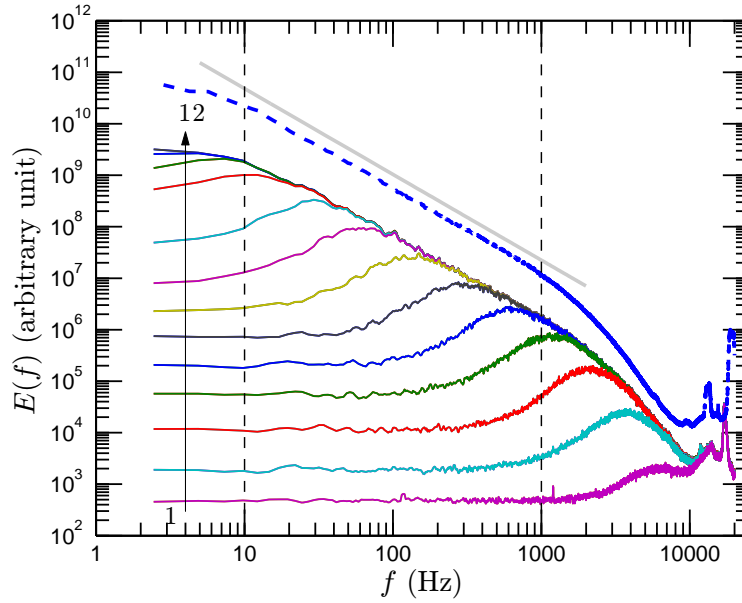


Figure 6.8: Fourier spectra for successive sums of IMF modes $\sum C_i$. The slope of the reference line is $-5/3$. The vertical dashed lines indicate the corresponding inertial subrange $10 \leq f \leq 1000$ Hz. With the mode index increasing, the spectrum is then asymptotically approached to the original spectrum.

zones of turbulence (injection scales, inertial range, dissipation scales) (Huang *et al.*, 1718
 2008). We then plot the Fourier spectrum of the cumulative sum of these IMF modes 1719
 in Fig. 6.8. For comparison, we also represent the Fourier spectrum of the original 1720
 longitude velocity u . The addition of more and more modes in the decomposition 1721
 is a progressive reconstruction of the original time series as can be seen from the 1722
 spectrum which asymptotically reaches the $-5/3$ behaviour. 1723

6.3 Joint pdf and dimensional analysis 1724

Here we consider the joint pdf in amplitude-frequency space, and obtain experimen- 1725
 tally new scaling result, for which we give some interpretation using dimensional 1726

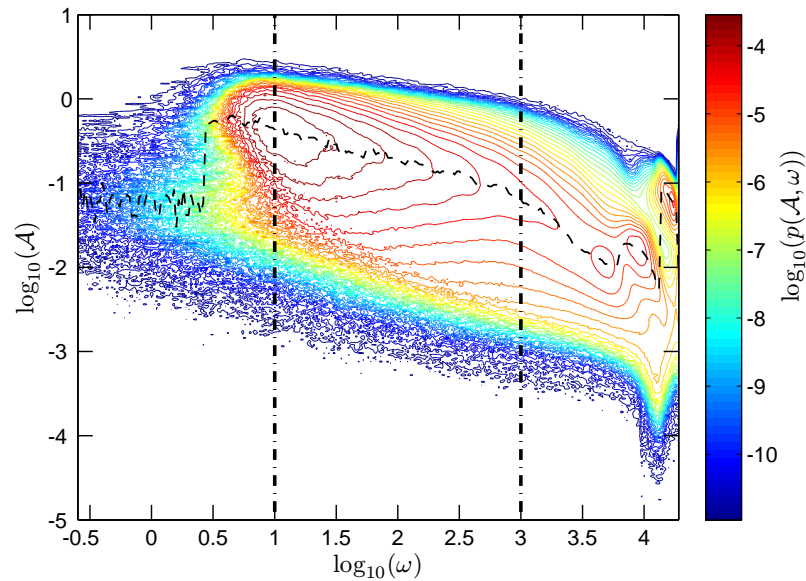


Figure 6.9: Representation of the joint pdf $p(\omega, \mathcal{A})$ (in log scale) of turbulent fluctuations in an amplitude-frequency space. The scaling range $10 < \omega < 1000$ Hz for frequencies is shown as vertical dashed-dotted lines. The dashed line shows the skeleton $\mathcal{A}_s(\omega)$ of the joint pdf, which is the amplitude for which the conditional pdf $p(\mathcal{A}|\omega)$ is maximum.

1727 analysis.

1728 Joint pdf $p(\omega, \mathcal{A})$

1729 The arbitrary order HSA methodological framework provides a way to represent tur-
 1730 bulent fluctuations in an amplitude-frequency space (Huang *et al.*, 2008, 2009d,a).
 1731 We represent the joint pdf $p(\omega, \mathcal{A})$ in Fig. 6.9 in a log-log view, where the vertical
 1732 dashed-dotted lines demonstrate the inertial subrange, $10 \leq \omega \leq 1000$ Hz. It can
 1733 be seen that the joint pdf $p(\omega, \mathcal{A})$ decrease with increasing frequencies, with a scal-
 1734 ing trend. We show in the same graph the skeleton $\mathcal{A}_s(\omega)$ of the joint pdf which

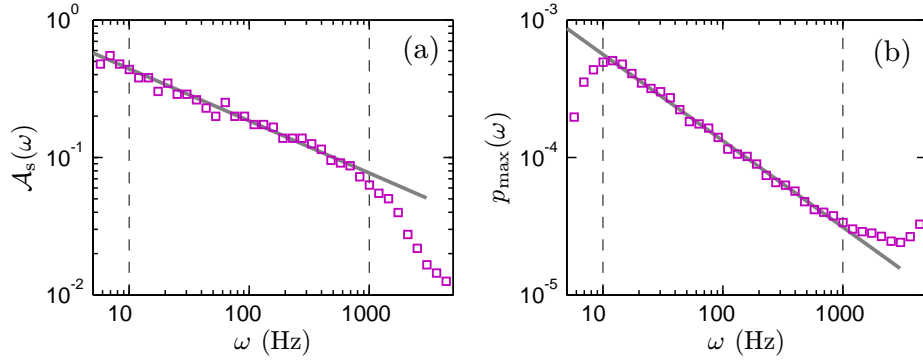


Figure 6.10: The skeleton of the joint pdf (a) $\mathcal{A}_s(\omega)$ in log-log plot. A power law behaviour is observed in the inertial subrange with scaling exponent 0.38, which is close to the Kolmogorov value $1/3$, and (b) $p_{\max}(\omega)$ in log-log plot. A power law behaviour is observed in the inertial subrange with scaling exponent 0.63. The vertical dashed lines show the corresponding inertial subrange $10 < \omega < 1000$ Hz.

corresponds to the amplitude for which the conditional pdf $p(\mathcal{A}|\omega)$ is maximum

1735

$$\mathcal{A}_s(\omega) = \mathcal{A}_0; p(\mathcal{A}_0, \omega) = \max_{\mathcal{A}} \{p(\mathcal{A}|\omega)\} \quad (6.3.1)$$

We then reproduce the skeleton in Fig. 6.10 in two different views: (a) $\mathcal{A}_s(\omega)$ in a log-log plot; (b) skeleton pdf $p_{\max}(\omega) = p(\mathcal{A}_s(\omega), \omega) = \max_{\mathcal{A}} \{p(\mathcal{A}|\omega)\}$ in a log-log plot, where the vertical dashed line indicates the inertial subrange. It is interesting to note that a power law behaviour is found for both representations

1736

1737

1738

1739

$$\mathcal{A}_s(\omega) \sim \omega^{-\beta_1} \quad (6.3.2a)$$

where $\beta_1 \simeq 0.38$, and

1740

$$p_{\max}(\omega) \sim \omega^{-\beta_2} \quad (6.3.2b)$$

where $\beta_2 \simeq 0.63$. Dimensional analysis to interpret these results is provided below.

1741

Table 6.2: The dimension of several physical quantities: wave number, k , arbitrary order Hilbert marginal spectrum $\mathcal{L}_q(k)$ and mean energy dissipation rate $\bar{\epsilon}$.

Quantity		Dimension	
Wave number	k	1/length	(L^{-1})
arbitrary order HMS	$\mathcal{L}_q(k)$	length $^{q+1}$ /time q	$(\text{L}^{q+1}\text{T}^{-q})$
Energy dissipation rate	$\bar{\epsilon}$	energy/time	$(\text{L}^2\text{T}^{-3})$

1742 Dimensional Analysis

1743 We rewrite here the arbitrary order Hilbert marginal spectrum in a wavenumber form

$$\mathcal{L}_q(k) = \int p(k, \mathcal{A}) \mathcal{A}^q \, d\mathcal{A} \quad (6.3.3)$$

1744 where k is the instantaneous wavenumber in the spatial domain, which corresponds
 1745 to the instantaneous frequency ω in the temporal domain, and \mathcal{A} is the instantaneous
 1746 amplitude. We list the dimensions for the arbitrary order Hilbert spectrum $\mathcal{L}_q(k)$,
 1747 the instantaneous wavenumber k , and the mean energy dissipation rate $\bar{\epsilon}$ in Table 6.2.
 1748 The amplitude \mathcal{A} has the same dimension as the velocity u

$$[\mathcal{A}_s] = [\mathcal{A}] = [u] = \text{LT}^{-1} \quad (6.3.4)$$

1749 in which $[\]$ means dimension of a variable. The dimension of the arbitrary order
 1750 Hilbert marginal spectrum by its physical meaning is

$$[\mathcal{L}_q(k)] = \frac{[\mathcal{A}]^q}{[k]} = \text{L}^{q+1}\text{T}^{-q} \quad (6.3.5)$$

1751 The dimension balance requires

$$[\mathcal{L}_q(k)] = [p(k, \mathcal{A})][\mathcal{A}]^{q+1} \quad (6.3.6)$$

1752 We thus have the dimension of $p(k, \mathcal{A})$

$$[p(k, \mathcal{A})] = \text{T} \quad (6.3.7)$$

If we take the mean energy dissipation rate $\bar{\epsilon}$ and the wavenumber k as basic dimensions, then we have

$$[\mathcal{L}_q(k)] = [\bar{\epsilon}]^{q/3} [k]^{-(q/3+1)} \quad (6.3.8a)$$

$$[\mathcal{A}_s] = [\bar{\epsilon}]^{1/3} [k]^{-1/3} \quad (6.3.8b)$$

$$[p_{\max}(k)] = [p(k, \mathcal{A})] = [\bar{\epsilon}]^{-1/3} [k]^{-2/3} \quad (6.3.8c)$$

Considering the Kolmogorov's first and second universality similarity hypothesis (Kolmogorov, 1941a; Monin & Yaglom, 1971; Frisch, 1995), we thus have the following power law in the so-called inertial subrange

$$\mathcal{L}_q(k) = C_q \bar{\epsilon}^{q/3} k^{-(q/3+1)} \sim k^{-(q/3+1)} \quad (6.3.9a)$$

$$\mathcal{A}_s = D_0 \bar{\epsilon}^{1/3} k^{-1/3} \sim k^{-1/3} \quad (6.3.9b)$$

$$p_{\max}(k) = P_0 \bar{\epsilon}^{-1/3} k^{-2/3} \sim k^{-2/3} \quad (6.3.9c)$$

where C_q , D_0 and P_0 are Kolmogorov constant¹. The argument presented above indicates that the arbitrary order HSA methodology can be used to characterize the intermittent properties of turbulence. We will further consider this topic in the next section.

We notice that the difference between the estimated values β and the Kolmogorov nonintermittent values may be an effect of the turbulent intermittency. We also note that the value $\beta_1 = 0.38$ is comparable with $\zeta(1) = 0.37$ estimation given in Ref van de Water & Herwijer (1999).

¹However, these Kolmogorov constants may depend on the detail of the turbulent flow. There is no reason to require them to be universal.

1770 **Maxima Amplitude**

1771 Inspired by the log-Poisson model (She & L ev eque, 1994; Dubrulle, 1994; She &
1772 Waymire, 1995), Vainshtein (2003) studied the most dissipative, most intense struc-
tures using a high Reynolds number experimental data. He found that the most

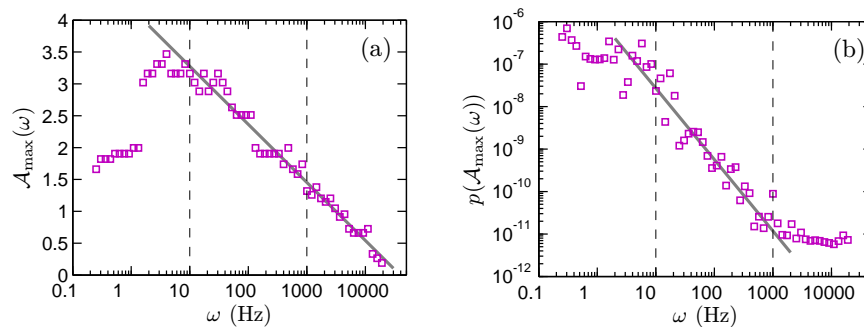


Figure 6.11: Representation of the maxima amplitude (a) $\mathcal{A}_{\max}(\omega)$ in log-linear plot, and (b) the corresponding $p(\mathcal{A}_{\max}(\omega))$ in log-log plot, respectively.

1773

1774 intense of the dissipation field $\max(\epsilon_r)$ satisfies a power law

$$\max(\epsilon_r) \sim \left(\frac{r}{\ell}\right)^{-\gamma} \quad (6.3.10)$$

1775 The scaling value γ is found 0.61 ± 0.01 , only slightly small than $2/3$ (Vainshtein,
1776 2003). We are here interested in the maxima amplitude \mathcal{A}_{\max} at given frequency ω

$$\mathcal{A}_{\max}(\omega) = \max\{\mathcal{A}|_{p(\mathcal{A}|\omega) \neq 0}\} \quad (6.3.11)$$

1777 Figure 6.11 shows the maxima amplitude $\mathcal{A}_{\max}(\omega)$ in two views: (a) \mathcal{A}_{\max} vs ω in
1778 a log-linear, and (b) $p(\mathcal{A}_{\max})$ vs ω in a log-log view, where the vertical dashed line
1779 demonstrates the inertial subrange $10 < \omega < 1000$ Hz. We obtain a law

$$\mathcal{A}_{\max}(\omega) = a \log_{10}(\omega) + b \quad (6.3.12)$$

in which $a \simeq -0.91$ and $b \simeq 4.19$ are obtained by using a least square fitting. We also observe a power law behaviour for $p(\mathcal{A}_{\max})$, which is written as

$$p(\mathcal{A}_{\max}) \sim \omega^{-\chi} \tag{6.3.13}$$

where $\chi \simeq 1.68$. Here the plot is quite scattered, but nevertheless the straight line trend in each representation is clear. We have no theoretical or dimensional explanation to propose for these relations. However, these findings may be linked to the nature of turbulence: this will be checked using more databases in the future studies.

Rescaled Conditional pdf

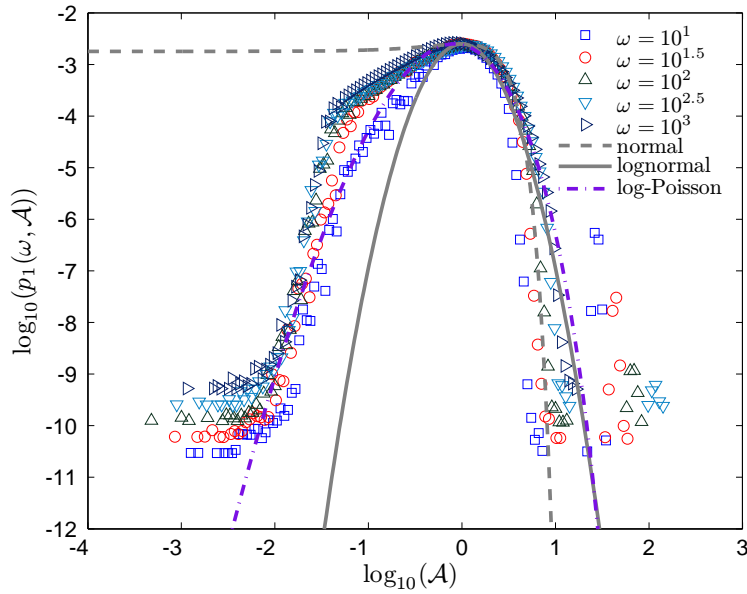


Figure 6.12: Representation of the rescaled conditional pdf $p_1(\mathcal{A}, \omega)$ in the inertial range, for fixed values of $\omega = 10$ (\square), $10^{1.5}$ (\circ), 10^2 (\triangle), $10^{2.5}$ (∇) and 10^3 Hz (\triangleright). For comparison, we also plot the normal distribution (dash line), log-normal distribution (solid line) and log-Poisson distribution (dashed-dotted line).

The power law relation for the skeleton indicates a rescaling relation for the pdf $p_1(\mathcal{A}, \omega) = \omega^{\beta_2} p(\mathcal{A}/\omega^{\beta_1}, \omega)$. We plot it in Fig. 6.12 for various fixed values of ω

1789 in the inertial subrange, where $\omega = 10$ (\square), $10^{1.5}$ (\circ), 10^2 (\triangle) and 10^3 (\triangleright) Hz,
 1790 respectively. In case of monoscaling, these pdfs should superpose perfectly; here the
 1791 plot is scattered, but nevertheless we note that the lack of superposition of these
 1792 rescaled pdfs is a signature of intermittency. Moments of this pdf are less noisy as
 1793 will be visible below. For comparison, we plot the normal distribution (dashed line),
 1794 lognormal distribution (solid line) and log-Poisson distribution (dashed-dotted line)
 1795 in the same figure. It seems that the log-Poisson distribution provides a better fit to
 1796 the pdf than the lognormal distribution for the left-hand part, whereas the lognormal
 1797 fit is better for the right-hand part.

1798 6.4 Intermittency

1799 Figure 6.13 shows $\mathcal{L}_q(\omega)$ for various orders of Hilbert marginal spectra (0, 1, 3, 4, 5
 1800 and 6). The moment of order 0 is the marginal pdf of the instantaneous frequency
 1801 ω , see Eq. (3.3.1) and the discussion in section 3.3. It is interesting to note that this
 1802 pdf is extremely “wild”, having a behaviour close to $\mathcal{L}_0(\omega) \sim \omega^{-1}$, corresponding
 1803 to a “sporadic” process whose probability density is not normalizable ($\int p(\omega) d\omega$
 1804 diverges). This result is only obtained when all modes are considered together;
 1805 such pdf is not found for the frequency pdf of an individual mode. This property
 1806 seems to be rather general: we observed such pdf for moment of order zero using
 1807 several other time series: for example surf-zone turbulence data, fBm (Huang *et al.*,
 1808 2009d,a), river flow discharge data (Huang *et al.*, 2009b). Hence it does not seem
 1809 to be linked to turbulence itself, but to be a main property of the HSA method,
 1810 see discussion in section 3.3. Such pdf indicates in fact that high frequencies have
 1811 a smaller probability than low frequencies, but still the decrease is very slow with a

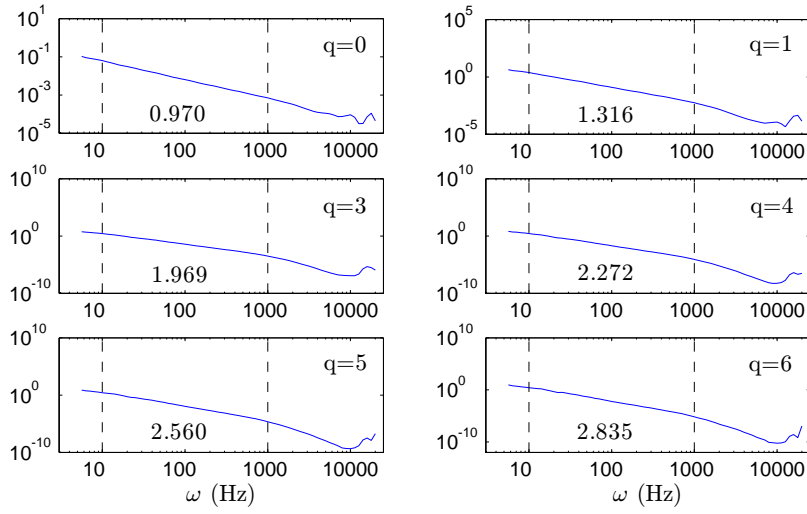


Figure 6.13: Representation of $\mathcal{L}_q(\omega)$, Hilbert spectral analysis of velocity intermittency, using different orders of moments (0, 1, 3, 4, 5 and 6). Power laws are observed on the range $10 < \omega < 1000$ Hz for all spectra. The scaling exponent $\xi(q)$ are estimated on the inertial subrange, which are indicated by the vertical dashed lines.

heavy tail giving large probability to extrema events. We observe the power laws in 1812
 range $10 < \omega < 1000$ Hz for all order moments. The values of scaling exponents $\xi(q)$ 1813
 are shown in each picture. This provides a way to estimate scaling exponents $\xi(q)$ for 1814
 every order of moment $q \geq 0^2$ on a continuous range of scales in the frequency space. 1815
 We show the corresponding scaling exponent $\xi(q)$ in Fig. 6.14, where the inset shows 1816
 the departure from the K41 law. For comparison, we also display the scaling exponent 1817
 provided by the Extended Self-Similarity (ESS) (Benzi *et al.*, 1993a,b, 1995) as dashed 1818
 line. It can be seen that $\xi(q) - 1$ is nonlinear and is close to $\zeta(q)$, but departure from 1819
 the K41 law shows that the curvature is not the same: $\xi(q)$ seems less concave than 1820
 $\zeta(q)$. We thus recover the classical structure function scaling exponent $\zeta(q)$ in an 1821
 amplitude-frequency space here for the first time. 1822

²As we have already indicated in chapter 3, the order of moment q can belong to the on range $q \geq -1$. However, we only consider the case $q \geq 0$ here.

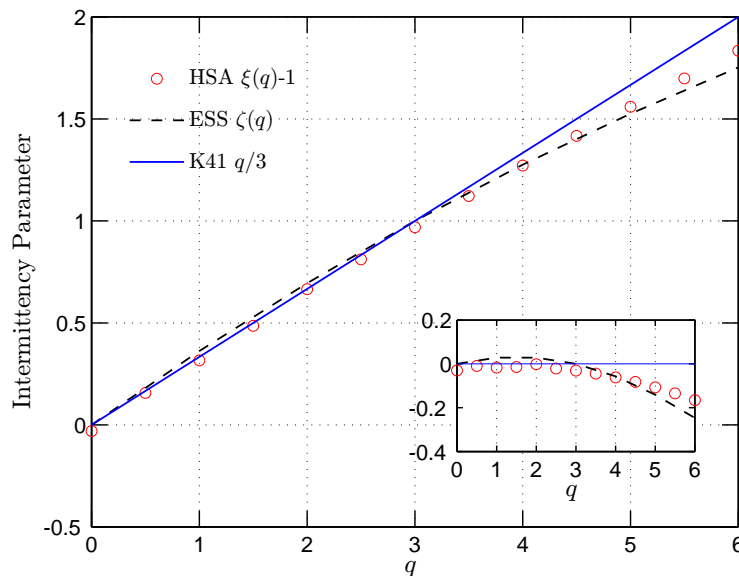


Figure 6.14: Comparison of the scaling exponents $\xi(q) - 1$ (\circ) with the classical $\zeta(q)$ obtained from structure functions analysis with the ESS method (dashed line) and K41 $q/3$ (solid line). The inset shows the departure from the K41 law.

1823 6.5 Isotropy ratio and isotropy scaling exponent

1824 In the database we consider here, for achieving high Reynolds number turbulent
 1825 flow, an active-grid technique is performed (Kang *et al.*, 2003), which may cause
 1826 the turbulent flow to violate the local isotropy hypothesis. In this section we check
 1827 the scale dependent local isotropy ratio $\mathcal{I}(\omega)$ and the corresponding isotropy scaling
 1828 exponent $\Gamma(q)$.

1829 Scale Dependent Isotropy Ratio

1830 A scale dependent isotropy ratio is defined as

$$\mathcal{I}(\omega) = \frac{\mathcal{L}_{u,2}(\omega)}{\mathcal{L}_{v,2}(\omega)} \quad (6.5.1)$$

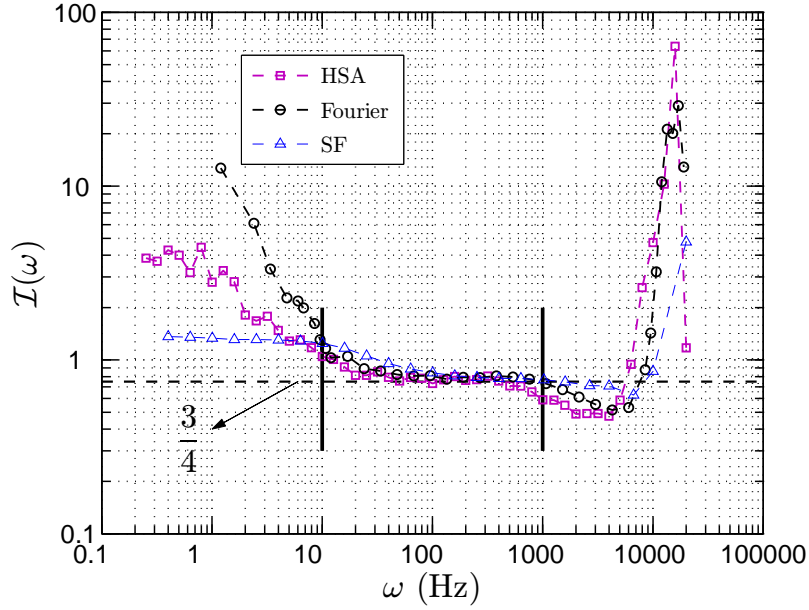


Figure 6.15: The scale dependent isotropy ratio $I(\omega) = \mathcal{L}_{u,2}(\omega)/\mathcal{L}_{v,2}(\omega)$ (\square), where the vertical solid line indicates the inertial range $10 < \omega < 1000$ Hz. The horizontal dashed line indicates theoretical value $3/4$ (Kolmogorov, 1941c). The direct estimation of the isotropy ratio is 1.16 (Kang *et al.*, 2003). For comparison, we also show the scale dependent isotropy ratio provided by Fourier spectrum (\circ) and structure function analysis (\triangle), respectively. Except for the large scale part ($\omega \leq 10$ Hz), all these approaches provide almost the same shape. The Fourier spectrum is taken from Ref. Kang *et al.* (2003).

where $\mathcal{L}_{u,2}(\omega)$ and $\mathcal{L}_{v,2}(\omega)$ are the second order Hilbert marginal spectrum of the 1831
longitudinal and transverse velocity components. This is an isotropy ratio because 1832
it quantifies the scale dependent energy ratio between longitudinal and transverse 1833
velocity components. The Kolmogorov theory predicts that $\mathcal{I}(\omega)$ equals $3/4$ if the 1834
scale ω in the inertial range (Kolmogorov, 1941c; Monin & Yaglom, 1971). Let us 1835
recall here how this isotropy ratio is obtained. The second order structure function 1836
of longitudinal and transverse velocities can be related as (Monin & Yaglom (1971) 1837

1838 p.352)

$$S_{\text{T}}^2(r) = S_{\text{L}}^2(r) + \frac{r}{2} \frac{dS_{\text{L}}^2(r)}{dr} \quad (6.5.2)$$

1839 It is a consequence of the continuity equation. Taking the Kolmogorov's second
1840 similarity hypothesis, we have in the inertial range

$$S_{\text{L}}^2(r) \simeq Cr^{2/3}, \quad S_{\text{T}}^2(r) \simeq C'r^{2/3} \quad (6.5.3)$$

1841 where C and C' are the universal constants. From Eq. (6.5.2) and Eq. (6.5.3), it is
1842 easy to show that

$$\mathcal{I} = \frac{C}{C'} = \frac{3}{4} \quad (6.5.4)$$

1843 A similar argument may apply to the Fourier power spectrum, see [Monin & Yaglom](#)
1844 (1971) for more details.

1845 Figure 6.15 shows the scale dependent local isotropy ratio $\mathcal{I}(\omega)$ (\square), where the
1846 vertical solid lines demonstrate the location of the inertial range $10 < \omega < 1000$ Hz,
1847 and the horizontal dashed line indicates the Kolmogorov value $3/4$. For comparison,
1848 we also show the scale dependent isotropy ratio provided by Fourier spectra (\circ) and
1849 structure function analysis (\triangle) in the same figure (the structure function is converted
1850 from physical space into spectral space by taking $f = 1/\tau$). Except for the large scale
1851 part ($\omega < 10$ Hz), all these methods give almost the same shape. The direct estimation
1852 of the isotropy ratio at this location is 1.16, which is estimated by the ratio of r.m.s.
1853 velocity $u_{1\text{r.m.s.}}/u_{2\text{r.m.s.}}$, see Table 6.1. This value may be influenced by the large scale
1854 anisotropy. We note that the plateau range provided by the structure function is
1855 slightly different from the others, see also Fig. 6.16 (b). We have shown previously
1856 that the structure function is strongly influenced by the large scales. The difference
1857 shown here could be an effect of the large scale anisotropy on the structure functions,
1858 see chapter 5 for more discussion on the structure function.

The isotropy ratio has a different behaviour depending on the scale: the large scale forcing, the inertial range, where the local isotropy ratio is close to Kolmogorov value, and the dissipation range. Due to the grid and boundary effects, the large scale structure is strongly anisotropic. With the scale decreasing (or the frequency increasing), the structure becomes more and more isotropic and value asymptotically the theoretical value $3/4$ in the inertial range. It then keeps this value until entering the dissipation range. In the dissipation range, the isotropy ratio deviates from its theoretical value and increases very fast, which is maybe also the effect of measurement noise. The mean isotropy ratio $\tilde{\mathcal{I}}$ are $\tilde{\mathcal{I}}^H = 0.77 \pm 0.05$, $\tilde{\mathcal{I}}^s = 0.79 \pm 0.03$, and $\tilde{\mathcal{I}}^F = 0.81 \pm 0.02$ for the HSA, structure function and Fourier estimators, respectively. It seems that the HSA approach provides the most isotropic prediction.

Generalized Isotropy Ratio

In order to quantify the evolution of the isotropy ratio for more and more intense events, and hence larger and larger moments we introduce the generalized isotropy ratio for arbitrary order Hilbert marginal spectra

$$\mathcal{I}_q(\omega) = \frac{\mathcal{L}_{u,q}(\omega)}{\mathcal{L}_{v,q}(\omega)} \sim \omega^{(\xi_T(q) - \xi_L(q))} \quad (6.5.5)$$

where $\xi_L(q)$ and $\xi_T(q)$ are the corresponding scaling exponent functions for longitudinal and transverse directions. We then expect $\mathcal{I}_q(\omega)$ to be independent from ω on the inertial range. Figure 6.16 (a) shows the $\mathcal{I}_q(\omega)$ for various q values in log-linear view on the range $8 < \omega < 2000$ Hz, where $q=0$ (\circ), 2 (\square), 4 (\triangle) and 6 (\diamond). The vertical solid lines indicate the plateau on the range $20 < \omega < 800$ Hz. The mean generalized isotropy ratio value $\tilde{\mathcal{I}}^H(q)$ is then estimated on this range, which are shown as thick horizontal dashed lines. The plateau range decreases with q . We apply the same idea

1881 on structure function analysis. Figure 6.16 (b) shows the estimated $\mathcal{I}_q(f)$ on the range
 1882 $8 < f(= 1/\tau) < 8000$ Hz for various q . As we have mentioned previously, the struc-
 1883 ture function is strongly influenced by the large scales. The beginning of the flatness
 1884 range is shifted of almost one decade. The range of plateau decreases with q . It seems
 1885 that the structure function approach decreases faster than for the HSA approach. The
 1886 mean isotropy ratio $\tilde{\mathcal{I}}^S(q)$ is estimated on the range $100 < f(= 1/\tau) < 2000$ Hz.

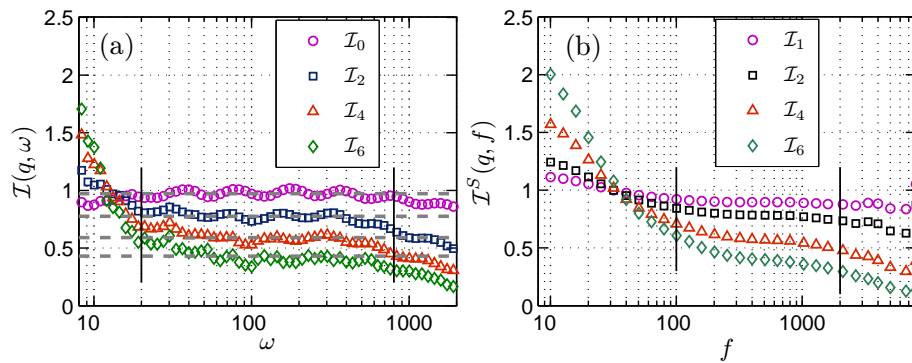


Figure 6.16: The scale dependent generalized isotropy ratio \mathcal{I} : (a) estimated by HSA approach on the range $8 < \omega < 2000$ Hz, where $q = 0$ (\circ), 2 (\square), 4 (\triangle) and 6 (\diamond); (b) estimated by structure function on the range $8 < f(= 1/\tau) < 8000$ Hz, where $q = 1$ (\circ), 2 (\square), 4 (\triangle) and 6 (\diamond). The vertical solid lines indicate the plateau range, where the mean isotropy ratio $\tilde{\mathcal{I}}(q)$ is estimated.

1887 Before plotting the result, we estimate the generalized isotropy ratio using the
 1888 skeleton representation. Figure 6.17 shows the isotropy ratio for the skeleton $\mathcal{A}_s(\omega)$
 1889 (\circ) of the joint pdf $p(\omega, \mathcal{A})$ and the corresponding conditional pdf $p_{\max}(\omega)$ (\square),
 1890 the maxima amplitude $\mathcal{A}_{\max}(\omega)$ (\triangle) and the corresponding conditional pdf $p_{\mathcal{A}_{\max}}(\omega)$
 1891 (solid line in inset). The ratio appears here noisy. However, except the condi-
 1892 tional pdf $p_{\mathcal{A}_{\max}}(\omega)$ for the maxima amplitude, a flatness trend exists for the others
 1893 on the inertial range. We estimate the mean isotropy ratio on the inertial range
 1894 $10 < \omega < 1000$ Hz. We then plot in Fig. 6.18 the mean generalized isotropy ratio

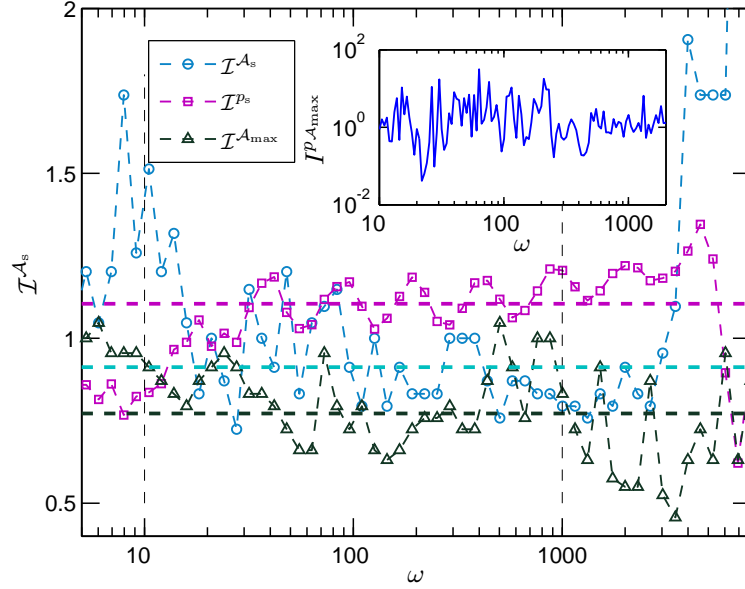


Figure 6.17: The scale dependent generalized isotropy ratio $\mathcal{I}(\omega)$ on range $5 < \omega < 8000$ Hz, where \mathcal{A}_s (\circ), $p_{\max}(\omega)$ (\square) and \mathcal{A}_{\max} (\triangle), respectively. The inset shows the isotropy ratio for $p_{\mathcal{A}_{\max}}$. The vertical dash lines indicate the inertial range $10 < \omega < 1000$ Hz. The mean isotropy ratio $\tilde{\mathcal{I}}$ is then estimated on this range.

$\tilde{\mathcal{I}}^H(q)$ (\square) estimated from the Hilbert spectra and the skeleton. A straight line trend 1895
 seems compatible with the data. It suggests that the mean generalized isotropy ratio 1896
 decreases linearly with q 1897

$$\tilde{\mathcal{I}}(q) = \hat{\alpha}q + \hat{\beta} \quad (6.5.6)$$

where $\hat{\alpha} \simeq -0.091$ and $\hat{\beta} \simeq 0.96$ obtained from a least square fitting. Let us note that 1898
 Antonia *et al.* (1997) provided a 9/16 isotropy ratio for the fourth order structure 1899
 function. If we assume that the generalized isotropy ratio decreases linearly with q , 1900
 and consider the two theoretical isotropy ratio values as boundary condition, we then 1901
 have the equation 1902

$$\tilde{\mathcal{I}}(q) = -\frac{3}{32}q + \frac{15}{16} \quad (6.5.7)$$

which is displayed as a dashed line in Fig. 6.18. It is rather good agreement with 1903

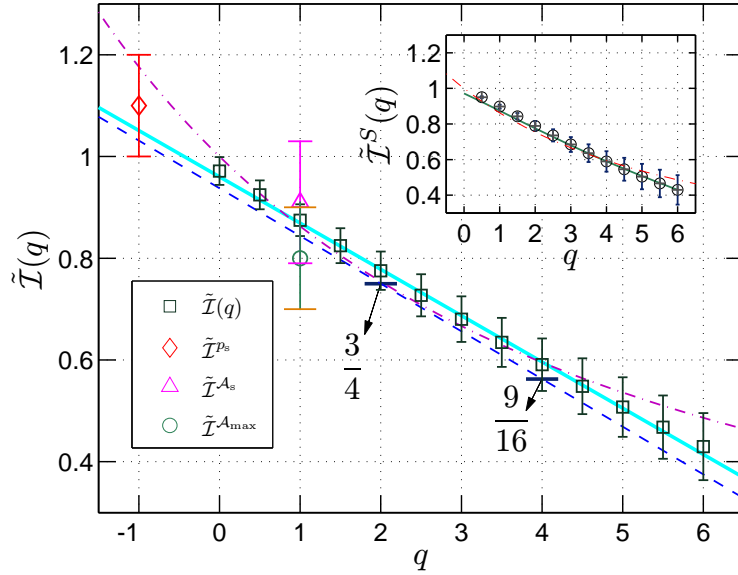


Figure 6.18: Representation of generalized isotropy ratio $\tilde{I}(q)$, estimated from the arbitrary order Hilbert marginal spectra $\mathcal{L}_q(\omega)$ (\square), the skeleton \mathcal{A}_s (\triangle), maxima amplitude (\circ) and the conditional pdf $p(\mathcal{A}_s)$ (\diamond). The dashed line indicates a linearity theoretical prediction by Eq. (6.5.7). The dashed-dotted line is an isotropy relation $\tilde{I}(q) = (2/3)^{\zeta_L(q)}$ provided by Siefert *et al.* (2005). The inset shows the generalized isotropy ratio for the structure function.

1904 experimental isotropy ratio. One interesting finding is that the mean isotropy ratio
 1905 for the skeleton and the maxima amplitude are also in agreement with this linear
 1906 prediction.

1907 Other predications for the generalized isotropy ratio exist in the literature such
 1908 as the one of Siefert *et al.* (2005). They assume of $2/3$ rescaled factor between
 1909 longitudinal and transverse velocity components, giving

$$\langle |u(r)|^q \rangle = \langle |v(\frac{2}{3}r)|^q \rangle = c_L^q r^{\zeta_L(q)} = c_T^q (\frac{2}{3}r)^{\zeta_T(q)} \quad (6.5.8)$$

1910 where $\zeta_L(q)$ and $\zeta_T(q)$ are the scaling exponent function for the longitudinal and
 1911 transverse velocities respectively, and the c^q constants are related to the Kolmogorov
 1912 constants (Siefert *et al.*, 2005). Assuming $\zeta_L(q) = \zeta_T(q)$, it then leads to the following

relation

$$\tilde{\mathcal{I}}(q) = \frac{c_L^q}{c_T^q} = \left(\frac{2}{3}\right)^{\zeta_L(q)} \quad (6.5.9)$$

We show this relation as dashed-dotted line in the same figure, where the scaling exponent $\zeta_L(q)$ correspond to mean values for experimental measurements (Schmitt, 2006). Both linear and convex relations are agreement with the experiment result on the range $0 < q < 5$. As a generalization of this approach, we can introduce $0 < a < 1$ for which

$$\tilde{\mathcal{I}}(q) = a^{\zeta_L(q)} \quad (6.5.10)$$

and try to find the best value of a . The best fitting vale of a is $a = 0.65 \pm 0.05$, quite close to $2/3$.

Isotropy Scaling Exponent

The existence of the plateau of the generalized isotropy ratio indicates that if we plot the longitudinal spectra $\mathcal{L}_{v,q}(\omega)$ against transverse one $\mathcal{L}_{u,q}(\omega)$, a power law behaviour with scaling exponent equal one should hold at least on the plateau range.

Figure 6.19 and 6.20 show respectively $\mathcal{L}_{v,q}(\omega)$ v.s. $\mathcal{L}_{u,q}(\omega)$ on the range $5 < \omega < 6000$ Hz, and $S_{v,q}(\tau)$ v.s. $S_{u,q}(\tau)$ on the range $5 < f(= 1/\tau) < 6000$ Hz for various q . Graphically, power law behaviour holds as expected

$$\mathcal{L}_{v,q}(\omega) \sim (\mathcal{L}_{u,q}(\omega))^{\Gamma(q)}, \quad \xi_T(q) = \xi_L(q)\Gamma(q) \quad (6.5.11)$$

which provides

$$\xi_T(q) = \xi_L(q)\Gamma(q) \quad (6.5.12)$$

If the assumption of local isotropy holds, the scaling exponent $\Gamma(q)$ is then exactly equal to 1. Figure 6.21 shows the corresponding scaling exponent $\Gamma(q)$ estimated from

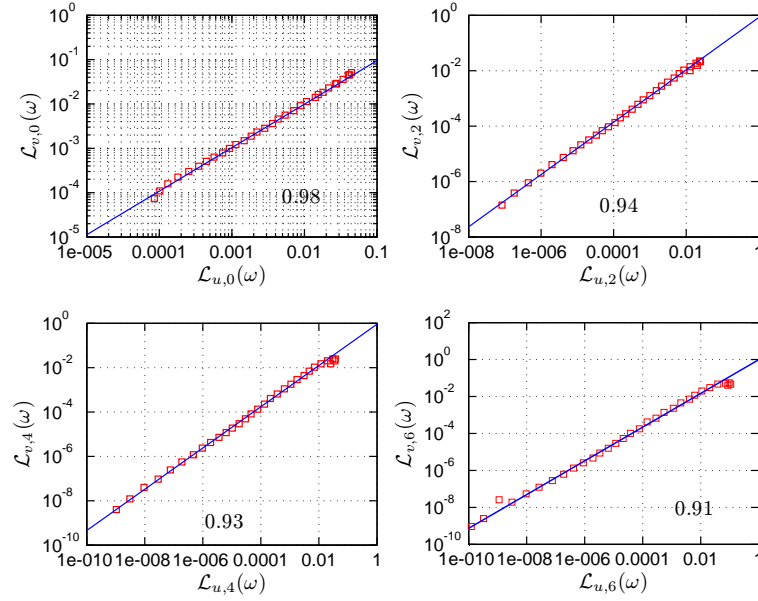


Figure 6.19: Representation of $\mathcal{L}_{v,q}(\omega)$ v.s. $\mathcal{L}_{u,q}(\omega)$ on the range $5 < \omega < 6000$ Hz, where $q = 0, 2, 4$ and 6 , respectively. Power law behaviour is observed for all cases. The corresponding scaling exponent $\Gamma(q)$ is estimated on the inertial range $10 < \omega < 1000$ Hz.

1931 the turbulent database. The isotropy scaling exponent $\Gamma(q)$ deviates from 1. The
 1932 isotropy scaling exponent $\Gamma(q)$ decreases with the order q , which indicates that the
 1933 anisotropy effect becomes more and more strong in high order statistical quantities.
 1934 The HSA approach provides the larger scaling exponent, which may be linked to
 1935 the local ability of the method. It may constrain the large scale anisotropy effect
 1936 both in physical domain and frequency domain. However, for the high order q , $\Gamma(q)$
 1937 is significant less than 1 within statistical uncertainty. For structure function, it
 1938 suggests an approximately linear expression

$$\Gamma^S(q) = -\hat{\gamma}q + \Gamma_o \quad (6.5.13)$$

1939 where $\hat{\gamma} \simeq 0.018$ and $\Gamma_o \simeq 0.97$ are obtained experimentally. However, the influ-
 1940 ence of the large anisotropy scale on the structure function should be investigated

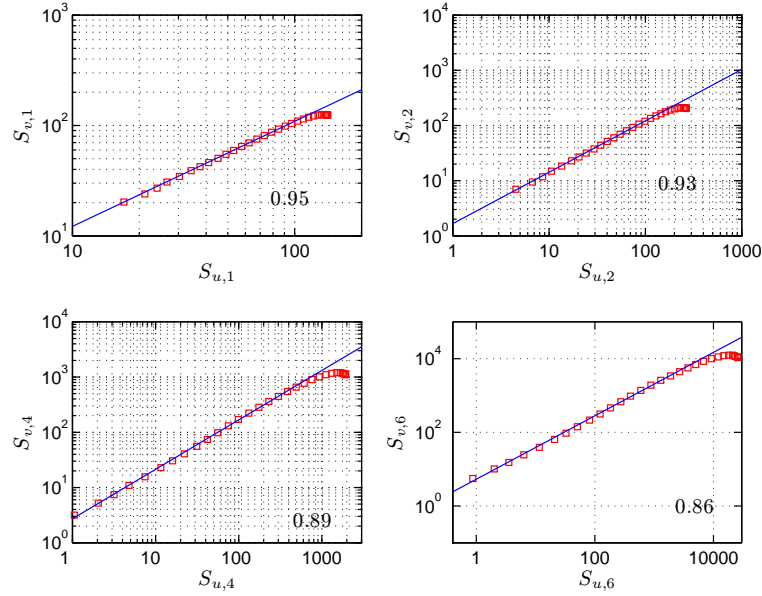


Figure 6.20: Representation of $S_{v,q}(\tau)$ v.s. $S_{u,q}(\tau)$ on the range $5 < f(= 1/\tau) < 6000$ Hz, where $q = 0, 2, 4$ and 6 . Power law behaviour is observed for all cases. The corresponding scaling exponent $\Gamma(q)$ is estimated on the inertial range $10 < f(= 1/\tau) < 1000$ Hz.

systematically in the future studies.

1941

Let us note that the two approaches we considered here are complementary, writing

1942

1943

$$\Gamma(q) = 1 - \beta(q) \tag{6.5.14}$$

We have

1944

$$\zeta_T(q) = \zeta_L(q)(1 - \beta(q)) \tag{6.5.15}$$

and hence

1945

$$\mathcal{I}(q)(\omega) \sim \omega^{\zeta_T(q) - \zeta_L(q)} \sim \omega^{-\beta(q)\zeta_L(q)} \tag{6.5.16}$$

This shows that if $\beta(q)$ is close to zero, $\mathcal{I}_q(\omega)$ has a flatness range and reciprocally if $\mathcal{I}_q(\omega)$ has a flatness range, $\beta(q)$ should close to zero. We cannot conclude on the best representation using the present experimental analysis.

1946

1947

1948

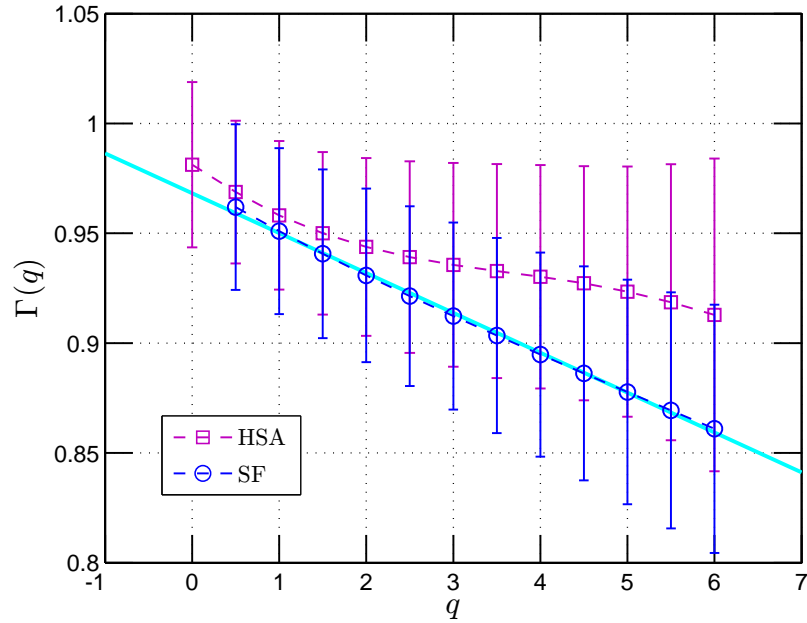


Figure 6.21: Representation of the isotropy scaling exponent $\Gamma(q)$, which are estimated from the arbitrary order Hilbert spectra $\mathcal{L}_q(\omega)$ (\square) and structure function (\circ). For structure function, we have $\Gamma^S(q) \simeq -0.018q + 0.97$, which is obtained by the least square fitting.

1949 Spatial Evolution

1950 We may also consider the spatial evolution of these anisotropy indicators. Figure 6.22
 1951 shows the scale dependent isotropy ratio \mathcal{I} at various downstream locations $x/M = 20$
 1952 (\circ), $x/M = 30$ (\square), $x/M = 40$ (\triangle) and $x/M = 48$ (\diamond), where the Kolmogorov
 1953 isotropy ratio $3/4$ is shown as horizontal solid line, and the vertical solid line illus-
 1954 trates the plateau range. The scale dependence isotropy ratio \mathcal{I} are estimated by
 1955 (a) the HSA approach, (b) the second order structure function and (c) the Fourier
 1956 power spectrum. As we have shown above, the HSA approach and the Fourier power
 1957 spectrum provide a similar shape of this ratio. The structure function is strongly
 1958 influenced by the large scale anisotropy structure. We then show the mean isotropy

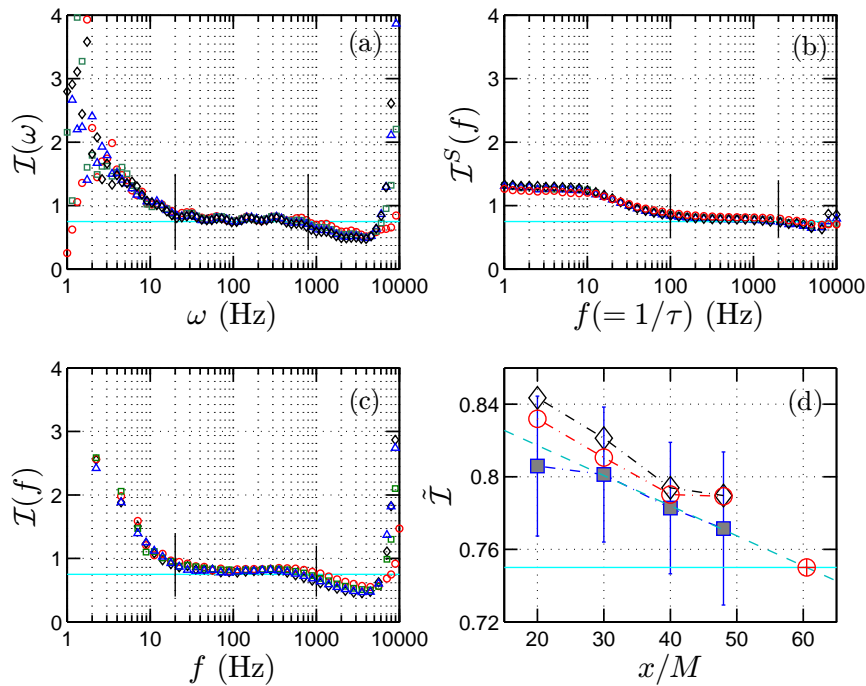


Figure 6.22: (a) The isotropy ratio $\mathcal{I}(\omega)$ estimated by the HSA approach at various downstream locations $x/M = 20$ (\circ), $x/M = 30$ (\square), $x/M = 40$ (\triangle) and $x/M = 48$ (\diamond); (b) the structure function; (c) the Fourier analysis. The vertical solid line indicates the plateau range, where the mean isotropy ratio $\tilde{\mathcal{I}}$ is estimated. The horizontal solid line illustrates the Kolmogorov value $3/4$. (d) The mean isotropy ratio $\tilde{\mathcal{I}}$, provided by the HSA approach (\square), the structure function (\circ) and the Fourier analysis (\diamond). The straight dashed line is the least square fit for the last three points of the HSA method. It predicts that the isotropy ratio may reach the Kolmogorov value at the downstream $x/M = 60.5$ (marked as \oplus).

ratio $\tilde{\mathcal{I}}$ in Fig. 6.22 (d), where the Kolmogorov isotropy value $3/4$ is displayed as a 1959
 horizontal solid line. It is interesting to note that both the Fourier approach and the 1960
 structure function provide a similar spatial evolution trend: the isotropy ratio first 1961
 decreases along the streamwise direction and reaches its minimum value at location 1962
 $x/M = 40$ and then seems to saturate. The isotropy ratio seems to never reach the 1963
 Kolmogorov value. The HSA approach gives a slightly different result. It seems that 1964
 the isotropy ratio provided first decreases slowly and then decreases linearly along 1965

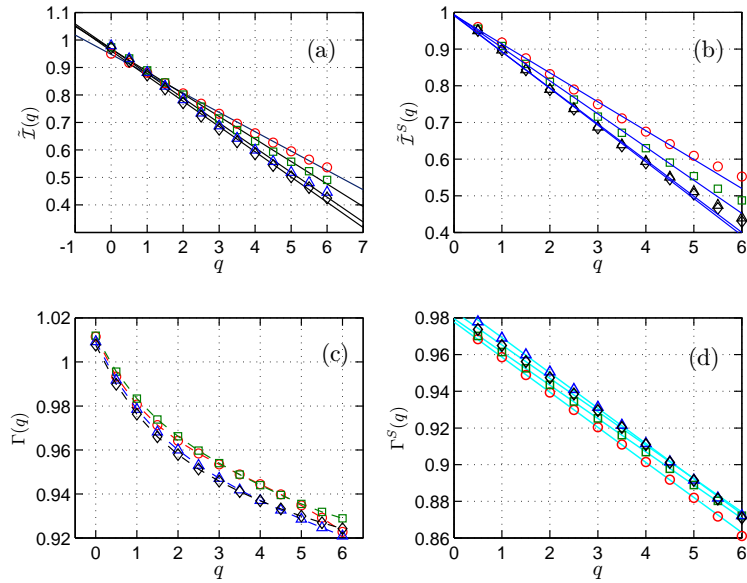


Figure 6.23: (a) The generalized mean isotropy ratio $\tilde{\mathcal{I}}(q)$ at various downstream, estimated by the HSA approach; (b) the structure function; (c) the isotropy scaling exponents $\Gamma(q)$ estimated by the HSA approach; (d) the structure function. The symbols are the same as Fig. 6.22 (a). The straight solid lines are the least square fit of each curve.

1966 the downstream direction $\tilde{\mathcal{I}}(x) \simeq -0.017x/M + 0.85$. According to this linear trend,
 1967 the isotropy ratio may reach its Kolmogorov value at the location $x/M = 60.5$, which
 1968 is marked as \oplus in Fig. 6.22 (d). Unfortunately, we do not have data on this location
 1969 to check this prediction.

1970 We now consider the downstream evolution for various orders q . Figure 6.23 shows
 1971 the mean generalized isotropy ratio $\tilde{\mathcal{I}}$ provided by (a) the HSA approach, and (b)
 1972 the structure function approach, and the isotropy scaling exponent $\Gamma(q)$ provided
 1973 by (c) the HSA approach, and (d) the structure function approach for different 4
 1974 downstream values. The symbols are the same as Fig. 6.22 (a). Except for the
 1975 Hilbert-based isotropy scaling exponent $\Gamma(q)$, see Fig. 6.23 (c), the others seem to
 1976 linearly decrease with q with various slopes. We then show in Fig. 6.24 (a) the slope

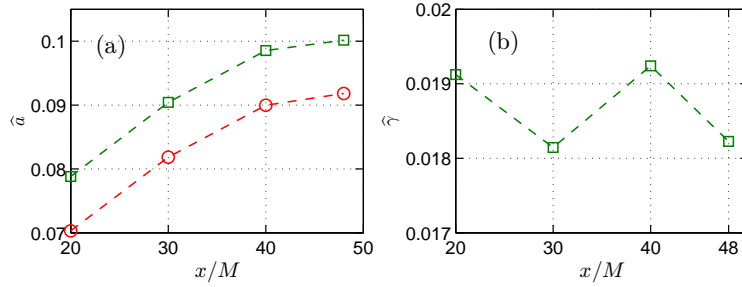


Figure 6.24: (a) The slope $\hat{\alpha}$ of the generalization isotropy ratio estimated by the Hilbert-based approach (\circ) and the structure function (\square); (b) The slope $\hat{\gamma}$ of isotropy scaling exponents estimated by structure function approach. The mean value is $\hat{\gamma} \simeq 0.187$.

$\hat{\alpha}$, and (b) the slope $\hat{\gamma}$. It seems that both Hilbert-based approach (\circ) and structure 1977
 functions (\square) provide the same evolution trend of $\hat{\alpha}$: they firstly increases with x/M 1978
 and then seem to saturate at large x/M . However, the former one is small than the 1979
 latter one. The slope of the isotropy scaling exponents is slight fluctuated around its 1980
 mean value 0.187. 1981

6.6 Summary 1982

To summarize the main results of this chapter, we applied the EMD and the arbitrary 1983
 order Hilbert spectral analysis methodology on an experimental homogeneous 1984
 and nearly isotropy turbulence database. We found that the EMD acts as a dyadic 1985
 filter bank for fully developed turbulence velocity time series. Based on the Fourier 1986
 spectrum of each mode, we termed the IMF modes into different terms: measure- 1987
 ment noise, dissipation range, inertial range and large forcing scale. We observed 1988
 a scaling trend in the joint pdf $p(\omega, \mathcal{A})$ with a scaling exponent close to the Kol- 1989
 mogorov value. We then recovered the structure function scaling exponents $\zeta(q)$ in 1990

1991 amplitude-frequency space for the first time.

1992 We tested the local isotropic hypothesis by considering the scale dependent isotropy
1993 ratio and the generalized isotropy ratio. The generalized isotropy ratio decreases lin-
1994 early with q . The spatial evolution of the isotropy ratio shows that the isotropy ratio
1995 may reach the Kolmogorov value at downstream $x/M = 60.5$. The isotropy scal-
1996 ing exponent $\Gamma(q)$ suggested by the existence of the plateau of the scale dependent
1997 isotropy ratio is also studied. These scaling exponents deviate from 1, the value indi-
1998 cated by the local isotropy hypothesis. Furthermore, the scaling exponent provided
1999 by the structure function decreases linearly with order q . It implies that the high
2000 order structure function is strongly influenced by the large anisotropy scale part.

2001 Chapter 7

2002 Passive Scalar Turbulence

2003 Another important issue in turbulence research is the passive scalar turbulence, which
2004 can be linked to many natural phenomena or engineering problems, such as pollutant
2005 diffusion, turbulent combustion, etc., see reviews by [Sreenivasan \(1996\)](#); [Shraiman](#)
2006 [& Siggia \(2000\)](#); [Warhaft \(2000\)](#). It has attracted huge interest during the last two
2007 decades ([Antonia *et al.*, 1984](#); [Sreenivasan, 1991, 1996](#); [Ruiz-Chavarria *et al.*, 1996](#);
2008 [Mydlarski & Warhaft, 1998](#); [Shraiman & Siggia, 2000](#); [Warhaft, 2000](#); [Moisy *et al.*,](#)
2009 [2001](#); [Tsinober, 2001](#); [Gylfason & Warhaft, 2004](#); [Celani *et al.*, 2005](#); [Schmitt, 2005](#)).
2010 In the spirit of Kolmogorov, the relevant Obukhov-Corrsin law is a 1/3 scaling relation
2011 that predicts

$$S^q(\ell) = \langle |\Delta\theta(\ell)|^q \rangle \sim \ell^{\zeta_\theta(q)} \quad (7.0.1)$$

2012 where $\Delta\theta(\ell) = \theta(x + \ell) - \theta(x)$, and $\zeta_\theta(q) = q/3$ is the corresponding scaling expo-
2013 nent. However, experimental evidence has shown that the scaling exponent $\zeta_\theta(q)$ is
2014 deviating from the simple KOC law, even with stronger deviation than the veloc-
2015 ity field ([Sreenivasan, 1991](#); [Shraiman & Siggia, 2000](#); [Warhaft, 2000](#)). For example,
2016 it is found that the scaling exponent $\zeta_\theta(q)$ is almost saturating for high order mo-
2017 ments ([Warhaft, 2000](#); [Celani *et al.*, 2000](#)). It is often believed that the so-called

“ramp-cliff” structures play an important role in scalar turbulent flows, see Fig. 7.1. 2018
 For high order statistical moments, it seems that the statistical quantities, such as 2019
 high order structure functions, are dominated by the ramp-cliff structure. Obviously, 2020
 the ramp-cliff structure is a large scale structure with a ramp and a sharp cliff. It is 2021
 believed that this structure couples with the small scales by the cliff structure. Thus 2022
 it may have strong influence on both the small scales and large scales statistics. 2023

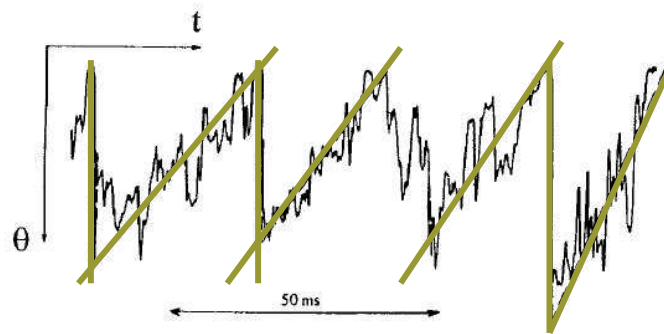


Figure 7.1: Illustration of the “ramp-cliff” structure. Graphically, the ramp-cliff structure is a large scale structure. Taken from Ref. Warhaft (2000)

We have shown previously that the structure functions are strongly influenced 2024
 by large scales. It may then be that the saturation of scalar turbulence structure 2025
 function is linked to the ramp-cliff structures. It could then be a shortcoming of the 2026
 analysis approach instead of a real saturation of the scaling exponent associated to 2027
 the most intense events. In this chapter, we check this hypothesis by considering 2028
 scalar turbulence intermittency using arbitrary order Hilbert spectral analysis. The 2029
 results presented in this chapter are not yet published. They will be in part included 2030
 in a paper prepared for submission Huang *et al.* (2009e)[Y. Huang, *et al. Phy. Rev.* 2031
Lett., 2009 (in preparation)]. 2032

2033 7.1 Temperature data

2034 The temperature data analyzed here are obtained from a jet experiment performed
 2035 at Joseph Fourier University by Y. Gagne and P. Fougairolles, where a hot air jets
 2036 from a nozzle into a cold ambient cross flow, see the sketch in Fig. 7.2. Along the flow
 2037 direction, the jet may be separated into four different regions (A) potential core, (B)
 developing range, (C) developed range and (D) decaying range. The measurement

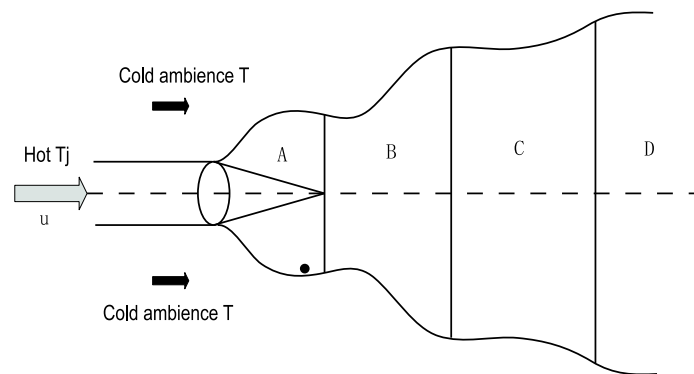


Figure 7.2: Sketch of the experiment. A hot air jets into the cold cross ambient flow from the nozzle: (A) potential core (B) developing range (C) developed range (D) decaying range. The measurement point (\bullet) is close to the nozzle and the mixing layer. Therefore the flow here demonstrates strong intermittency properties.

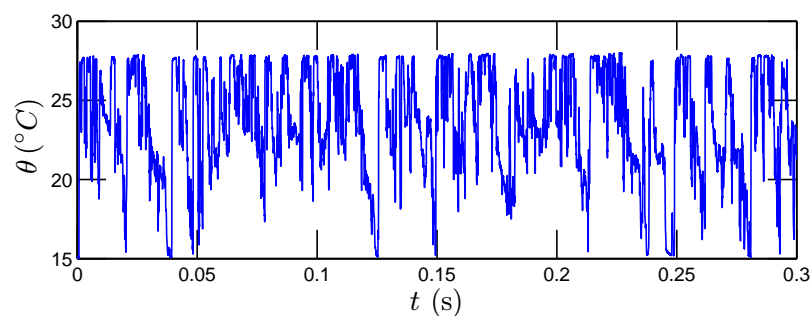


Figure 7.3: A 0.3s portion of temperature time series. It illustrates the "ramp-cliff" structures and intermittent nature of passive scalar turbulence.

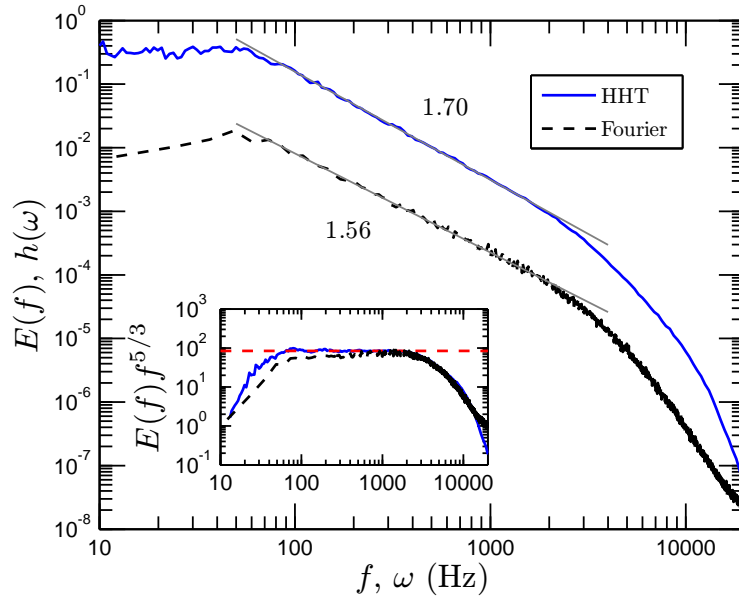


Figure 7.4: Comparison of the second order Hilbert marginal spectrum and Fourier spectrum. The inset shows the compensated spectrum $E(f)f^{5/3}$, which indicates a more than 1.4 decades of inertial range $80 < f < 2000$ Hz in both spectra. Since both EMD and HSA have very local abilities, they can constrain the ramp-cliff effects as much as they can, thus predict a steeper spectrum.

location is situated at the edge of the mixing layer and close to the nozzle. The initial 2039
temperature of the two flows are respectively $T_J=27.8^\circ\text{C}$ and $T=14.8^\circ\text{C}$. The bulk 2040
Reynolds numbers are about $Re_J = 60000$ (based on the hydraulic diameter of the 2041
jet nozzle) and $Re_M = 1100$ (based on the mesh size of the turbulence grid of the 2042
cross flow channel). The Taylor-microscale based Reynolds number is estimated as 2043
 $Re_\lambda = 250$. The sampling frequency is 50 kHz with a total 5×10^5 data points. A 0.3 s 2044
portion temperature time series is reproduced in Fig. 7.3. It illustrates a strong ramp- 2045
cliff structure and the intermittent nature of this passive scalar turbulence. Figure 7.4 2046
shows the Fourier spectrum (dashed line) and Hilbert marginal spectrum (solid line), 2047
where the inset shows the corresponding compensated spectra. Power law behaviour 2048
is observed in both spectra on the range $80 < f(\text{ or } \omega) < 2000$ Hz, about 1.4 decades, 2049

2050 with scaling exponent 1.56 and 1.70 respectively for the Fourier power spectrum and
 2051 the Hilbert spectrum. For the former one, it agrees with the value reported in other
 2052 literatures, for example, see Refs. Sreenivasan (1996); Warhaft (2000). The latter is
 2053 quite close to the scaling value of the longitude velocity in fully developed turbulent
 2054 flows (Anselmet *et al.*, 1984; Benzi *et al.*, 1995; Frisch, 1995; Sreenivasan & Antonia,
 2055 1997).

2056 7.2 EMD results

2057 We divided the whole data into 122 segments (without overlapping), with 2^{12} data
 2058 points each. After decomposition each segment is decomposed into several IMF
 2059 modes, from 9 to 12 with one residual. We first check the mean frequency of each
 mode. The mean frequency $\bar{\omega}$ is defined by Eq. (6.2.1). Figure 7.5 shows the mean

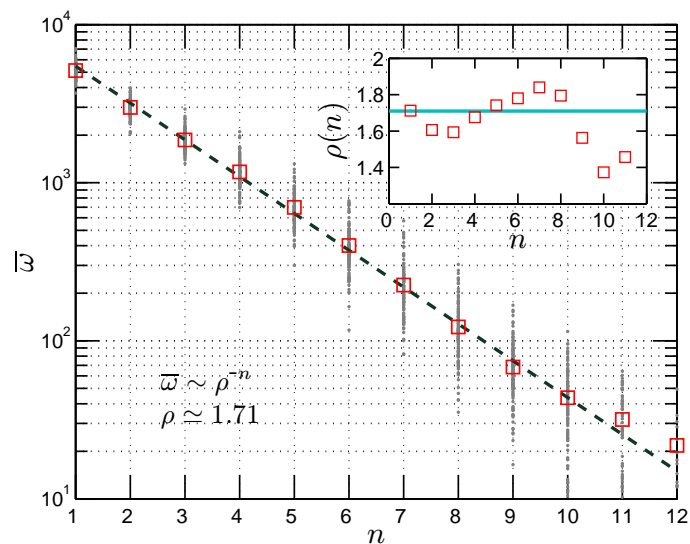


Figure 7.5: The mean frequency of IMF modes $\bar{\omega}$ vs modes n . Local slope $\rho(n)$ is shown as inset.

frequency $\bar{\omega}$, where the inset shows the local slope $\rho(n)$. One can find that, compared with the result for velocity, see Fig. 6.6, the mean frequency of each realization is rather scattered. However, the averaged mean value for all segments $\langle \bar{\omega} \rangle$ (\square) exponential decrease with mode index n as

$$\bar{\omega}(n) \sim \rho^{-n} \quad (7.2.1)$$

where $\rho \simeq 1.71$. This means that each mode is associated to a time scale almost 1.71 times larger than the previous one; this property is similar to a filter bank in the frequency domain (Flandrin & Gonçalves, 2004; Wu & Huang, 2004; Huang *et al.*, 2008). We note that the deviation from a dyadic filter bank could be an effect of the ramp-cliff structure.

7.3 HSA results

Figure 7.6 shows the joint pdf $p(\omega, \mathcal{A})$, where the vertical dashed line illustrates the inertial range $80 < \omega < 2000$ Hz. We observe a scaling trend. However, the length of data we have here is about 500,000 points. It is not long enough to get a smooth skeleton of this joint pdf. But nevertheless, as we show later, the arbitrary order Hilbert marginal spectrum is stable and convergent.

We provide here more comments on the marginal Hilbert spectrum and Fourier spectrum, see in Fig. 7.4. As mentioned previously, the Fourier transform is a linear asymptotic approach: it requires high order harmonic components to mimic nonlinear and nonstationary process. In this case, the high order harmonic component may lead an artificial energy transfer flux from a large scale (low frequency) to a small

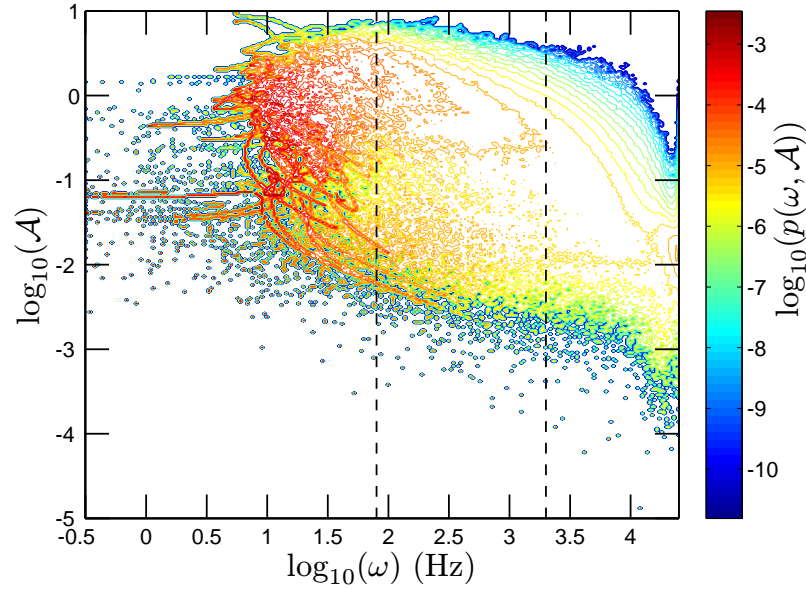


Figure 7.6: Representation of the joint pdf $p(\omega, \mathcal{A})$ for temperature fluctuations. The vertical dashed line indicates the inertial subrange. A scaling trend is observed in such presentation. However, due to the sample size, the skeleton of the joint pdf (not shown here) is rather scattered.

2081 scale (high frequency). The artificial energy transfer may give a less steep power spec-
 2082 trum. We know that both EMD and HSA methodology have very local abilities both
 2083 in physical and spectral domains: the Hilbert-based methodology can constrain the
 2084 nonlinear and nonstationary effects (Huang *et al.*, 1998, 1999; Huang, 2005; Huang
 2085 *et al.*, 2009d). In other words, it does not require any higher order harmonic compo-
 2086 nents to simulate the nonlinear and nonstationary events. Thus, the Hilbert spectrum
 2087 may reveal a less pertubated relation between the energy and the frequency.

2088 Figure 7.7 shows the arbitrary order Hilbert marginal spectrum $\mathcal{L}_q(\omega)$, where
 2089 $q = 0, 1, 3, 4, 5$ and 6. The vertical dashed line indicates the inertial subrange
 2090 $80 < \omega < 2000$ Hz. Power law behaviour is observed in each plot on the inertial
 2091 range, and the corresponding scaling exponents $\xi_\theta(q)$ are estimated on this range by

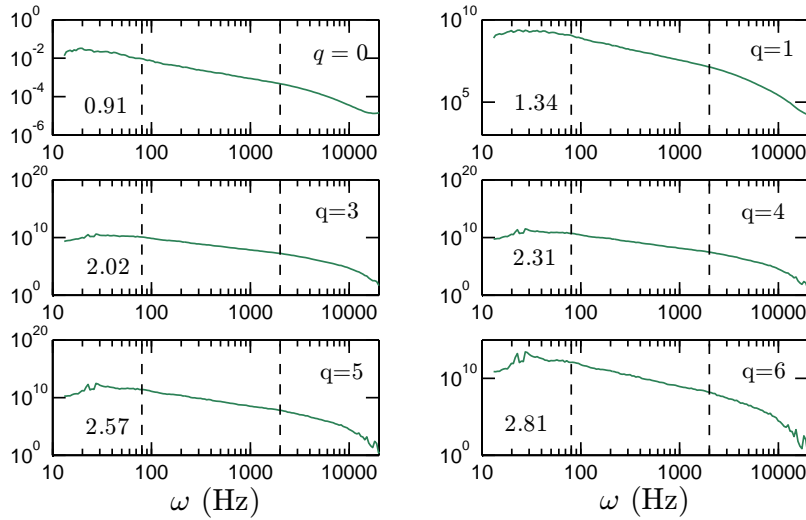


Figure 7.7: Arbitrary order Hilbert marginal spectrum $\mathcal{L}_q(\omega)$, where $q = 0, 1, 3, 4, 5$ and 6 . Power law behaviour is observed on the range $80 < \omega < 2000$ Hz in all cases. The corresponding scaling exponents $\xi_\theta(q)$ is shown in each figure.

a least square fitting algorithm. We compare the scaling exponents $\xi_\theta(q) - 1$ (\circ), 2092
 $\zeta_\theta(q)$ from structure function (\diamond), the value $\zeta_\theta(q)$ complied by Schmitt (2005) (\square with 2093
error bar) with the theoretical value $q/3$ (solid line) in Fig. 7.8. The inset shows the 2094
scaling exponents departure from the theoretical KOC value. The classical structure 2095
function analysis method, as we will show in next section, it is strongly influenced 2096
by the ramp-cliff structure. The scaling exponent is then estimated by a least square 2097
fitting algorithm and by choosing the range case by case. The scaling exponent begins 2098
to be saturated when $q > 3$. It is usually interpreted as an evidence that the passive 2099
scalar field is more intermittent than the velocity field (Sreenivasan, 1991; Shraiman 2100
& Siggia, 2000; Warhaft, 2000). Using the HSA approach, a more clear inertial range 2101
holds for each plot, up to order 8. To compare with the velocity field, we plot the 2102
ESS result $\zeta(q)$ (dashed line) for longitude velocity (Benzi *et al.*, 1995) in the same 2103
figure. We find that the scaling exponent $\xi(q)$ is quite close to the ESS result for the 2104

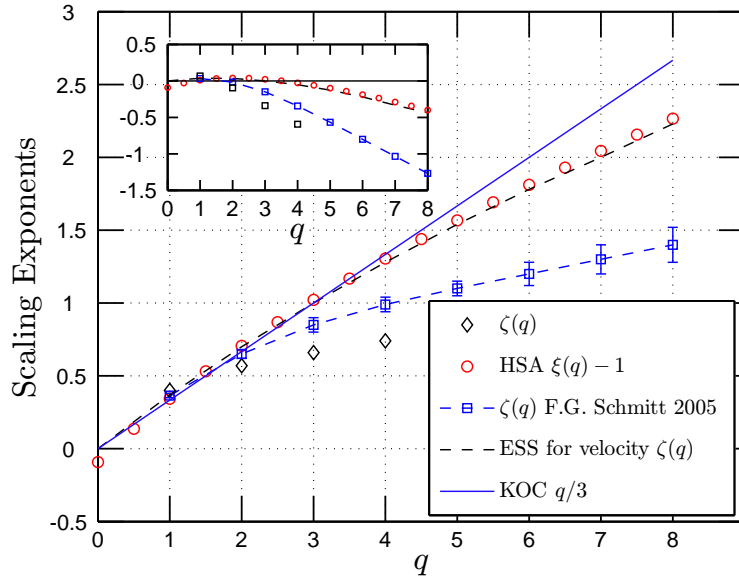


Figure 7.8: Comparison of the scaling exponents, which are estimated by the HSA $\xi_\theta(q) - 1$ (\circ), the structure functions $\zeta_\theta(q)$ (\diamond), the value compiled by Schmitt (2005) (\square with error bar) and the theoretical value $q/3$ (solid line). We also show the ESS result (dashed line) for longitudinal velocity (Benzi *et al.*, 1995). The inset shows the departure from the KOC theoretical value.

2105 velocity, which may indicate that the scalar field is not so intermittent as what we
 2106 have believed before. This is obtained here for one database, and should be confirmed
 2107 using other database before a firm conclusion can be proposed.

2108 7.4 Structure function analysis

2109 As already noticed by several authors, for example, Antonia (Antonia *et al.*, 1984),
 2110 Ruiz-Chavarria (Ruiz-Chavarria *et al.*, 1996) and Warhaft (Warhaft, 2000), for scalar
 2111 turbulence, the scaling exponents of Fourier spectrum β_θ is not consistent with the
 2112 second order structure function $\zeta_\theta(2)$: the relation $\zeta_\theta(2) = \beta_\theta - 1$ is not verified.
 2113 This may be an effect of the ramp-cliff structure. Furthermore, it has been reported

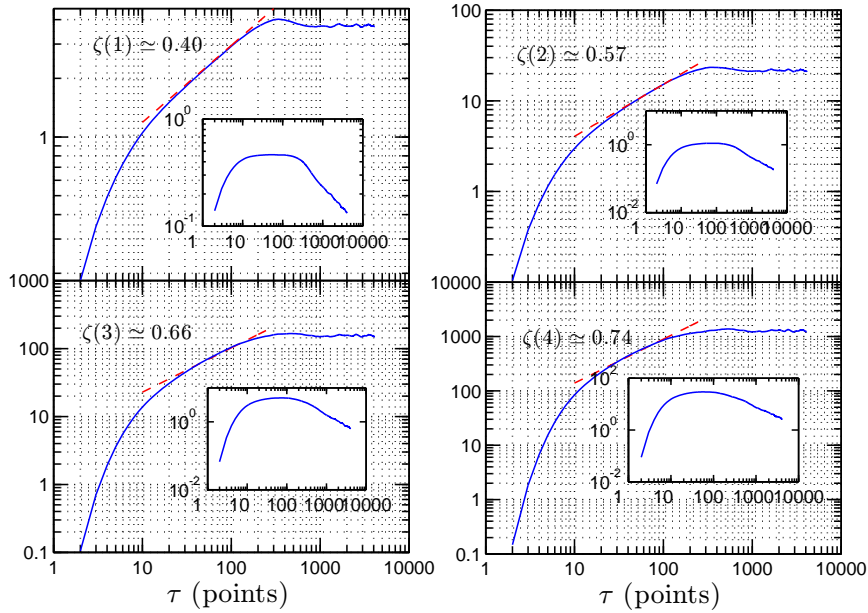


Figure 7.9: The structure function of temperature $S^q(\ell)$, $q = 1, 2, 3, 4$. The inset shows the corresponding compensated spectrum $S^q(\ell)\ell^{\zeta(q)}$. Power law range decreases with the order q , which may be interpreted as the effects of the ramp-cliff structure.

that the scalar spectrum has a larger scaling range than the velocity field at the 2114 same Re_λ (Jayesh & Warhaft, 1994; Gylfason & Warhaft, 2004). We have discussed 2115 previously that, in case of possessing large energetic nonlinear structures, the Fourier 2116 analysis needs high order harmonic components. Thus, both the inertial range and 2117 the scaling exponents may be contaminated by the ramp-cliff structure. 2118

Figure 7.9 shows the first fourth order structure functions, where the inset shows 2119 the corresponding compensated spectrum by taking the estimated scaling exponent 2120 $\zeta_\theta(q)$. Due to the effect of the ramp-cliff structure, the inertial range decreases with 2121 the order q . When $q > 4$, there is no clear power law any more. It is believed that the 2122 structure function itself is then dominated by the ramp-cliff structure for high order 2123 structure function (Gylfason & Warhaft, 2004). 2124

2125 7.5 Summary

2126 In this chapter, we applied the EMD and arbitrary order Hilbert spectral analysis to a
2127 temperature from a jet experiment. The data have very strong ramp-cliff structures,
2128 which have been considered as an important signature of passive turbulence. We find
2129 that the EMD algorithm acts a filter bank. Due to the effect of ramp-cliff structure,
2130 it deviates from a dyadic filter bank, which have been obtained previously using
2131 stochastic simulations of Gaussian noise, fractional Gaussian noise (fGn) and the
2132 fully developed turbulence velocity (Wu & Huang, 2004; Flandrin & Gonçalves, 2004;
2133 Huang *et al.*, 2008).

2134 We then considered the intermittency property of these data. It is found that the
2135 scaling exponent $\xi_\theta(q)$ provided by the Hilbert-based methodology is quite close to
2136 the ESS-based scaling exponent $\zeta(q)$ of the longitudinal velocity. Due to the very
2137 local ability of the Hilbert-based approach and the intrawave frequency modulation
2138 mechanism of the nonlinear process, the present method does not require high order
2139 harmonic components to mimic the ramp-cliff structure. Thus, the scalar turbulence
2140 may be not so intermittent as what we believed before. We should reconsider the
2141 role of the ramp-cliff structure in this framework. These results need to be confirmed
2142 using other passive scalar databases. This will be done in future work.

2143 Chapter 8

2144 Extended Self-Similarity and 2145 Hierarchy Model

2146 During the last 2 or 3 decades, to extract the scaling exponents $\zeta(q)$ from various
2147 turbulent flows became a quite general approach in turbulent research (Anselmet
2148 *et al.*, 1984; Antonia *et al.*, 1984; Benzi *et al.*, 1993a; Frisch, 1995; Arneodo *et al.*,
2149 1996; Sreenivasan & Antonia, 1997). One interesting improvement methodology is the
2150 so-called Extended-Self Similarity (ESS), which was proposed by Benzi *et al.* (1993a,b,
2151 1995). It is believed that the ESS approach provides a more accuracy estimation of
2152 the scaling exponents $\zeta(q)$ and extends the power law range (Benzi *et al.*, 1993a). In
2153 this chapter, we will adapt the ESS idea into the Hilbert frame.

2154 We recall Benzi's ESS theory here. According to Kolmogorov's refined similarity
2155 hypothesis (Kolmogorov, 1962; Frisch, 1995), the statistical properties of small scales
2156 are uniquely determined by the local energy dissipation rate ϵ_r and the scale r , where

$$\epsilon_r(x, t) = \frac{6}{\pi r^3} \int_{|r'| < r/2} \epsilon(x + r', t) dr' \quad (8.0.1)$$

2157 where $r/2$ is radius of the sphere. The q th order structure function is written

$$S^q(r) = \langle |u(x+r) - u(x)|^q \rangle \sim \langle \epsilon_r^{q/3} \rangle r^{q/3} \quad (8.0.2)$$

where $\langle \rangle$ is ensemble average. If the local energy dissipation rate ϵ_r itself has scaling law

$$\langle \epsilon_r^q \rangle \sim r^{K(q)} \quad (8.0.3)$$

where $K(0) = 0$. It then follows

$$\zeta(q) = q/3 - K(q/3) \quad (8.0.4)$$

The above equation connects the scaling exponents $\zeta(q)$ with the scaling intermittency of the dissipation since the mean dissipation is assumed to be conserved, $\langle \epsilon_\ell \rangle = \bar{\epsilon}$. So that $K(1) = 0$ and $\zeta(3) = 1$. This can be also obtained from the Kolmogorov (1941c) equation, for $r \gg \eta$ ($\eta \equiv \nu^{3/4} \epsilon^{-1/4}$ is Kolmogorov scale), one has

$$S^3(r) = -\frac{4}{5} \epsilon r \quad (8.0.5)$$

This is the famous Kolmogorov Four-Fifths law (Kolmogorov, 1941c; Monin & Yaglom, 1971; Frisch, 1995), which is the only one exactly statistical solution of Navier-Stokes equation for turbulence. It confirms the relation $K(1) = 0$ and $\zeta(3) = 1$, which means that the third order structure function $S^3(r)$ is free from the intermittency correction. Benzi *et al.* (1993a) suggested to plot $S^q(r)$ vs $S^3(r)$ instead of $S^q(r)$ vs r in structure function analysis, which reads

$$S^q(r) \sim S^3(r)^{\zeta^*(q)} \quad (8.0.6)$$

Since $S^3(r)$ is proportional to r , the scaling exponent $\zeta^*(q)$ is supposed to be the same as $\zeta(q)$. It has been found that ESS is valid not only for high Reynolds number turbulent flows but also for moderate Reynolds numbers, even when there is no clear inertial range (Benzi *et al.*, 1993a,b, 1995). The method was therefore extensively used in turbulence research and even in other fields such as natural science or finance. In the next section we consider this approach in the Hilbert spectral analysis framework.

2177 8.1 Extended-Self similarity

2178 Considering the Kolmogorov refined similarity hypothesis, we have the following re-
2179 lation for the arbitrary order Hilbert spectra in the Hilbert frame

$$\mathcal{L}_q(\omega) \sim \langle \epsilon_r^{q/3} \rangle \omega^{-(1+q/3)} \quad (8.1.1)$$

2180 where $q \geq 0$. We have here two special cases $q = 0^1$ and $q = 3$, which are free from
2181 intermittency effect. Following the ESS idea of [Benzi *et al.* \(1993a,b\)](#), we link the
2182 arbitrary order Hilbert spectrum $\mathcal{L}_q(\omega)$ with these two special cases

$$\mathcal{L}_q(\omega) \sim (\mathcal{L}_p(\omega))^{\xi_p(q)/\xi(p)} \quad (8.1.2)$$

2183 where $p = 0$ or $p = 3$. We denote $\xi_0(q)$ and $\xi_3(q)$ the corresponding scaling exponents.

2184

2185 Figure 8.1 shows a test of the ESS of the case $p = 0$ for various q on the range $10 <$
2186 $\omega < 6000$ Hz. The vertical dashed line illustrates the inertial range $10 < \omega < 1000$ Hz.
2187 A power law behaviour is observed in each plot on the inertial range, and the scaling
2188 exponents $\xi_0(q)$ is estimated on this range by using a least square fitting algorithm
2189 on the inertial range. Figure 8.2 shows the case $p = 3$, where the vertical dashed line
2190 demonstrates the inertial range $10 < \omega < 1000$ Hz, and the thick solid line indicates
2191 the location $\omega = 3000$ Hz. It seems that, except the zeroth order Hilbert marginal
2192 spectrum, the power law range extends as expected. We take the $\mathcal{L}_7(\omega)$ as example:
2193 the scaling range extends to $\omega = 3000$ Hz. This is similar with the observations
2194 done for the traditional ESS ([Benzi *et al.*, 1993b, 1995](#)). The corresponding scaling
2195 exponent $\xi_3(q)$ is then estimated on the range $10 < \omega < 3000$ Hz.

¹As mentioned in chapter 3, the zeroth order Hilbert marginal spectrum is the marginal pdf of the instantaneous frequency. We have found the general property that such marginal pdf itself has a power law behaviour, and the corresponding scaling exponent $\xi(0)$ is close to 1, which is rather natural since it corresponds to $\zeta(0) = 0$.

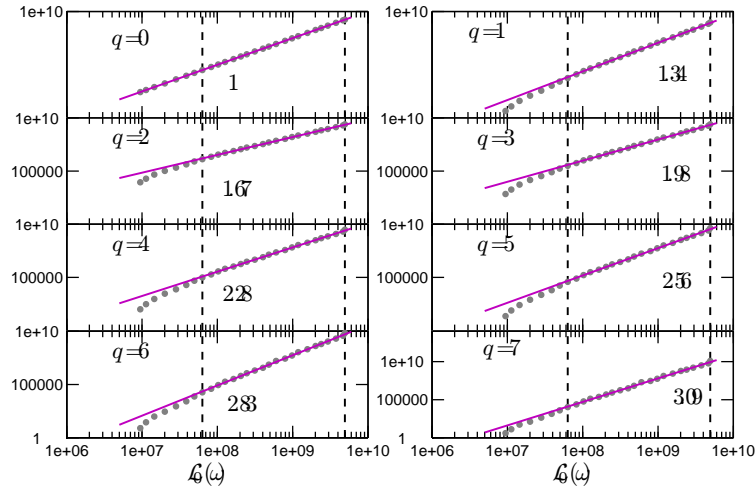


Figure 8.1: A test of Extended Self-Similarity of arbitrary order Hilbert spectra $\mathcal{L}_q(\omega)$ V.S. $\mathcal{L}_0(\omega)$ for the longitudinal velocity, $q = 0, 1, 2, 3, 4, 5, 6$ and 7 on the range $10 < \omega < 6000$ Hz. The dashed line indicates the inertial range $10 < \omega < 1000$ Hz. The scaling exponent $\xi(q)$ is then estimated on this range.

We then compare the scaling exponents $\xi(q)$ in Fig. 8.3 for different estimators², 2196
HSA result $\xi(q) - 1$ (\times), Hilbert-based ESS $\xi_0(q) - 1$ (\square) and $\xi_3(q) - 1$ (\triangleleft), $\zeta(q)$ 2197
(dashed line) provided by the traditional ESS (Benzi *et al.*, 1995), and the K41 2198
prediction (solid line), see also Tab. 8.1. The inset shows the departure from the K41 2199
 $q/3$ law. The scaling exponents $\xi_0(q)$ and $\xi_3(q)$ are in good agreement with $\zeta(q)$ when 2200
 $q \leq 4$. When $q > 4$, the Hilbert-based estimators display a larger scaling exponents 2201
than the structure function based ESS $\zeta(q)$. 2202

For comparison, we consider the log-Lévy model and the log-normal model here (Frisch, 2203
1995; Schertzer *et al.*, 1997). The log-Lévy model (Schertzer & Lovejoy, 1987; Kida, 2204
1991; Schmitt *et al.*, 1992; Schertzer *et al.*, 1997) predicts a scaling exponent 2205

$$\zeta(q) = q/3 - \frac{C_1}{\alpha - 1} [(q/3)^\alpha - q/3] \quad (8.1.3)$$

where C_1 is the codimension of the mean events ($0 \leq C_1 \leq d$, where d is the dimension 2206

²We do not apply here the structure function analysis on these database.

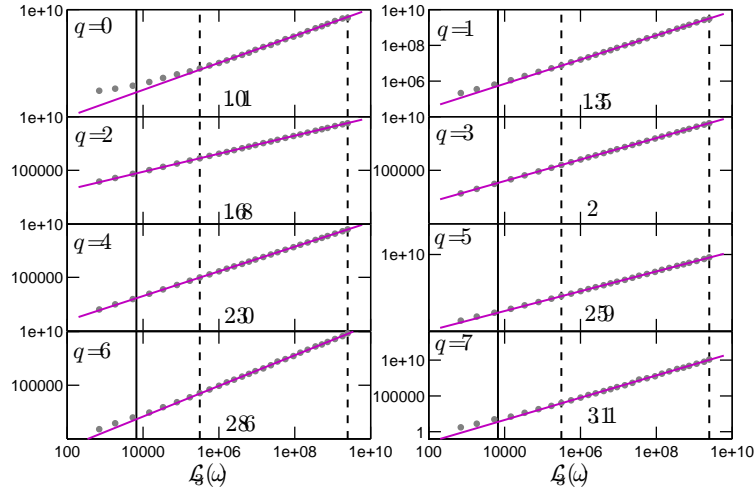


Figure 8.2: A test of Extended Self-Similarity of arbitrary order Hilbert spectra $\mathcal{L}_q(\omega)$ V.S. $\mathcal{L}_3(\omega)$ for the longitudinal velocity, $q = 0, 1, 2, 3, 4, 5, 6$ and 7 on the range $10 < \omega < 6000$ Hz, where the dash line indicates the inertial range $10 < \omega < 1000$ Hz. The vertical thick solid line indicates the location of 3000 Hz. The scaling exponent $\xi(q)$ is then estimated on this range.

2207 of the observation space), and α is the Lévy index, bounded between 0 and 2 . We
 2208 fix $\alpha = 1.5$ (Schertzer *et al.*, 1997) and consider C_1 as a free parameter. We fit
 2209 experimental data by a least square fitting algorithm. C_1 is found to be 0.095 for
 2210 Hilbert-based ESS scaling exponent. The log-normal model predicts

$$\zeta(q) = \frac{q}{3} - \frac{\mu}{18} (q^2 - 3q) \quad (8.1.4)$$

2211 where μ is the so-called intermittency parameter (Frisch, 1995; Schertzer *et al.*, 1997).
 2212 We take here μ as a free parameter. The μ is found to be 0.15 , which is comparable
 2213 with 0.2 , an estimation value provided by Anselmet *et al.* (1984). Graphically, both
 2214 of these two models with the present chosen parameter predict the same scaling
 2215 exponents.

2216 As we have mentioned previously, the data we used here are generated by the
 2217 active-grid technique. The results presented here may be influenced by a lack of

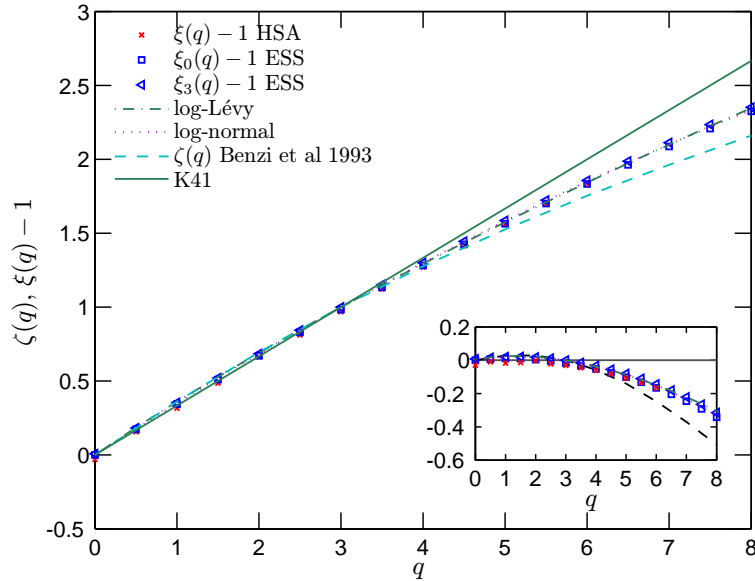


Figure 8.3: Comparison of the scaling exponents $\xi(q) - 1$ (\times), ESS $\xi_0(q) - 1$ (\square), ESS $\xi_3(q) - 1$ (\triangleleft), the $\zeta(q)$ provided by the ESS method (Benzi *et al.*, 1995) (dashed line) and K41 $q/3$ (solid line). We also show a best fitting of the data by log-Lévy model (dashed-dotted line) with $C_1 = 0.095$ and $\alpha = 1.5$, log-normal model (dotted line) with $\mu = 0.15$. The inset shows the departure from the K41 law.

isotropy, see chapter 6, we thus should check this ESS idea on more databases.

2218

8.2 Hierarchy model

2219

We have shown in chapter 6 that the skeleton $\mathcal{A}_s(\omega)$ and its corresponding conditional

pdf $p_{\max}(\omega)$ of the joint pdf $p(\omega, \mathcal{A})$ have a power law behaviour on the inertial range

$10 < \omega < 1000$ Hz, where ω is the instantaneous frequency and \mathcal{A} is the amplitude.

This power law is written as

2223

$$\mathcal{A}_s(\omega) \sim \omega^{-\beta_1}, \quad p_{\max}(\omega) \sim \omega^{-\beta_2} \quad (8.2.1)$$

2224 where $\beta_1 = 0.38 \pm 0.05$ and $\beta_2 = 0.63 \pm 0.05$, see Fig. 6.10. We also found dimensionally
 2225 that without intermittency we have

$$\beta_1 = \frac{1}{3}, \quad \beta_2 = \frac{2}{3} \quad (8.2.2)$$

2226 see chapter 6. Following She and L ev eque's hierarchy model (She & L ev eque, 1994),
 2227 we present a hierarchy model in the following.

2228 A Weighted Function For Hilbert Marginal Spectra

2229 We have shown previously that the joint pdf $p(\omega, \mathcal{A})$ is strongly peaked around $\mathcal{A}_s(\omega)$,
 2230 see Fig. 6.12. The arbitrary order Hilbert marginal spectrum $\mathcal{L}_q(\omega)$ can be rewritten
 2231 as

$$\mathcal{L}_q(\omega) = \mathcal{G}(\omega, q) p_{\max}(\omega) \mathcal{A}_s(\omega)^{1+q} \quad (8.2.3)$$

2232 where $\mathcal{G}(\omega, q)$ is a weighted function. It may be determined by different distribution
 2233 functions for $p(\omega, \mathcal{A})$. For high Reynolds number turbulent flows, where the local
 2234 homogeneous and isotropy hypotheses hold, we assume that Eq. (8.2.1) is valid at
 2235 least on the inertial subrange. It indicates that

$$\mathcal{L}_q(\omega) \sim \mathcal{G}(\omega, q) \omega^{-((1+q)\beta_1 + \beta_2)} \quad (8.2.4)$$

2236 For discussion convenience, we assume that the intermittency does not affect the
 2237 skeleton $\mathcal{A}_s(\omega)$ and the corresponding conditional pdf $p_{\max}(\omega)$.³ We then have

$$\mathcal{L}_q(\omega) \sim \mathcal{G}(\omega, q) \omega^{-(1+q/3)} \quad (8.2.5)$$

2238 For different distribution models of the joint pdf $p(\omega, \mathcal{A})$, the weight function $\mathcal{G}(\omega, q)$
 2239 may have different forms. It may be universal for high Reynolds turbulent flow. For

³Based on the observation of the joint pdf $p(\omega, \mathcal{A})$, the intermittency does influence on $\mathcal{A}_s(\omega)$ and $p_{\max}(\omega)$, see Fig. 6.10.

example, if $\mathcal{G}(\omega, q)$ is independent from ω and q , Eq. (8.2.5) then one recovers the K41 prediction.

The weighted function $\mathcal{G}(\omega, q)$ may be determined by considering the compensated arbitrary order Hilbert marginal spectrum

$$\mathcal{G}(\omega, q) \sim \mathcal{L}_q(\omega) \omega^{1+q/3} \sim \omega^{-\Lambda(q)} \quad (8.2.6)$$

Thus $\Lambda(q)$ measures the departure from the K41 theory. This finally give

$$\Lambda(q) = \xi(q) - \left(1 + \frac{q}{3}\right) \quad (8.2.7)$$

According to Kolmogorov's 1962 refined similarity hypothesis (Kolmogorov, 1962), we have $\Lambda(0) = \Lambda(3) = 0$, which means they are free with the intermittency effect.

A Hierarchical Model

Following the hierarchical model idea of She & Lévéque (1994), we define a hierarchical spectral function $\mathcal{L}^{(q)}(\omega)$ by the ratio of two successive arbitrary order Hilbert spectra

$$\mathcal{L}^{(q)}(\omega) = \frac{\int p(\omega, \mathcal{A}) \mathcal{A}^{q+1} d\mathcal{A}}{\int p(\omega, \mathcal{A}) \mathcal{A}^q d\mathcal{A}} = \int \mathcal{Q}_q(\omega, \mathcal{A}) \mathcal{A} d\mathcal{A} \quad (8.2.8)$$

where $q \geq 0$, and $\mathcal{Q}_q(\omega, \mathcal{A}) = p(\omega, \mathcal{A}) \mathcal{A}^{q+1} / \int p(\omega, \mathcal{A}) \mathcal{A}^q d\mathcal{A}$ is weighted pdf for which $\mathcal{L}^{(q)}(\omega)$ is a mathematical expectation. Similar with $\epsilon_r^{(q)} = \langle \epsilon_r^{q+1} \rangle / \langle \epsilon_r^q \rangle$, when $q \rightarrow \infty$, $\mathcal{L}^{(\infty)}(\omega)$ measures the most intermittent structures (She & Lévéque, 1994).

We then expect that the power law behaviour holds at least in the inertial range

$$\mathcal{L}^{(q)}(\omega) \sim \omega^{-\Pi(q)} \quad (8.2.9)$$

where

$$\Pi(q) = \xi(q+1) - \xi(q) \quad (8.2.10)$$

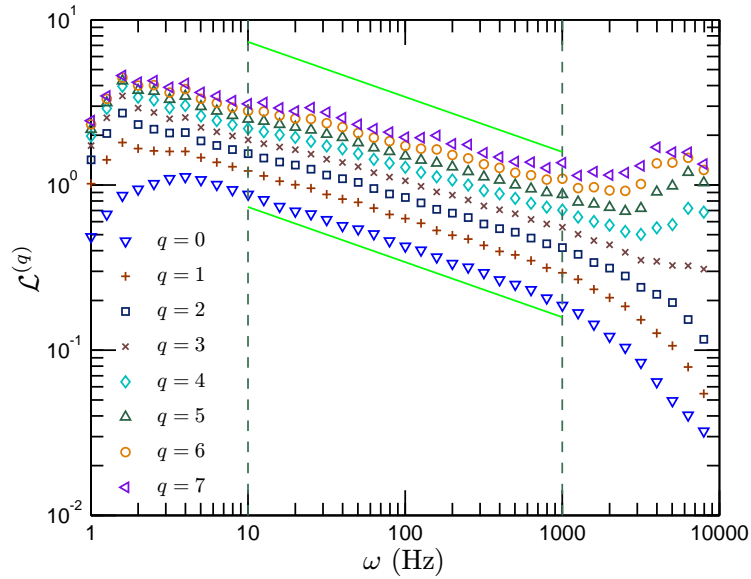


Figure 8.4: Representation of the hierarchical spectral function $\mathcal{L}^{(q)}(\omega)$, where $q = 0$ (∇), 1 ($+$), 2 (\square), 3 (\times), 4 (\diamond), 5 (\triangle), 6 (\circ) and 7 (\triangleleft). A power law behaviour is observed in the inertial range $10 < \omega < 1000$ Hz, which is indicated by the vertical dashed line. The solid line demonstrates the Kolmogorov value $1/3$.

2255 The dimensional consideration indicates for the non-intermittency case

$$[\mathcal{L}^{(q)}] = [\mathcal{A}], \quad \Pi(q) = \frac{1}{3} \quad (8.2.11)$$

2256 Figure 8.4 shows the hierarchical spectral function $\mathcal{L}^{(q)}(\omega)$ for various $q = 0$ (∇),
 2257 1 ($+$), 2 (\square), 3 (\times), 4 (\diamond), 5 (\triangle), 6 (\circ) and 7 (\triangleleft). The solid line indicates the
 2258 Kolmogorov value $1/3$ for the nonintermittent case, and the vertical dashed line il-
 2259 lustrates the inertial range $10 < \omega < 1000$ Hz. A power law behaviour is observed on
 2260 this inertial range for all curves. The slope shows departure from the nonintermittent
 2261 value when q is increasing. We estimate the scaling exponent $\Pi(q)$ on the inertial
 2262 range. The corresponding scaling value $\Pi(q)$ (\circ) is shown in Fig. 8.5, where the hor-
 2263 izontal thick solid line indicates the Kolmogorov value $1/3$. For comparison, we also
 2264 show the corresponding $\Pi(q)$ estimated from the Hilbert-based ESS $\xi_3(q)$ (\square), the

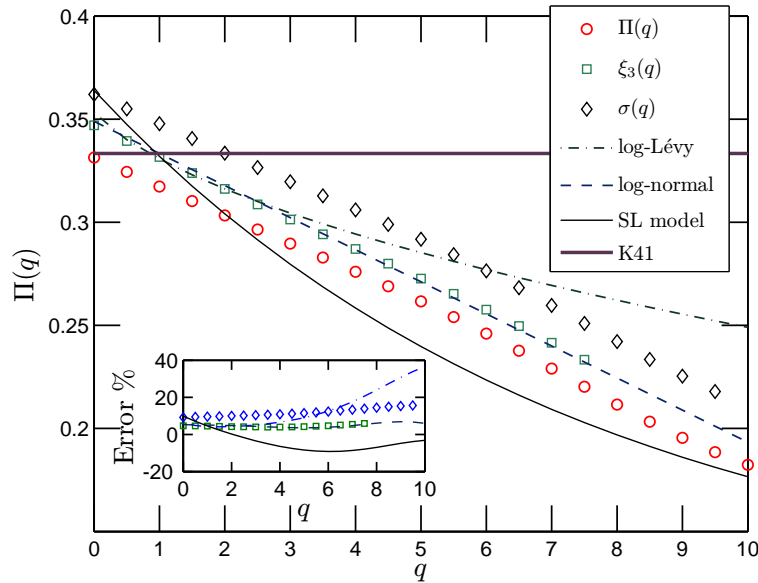


Figure 8.5: Representation of the scaling exponents $\Pi(q)$ (\circ) for the hierarchical spectral function $\mathcal{L}^{(q)}(\omega)$. The horizontal thick line indicates Kolmogorov value $1/3$. The corresponding scaling exponent $\Pi(q)$ is estimated on the inertial subrange $10 < \omega < 1000$ Hz. For comparison, we also show the corresponding scaling exponents from $\xi_3(q)$ (\square), $\sigma(q)$ (\diamond), the log-Lévy model with $C_1 = 0.07$, $\alpha = 1.5$ (dashed-dotted line), log-normal model with $\mu = 0.11$ (dashed line) and SL model (solid line). The inset shows the relative error from $\Pi(q)$.

Hilbert-based generalized ESS $\sigma(q)$ (\diamond) (see below), log-Lévy model with $C_1 = 0.07$ 2265
and $\alpha = 1.5$ (dashed-dotted line), log-normal model with $\mu = 0.11$ (dashed line)⁴ and 2266
SL model (thin solid line). The relative error from the direct estimated $\Pi(q)$ is shown 2267
as inset. The estimated $\Pi(q)$ decreases linearly with q with the same 0.015 obtained 2268
graphically. In this case, only log-normal model provides a linear prediction of $\Pi(q)$. 2269
Based on this observation, the log-normal model with such chosen parameter seems 2270
to give the best fitting among these three models. 2271

⁴The parameters we choose here is based on the Hilbert-based ESS $\xi_3(q)$. This means that we fit $\xi_3(q)$ -based $\Pi(q)$ to determine the parameters C_1 and μ .

2272 8.3 Generalized Extended-Self similarity

2273 Following the idea of generalized extended self-similarity of [Benzi *et al.* \(1996\)](#), let us
2274 introduce a dimensionless arbitrary order Hilbert marginal spectrum

$$\mathcal{Z}_q(\omega) = \frac{\mathcal{L}_q(\omega)}{\mathcal{L}_3(\omega)^{q/3}} \sim \omega^{-\sigma(q)} \quad (8.3.1)$$

2275 in which

$$\sigma(q) = \xi(q) - \frac{\xi(3)q}{3} \quad (8.3.2)$$

2276 where $\xi(q)$ is the scaling exponent. We expect that the dimensionless arbitrary order
2277 Hilbert marginal spectrum $\mathcal{Z}_q(\omega)$ itself has power law behaviour. We postulate a
2278 Generalized Extended-Self Similarity (GESS) ([Benzi *et al.*, 1996](#)), which is written as

$$\mathcal{Z}_q(\omega) \sim (\mathcal{Z}_p(\omega))^{\rho(q,p)} \quad (8.3.3)$$

2279 By the definition we have

$$\rho(q,p) = \frac{\sigma(q)}{\sigma(p)}, p \neq 3 \quad (8.3.4)$$

2280 Figure 8.6 shows the dimensionless arbitrary order Hilbert marginal spectrum
2281 $\mathcal{Z}_q(\omega)$ for various q , 0 (\circ), 2 (\square), 4 (\triangle), 6 (\diamond), 8 (\triangleleft), 10 (\triangleright). The vertical dashed
2282 line demonstrates the inertial subrange $10 < \omega < 1000$ Hz. A power law behaviour is
2283 observed in each representation. We estimate the corresponding $\sigma(q)$ on the inertial
2284 range by using a least square fitting algorithm. The scaling exponent $\sigma(q)$ (\circ) is
2285 shown in Fig. 8.7. For comparison, we also show the corresponding scaling value in
2286 the same figure, provided by the Hilbert-based ESS $\xi_3(q)$ (\triangleleft), the log-Lévy model
2287 with $C_1 = 0.07$ and $\alpha = 1.5$ (dashed line), the log-normal model with $\mu = 0.11$
2288 (dashed-dotted line) and the SL model (solid line). The inset shows the relative
2289 error from $\sigma(q)$. The Hilbert-based ESS predicts almost the same value $\sigma(q)$ as the

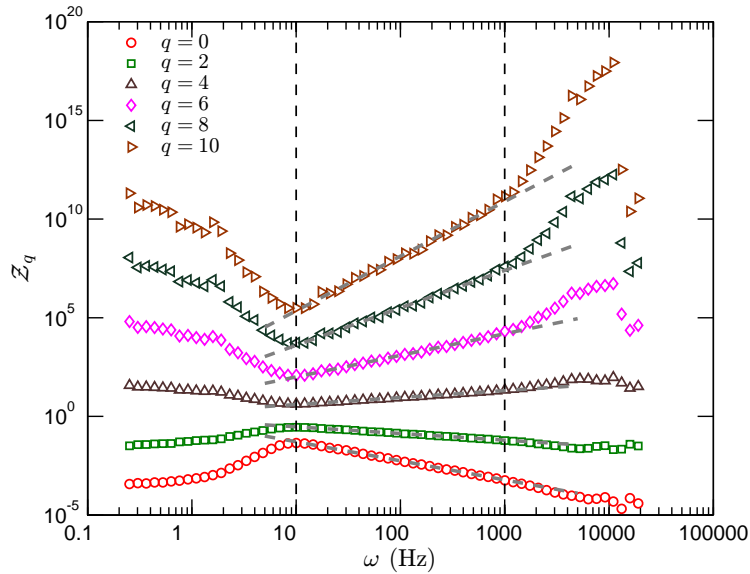


Figure 8.6: Representation of the dimensionless arbitrary order Hilbert marginal spectra function $\mathcal{Z}_q(\omega)$, where $q = 0$ (\circ), 2 (\square), 4 (\triangle), 6 (\diamond), 8 (\triangleleft) and 10 (\triangleright). The vertical dashed line demonstrates the inertial subrange $10 < \omega < 1000$ Hz. The dashed line is the least square fitting on the inertial range.

dimensionless arbitrary order Hilbert marginal spectrum $\mathcal{Z}_q(\omega)$. We also note that 2290
the log-normal model with the parameter $\mu = 0.11$ gives the best fit of $\sigma(q)$. 2291

We represent the dimensionless arbitrary order Hilbert marginal spectrum $\mathcal{Z}_q(\omega)$ 2292
vs $\mathcal{Z}_p(\omega)$ on the range $10 < \omega < 7000$ Hz in Fig. 8.8 for various p (a) $p = 0$, (b) 2293
 $p = 1$, (c) $p = 2$ and (d) $p = 4$, where $q = 0$ (\circ), 2 (\square), 4 (\triangle), 6 (\diamond), 8 (\triangleright) and 2294
 10 (\triangleright). The vertical dashed line indicates the inertial subrange $10 < \omega < 1000$ Hz. 2295
A power law behaviour is observed as expected in all cases. The power law range is 2296
also extended as expected, which may depend on each case. However, we estimate 2297
the scaling exponent $\rho(q, p)$ on the inertial subrange by using a least square fitting. 2298
Figure 8.9 shows the corresponding $\rho(q, p)$ for various p , 0 (\triangle), 1 (\circ), 2 (\square), 4 (\diamond) and 2299
 5 (\triangleleft). We compare the experimental result with (a) the SL model, (b) the log-Lévy 2300
model with $C_1 = 0.07$ and $\alpha = 1.5$, and (c) the log-normal model with $\mu = 0.11$. We 2301

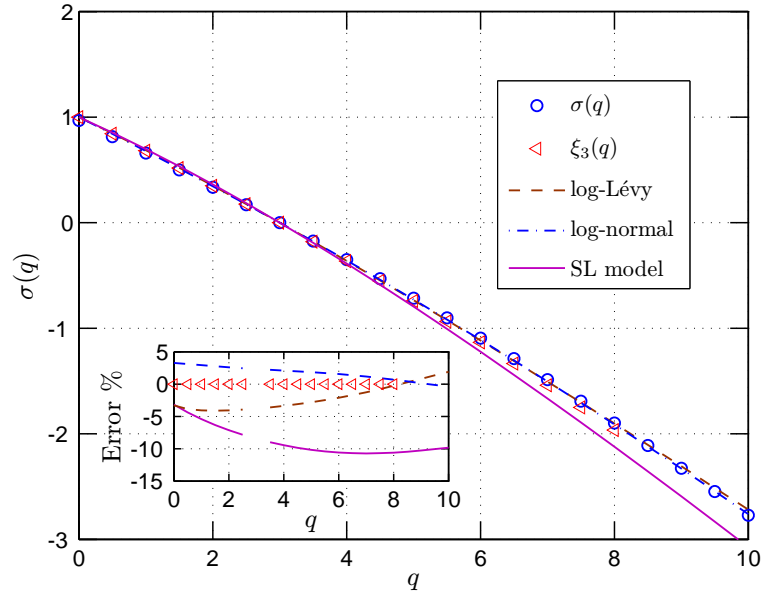


Figure 8.7: Representation of the scaling exponent $\sigma(q)$ (\circ), where q goes from 0 to 10. For comparison, we also show the corresponding scaling exponent estimated from the Hilbert-based ESS $\xi_3(q)$ (\triangleleft), the log-Lévy model with $C_1 = 0.07$, $\alpha = 1.5$ (dashed line), the log-normal model with $\mu = 0.11$ (dashed-dotted line) and the SL model (solid line). The inset shows the relative error from $\sigma(q)$.

2302 show the relative error in the right part of these figures. For each model, the relative
 2303 error have a similar shape and is parallel with each other. We also note that the
 2304 log-normal model with present choice of μ has smaller relative error.

2305 Figure 8.10 shows \mathcal{Z}_q v.s. \mathcal{Z}_{q-1} for various q (1, 5, 8 and 10) on the range $10 <$
 2306 $\omega < 7000$ Hz. A power law behaviour holds on this range for each plot, which is
 2307 significant larger than the inertial range $10 < \omega < 1000$ Hz. We still estimate the
 2308 scaling exponent $\rho(q, q - 1)$ on the inertial range. The estimated $\rho(q, q - 1)$ (\square) are
 2309 shown in Fig. 8.11. For comparison, the log-Lévy model with $C_1 = 0.07$ and $\alpha = 1.5$
 2310 (dashed-dotted line), log-normal model with $\mu = 0.11$ (dashed line) and the SL model
 2311 (solid line) are also shown. The inset shows the relative error from experimental value
 2312 $\rho(q, q - 1)$. There is no significant different among these three models. However, it

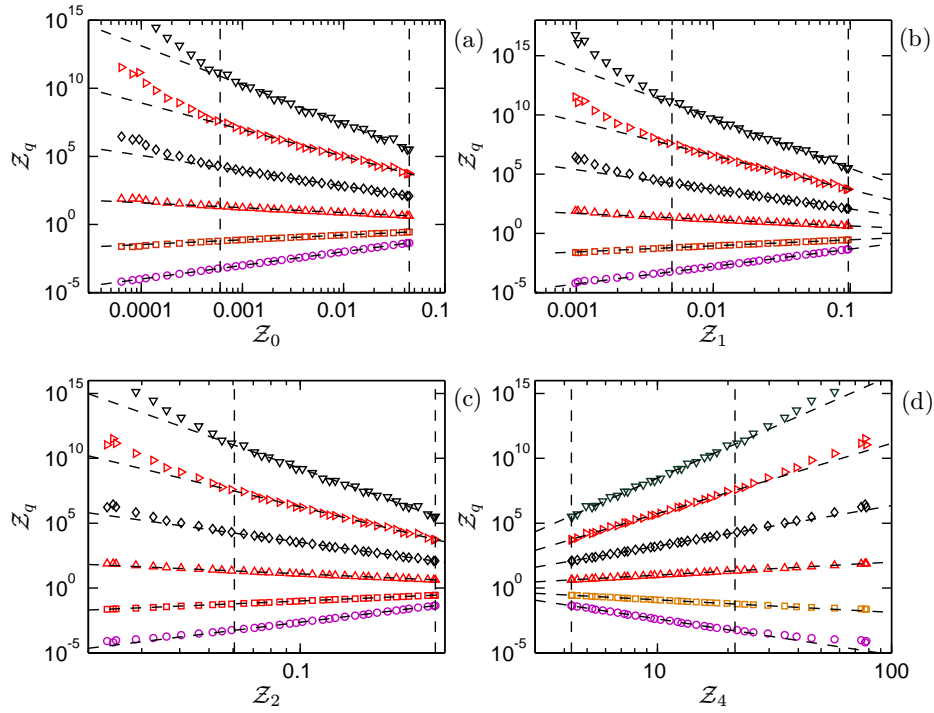


Figure 8.8: Representation of GESS $Z_q(\omega)$ vs $Z_p(\omega)$ for various p (a) $p = 0$, (b) $p = 1$, (c) $p = 2$ and (d) $p = 4$, where $q = 0$ (\circ), 2 (\square), 4 (\triangle), 6 (\diamond), 8 (\triangleright) and 10 (∇). The vertical dashed line demonstrates the inertial subrange $10 < \omega < 1000$ Hz. The dashed line is the least square fitting on inertial range.

seems that the log-normal model with present parameter provides the smallest relative error. 2313
2314

Considering Eq. (8.2.7) and Eq. (8.3.2), we may link $\sigma(q)$ and $\rho(q, p)$ to the scaling exponent $\xi(q)$, which is written as 2315
2316

$$\xi(q) = \frac{2q}{3} + \sigma(q) \quad (8.3.5a)$$

and 2317

$$\xi(q) = \frac{2q}{3} + \rho(q, p)\sigma(p), \quad p \neq 3 \quad (8.3.5b)$$

A potential application of $\rho(q, q-1)$ is to estimate $\xi(q)$ for high order q , if the quantity 2318

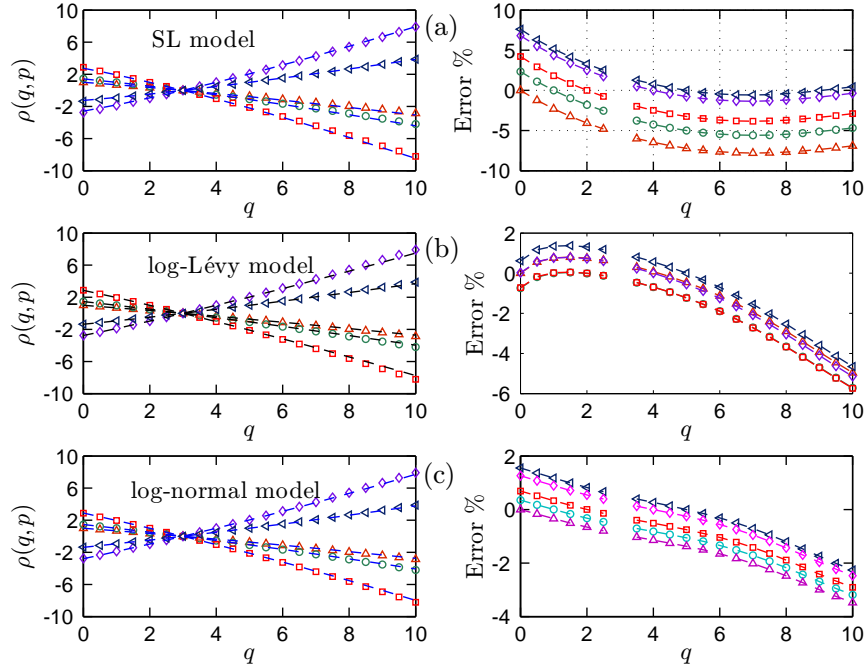


Figure 8.9: Representation of the scaling ratio $\rho(q, p)$ of GESS, where q goes from 0 to 10, $p = 0$ (Δ), 1 (\circ), 2 (\square), 4 (\diamond) and 5 (\triangleleft). For comparison, we present three different model, (a) SL model, (b) log-Lévy model, and (c) log-normal model. The right part shows the relative error.

2319 of the data is available. One may estimate $\sigma(q)$ and $\xi(q)$ by the following formula

$$\sigma(q) = \prod_{i=5}^q \rho(i, i-1) \sigma(4), \quad q \geq 5 \quad (8.3.6)$$

2320 and

$$\xi(q) = \frac{2q}{3} + \prod_{i=5}^q \rho(i, i-1) \sigma(4), \quad q \geq 5 \quad (8.3.7)$$

2321 We show the estimated $\zeta(q)$ (corresponding to $\xi(q) - 1$) in Fig. 8.12, based on
 2322 $\sigma(q)$ (dashed-dotted line), $\rho(q, p)$ (\diamond)⁵ and Hilbert-based ESS (\triangleleft). For comparison,
 2323 we show the log-normal model with two different intermittency parameter $\mu = 0.11$
 2324 (dashed-dotted line) fitting for $\sigma(q)$ and $\mu = 0.15$ (dashed line) fitting for $\xi(q) - 1$

⁵Here different p gives almost the same $\xi(q)$. Therefore, we only present the mean value of them, which is denoted as $\rho(q, p)$.

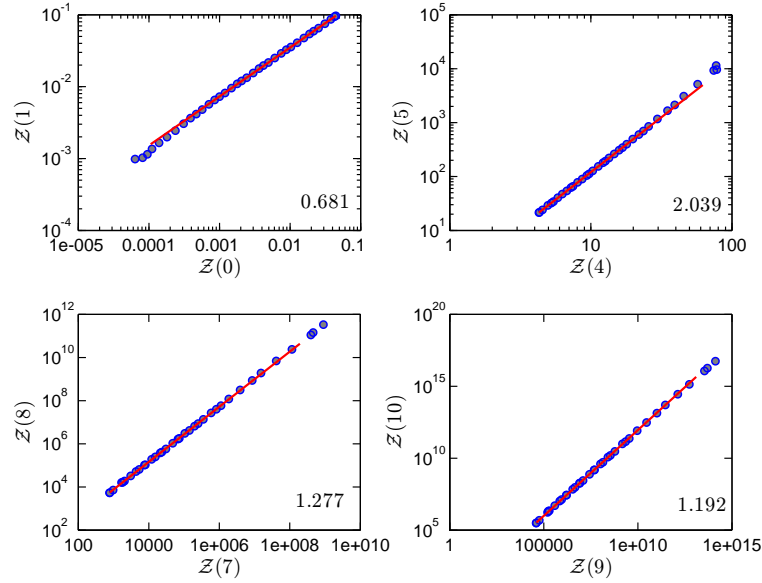


Figure 8.10: Representation of the GESS $Z(q)$ vs $Z(q-1)$ on the range $10 < \omega < 7000$ Hz, where $q = 1, 5, 8$ and 10 . Power law is observed in all cases.

from Hilbert-based ESS $\xi_0(q)$ and $\xi_3(q)$. The SL model is shown in the same picture 2325
as thin solid line. The GESS scaling exponent is quite close to the Hilbert-based ESS 2326
one, and significantly larger than SL model when q is greater than 5. We reproduce 2327
these scaling exponents from different approaches in Tab. 8.1. 2328

Taking Benzi's ESS result (Benzi *et al.*, 1993a,b; Arneodo *et al.*, 1996) as a ref- 2329
erence line, we show in Fig. 8.13 the absolute error and relative error from $\zeta(q)$ for 2330
different estimators $\xi(q)$ (\triangleright), $\xi_0(q)$ (\square), $\xi_3(q)$ (\diamond), $\Pi(q)$ (\circ), $\sigma(q)$ (\triangleleft) and $\rho(q, p)$ 2331
(\triangle). One can find that the relative error is decreasing with q when $q \leq 4$. When 2332
 $q \geq 4$, the relative error is then increasing with q . However, the relative error is less 2333
than 10% when $2 \leq q \leq 8$. 2334

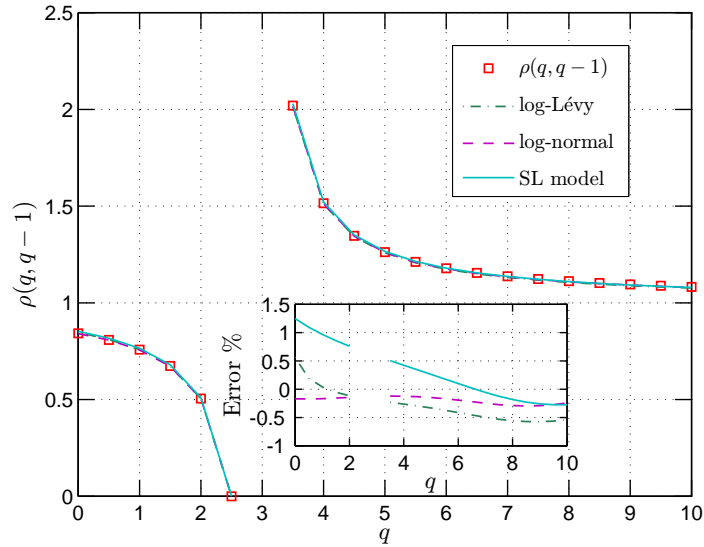


Figure 8.11: Representation of the scaling exponent ratio $\rho(q, q - 1)$ from GESS (\square), where q goes from 0 to 10. For comparison, log-Lévy model with $C_1 = 0.07$ and $\alpha = 1.5$ (dashed-dotted line), log-normal model with $\mu = 0.11$ (dashed line) and SL model (solid line) are also presented. The inset shows the relative error.

8.4 Summary

2335 **8.4 Summary**

2336 In this chapter, we extended Benzi's idea of Extended Self-Similarity into the Hilbert
 2337 frame. According to Kolmogorov's refined similarity hypothesis (Kolmogorov, 1962;
 2338 Monin & Yaglom, 1971; Frisch, 1995), we have two special cases, $\mathcal{L}_0(\omega)$ and $\mathcal{L}_3(\omega)$,
 2339 which are free from the intermittency effect. We therefore use $\mathcal{L}_0(\omega)$ and $\mathcal{L}_3(\omega)$ to
 2340 define the so-called ESS. They provide almost the same scaling exponents $\xi(q)$, which
 2341 are slightly larger than SL model for high order q . We then proposed a hierarchy
 2342 model by defining a hierarchical spectral function. The scaling exponent $\Pi(q)$ of
 2343 the hierarchical spectral function decreases linearly with q . We finally presented a
 2344 generalized ESS by considering a dimensionless arbitrary order Hilbert spectrum. The
 2345 scaling exponents provided by the dimensionless spectrum and the GESS are in good
 2346 agreement with each other.

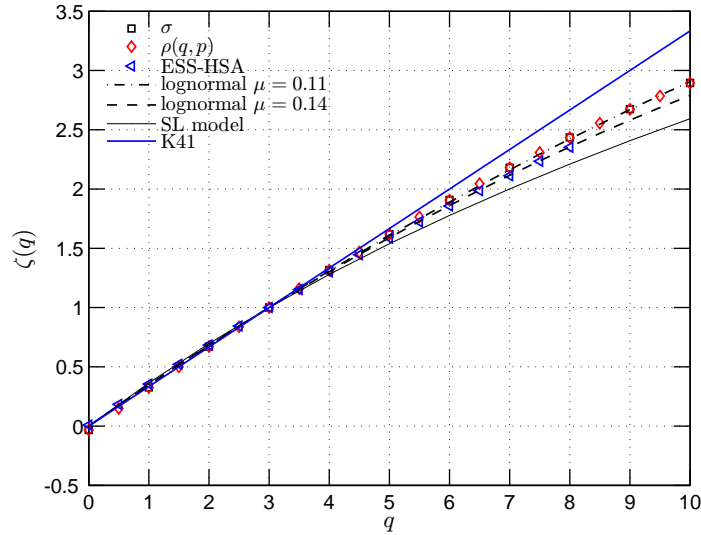


Figure 8.12: Comparison of the scaling exponents $\zeta(q)$ from GESS, $\sigma(q)$ (\square), $\rho(q,p)$ (\diamond), and the direct estimation by ESS-HSA (\triangleleft). For comparison, the SL model is also shown in the same picture as thin solid line. We also fit the data by the log-normal model with $\mu = 0.11$ (dashed-dotted line) and $\mu = 0.15$ (thin dashed line)

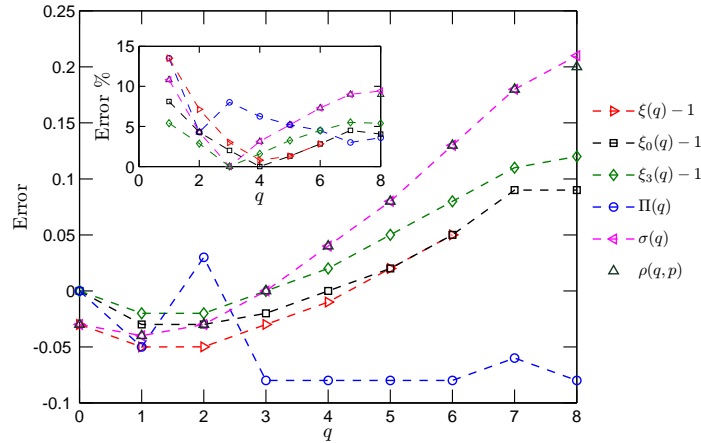


Figure 8.13: Absolute error from $\zeta(q)$ (Benzi *et al.*, 1993b), where the scaling exponents are estimated by $\xi(q) - 1$ (\triangleright), $\xi_0(q) - 1$ (\square), $\xi_3(q) - 1$ (\diamond), $\Pi(q)$ (\circ), $\sigma(q)$ (\triangleleft) and $\rho(q,p)$ (\triangle). The inset shows the relative error.

Table 8.1: Scaling exponents $\zeta(q)$ from different approaches: the ESS $\zeta(q)$ (Benzi *et al.*, 1996), the Hilbert-based $\xi(q) - 1$ (Eq. (3.1.3)), the Hilbert-based ESS $\xi_0(q) - 1$ (Eq. (8.1.2)), the Hilbert-based ESS $\xi_3(q) - 1$ (Eq. (8.1.2)), the dimensionless Hilbert spectrum $\sigma(q)$ (Eq. (8.3.5a)) and the GESS $\rho(q, p)$ (Eq. (8.3.5b)).

q	$\zeta(q)$	$\xi(q) - 1$	$\xi_0(q) - 1$	$\xi_3(q) - 1$	$\sigma(q)$	$\rho(q, p)$
0	0.00	-0.03	0.00	0.00	-0.03	-0.03
1	0.37	0.32	0.34	0.35	0.33	0.33
2	0.70	0.65	0.67	0.68	0.67	0.67
3	1.00	0.97	0.98	1.00	1.00	1.00
4	1.28	1.27	1.28	1.30	1.32	1.32
5	1.54	1.56	1.56	1.59	1.62	1.62
6	1.78	1.83	1.83	1.86	1.91	1.91
7	2.00		2.09	2.11	2.18	2.18
8	2.23		2.32	2.35	2.44	2.43

2347

Part III

2348

Application to Environmental

2349

Time Series

2350 Chapter 9

2351 Analysis of River Flow 2352 Fluctuations

2353 A better understanding of river flow fluctuations is of sharp practical importance,
2354 e.g. for ecosystem studies (transport properties), and for flood understanding and
2355 forecasting. River flows fluctuate on many different scales: at small scales, river
2356 turbulence induces stochastic fluctuations and at larger scales (from days to years) the
2357 river flow fluctuations are the result of complex nonlinear interactions between rainfall
2358 processes, topography and geography (Schumm, 2005). They are also impacted by
2359 solar forcing and other large scale variations of the climate system (Mauas *et al.*, 2008).
2360 Daily river flow time series thus show fluctuations possessing stochastic properties,
2361 as well as deterministic forcing resulting from seasonal or annual meteorological and
2362 climatic cycles.

2363 In this chapter, we apply the empirical mode decomposition (EMD) and the arbitrary
2364 order Hilbert spectral analysis (HSA) on river flow discharge fluctuations data.
2365 to characterize the scale invariant properties of small scale in amplitude-frequency
2366 space. The results presented in this chapter are published in Huang *et al.* (2009b)[Y.
2367 Huang, *et al. J. Hydrol.*, 373, 103-111, 2009.].

9.1 Introduction

2368

Since Hurst (1951) revealed the long-range dependent properties in river flow, associated to scaling properties, researchers have tried different methods to characterize the (multi)scaling properties in river flows (Hurst *et al.*, 1965; Tessier *et al.*, 1996; Pandey *et al.*, 1998; Jánosi & Gallas, 1999; Kantelhardt *et al.*, 2003, 2006; Livina *et al.*, 2003b,a; Koscielny-Bunde *et al.*, 2006; Mauas *et al.*, 2008). Below we quickly review the approaches undertaken in these studies.

Tessier *et al.* (1996) analyzed the relation between rainfall and river flow of 30 rivers and basins in France. They used the double trace moment technique to characterize the multifractal properties. They found that a scaling break occurs at a scale about 16 days. They argued that the rain field itself is the source of the river flow, therefore typical scales in the rain field will also be present in the river flow.

Dahlstedt & Jensen (2005) investigated the Danube and the Mississippi river flows and levels by using finite-size-scaling hypothesis (Aji & Goldenfeld, 2001). They considered the river flow basin size L from different locations. They characterized the multiscaling properties of river flow and level records by considering the relative and general relative scaling (or Extended-Self-Similarity and Generalized Extended-Self-Similarity in the turbulent community). They found that the Fourier spectrum may be different from location to location due to the size effect of the basin area.

More recently, several authors applied the so-called detrended fluctuation analysis (DFA) and its multifractal version to describe the scaling and multiscaling properties of river flows (Kantelhardt *et al.*, 2003; Livina *et al.*, 2003b,b; Kantelhardt *et al.*, 2006; Koscielny-Bunde *et al.*, 2006; Livina *et al.*, 2007; Zhang *et al.*, 2008, 2009). Livina *et al.* (2003a,b) argued that the climate is strongly forced by the periodic variations

2392 of the Earth with respect to the state of the solar system. The seasonal variations in
2393 the solar radiation cause periodic changes in temperature and precipitations, which
2394 eventually lead to a seasonal periodicity of river flows. The Fourier and structure
2395 function analyses are impacted by this strong periodicity (Livina *et al.*, 2003a,b;
2396 Kantelhardt *et al.*, 2003; Koscielny-Bunde *et al.*, 2006). According to these authors,
2397 the DFA approach is an efficient method to eliminate the trend effects.

2398 Koscielny-Bunde *et al.* (2006) found that the Hurst number H varies from river
2399 to river between $0.55 \sim 0.95$ in a non-universal manner independent of the size of the
2400 basin. They found that at large time scales, $F_q(s)$ scales as $s^{h(q)}$, and they further
2401 proposed a simple function form with two parameters a and b , $h(q) = 1/q - [\ln a^q +$
2402 $b^q]/[q \ln(2)]$ to describe the scaling exponent $h(q)$ of all moments (Kantelhardt *et al.*,
2403 2003). Kantelhardt *et al.* (2006) also found that the Hurst number H estimated
2404 from 99 precipitation and 42 river runoff records data are not consistent with the
2405 hypothesis that the scaling is universal with an exponent close to 0.75 (Hurst *et al.*,
2406 1965; Peters *et al.*, 2002).

2407 9.2 Seine River and Wimereux River

2408 The Seine river is the third largest river in France. Its length is 776 km, and its basin
2409 is 78650 km². It is economically important for France, with 25% of its population as
2410 well as 40% of its industry and agriculture concentrated in and around it (Dauvin,
2411 2007). The flow data is provided by the Service de Navigation de la Seine (SNS). This
2412 corresponds to daily flow data Q (m³s⁻¹), recorded from 1 January 1976 to 28 April
2413 2008. There are 11828 data values, with some missing values due to interruptions for
2414 maintenance or because of the failure of measuring devices. Due to the local ability

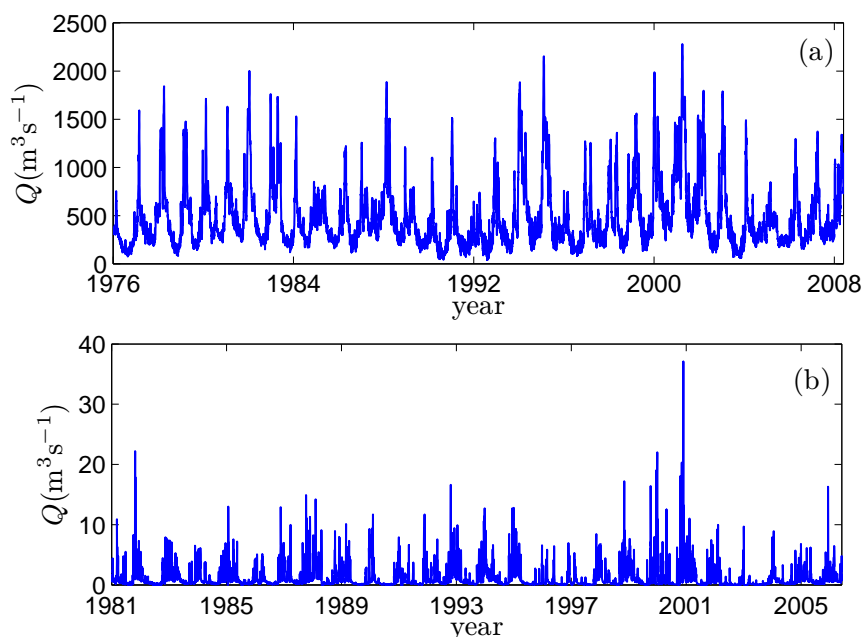


Figure 9.1: The river flow discharge time series of (a) Seine River, recorded from 1 January 1976 to 28 April 2008, (b) Wimereux river, recorded from 1 January 1981 to 27 May 2006. The data illustrate clear strong annual cycles with huge fluctuations. The total lengths are 11828 and 9278 data points for the Seine river and the Wimereux river, respectively.

of HSA approach, which is performed through spline interpolation, the missing values 2415
 in the time series do not change the results, since the method can be applied even 2416
 for irregular sampling. The data are shown in Fig. 9.1 (a), demonstrating some large 2417
 fluctuations at all scales. The mean and standard deviation of the discharge are 2418
 $488 \text{ m}^3\text{s}^{-1}$ and $349 \text{ m}^3\text{s}^{-1}$, respectively. This figure shows a complex and stochastic 2419
 behavior, with a visible strong annual cycle. 2420

The Wimereux river is a small river in the North of France¹. Its length is 22 km, 2421
 and its basin is 78 km^2 . It can have strong fluctuations due to fast increase of the 2422
 flow in case of heavy rain. The daily flow discharge is recorded from 1 January 1981 2423

¹The Wimereux river is the local river in Wimereux city, the coastal host city of the laboratory of Oceanology and Geosciences.

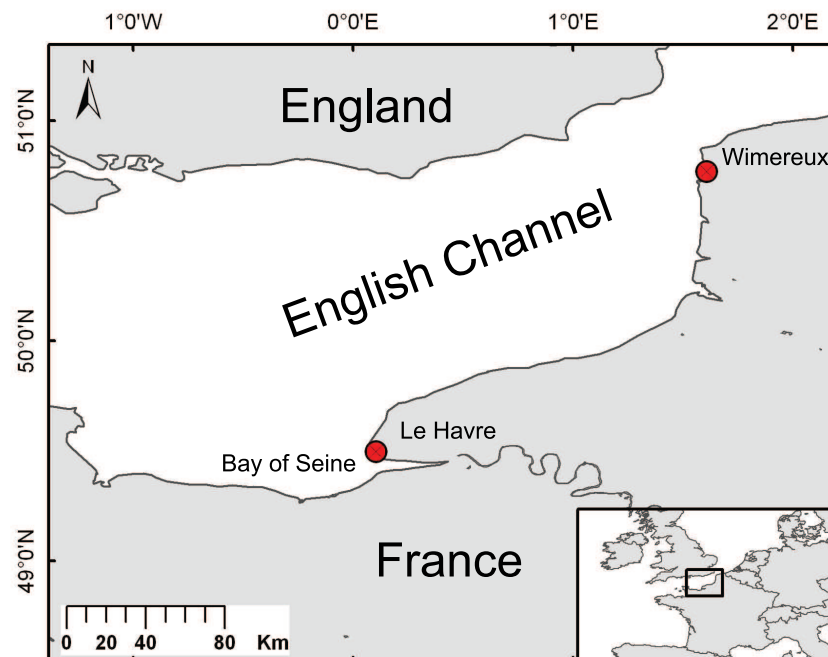


Figure 9.2: A map showing the location of the Seine river and the Wimereux river, in the eastern English Channel. The distance between them is about 300 km.

2424 to 27 May 2006, with a total length of 9278 points values with some missing, see
 2425 Fig. 9.1 (b). The mean and standard deviation of the discharge data are $1.02 \text{ m}^3\text{s}^{-1}$
 2426 and $1.73 \text{ m}^3\text{s}^{-1}$.

2427 Figure 9.2 shows the location of these two rivers, where the Seine river is repre-
 2428 sented as a solid line. The Wimereux river is too small to be displayed in the same
 2429 figure. The difference between these two rivers is clear: the Seine river is a real big
 2430 one, and the Wimereux river is much smaller and strongly influenced by the local
 2431 rainfall conditions. The distance between them is about 300 km, see Fig. 9.2. Both of
 2432 them are affected by the same large scale climatic factors and belong to the marine
 2433 west coast climate of Northern France. This climate is found on the west coast of
 2434 middle latitude regions and can be quite humid. Indeed it is subject to western wind

bringing important variability and intermittent clouds, important precipitation and 2435
 temperate temperatures. The direct estimation of the cross correlation between these 2436
 two recorded data is about 0.256, a value that may be contaminated by the small 2437
 scale fluctuations. We will apply to these two data sets by the EMD method in the 2438
 following section. 2439

9.3 EMD Results 2440

After the application of the EMD method, the original data are separated into several 2441
 IMF modes. We then represent the IMF modes in Fig. 9.3 and Fig. 9.4 for the Seine 2442
 river and the Wimereux river, respectively. For display convenience, we exclude the 2443
 residual for the Seine river. Graphically, one can see that the characteristic scale 2444
 is increasing with the mode index n . Let us note that the number of IMF modes 2445
 is produced by the algorithm and depends on the length and the complexity of the 2446
 data. In practice, based on the dyadic filter bank property of the EMD method, this 2447
 number is usually less than $\log_2(N)$, where N is the length of the data (Flandrin & 2448
 Gonçalves, 2004; Flandrin *et al.*, 2004; Wu & Huang, 2004; Huang *et al.*, 2008). First, 2449
 we estimate the mean frequency $\bar{\omega}$ of each IMF mode. We use the following three 2450
 definitions of mean frequency $\bar{\omega}$. The first one was proposed by Huang *et al.* (1998), 2451
 which is written as 2452

$$\bar{\omega}_i = \frac{\int_0^\infty f S_i(f) df}{\int_0^\infty S_i(f) df} \quad (9.3.1)$$

where $S_i(f)$ is Fourier spectrum of \mathbb{C}_i . It is an energy weighted average in Fourier 2453
 space. The second one was given by Flandrin (Flandrin *et al.*, 2004; Flandrin & 2454

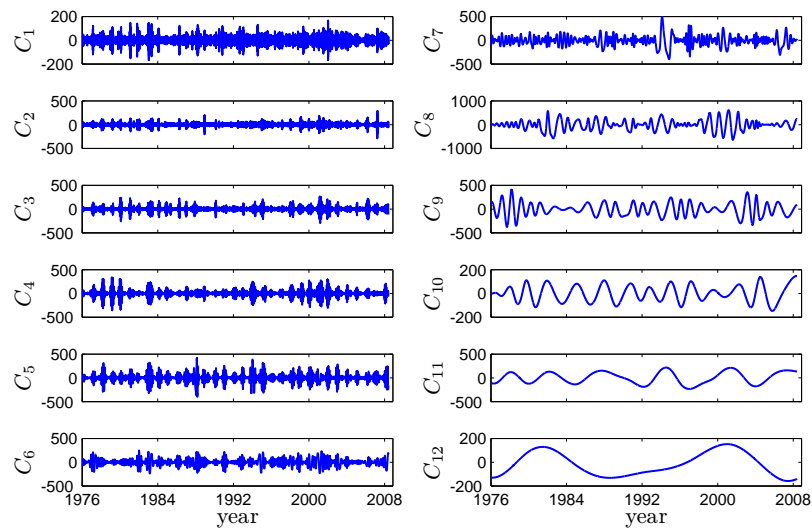


Figure 9.3: IMF modes (excluding the residual) from EMD for the Seine river. Here the data are taken from 1 January 1976 to 28 April 2008. The characteristic scale is increasing with the mode index number n .

2455 Gonçalvès, 2004), and is written as

$$\bar{\omega}_i = \frac{N^0 - 1}{L^0} \quad (9.3.2)$$

2456 where N^0 is the zero-crossing number, and L^0 is the distance between the first and
 2457 last zero-crossing. The third one is introduced here for the first time, and is defined

Table 9.1: The mean period (in days) of each IMF mode (excluding the residual) of the Seine river and the Wimereux river, respectively. Here the mean period is estimated as $\bar{T} = 1/\bar{\omega}$, where $\bar{\omega}$ is calculated by Eq. (9.3.1). The 8th and 9th IMF modes of the Seine river and Wimereux river, respectively, are close to the annual cycle.

	1	2	3	4	5	6	7	8	9	10	11	12	13
Seine	3	8	19	33	55	86	185	358	452	869	1823	5551	
Wimereux	5	9	16	25	36	58	103	182	376	574	2149	2785	3125

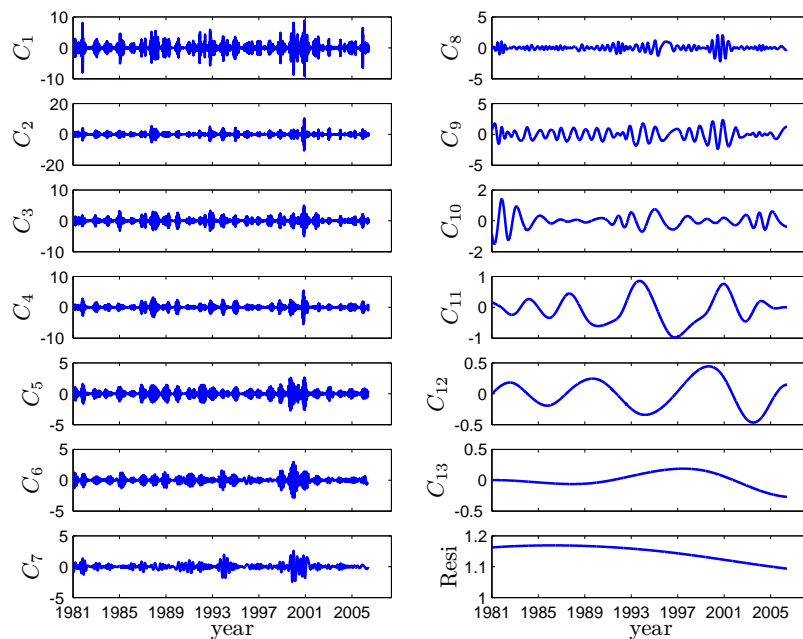


Figure 9.4: IMF modes from EMD for Wimereux river. Here the data are taken from 1 January 1981 to 27 May 2006.

as

2458

$$\bar{\omega}_i = \frac{\int_0^\infty \omega h_i(\omega) d\omega}{\int_0^\infty h_i(\omega) d\omega} \quad (9.3.3)$$

where $h_i(\omega)$ is the Hilbert marginal spectrum for the i^{th} mode. This definition is 2459
 similar to the first one: it is an energy weighted measurement of the mean frequency 2460
 in Hilbert space. We then represent the mean frequency $\bar{\omega}$ estimated by these three 2461
 definitions Eq. (9.3.1) (\circ), (9.3.2) (\square) and (9.3.3) (\times) for each mode in Fig. 9.5 for 2462
 (a) the Seine river, and (b) the Wimereux river. One can see that the two energy 2463
 weighted estimators give almost the same mean frequency. However, they are slightly 2464
 smaller than the zero-crossing based estimator. Graphically, all these three estimators 2465
 suggest the following exponential law 2466

$$\bar{\omega}(n) \sim \gamma^{-n} \quad (9.3.4)$$

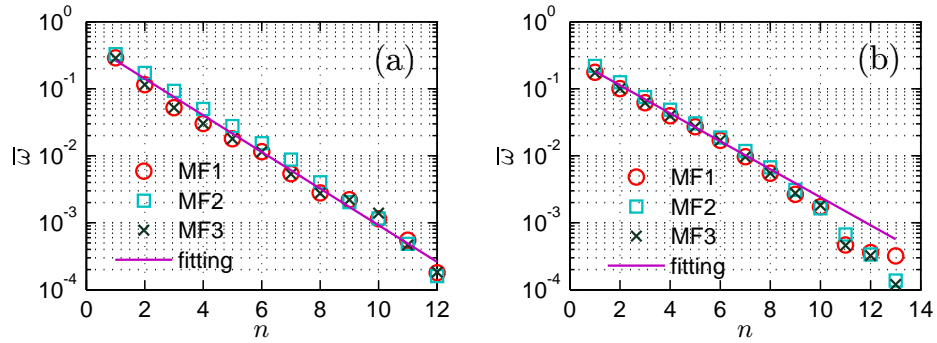


Figure 9.5: Representation of the mean frequency $\bar{\omega}$ vs the mode index n in log-linear view: (a) Seine river, (b) Wimereux river, where the mean frequency $\bar{\omega}$ are estimated by using Eqs. (9.3.1) (\circ), (9.3.2) (\square) and (9.3.3) (\times), respectively. An exponential law is observed for each representation. The straight line is the least square fit of the data.

2467 where $\gamma_s \simeq 1.88$, $\gamma_w \simeq 1.62$ are estimated by using the least square fitting for the
 2468 Seine river and the Wimereux river, respectively. This result implies that the mean
 2469 frequency of a given mode is γ times larger than the mean frequency of next one. We
 2470 notice that these values are significantly different from 2, which would correspond to a
 2471 dyadic filter bank, which are reported for white noise (Wu & Huang, 2004), fractional
 2472 Gaussian noise (Flandrin *et al.*, 2004; Flandrin & Gonçalves, 2004) and turbulence
 2473 time series (Huang *et al.*, 2008). However, it still indicates that the EMD algorithm
 2474 acts a filter bank here.

2475 We list the mean period \bar{T} (in days) in Table 9.1, where $\bar{T} = 1/\bar{\omega}$. Since the
 2476 three above mentioned mean frequency estimators give almost the same value, we
 2477 thus only present the value estimated by Eq. (9.3.1). One can find that the EMD
 2478 approach captures the annual cycle, which is the 8th and 9th mode for the Seine river
 2479 and Wimereux river, respectively. Both rivers belong to the same climate and it is
 2480 expected that large scale modes are correlated. However, the data at daily scale are
 2481 not (the cross-correlation at this scale is 0.256); this is due to the influence of small

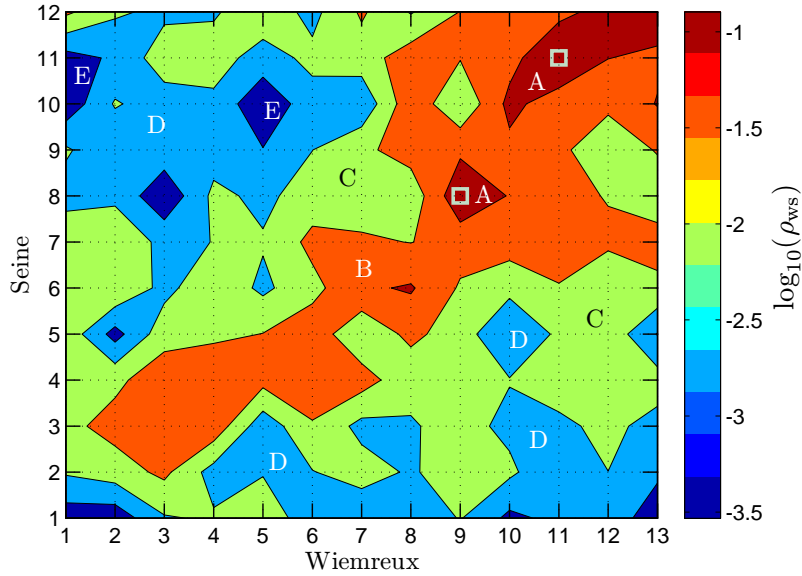


Figure 9.6: Representation of the cross-correlation ρ_{ws} between IMF modes from the Seine and Wimereux rivers. The data span is taken from 1 January 1981 to 27 May 2006 for both series. For convenience, we consider the coefficient value $\log_{10}(\rho_{ws}(i, j))$. As expected, the annual cycle shows a strong correlation with a coefficient $\rho_{ws}(9, 8) = 0.426$. The coefficient of the most correlated modes is $\rho_{ws}(11, 11) = 0.579$. These two strong correlations are then marked by \square .

scales. The cross-correlation between two IMF modes is defined as

2482

$$\rho_{ws}(i, j) = \frac{\langle C_{w,i} C_{s,j} \rangle}{\langle C_{w,i}^2 \rangle^{1/2} \langle C_{s,i}^2 \rangle^{1/2}} \quad (9.3.5)$$

where $\langle \cdot \rangle$ means ensemble average. The corresponding cross-correlation $\rho_{ws}(i, j)$ is then plotted in Fig. 9.6, where the most correlated modes are marked by \square . The large scale modes are correlated as expected. More precisely, we observe a larger cross-correlation between the annual cycle modes, $\rho_{ws}(9, 8) = 0.426$, and the most correlation coefficient is $\rho_{ws}(11, 11) = 0.579$, with mean periods of about 6 and 8 years for the Seine river and the Wimereux river, respectively.

We then replot the annual cycle for the Seine river (thin solid line) and Wimereux river (thick solid line) in Fig. 9.7 (a). One can find that their shapes are almost the

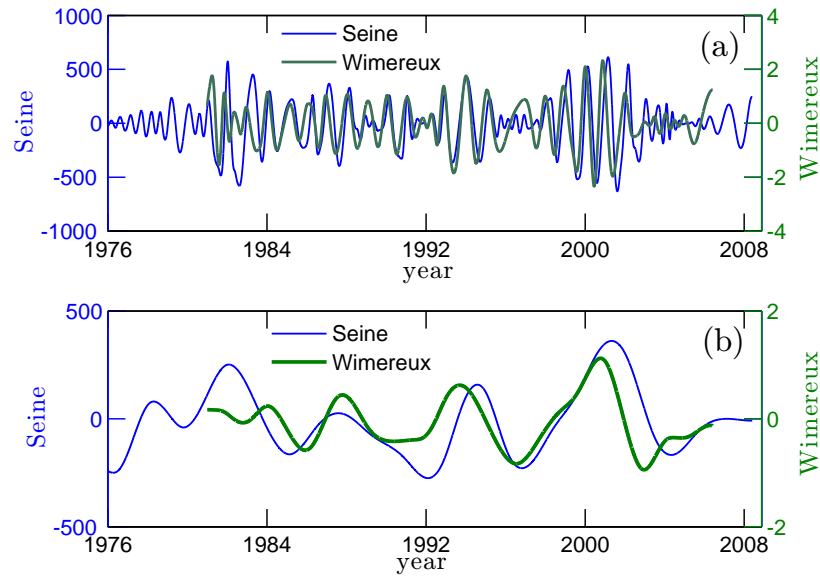


Figure 9.7: Most correlated IMF modes: (a) the annual cycle mode for the Seine river (thin solid line) and the Wimereux river (thick solid line), (b) the reconstruction of the large scale part for the Seine river (thin solid line) and the Wimereux river (thick solid line). We took the IMF modes 11 ~ 12 from the Seine river and 11 ~ 13 from the Wimereux river, which means periods larger than 3 years, to reconstruct the large scale part. Graphically, they have the same evolution trend on range 1 January 1981 to 28 May 2006.

2491 same on the range from 1 January 1981 to 28 May 2006. We also reconstruct the
 2492 large scale signal from those modes, with mean period larger than 3 years, 11th and
 2493 12th from the Seine river (thin solid line), and 11th to 13th from the Wimereux river
 2494 (thick solid line). The result is shown in Fig. 9.7 (b): they have almost the same
 2495 shape and evolution trend.

2496 9.4 HSA Results

2497 In order to characterize the intermittent properties of river flow fluctuations, we
 2498 consider here HSA and arbitrary order HSA analysis. We first compare the Hilbert

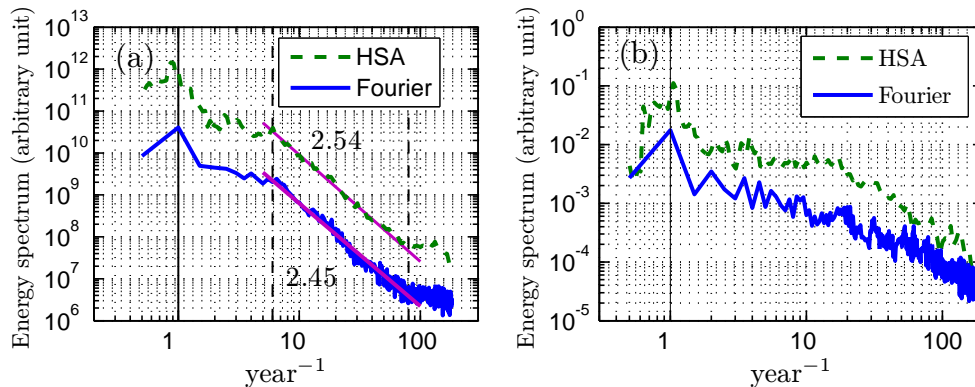


Figure 9.8: Comparison of the Hilbert marginal spectrum (dashed line) and Fourier spectrum (solid line) for (a) the Seine river, (b) the Wimereux river. For the Seine river, a power law behaviour is observed on the range $6 < \omega < 80 \text{ year}^{-1}$, or $4.5 \sim 60$ days: this range is marked by the vertical dashed lines. The scaling values are 2.54 and 2.45 for Hilbert spectrum and Fourier spectrum, respectively. The vertical solid line indicates the annual cycle.

marginal spectrum (dashed line) and Fourier spectrum (solid line) in Fig. 9.8 for (a) 2499
the Seine river, and (b) the Wimereux river to identify the power law range, where 2500
the scale invariance holds. For the Seine river, both methods capture the annual cycle 2501
(vertical solid line) and show power law behaviour on the range $6 < \omega < 80 \text{ year}^{-1}$ or 2502
from 4.5 to 60 days, with scaling exponent 2.54 and 2.45, respectively. The power law 2503
range is between synoptic and intraseasonal scales (Zhang, 2005). The latter may be 2504
linked to the Madden-Julian Oscillation (MJO), since some connection between and 2505
the North Atlantic Oscillation (NAO) and MJO have been found (Cassou, 2008). For 2506
the Wimereux river, the power law range is less clear. We therefore only apply below 2507
the arbitrary order HSA analysis on the Seine river. 2508

Since we are concerned with the scaling property in the above range, we thus 2509
divide the entire time series into 16 segments, each one has 2×365 points, 2 years 2510
each. The arbitrary order Hilbert marginal spectra are shown in Fig. 9.9, for $q = 0$, 2511

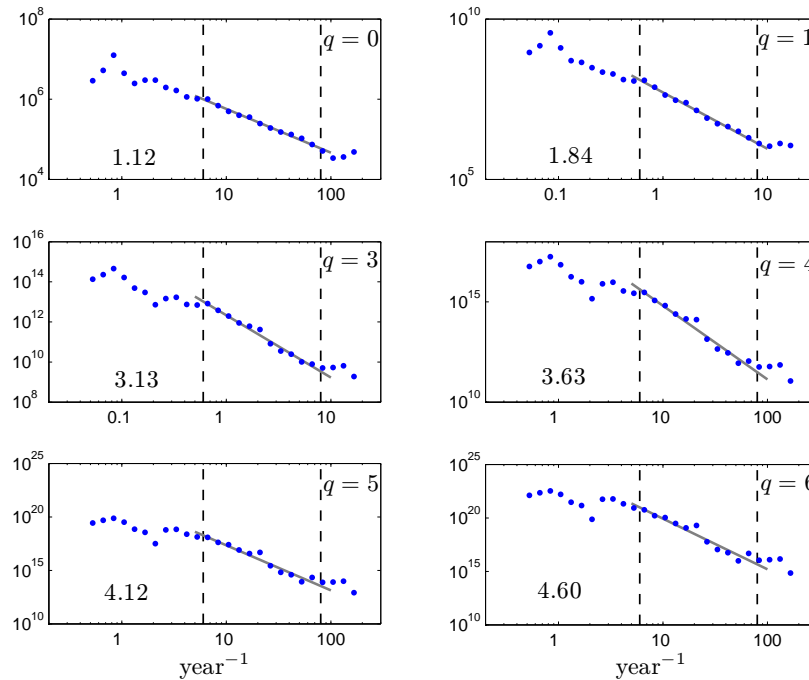


Figure 9.9: Representation of arbitrary order Hilbert marginal amplitude spectra $\mathcal{L}_q(\omega)$ for the Seine river, where $q = 0, 1, 3, 4, 5$ and 6 . A power law behaviour is observed in all cases on the range $6 < \omega < 80 \text{ year}^{-1}$. The vertical dashed lines indicate the power law range. The corresponding scaling values are shown in each figure.

2512 1, 3, 4, 5 and 6. Power law behaviour is then observed in all cases on the range
 2513 $6 < \omega < 80 \text{ year}^{-1}$. The corresponding scaling exponents $\xi(q)$ are estimated on this
 2514 range by using least square fitting with 95% confidence limit, Fig. 9.10 shows the
 2515 scaling exponents $\xi(q)$ (\circ). This curve is concave, which indicates the multifractal
 2516 properties of the river flow discharge (Pandey *et al.*, 1998; Kantelhardt *et al.*, 2003,
 2517 2006). For comparison, we also show a reference line $qH + 1$ (solid line), where
 2518 $H = \xi(1) - 1 = 0.84 \pm 0.08$, which corresponds to the mono-scaling case. The
 2519 departure from this reference mono-scaling line is then shown in inset.

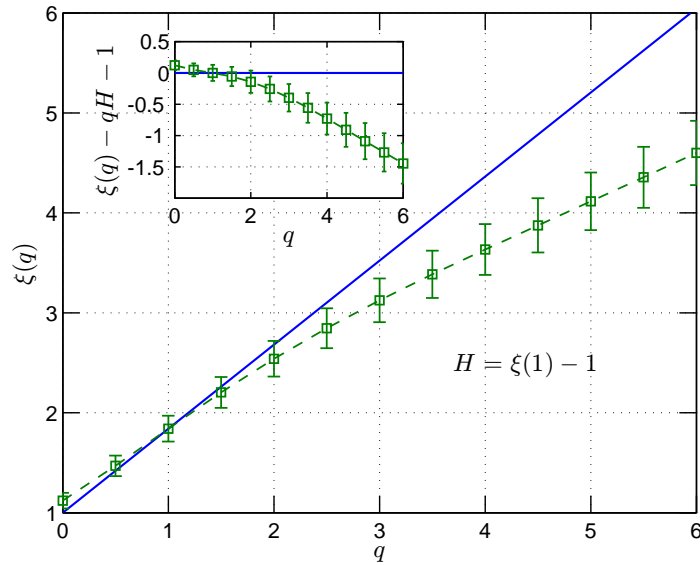


Figure 9.10: Scaling exponents $\xi(q)$ (\square) for the Seine river. The inset shows the departure from the reference line $qH + 1$, where $H = \xi(1) - 1$. The shape of these scaling exponents is concave, which indicates the small scale intermittency nature of river flow.

9.5 Discussion

2520

We compare the above observation with the conventional structure function analysis, 2521
the traditional way to extract the scaling exponents. We plot the result in Fig. 9.11, 2522
where $q = 1$ (\square), 2 (\circ) and 3 (\diamond), respectively. Some scaling portion are visible on 2523
these figures, of a relatively limited amplitude. To reveal the scale invariance more 2524
clearly, we consider the Extended Self-Similarity (ESS) properties, a relative scaling 2525
expressed as (Benzi *et al.*, 1993b) 2526

$$\langle \Delta x^q \rangle \sim \langle \Delta x \rangle^{\psi(q)} \quad (9.5.1)$$

where in case of scaling, we have $\zeta(q) = H\psi(q)$. Eq. (9.5.1) can be used to estimate 2527
more accurately the exponents $\psi(q)$. The ESS is verified for the Seine river on range 2528
 $2 < \tau < 60$ days, see Fig. 9.12. Figure 9.13 shows the ESS result for the Wimereux 2529

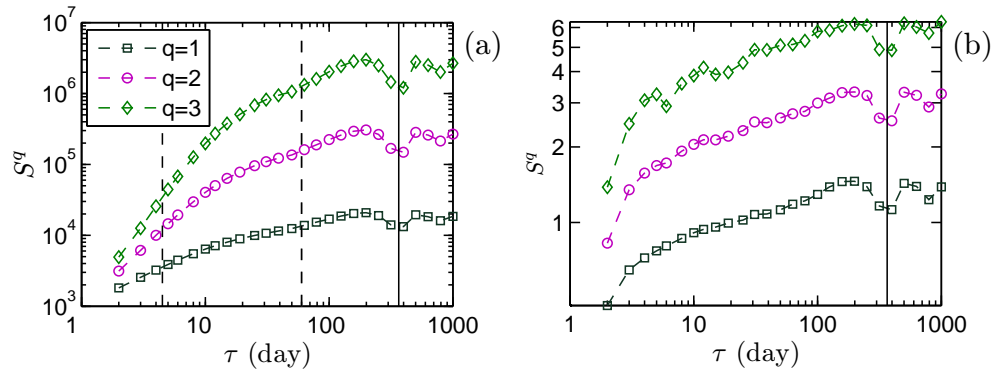


Figure 9.11: Structure function for (a) the Seine river, and (b) the Wimereux river, where $q = 1$ (\square), 2 (\circ) and 3 (\diamond). The vertical dashed lines indicate the range $4.5 \sim 60$ days. The annual cycle influence is also indicated by the solid line.

2530 river. It is scaling and is rather scattered. We then show the relative scaling exponents
 2531 $\psi(q)$ and the normalized scaling exponents $(\xi(q) - 1)/(\xi(1) - 1)$ in Fig. 9.14. In the
 2532 mono-scaling case and when there is no large scale forcing, they should collapse on a
 2533 solid line $\psi(q) = q$. The same approach is applied to the Wimereux river. In this case
 2534 the HSA approach is not displaying any clear scaling range. We thus use the ESS
 2535 approach and compare the resulting curve $\psi(q)$ to the one obtained from the Seine
 2536 river. The Wimereux river scaling exponents are saturating at $\psi(q = 1)$, and the curve
 2537 is quite different from the Seine river. This shows that the Wimereux river is more
 2538 intermittent than the Seine river: which may come from the fact that its catchment
 2539 basin is much smaller, hence its discharge variation can be more rapid. This may also
 2540 be an effect of strong oscillations that reduce the multifractal degree (see Telesca &
 2541 Macchiato (2004); Bolzan *et al.* (2009)). It is also interesting to see in the same graph
 2542 the difference between the HSA based exponents and structure function's exponents
 2543 for the Seine river. The discrepancy can be interpreted as coming from the influence
 2544 of the periodic component in the time series. Indeed we have shown in Huang *et al.*

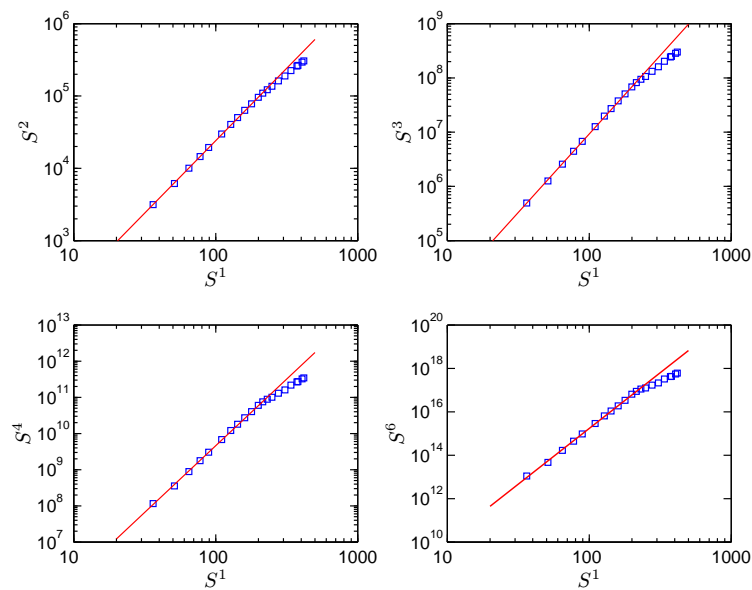


Figure 9.12: Extended self-similarity test of the Seine river on range $2 < \tau < 300$ day. The relative scaling is very well captured for all moments.

(2009d,a), see also chapter 5, that the influence of periodic components is stronger 2545
 on structure function than on HSA exponents, which can be linked to the fact 2546
 EMD acts a filter bank (Flandrin & Gonçalves, 2004; Flandrin *et al.*, 2004; Huang 2547
et al., 2008; Wu & Huang, 2004). Periodic components tend to increase the value of 2548
 $\zeta(q)$ relative to the real theoretical curve. 2549

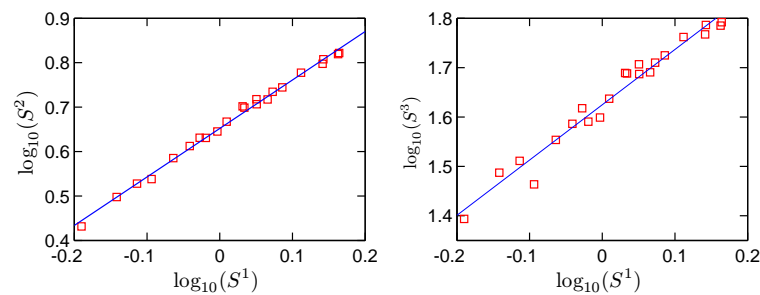


Figure 9.13: Extended self-similarity test of the Wimereux river on range $2 < \tau < 300$ day.

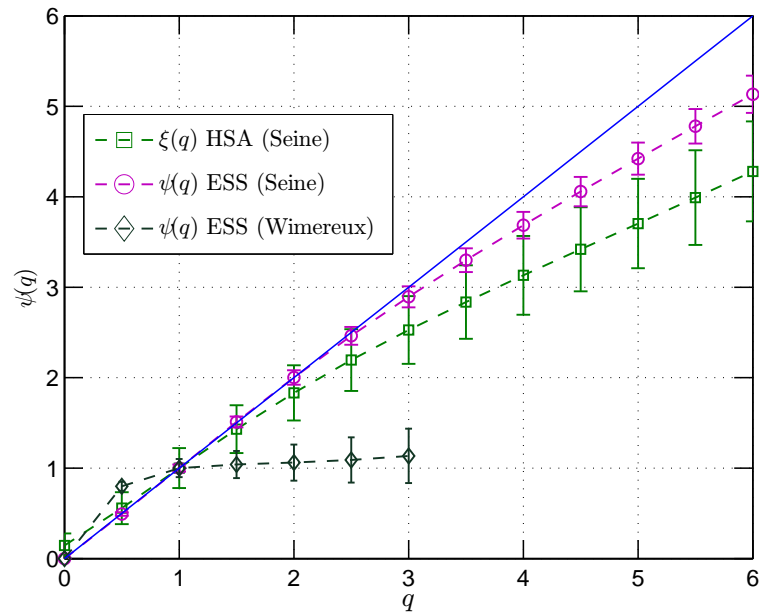


Figure 9.14: Comparison of the relative scaling exponents $\psi(q)$ (\square) and $(\xi(q) - 1)/(\xi(1) - 1)$ (\circ).

2550 9.6 Summary

2551 In this chapter we applied for the first time the EMD methodology to river flow time
 2552 series. Using daily river flow discharge data, 32 years recorded in the Seine river
 2553 (France), and 25 years recorded in the Wimereux river (France), we have shown that
 2554 the time series can be successfully separated into several IMF modes. Exponential
 2555 laws for the mean frequency of each mode have been found, with exponents $\gamma_s = 1.88$
 2556 and $\gamma_w = 1.62$ for the Seine river and the Wimereux river, respectively. These values
 2557 are smaller than 2, the value for dyadic filter bank. Even though, it still confirmed
 2558 that the EMD algorithm acts as a filter bank for river flow data. Furthermore, strong
 2559 cross-correlation have been observed between annual cycles and the large scale modes
 2560 having a mean period larger than 3 years. Based on the correlation analysis results,
 2561 we have found that the annual cycle mode and the reconstructed large scale part have

almost the same evolution trends.

2562

We have also characterized the intermittency of the time series over the ranges showing scaling properties. For the Seine river, we observed power laws for the first six order Hilbert marginal spectra on the range $6 < \omega < 80 \text{ year}^{-1}$ or $4.5 \sim 60$ days, between synoptic and intraseasonal scales. The corresponding scaling exponents $\xi(q)$ indicate the small scale multifractal nature of the river flow data analyzed here. The differences obtained using the structure functions approach and the frequency based HSA approach have been emphasized, which is especially clear for large order moments associated to the more active fluctuations. We have interpreted this difference as coming from the strong annual cycle which has more influence on structure functions scaling exponents than on the Hilbert-based approach. We have also compared the scaling exponents estimated from the ESS method, for the Seine river and Wimereux river; the much smaller exponents obtained for the Wimereux river express a higher degree of multifractality, which was interpreted as coming from the inertia associated to the large scale basin for the Seine river, whereas small rivers such as the Wimereux river may be more sensitive to local precipitation events.

2563

2564

2565

2566

2567

2568

2569

2570

2571

2572

2573

2574

2575

2576

2577

Several previous studies have considered scaling properties of river flows using other methods such as rescaled range analysis, trace moments, double trace moments, wavelet analysis, multifractal detrended fluctuation analysis (MFDA). We applied here a new method which gives results similar to the classical methods (structure functions, wavelet analysis, MFDA) for fractional Brownian motion or pure multifractal processes (Huang *et al.*, 2009a), see also chapter 3. However, we have shown in the same chapter that strong deterministic forcing had important influence on classical methods, whereas the Hilbert-based approach was much more stable and presented

2578

2579

2580

2581

2582

2583

2584

2585

2586 less influence (Huang *et al.*, 2009d,a), see also chapter 3. This method seems hence
2587 more appropriate for environmental time series that possess often strong periodic
2588 components superposed to scaling regimes. The origin of this stability property is
2589 the adaptative and local approach which is at the heart of the Hilbert-based method.

2590 We have compared here two rivers of very different size and catchment basin in
2591 order to compare their scaling properties. One of the objectives of scaling analy-
2592 ses of river flow time series is indeed to detect some differences among rivers, but
2593 also to evaluate some universality, i.e. some general similarity in statistical proper-
2594 ties. This was done for normalized pdfs (Dahlstedt & Jensen, 2005), for river flow
2595 volatilities (Livina *et al.*, 2003b,a), and for scaling regimes (Tessier *et al.*, 1996) or
2596 multifractal parameters (Pandey *et al.*, 1998). We hope that the method presented
2597 in this paper, which we claim to be well adapted to environmental time series, will
2598 help this quest for universal properties of river flow scaling statistics.

2599 Chapter 10

2600 Marine Turbulence in the Surf 2601 Zone

2602 One of the main properties of fully developed turbulence is its inertial range intermit-
2603 tent properties, between a large-scale injection of energy and a small-scale dissipa-
2604 tion (Frisch, 1995; Pope, 2000). In the surf zone, when waves break, the wave energy
2605 is transferred into turbulent motions through a violent, highly energetic process asso-
2606 ciated with breaking wave times scales, typically a few seconds, and then turbulence
2607 is dissipated at smaller scales (Svendsen, 1987; Battjes, 1988; Svendsen, 2005). The
2608 surf zone environment is a complex system: there are water turbulent motion at
2609 different scales, breaking waves feeding turbulence at the surface, and residual tur-
2610 bulence persisting from one wave to the next (Svendsen, 1987; Jaffe & Rubin, 1996).
2611 This highly energetic system has a strong effect on sediment transport dynamics,
2612 morphological changes associated with it, and shoreline evolution processes (Jaffe &
2613 Rubin, 1996; Cox *et al.*, 1996; Trowbridge & Elgar, 2001; Masselink & Russell, 2006;
2614 Torres-Freyermuth *et al.*, 2007), and also on ecological processes through influences

on feeding, settlement, fertilization, bloom dynamics, etc. (Denny & Shibata, 1989; Du Preez *et al.*, 1990; Mead & Denny, 1995).

In the intertidal zone, transport models for either sediments or living organisms need the description of surf zone velocity fluctuations. It is then important in this context to be able to characterize these velocity fluctuations for a wide range of scales, including highly energetic breaking waves scales and smaller turbulent scales. This is not an easy task because of the unsteadiness of breaking waves: phase-average methods are not straightforward since the wave forcing is not monochromatic; ocean breaking waves are nonlinear and present random components.

We use here for this the Empirical Mode Decomposition method and the Hilbert spectral analysis. It has already been applied to nonstationary ocean wave data (Hwang *et al.*, 2003; Veltcheva & Soares, 2004), but these studies focus on deep water ocean waves, which are different from surf zone breaking waves. Here we consider experimental turbulent velocity time series recorded in the surf zone. The results presented in this chapter are published in Schmitt *et al.* (2009)[Schmitt, *et al. J. Mar. Sys.*, 77, 473-481, 2009.]

10.1 Characterization of intermittency using cumulants

Structure Functions and Cumulants

One of the characteristic features of fully developed turbulence is the intermittent nature of velocity fluctuations (Frisch, 1995). Intermittency provides corrections to Kolmogorov's scaling law (Kolmogorov, 1941a), which are now well established and

received considerable attention in the last twenty years. Let us recall how to quantify intermittency effects on scaling laws for Eulerian isotropic turbulence. Denoting $\Delta V_\ell = V(x + \ell) - V(x)$ the longitudinal increments of the Eulerian velocity field at a spatial scale ℓ , their fluctuations are characterized, in the inertial range, using the scale invariant moment function $\zeta(q)$

$$\langle |\Delta V_\ell|^q \rangle = A_q \ell^{\zeta(q)} \quad (10.1.1)$$

where $q > 0$ is the order of moment and A_q is a constant that may depend on q . Kolmogorov's initial proposal, for a non-intermittent constant dissipation, leads to $\zeta(q) = q/3$ (Kolmogorov, 1941a). For intermittent turbulence, $\zeta(q)$ is proportional to a cumulant generating function, and is nonlinear and concave; only the third order moment has no intermittency correction: $\zeta(3) = 1$. The accuracy of the scaling of Eq. (10.1.1) is usually tested for each order of moment, for various values of ℓ in log-log plot, using a least-square regression (Anselmet *et al.*, 1984). The values of $\zeta(q)$ which are then obtained may be compared and fitted to different multifractal models (among many studies, see She & Lévéque (1994); Chen & Cao (1995); Arneodo *et al.* (1996); Boratav (1997); Schertzer *et al.* (1997); van de Water & Herwijer (1999); Anselmet *et al.* (2001)). This way of estimating $\zeta(q)$ depends on the choice of the scaling range: one usually estimates $\zeta(q)$ for the range of scales where the exact relation $\zeta(3) = 1$ is verified, assuming that the scaling range is the same for each order of moment.

Here there is no large scaling range: we therefore consider another approach: instead of studying the scale dependence for each moment, we focus on the moment dependence using cumulants at a given scale. The cumulant approach has already been undertaken in the scaling turbulence framework in a few studies (see e.g. Delour *et al.* (2001); Eggers *et al.* (2001); Chevillard *et al.* (2005)), where the cumulants of

the cascade process (Eggers *et al.*, 2001) or a polynomial development of the cumulant generating function (Delour *et al.*, 2001; Chevillard *et al.*, 2005) have been considered; see also Ref. Venugopal *et al.* (2006) for an application to multifractal properties of rainfall.

Non Analytical Cumulant Generating Functions

We consider here a random variable X . The cumulant generating function of its generator $g = \log |X|$ is defined as (Gardiner, 2004)

$$\Psi(q) = \log \langle |X|^q \rangle \quad (10.1.2)$$

The function $\Psi(q)$ is also the second Laplace characteristic function of the generator: $\Psi(q) = \log \langle e^{qg} \rangle$. As a second characteristic function, it is convex (Feller, 1971), and can be developed using the cumulants

$$\Psi(q) = \sum_{p=1}^{\infty} c_p \frac{q^p}{p!} \quad (10.1.3)$$

where c_p is the p^{th} cumulant. Let us recall the expression for the first cumulant

$$c_1 = \langle g \rangle = \langle \log |X| \rangle \quad (10.1.4)$$

We also know that $c_2 = \langle g^2 \rangle - c_1^2$, and c_n depends on all moments $\langle g^p \rangle$ ($1 \leq p \leq n$). The theorem of Marcinkiewicz states that, if it exists, the development in Eq. (10.1.3) is either infinite, or if finite, of degree not higher than 2 (Gardiner, 2004). In fact, the development in Eq. (10.1.3) may not exist in case of non-analyticity of $\Psi(q)$. This is the case when g is a stable process whose second order moment (and hence second order cumulant) diverges (Feller, 1971; Taqqu & Samorodnisky, 1994). Stable random

2677 variables (sometimes also called “Lévy” in the physics literature) correspond to vari-
 2678 ables that have a domain of attraction and being stable under addition (Feller, 1971;
 2679 Taquu & Samorodnisky, 1994; Janicki & Weron, 1994). They have been introduced
 2680 in the 1930s by Paul Lévy and correspond to a generalisation of the Gaussian law.
 2681 The main parameter is the index α bounded between 0 and 2. The case $\alpha = 2$ corre-
 2682 sponds to the Gaussian law. Log-stable models for turbulent intermittency (Schertzer
 2683 & Lovejoy, 1987; Kida, 1991) correspond to a nonanalytic scaling moment function
 2684 (see also Schertzer *et al.* (1997)). In this case, we have instead of Eq. (10.1.3)

$$\Psi(q) = c_1 q + c_\alpha q^\alpha \quad (10.1.5)$$

2685 where $0 \leq \alpha \leq 2$ is the index of the stable process and c_α is the cumulant of order α .
 2686 When $\alpha = 2$ the generator is a Gaussian process and there are only two cumulants
 2687 in the development of Eq. (10.1.3). To check this model, we consider in the following
 2688 the function

$$\Phi(q) = \Psi(q) - c_1 q \quad (10.1.6)$$

2689 For a stable law, $\Phi(q)$ should be proportional to q^α ; we check this below in log-log
 2690 plot using experimental data, for a given time or frequency scale.

2691 Concerning the choice of the random variable w , we will compare the structure
 2692 function approach ($X = |\Delta V_\ell|$, where ℓ is the time scale) and the EMD-Hilbert
 2693 spectral analysis approach ($X = \mathcal{A}$, the moments being estimated from the pdf
 2694 $p(\mathcal{A}|\omega)$ for a given frequency value ω).

10.2 Presentation of the experimental database

2695

The data analyzed here have been recorded using an Acoustic Doppler Velocimeter (ADV) from Sontek/YSI, operating under autonomous operation conditions, at a 25 Hz sampling rate, and providing the 3D velocity vector averaged over a small volume of about 250 mm^3 at a 5 cm distance from the ADV probe, with an accuracy of 1% of the measured value. Measurements have been performed in the beach in front of the research laboratory for Littoral and Coastal Ecosystems (ELICO): Eastern English Channel at Wimereux city (North of France, near Boulogne-sur-mer): this is a flat sand beach with a megatidal regime that varies between 8 to 11 m (see Fig. 10.1). A heavy metallic structure has been built in the laboratory ELICO as a support for the ADV, its electronics canister, and its battery canister (see Fig. 10.2). The measurement location is the intertidal zone in the beach, corresponding to the surf zone. The Eastern English Channel is a megatidal sea with strong currents. The metallic structure has been fixed to the ground using hooks; it was built in thin tubes to avoid a too strong stress on the structure from the tide and currents.

2709

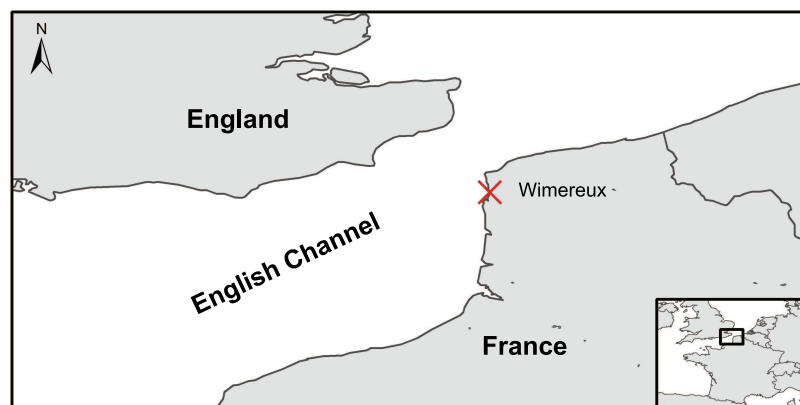


Figure 10.1: A map showing the location of the measurements, in the French coast of the Eastern English Channel (marked "X" in the map).



Figure 10.2: A photography of the ADV measuring device and its support, in the intertidal zone, before being submerged by the tide.

2710 The measurements have been done on 9 and 10 June, 2004, during 2 tidal cycles,
2711 at a height of 50 cm from the bottom. Measurements have been considered when
2712 there was approximately at least 1 m of water above the experimental device. Due to
2713 the tidal activity, this distance was between 1 to 3 m. We considered 27 m sections
2714 of the U component of the velocity vector, corresponding to the direction perpendic-
2715 ular to the shore, each of length 32,000 data points (each of 21 min duration). We
2716 cannot consider longer sections, since the internal programming of the ADV inter-
2717 rupts the continuous recording of data, to synchronise the different clocks. The 27
2718 sections have been chosen among the whole data set, in order to have a large enough
2719 internal correlation of bursts, corresponding to a precise enough estimation of the
2720 velocity. We have thus a total of 864,000 data points, separated into 27 sections.
2721 A one minute portion is shown in Fig. 10.3: strong fluctuations at small scales are
2722 visible, but the whole time series seems stationary. In the following we analyze the

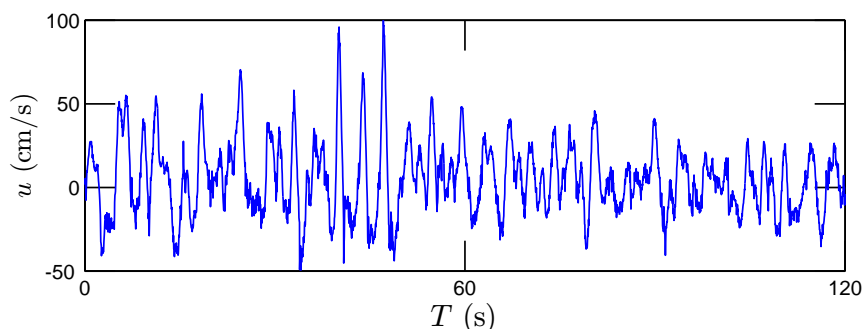


Figure 10.3: A two minutes portion of the experimental velocity data, showing their high variability at small scales.

data using the EMD method, the Hilbert-based amplitude-frequency method, and
cumulant generating functions.

10.3 EMD and HSA results

EMD Results

The analyses below are performed over the entire dataset, and the results displayed
after performing an ensemble average over 27 realizations, where each segment of
length 32,000 data points is one realization. After decomposition, the original ve-
locity series is decomposed into several IMFs (see Fig. 10.4), from 13 to 16 modes
(depending on the segment) with one residual. As visible in this figure, the time
scale is increasing with the mode; each mode has a different mean frequency, which
is estimated by considering the energy weighted mean frequency in the Fourier power
spectrum of each mode time series; the relation between mode number m and mean
time scale is displayed in Fig. 10.5. The straight line which is obtained in log-linear
plot suggests the following relation between the mean time scale T and m , for modes

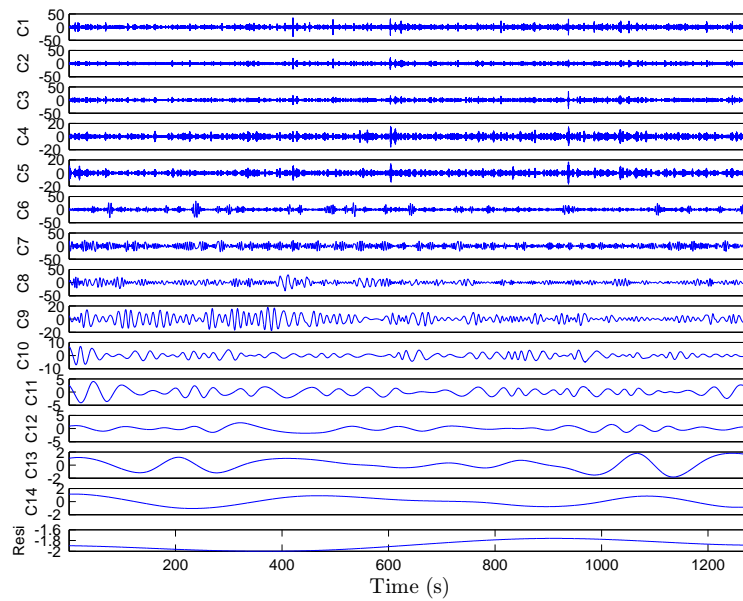


Figure 10.4: IMFs estimated from one 32,000 data points segment of the velocity time series: mode number increasing from top to below. The time scale is increasing with the mode. The residual time series is also plotted.

2737 between 4 and 13

$$T = T_0 e^{\lambda m} \quad (10.3.1)$$

2738 where $T_0 = 0.038$ is a constant and the coefficient $\lambda = 0.667$ is graphically estimated.
 2739 We remark that $e^\lambda = 1.94$ is close to 2, showing that each mode is associated with a
 2740 time scale almost twice as large as the time scale of the preceding mode; this property
 2741 corresponds to a dyadic filter bank in the time domain. This property was shown
 2742 previously using stochastic simulations of Gaussian noise and fractional Gaussian
 2743 noise (fGn) (Flandrin & Gonçalves, 2004; Wu & Huang, 2004), and also for fully
 2744 developed turbulence data (Huang *et al.*, 2008). It is interesting to note here that
 2745 this is still verified for surf zone turbulence data possessing a strong forcing in the
 2746 middle of the studied range.

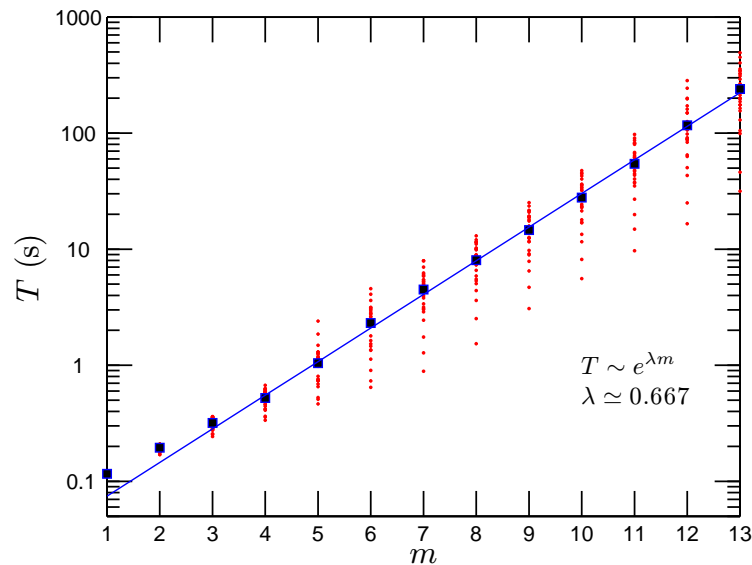


Figure 10.5: Mean time scales associated with each mode. There is an exponential increase for mode numbers between 4 and 13.

HSA Results

2747

Figure 10.6 represents the averaged Fourier power spectrum of the data, superposed 2748
with the Hilbert-Huang power spectrum. It is visible that the wind wave breaking 2749
scales (between 2 and 16 s) correspond to a strong forcing of the data. This power 2750
spectrum is similar to power spectra presented by Trowbridge & Elgar (2001) for surf 2751
zone turbulent data recorded in a sandy Atlantic beach near Duck, North Carolina. 2752
A $-5/3$ power spectrum can be found for large scales (minutes or larger) and scales 2753
smaller than 1 s could also be characterized by such spectrum: the range is too small 2754
to be affirmative on this last point. The Hilbert-Huang spectrum which is superposed 2755
presents a similar shape, despite its different mathematical definition for the frequency 2756
as well as for the spectrum. For the smaller scales, the shape is different, since the 2757
Hilbert-Huang power spectrum falls down very quickly. 2758

The EMD and Hilbert spectral analysis methodological frameworks provide a way 2759

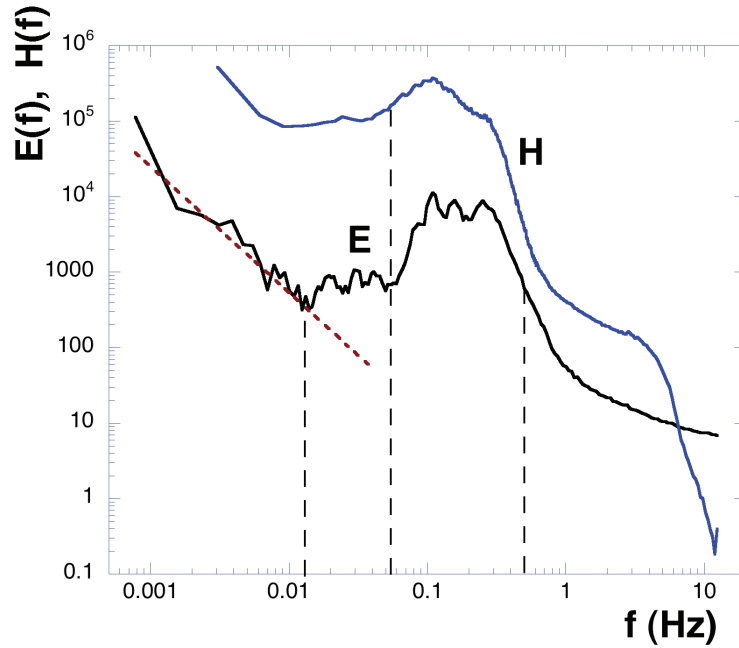


Figure 10.6: Fourier spectrum of the data ($E(f)$), superposed to the Hilbert marginal spectrum ($H(f)$). The latter has been vertically shifted for clarity. A strong wind wave breaking at scales between 2 and 16 s is clearly visible on both power spectra. It is interesting to notice that except for the smaller scales, they have the same shape, despite a different mathematical definition. The dotted straight line has a slope of $-5/3$.

2760 to represent the fluctuations in an amplitude-frequency space: the joint pdf $p(\omega, \mathcal{A})$
 2761 is shown in Fig. 10.7. It can be seen graphically that the amplitudes decrease with
 2762 increasing frequencies. This pdf can be used to estimate many statistical information
 2763 such as the Hilbert spectrum, and the cumulants as shown below. It can also be
 2764 used to estimate the skeleton $\mathcal{A}_s(\omega)$ which corresponds to the amplitude for which
 2765 the conditional pdf $p(\mathcal{A}|\omega)$ is maximum:

$$\mathcal{A}_s(\omega) = \mathcal{A}_0; p(\mathcal{A}_0, \omega) = \max_{\mathcal{A}} \{p(\mathcal{A}|\omega)\} \quad (10.3.2)$$

2766 and the skeleton pdf $p_{\max}(\omega) = p(\mathcal{A}_s(\omega), \omega) = \max_{\mathcal{A}} \{p(\mathcal{A}|\omega)\}$, which is shown in

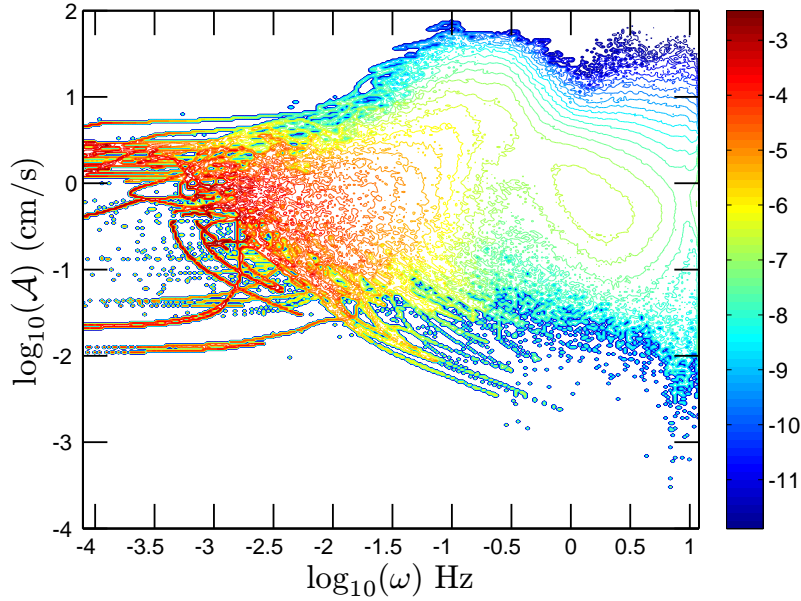


Figure 10.7: Representation of the joint pdf $p(\omega, \mathcal{A})$ (in log scale) of velocity fluctuations in an amplitude-frequency space.

Fig. 10.8. A power law behaviour is found :

2767

$$p_{\max}(\omega) \sim \omega^{-\beta_2} \quad (10.3.3)$$

where $\beta_2 \simeq 1.7$, close to the Kolmogorov value $5/3$. This new result corresponds to an experimental fact that needs further investigation in future studies.

2768

2769

10.4 Non analytic cumulant generating function

2770

We consider here the cumulant analysis applied to the velocity fluctuations, using the EMD and Hilbert spectral analysis described above, and compare this to the same analysis using structure functions.

2771

2772

2773

We first show the estimation of the first cumulant c_1 in Fig. 10.9. In this figure, the first cumulant is estimated as given by Eq. (10.1.4), using on the one hand, the

2774

2775

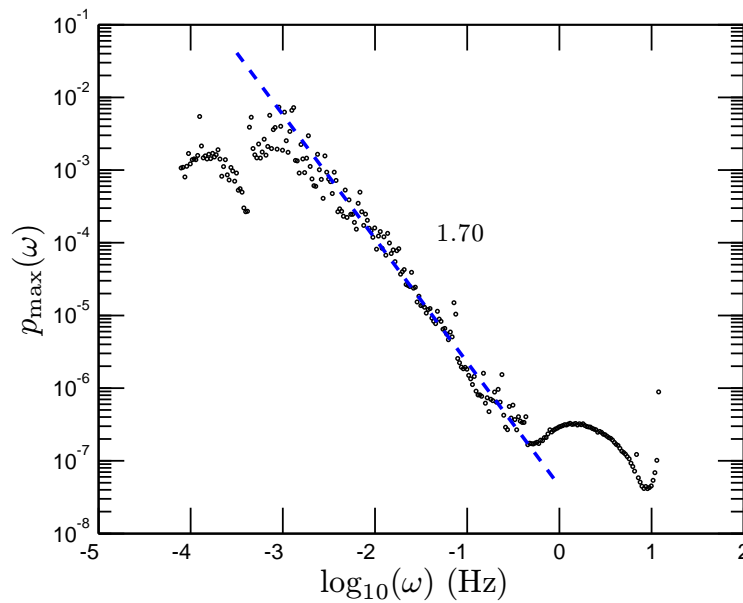


Figure 10.8: The skeleton of the joint pdf $p_{\max}(\omega)$ in log-log plot. A power law behaviour is observed in the inertial subrange with scaling exponent 1.70.

2776 amplitude-frequency pdf for a given value of ω , and taking the time scale $\ell = 1/\omega$
 2777 (denoted “HSA” on the figure). On the other hand, it is superposed to the estimate of
 2778 the first cumulants estimated for all modes separately, as function of scale, through
 2779 the correspondence given by Fig. 10.5 (denoted “EMD” in the figure). It is also
 2780 superposed to the first cumulants estimated using the structure function approach,
 2781 where the scale is the time increment: this value of c_1 has been vertically shifted
 2782 by 0.6 to be compared to the other curves. Figure 10.9 shows that c_1 increases
 2783 strongly for energetic scales associated with wave breaking, between 2 and 20 s. It
 2784 also shows that the EMD-based first cumulant is very close to the Hilbert spectral
 2785 analysis one (HSA). However the HSA approach is able to provide the first cumulant
 2786 on a continuous range, since it is based on a frequency estimation, whereas the EMD
 2787 curve is discrete in scale, being associated with the characteristic scale of each mode.

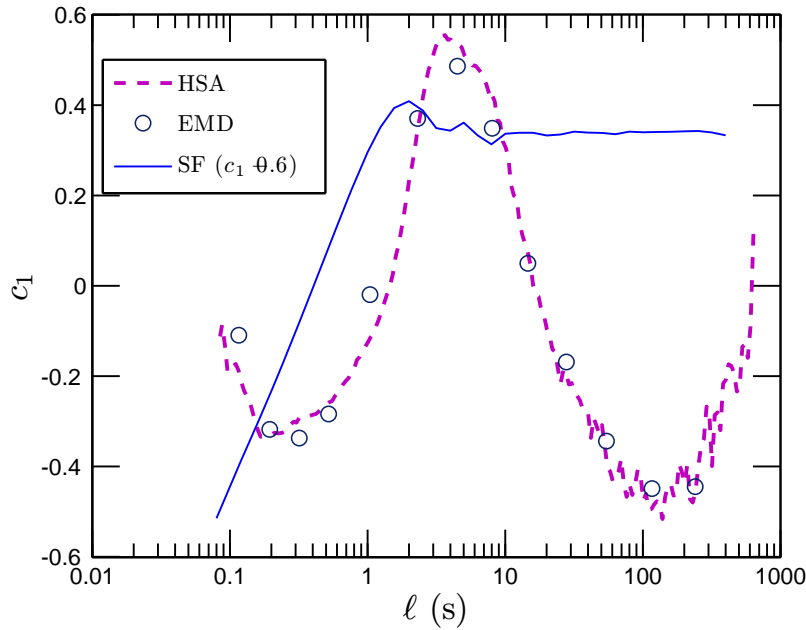


Figure 10.9: Estimation of the first cumulant c_1 , using three different methods: (i) estimation in frequency space using the joint amplitude-frequency pdf (dotted line denoted HSA); (ii) estimation using the empirical mode decomposition, done for each mode, where the time scale is estimated using the mode-scale correspondence (open dots, denoted EMD); and (iii) estimation using the structure

We also see from this figure that the first cumulant estimated using the structure 2788
function is quite far from the other estimates: the plateau obtained at large scales 2789
comes from the fact that the difference $V(t + \ell) - V(t)$ is not removing the forcing 2790
when the scale ℓ is larger than the forcing scale. This shows that for such data, the 2791
EMD and HSA methods provide a more reliable estimation of the first cumulant. 2792

The functions $\Phi(q)$ are then estimated, for moments from 0 to 8, for scales between 2793
1/25 s to 10 minutes. For comparison purposes, the analysis is done using the HSA 2794
approach in Eq. (3.1.3) and using the structure functions. An example is shown in 2795
Figures 10a-d, for fluctuations at the scale of 2 s. Figures 10a-b show the analyses 2796
using the HSA approach, in lin-lin and log-log plots, and Fig. 10.10 c-d show the same 2797

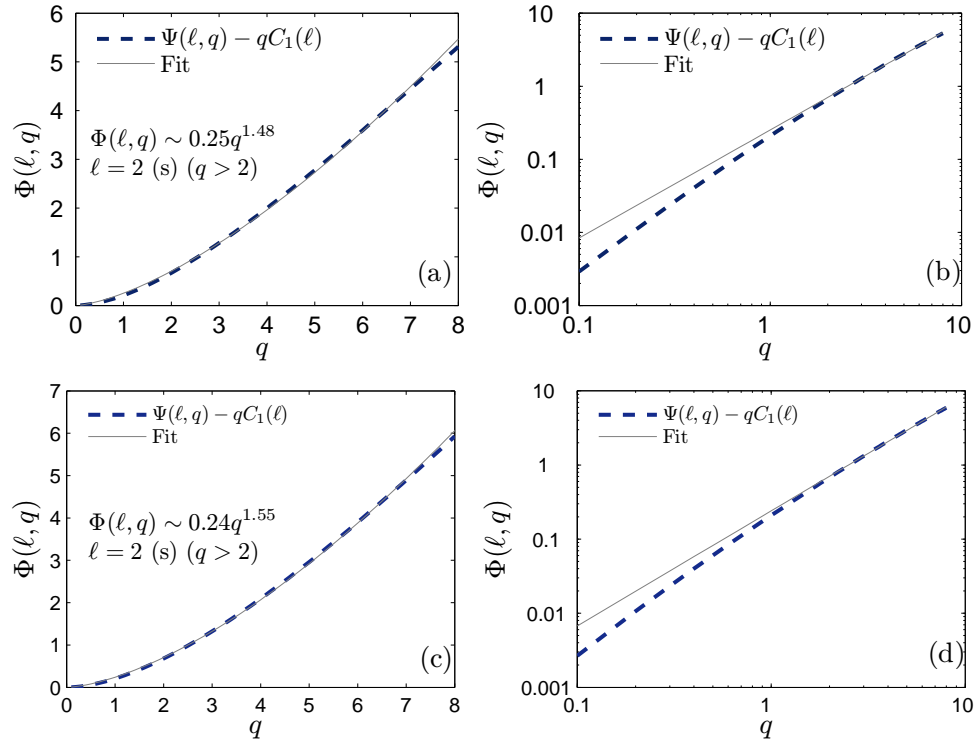


Figure 10.10: $\Phi(q)$ vs. q estimated for q between 0 and 8 for a scale $\ell = 2$ s, chosen here for illustration purpose. Experimental values are given by continuous lines whereas dotted lines correspond to power-law fits. The proportionalities of $\Phi_\ell(q)$ to q^α confirm the nonanalytic framework applied here. (a): lin-lin plot using HSA method; (b): log-log plot using HSA method; (c) lin-lin plot using the structure functions; (d) log-log plot using the structure functions.

2798 for the structure functions. Figures 10.10a and 10.10c show convex and increasing
 2799 functions. The non-analytical behaviour of these curves are emphasized in log-log
 2800 plots (Fig. 10.10 b and d). The straight lines which are obtained confirm the non-
 2801 analyticity. Using a best fit, the slopes of these straight lines are estimated for all
 2802 scales, giving directly the exponent α in Eq. (10.1.6). Figure 10.11 shows the values
 2803 of α estimated for different scales ℓ , for both the HSA and the structure function
 2804 methods. Except at both ends, the values are relatively independent of scale, and
 2805 we can estimate a mean value: we find $\alpha = 1.52 \pm 0.07$ for the HSA estimates

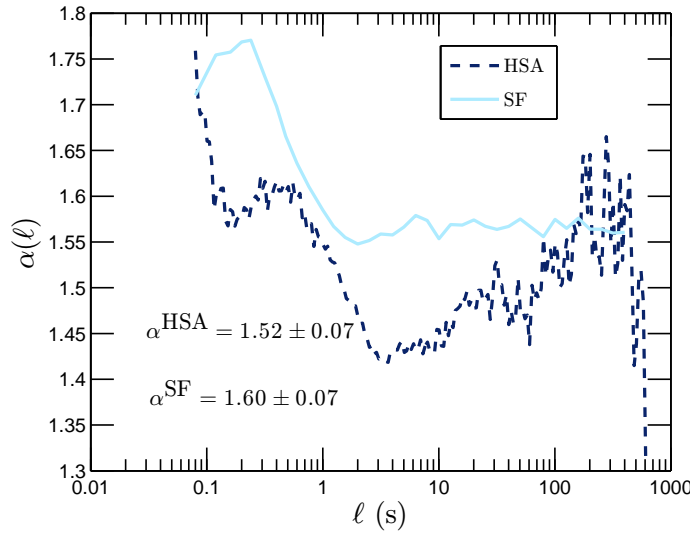


Figure 10.11: Values of α estimated for different scales ℓ : comparison between the HSA and structure functions methods.

and $\alpha = 1.60 \pm 0.07$ for the structure functions estimates, where error bars are 2806
 coming from different scales. These values are below 2 and approximately compatible 2807
 between the two methods. Figure 10.12 shows the non-analytical cumulant (it cannot 2808
 be denoted second cumulant) $c_\alpha(\ell)$ given by Eq. (10.1.5). The curves are different 2809
 for both methods, but their mean values are close. These results show that the log- 2810
 normal framework is not adequate, to be replaced by a log-Lévy stochastic modelling. 2811
 Simulations of such random variables can be performed using available stochastic 2812
 simulation algorithms (Janicki & Weron, 1994). 2813

10.5 Summary 2814

We have considered here surf zone velocity measurements recorded in the Eastern 2815
 English Channel using a 25 Hz sampling sonic anemometer. Such data is character- 2816
 ized by the transformation of wave motion into small-scale turbulent motion (Battjes, 2817

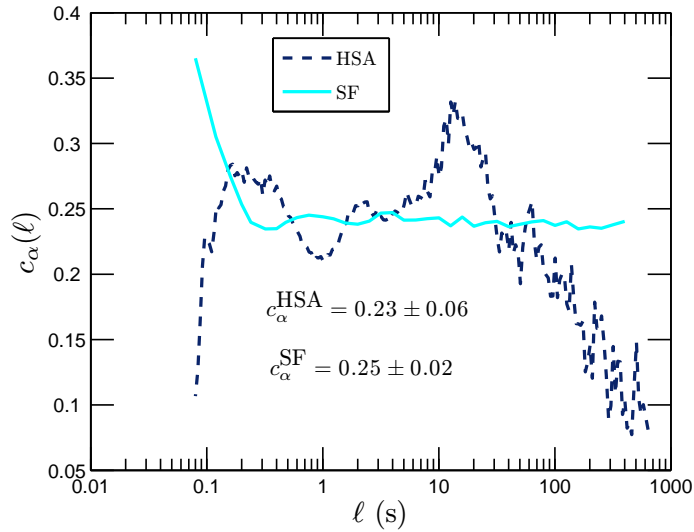


Figure 10.12: Values of $c_\alpha(\ell)$ estimated for different scales ℓ : comparison between the HSA and structure functions methods.

2818 1988). An important issue in this complex framework is to be able to characterize
 2819 the contribution of each scale to velocity fluctuations, since the modelling of sediment
 2820 and living organisms transport and suspension is associated with such velocity fluc-
 2821 tuations (Cox *et al.*, 1996; Svendsen, 2005; Torres-Freyermuth *et al.*, 2007). We have
 2822 analysed this series here using the EMD methodology, associated with Hilbert spec-
 2823 tral analysis. We have provided the mode versus time scale relationship, showing that
 2824 for such data base, the dyadic mode decomposition which has been found in Gaussian
 2825 noise is still valid. We have also provided the Fourier and Hilbert Huang marginal
 2826 spectrum, showing the high energy associated with wave breaking scales, between 2
 2827 and 20 s. In another section, we have analyzed the fluctuations at each scale using
 2828 cumulants. The cumulants could be estimated on a continuous range of scales using
 2829 the joint amplitude-frequency pdf of velocity fluctuations that was estimated using
 2830 the EMD-HSA framework. The non-analytical properties of cumulants was shown for

each scale, for both methods. We showed, using the first cumulant, that the structure 2831
function approach saturates at large scales, whereas the HSA based method is more 2832
precise in its scale approach; this therefore shows the strength and usefulness of this 2833
new EMD-HSA method combined to cumulant analysis. It was shown here to be 2834
efficient for surf zone velocity analysis, but could be also applied to other time series. 2835

Let us note that our approach has considered the time series globally, while the 2836
depth of the water varied between 1 and 3 meters. It may be that some statistical 2837
properties depend on the depth of the water, requesting a more precise analysis, 2838
considering separately different sections of the time series. We have checked that 2839
this is indeed the case (not shown here), considering the power spectra; however, 2840
the shape of the latter did not vary much. We then keep for future studies a more 2841
precise analysis of the depth relation, noting here that the results we obtained must 2842
be considered as a mean value for different depths between 1 and 3 meters. 2843

We have shown that the log-stable model applies very well, with a characteristic 2844
exponent of $\alpha = 1.60 \pm 0.07$ valid for all scales. This property may be used for 2845
stochastic simulations. Such modelling in the surf zone may be useful for several 2846
applications, such as plankton-turbulence coupling, energetics studies associated with 2847
bloom formation, to fertilization processes, or feeding rate of small fishes, or also 2848
sediment transport characterization and modelling. 2849

2850

Part IV

2851

Conclusion and Discussion

2852 **Discussion and Conclusion**

2853 In this chapter, we summarize the main results and conclusions of this thesis. We
2854 provide also some comments on these results.

2855 **Main Results**

2856 The Hilbert-Huang transform is a scale dependent decomposition method with very
2857 local ability in both physical and spectral domains. The method, we proposed here,
2858 arbitrary order Hilbert spectral analysis, is an extended version of the HHT devoted
2859 to take into account intermittency in a scaling framework. It inherits all the advan-
2860 tages and shortcomings of the HHT. The main advantages of the present methodology
2861 are the very local abilities both in physical and spectral domains, and the fully adap-
2862 tiveness. The main drawback is its lack of rigorous mathematical foundation.

2863 **Arbitrary Order Hilbert Spectral Analysis**

2864 We validated the idea of the arbitrary order Hilbert spectral analysis by using a
2865 simulated fractional Brownian motion time series and synthesized multifractal time
2866 series. We found that the Hilbert-based approach provides a more precise estimator
2867 of the scaling exponents than the classical structure function. We also found a general
2868 property of the zeroth order Hilbert marginal spectrum $\mathcal{L}_0(\omega)$, the marginal probabil-
2869 ity density function (pdf) of the instantaneous frequency ω , with a scaling exponent

$\xi(0) \simeq 1$. This implies that not only the amplitude has a distribution law, but also the scale (instantaneous frequency) itself has a distribution law. However, we still need more theoretical work to fully understand the empirical mode decomposition, the first step of the present methodology, and the arbitrary order Hilbert spectral analysis.

Structure Function and Autocorrelation Function of Velocity Increments

We investigated the structure function and the autocorrelation function of the velocity increments time series $\Delta u_\ell(t)$. Based on statistical stationarity assumption, we proposed an analytical model for them. By a definition of a cumulative function, we found that the structure function is strongly influenced by the large scales. We also shown experimentally that it is also strongly influenced by a single scale (or large scale deterministic forcing). We proved analytically that the autocorrelation function of the velocity increments has its minima value at the separation scale ℓ . A power law relation is also suggested by our analytical model. The power law is then verified by fractional Brownian motion and confirmed by the turbulent database.

Experimental Homogeneous and isotropy Turbulent Database

We applied the empirical mode decomposition and arbitrary order Hilbert spectral analysis to an experimental homogeneous and isotropy turbulent database. We found that the EMD algorithm acts a dyadic filter bank. We observed a scaling trend on the joint pdf of the velocity fluctuations with the scaling exponent quite close to the Kolmogorov value. We recovered the structure function scaling exponent in an amplitude-frequency space for the first time. We then tested the isotropy ratio in Hilbert frame. It is found that the generalized isotropy ratio decreases linearly with

2893 q .

2894 **Passive Scalar**

2895 We applied the empirical mode decomposition and arbitrary order Hilbert spectral
2896 analysis to a passive scalar (temperature). Due to the strong ramp-cliff structures,
2897 the classical structure function fails. The Hilbert-based approach provides a scaling
2898 exponent $\xi_{\Theta}(q) - 1$ quite close to the scaling exponent $\zeta(q)$ of the fully developed
2899 turbulent velocity field. It indicates that the scalar field may be not so intermittent
2900 as what we believed before. However, more passive database should be investigated
2901 under the present Hilbert framework to confirm the role of the ramp-cliff structures.

2902 **Extended Self-Similarity and Hierarchical Model**

2903 We generalized the traditional extended self-similarity into Hilbert frame. In the
2904 present framework, according to the Kolmogorov 1962 theory, we have two special
2905 case $q = 0$ and $q = 3$, which are not influenced by the intermittent effect. We
2906 therefore proposed two ESS formula by plotting the arbitrary order Hilbert spectra
2907 $\mathcal{L}_q(\omega)$ against $\mathcal{L}_p(\omega)$, where $p = 0$ or $p = 3$. It is found experimentally that both
2908 of them provide the same scaling exponents. We then define a hierarchical spectral
2909 function $\mathcal{L}^q(\omega)$ by considering the ratio of two successive arbitrary order Hilbert
2910 spectra $\mathcal{L}_p(\omega)$. The scaling exponents $\Pi(q)$ of the hierarchical functions decrease
2911 linearly with q .

2912 **River Flow Discharge**

2913 We applied the Hilbert-based methodology to the daily river flow discharges of the
2914 Seine river and Wimereux river. Both rivers are controlled by the marine west coast
2915 climate of Northern France. After EMD decomposition, the original time series are

separated into several IMF modes. We observed large correlation among the large 2916
scale IMF modes. We found the same evolution trend for the annual cycles and 2917
the reconstructed large scale between the Seine river and Wimereux river. We then 2918
characterized the small scale intermittent property in the Hilbert frame. Due to the 2919
effect of the strong annual cycle, the structure functions fail. 2920

Surf Zone Marine Turbulence 2921

We analyzed a surf zone marine turbulence time series. We characterized the scale 2922
invariant properties by considering the nonanalytical cumulant analysis. The log- 2923
stable model provides a characteristic exponent of $\alpha = 1.6 \pm 0.07$ for all scales. These 2924
results may provide a new approach to separate waves from small scale turbulent 2925
motions. 2926

Future studies 2927

The results we shown in this thesis may be useful for modelling, which we do not 2928
consider here. However, it should be done in future studies. We list here some topics 2929
we may consider in future studies. 2930

1. Skeleton of the joint pdf $p(\omega, \mathcal{A})$ 2931

We found experimentally a skeleton of the joint pdf with a scaling behaviour. 2932
However, the exactly physical/mathematical meaning of this skeleton is not 2933
understood. We need more experimental and theoretical work on this topic to 2934
provide more understanding of the scaling property of the skeleton. 2935

2. Zeroth order Hilbert marginal spectrum $\mathcal{L}_0(\omega)$ 2936

The corresponding scaling exponent $\xi(0)$ of the zeroth order Hilbert marginal 2937

2938 spectrum is found to be approximately equal to 1. The mathematical mean-
2939 ing of the zeroth order Hilbert marginal spectrum is the marginal pdf of the
2940 instantaneous frequency. It seems that it is a general property of the present
2941 methodology. It implies that not only the amplitude, but also the scale (in-
2942 stantaneous frequency) has a distribution law. But what is the exactly physical
2943 meaning of this $\xi(0) = 1$ scaling exponent?

2944 3. Kolmogorov 4/5 law

2945 The famous Kolmogorov 4/5 law for the third order structure function is an
2946 exact statistical solution of the Navier-Stokes equations. Does it hold for the
2947 third order Hilbert marginal spectrum? The turbulent database we considered
2948 in this thesis has no resolution on Kolmogorov scale. Thus we did not check
2949 this topic in this thesis. It should be checked using other databases.

2950 4. Turbulence modelling

2951 We believe that the results presented in this thesis provide useful information
2952 for turbulence modelling. We will link our results with turbulence modelling in
2953 future studies. We need for this to be able to extend the present 1D to tensorial
2954 quantities.

2955 5. Passive scalar: ramp-cliff structure

2956 The ramp-cliff structure is an important signature of passive scalar turbulence.
2957 The structure functions, especially for high order moments, are strongly influ-
2958 enced by this large scale structure. Thus, we should check more passive scalar
2959 turbulence databases under the present framework in future studies.

2960 Appendix A

2961 List of Publications

2962 Publications before the Ph.D thesis or in other subjects

- 2963 1. **Y. Huang**, and Z. Lu. Application of Hilbert-Huang Transform in analy-
2964 sis of Duffing equation and wake flow over a cylinder. *Chinese Quarterly of*
2965 *Mechanics*, (in Chinese) 26(2), 2005.

- 2966 2. **Y. Huang**, Z. Lu, and Y. Liu. Analysis of an atmospheric turbulence data
2967 by Hilbert-Huang Transform. *Journal of Hydrodynamics*, (in Chinese) 21(3),
2968 2006.

- 2969 3. X. Qiu, **Y. Huang**, Z. Lu, and Y. Liu. Application of LIF and PIV in Ex-
2970 perimental Measurements of Stratified Turbulence. *Journal of Experiments in*
2971 *Fluid Mechanics*, (in Chinese) 22(2):1-9, 2008.

- 2972 4. X. Qiu, **Y. Huang**, Z. Lu, Y. Liu. Large eddy simulation of turbulent statistical
2973 and transport properties in stably stratified flows. *Applied Mathematics and*
2974 *Mechanics*, 30(2),153-162, 2009.

Publications directly with the Ph.D thesis

- 2975
1. F.G. Schmitt, **Y. Huang**, Z. Lu, S.B. Zongo, J.C. Molinero, and Y. Liu. Anal- 2976
 ysis of nonlinear biophysical time series in aquatic environments : scaling prop- 2977
 erties and empirical mode decomposition. *Nonlinear Dynamics in Geosciences*, 2978
 edited by A. Tsonis and J. Elsner, pp. 261-290, Springer, 2007. 2979
 2. **Y. Huang**, F.G. Schmitt, Z. Lu, and Y. Liu. An amplitude-frequency study 2980
 of turbulent scaling intermittency using Empirical Mode Decomposition and 2981
 Hilbert Spectral Analysis. *Europhysics Letters*, 84, 40010, 2008. 2982
 3. F.G. Schmitt, **Y. Huang**, Z. Lu, Y. Liu, and Nicolas Fernandez. Analysis of 2983
 velocity fluctuations and their intermittency properties in the surf zone using 2984
 empirical mode decomposition. *Journal of Marine System*, 77, 473-481, 2009. 2985
 4. **Y. Huang**, F.G. Schmitt, Z. Lu, and Y. Liu. Analysis of daily river flow 2986
 fluctuations using empirical mode decomposition and arbitrary order Hilbert 2987
 spectral analysis, *Journal of Hydrology*, 373, 103-111, 2009. 2988
 5. **Y. Huang**, F.G. Schmitt, Z. Lu, and Y. Liu. Autocorrelation function of ve- 2989
 locity increments in fully developed turbulence, *Europhysics Letters*,86, 40010, 2990
 2009. 2991
 6. **Y. Huang**, F.G. Schmitt, Z. Lu, and Y. Liu. Analyse de l'invariance d'échelle 2992
 de séries temporelles par la décomposition modale empirique et l'analyse spec- 2993
 trale de Hilbert . *Traitement du Signal*, (in French) 25, 481-492, 2008. 2994
 7. **Y. Huang**, F.G. Schmitt, Z. Lu, and Y. Liu. Arbitrary order Hilbert spectral 2995
 analysis for time series possessing scaling statistic: definition and validation, 2996

2997 *Physical Review E*, 2009 (submitted).

2998 8. **Y. Huang**, F.G. Schmitt, Z. Lu, and Y. Liu. Second order structure function
2999 in fully developed turbulence, *Physical Review Letters*, 2009 (in preparation).

3000 Bibliography

- 3001 Abry, P., & Sellan, F. 1996. The Wavelet-Based Synthesis for Fractional Brownian
3002 Motion Proposed by F. Sellan and Y. Meyer: Remarks and Fast Implementation.
3003 *Appl. Comput. Harmon. Anal.*, **3**(4), 377–383.
- 3004 Aji, V., & Goldenfeld, N. 2001. Fluctuations in Finite Critical and Turbulent Systems.
3005 *Phys. Rev. Lett.*, **86**(6), 1007–1010.
- 3006 Anselmet, F., Gagne, Y., Hopfinger, E. J., & Antonia, R. A. 1984. High-order velocity
3007 structure functions in turbulent shear flows. *J. Fluid Mech.*, **140**, 63–89.
- 3008 Anselmet, F., Antonia, R. A., & Danaila, L. 2001. Turbulent flows and intermittency
3009 in laboratory experiments. *Plan. Space Sci.*, **49**(12), 1177–1191.
- 3010 Antonia, RA, Hopfinger, EJ, Gagne, Y., & Anselmet, F. 1984. Temperature structure
3011 functions in turbulent shear flows. *Phys. Rev. A*, **30**(5), 2704–2707.
- 3012 Antonia, RA, Ould-Rouis, M., Zhu, Y., & Anselmet, F. 1997. Fourth-order moments
3013 of longitudinal-and transverse-velocity structure functions. *Europhys. Lett.*, **37**(2),
3014 85–90.
- 3015 Arneodo, A., Baudet, C., Belin, F., Benzi, R., Castaing, B., Chabaud, B., Chavarria,
3016 R., Ciliberto, S., Camussi, R., & Chilla, F. 1996. Structure functions in turbulence,
3017 in various flow configurations, at Reynolds number between 30 and 5000, using
3018 extended self-similarity. *Europhys. Lett.*, **34**(6), 411–416.

- Bacry, E., Delour, J., & Muzy, JF. 2001. Multifractal random walk. *Phys. Rev. E*, **64**(2). 3019
3020
- Balocchi, R., Menicucci, D., Santarcangelo, E., Sebastiani, L., Gemignani, A., Ghelarducci, B., & Varanini, M. 2004. Deriving the respiratory sinus arrhythmia from the heartbeat time series using empirical mode decomposition. *Chaos Soliton Fract.*, **20**(1), 171–177. 3021
3022
3023
3024
- Batchelor, GK, & Townsend, AA. 1949. The nature of turbulent motion at large wave-numbers. *Proc. R. Soc. London, Ser. A*, 238–255. 3025
3026
- Battjes, J. A. 1988. Surf Zone Dynamics. *Annu. Rev. Fluid Mech.*, **20**(1), 257–291. 3027
- Benzi, R., Paladin, G., Vulpiani, A., & Parisi, G. 1984. On the multifractal nature of fully developed turbulence and chaotic systems. *J. Phys. A*, **17**, 3521–3531. 3028
3029
- Benzi, R., Ciliberto, S., Baudet, C., Chavarria, G.R., & Tripicciono, R. 1993a. Extended self-similarity in the dissipation range of fully developed turbulence. *Europhys. Lett*, **24**(4), 275–279. 3030
3031
3032
- Benzi, R., Ciliberto, S., Tripicciono, R., Baudet, C., Massaioli, F., & Succi, S. 1993b. Extended self-similarity in turbulent flows. *Phys. Rev. E*, **48**(1), 29–32. 3033
3034
- Benzi, R., Ciliberto, S., Baudet, C., & Chavarria, GR. 1995. On the scaling of three-dimensional homogeneous and isotropic turbulence. *Physica D*, **80**(4), 385–398. 3035
3036
- Benzi, R., Biferale, L., Ciliberto, S., Struglia, MV, & Tripicciono, R. 1996. Generalized scaling in fully developed turbulence. *Physica D*, **96**(1-4), 162–181. 3037
3038
- Beran, J. 1994. *Statistics for Long-Memory Processes*. CRC Press. 3039
- Biagini, F., Hu, Y., Oksendal, B., & Zhang, T. 2008. *Stochastic calculus for fractional Brownian motion and applications*. Springer Verlag. 3040
3041

- 3042 Bohr, T., Jensen, MH, Paladin, G., & Vulpiani, A. 1998. Dynamical systems approach
3043 to turbulence.
- 3044 Bolzan, MJA, Rosa, RR, & Sahai, Y. 2009. Multifractal analysis of low-latitude
3045 geomagnetic fluctuations. *Ann. Geophys*, **27**, 569–576.
- 3046 Boratav, O. N. 1997. On recent intermittency models of turbulence. *Phys. Fluids*, **9**,
3047 1206.
- 3048 Calvet, L., & Fisher, A. 2002. Multifractality in asset returns: theory and evidence.
3049 *Rev. Econ. Statist.*, **84**(3), 381–406.
- 3050 Cassou, C. 2008. Intraseasonal interaction between the Madden–Julian Oscillation
3051 and the North Atlantic Oscillation. *Nature*, **455**(7212), 523–527.
- 3052 Celani, A., Lanotte, A., Mazzino, A., & M., Vergassola. 2000. Universality and
3053 Saturation of Intermittency in Passive Scalar Turbulence. *Phys. Rev. Lett.*, **84**,
3054 2385–2388.
- 3055 Celani, A., Cencini, M., Vergassola, M., Villermaux, E., & Vincenzi, D. 2005. Shear
3056 effects on passive scalar spectra. *J. Fluid Mech.*, **523**, 99–108.
- 3057 Chen, J., Xu, Y. L., & Zhang, R. C. 2004. Modal parameter identification of Tsing
3058 Ma suspension bridge under Typhoon Victor: EMD-HT method. *J. Wind Eng.*
3059 *Ind. Aerodyn.*, **92**(10), 805–827.
- 3060 Chen, S., & Cao, N. 1995. Inertial range scaling in turbulence. *Phys. Rev. E*, **52**(6),
3061 5757–5759.
- 3062 Chevillard, L., Roux, SG, Lévêque, E., Mordant, N., Pinton, J. F., & Arnéodo, A.
3063 2005. Intermittency of Velocity Time Increments in Turbulence. *Phys. Rev. Lett.*,
3064 **95**(6), 64501.
- 3065 Cohen, L. 1995. *Time-frequency analysis*. Prentice Hall PTR Englewood Cliffs, NJ.

- Comte-Bellot, G., & Corrsin, S. 1966. The use of a contraction to improve the isotropy of grid-generated turbulence. *J. Fluid. Mech.*, **25**(04), 657–682. 3066
3067
- Comte-Bellot, G., & Corrsin, S. 1971. Simple Eulerian time correlation of full-and narrow-band velocity signals in grid-generated, ‘isotropic’ turbulence. *J. Fluid. Mech.*, **48**(02), 273–337. 3068
3069
3070
- Corrsin, S. 1951. On the spectrum of isotropic temperature fluctuations in an isotropic turbulence. *J. Appl. Phys.*, **22**, 469. 3071
3072
- Coughlin, K. T., & Tung, K. K. 2004. 11-Year solar cycle in the stratosphere extracted by the empirical mode decomposition method. *Adv. Space Res.*, **34**(2), 323–329. 3073
3074
- Cox, D.T., Kobayashi, N., & Okayasu, A. 1996. Bottom shear stress in the surf zone. *J. Geophys. Res.*, **101**(C6), 14337–14348. 3075
3076
- Dahlstedt, K., & Jensen, H.J. 2005. Fluctuation spectrum and size scaling of river flow and level. *Physica A*, **348**, 596–610. 3077
3078
- Daubechies, I. 1992. *Ten lectures on wavelets*. 3079
- Dauvin, J. C. 2007. Paradox of estuarine quality: Benthic indicators and indices, consensus or debate for the future. *Mar. Pollut. Bull.*, **55**(1-6), 271–281. 3080
3081
- De Lima, M., & Grasman, J. 1999. Multifractal analysis of 15-min and daily rainfall from a semi-arid region in Portugal. *J. Hydrol.*, **220**(1-2), 1–11. 3082
3083
- Delour, J., Muzy, JF, & Arnéodo, A. 2001. Intermittency of 1D velocity spatial profiles in turbulence: a magnitude cumulant analysis. *Eur. Phys. J. B*, **23**(2), 243–248. 3084
3085
3086
- Denny, M. W., & Shibata, M. F. 1989. Consequences of Surf-Zone Turbulence for Settlement and External Fertilization. *Am. Nat.*, **134**(6), 859–889. 3087
3088

- 3089 Doukhan, P., Taqqu, M.S., & Oppenheim, G. 2003. *Theory and Applications of*
3090 *Long-Range Dependence*. Birkhauser.
- 3091 Du Preez, H. H., McLachlan, A., Marais, J. F. K., & Cockcroft, A. C. 1990. Bioen-
3092 ergetics of fishes in a high-energy surf-zone. *Mar. Biol.*, **106**(1), 1–12.
- 3093 Dubrulle, B. 1994. Intermittency in fully developed turbulence: Log-Poisson statistics
3094 and generalized scale covariance. *Phys. Rev. Lett.*, **73**(7), 959–962.
- 3095 Dur, G., Schmitt, F. G., & Souissi, S. 2007. Analysis of high frequency tempera-
3096 ture time series in the Seine estuary from the Marel autonomous monitoring buoy.
3097 *Hydrobiologia*, **588**, 5968.
- 3098 Echeverria, J. C., Crowe, J. A., Woolfson, M. S., & Hayes-Gill, B. R. 2001. Application
3099 of empirical mode decomposition to heart rate variability analysis. *Med. Biol. Eng.*
3100 *Comput.*, **39**(4), 471–479.
- 3101 Eggers, H. C., Dziekan, T., & Greiner, M. 2001. Translationally invariant cumulants
3102 in energy cascade models of turbulence. *Phys. Lett. A*, **281**, 249–255.
- 3103 Feller, W. 1971. *An introduction to probability theory and its applications*. New York:
3104 Wiley.
- 3105 Feynman, R.P. 1964. *The Feynman lectures on physics*. Vol. 6. by Leighton, R.B.
3106 and Sands, M., Addison-Wesley, Redwood City.
- 3107 Flandrin, P. 1992. Wavelet analysis and synthesis of fractional Brownian motion.
3108 *IEEE Trans. Inf. Theory*, **38**(2 Part 2), 910–917.
- 3109 Flandrin, P. 1998. *Time-frequency/time-scale analysis*. Academic Press.
- 3110 Flandrin, P., & Gonçalves, P. 2004. Empirical Mode Decompositions as Data-Driven
3111 Wavelet-Like Expansions. *Int. J. Wavelets, Multires. Info. Proc.*, **2**(4), 477–496.

- Flandrin, P., Rilling, G., & Gonçalvès, P. 2004. Empirical mode decomposition as a filter bank. *IEEE Sig. Proc. Lett.*, **11**(2), 112–114.
- Frisch, U. 1995. *Turbulence: the legacy of AN Kolmogorov*. Cambridge University Press.
- Frisch, U., Sulem, P.L., & Nelkin, M. 1978. A simple dynamical model of intermittently developed turbulence. *J. Fluid Mech.*, **87**(04), 719–736.
- Gardiner, C. W. 2004. *Handbook of Stochastic Methods*. Springer, Berlin, third edition.
- Ghashghaie, S., & Dodge, Y. 1996. Turbulent cascades in foreign exchange markets. *Nature*, **381**, 27.
- Grant, HL, Stewart, RW, & Moilliet, A. 1962. Turbulence spectra from a tidal channel. *J. Fluid. Mech.*, **12**(02), 241–268.
- Grassberger, P. 1986. Estimating the fractal dimensions and entropies of strange attractors. *Chaos*, 291.
- Grassberger, P., & Procaccia, I. 1983. Generalized dimensions of strange attractors. *Phy. Rev. Lett.*, **50**(6), 346.
- Gurvich, AS, & Zubkovskii, SL. 1963. Experimental estimate of fluctuations in the turbulent energy dissipation. *Izv. Akad. Nauk SSSR, Ser. Geofiz*, **12**, 1856–1858.
- Gylfason, A., & Warhaft, Z. 2004. On higher order passive scalar structure functions in grid turbulence. *Phys. Fluids*, **16**, 4012.
- Halsey, T.C., Jensen, M.H., Kadanoff, L.P., Procaccia, I., & Shraiman, B.I. 1986. Fractal measures and their singularities: the characterization of strange sets. *Phys. Rev. A*, **33**(2), 1141–1151.

- 3135 Hentschel, HGE, & Procaccia, I. 1983. The infinite number of generalized dimensions
3136 of fractals and strange attractors. *Physica. D*, **8**(3), 435–444.
- 3137 Hou, T.Y., Wu, X.H., Chen, S., & Zhou, Y. 1998. Effect of finite computational
3138 domain on turbulence scaling law in both physical and spectral spaces. *Phys. Rev.*
3139 *E*, **58**(5), 5841–5844.
- 3140 Huang, N. E. 2005. *Hilbert-Huang Transform and Its Applications*. World Scientific.
3141 Chap. 1. Introduction to the Hilbert-Huang transform and its related mathematical
3142 problems, pages 1–26.
- 3143 Huang, N. E., Shen, Z., Long, S. R., Wu, M. C., Shih, H. H., Zheng, Q., Yen, N.C.,
3144 Tung, C. C., & Liu, H. H. 1998. The empirical mode decomposition and the
3145 Hilbert spectrum for nonlinear and non-stationary time series analysis. *Proc. R.*
3146 *Soc. London, Ser. A*, **454**(1971), 903–995.
- 3147 Huang, N. E., Shen, Z., Long, S. R., *et al.* 1999. A new view of nonlinear water waves:
3148 The Hilbert Spectrum . *Annu. Rev. Fluid Mech.*, **31**(1), 417–457.
- 3149 Huang, N. E., Wu, M. L., Long, S. R., Shen, S. S. P., Qu, W., Gloersen, P., & Fan,
3150 K. L/. 2003a. A confidence limit for the empirical mode decomposition and Hilbert
3151 spectral analysis. *Proc. R. Soc. London, Ser. A*, **459**(2037), 2317–2345.
- 3152 Huang, N. E., Wu, M. L., Qu, W., Long, S. R., & Shen, S. S. P. 2003b. Applications
3153 of Hilbert-Huang transform to non-stationary financial time series analysis. *Appl.*
3154 *Stoch. Model Bus.*, **19**(3), 245–268.
- 3155 Huang, Y., Schmitt, F. G., Lu, Z., & Liu, Y. 2009a. Analyse de l’invariance d’échelle
3156 de séries temporelles par la décomposition modale empirique et l’analyse spectrale
3157 de Hilbert. *Traitement du Signal*, **25**, 481-492.

- Huang, Y., Schmitt, F. G., Lu, Z., & Liu, Y. 2009b. Analysis of Daily River Flow
Fluctuations Using Empirical Mode Decomposition and Arbitrary Order Hilbert
Spectral Analysis. *J. Hydrol.*, **373**, 103-111.
- Huang, Y., Schmitt, F. G., Lu, Z., & Liu, Y. 2009c. Autocorrelation function of
velocity increments in fully developed turbulence. *Europhys. Lett.* **86**, 40010, 2009.
- Huang, Y., Schmitt, F. G., Lu, Z., & Liu, Y. 2009d. Arbitrary order Hilbert spectral
analysis for time series possessing scaling statistics: definition and validation. *Phys.*
Rev. E (submitted).
- Huang, Y., Schmitt, F. G., Lu, Z., & Liu, Y. 2009e. Second order structure function
in fully developed turbulence. *Phys. Rev. Lett. (to be submitted)*.
- Huang, Y., Schmitt, F. G., Lu, Z., & Liu, Y. 2008. An amplitude-frequency study
of turbulent scaling intermittency using Hilbert spectral analysis. *Europhys. Lett.*,
84, 40010.
- Hurst, H. E. 1951. Long-term Storage Capacity of Reservoirs. *Trans. Am. Soc. Civ.*
Eng., **116**, 770–808.
- Hurst, H.E., Black, RP, & Simaika, YM. 1965. Long-term storage: an experimental
study.
- Hwang, P. A., Huang, N. E., & Wang, D. W. 2003. A note on analyzing nonlinear
and nonstationary ocean wave data. *Appl. Ocean Res.*, **25**(4), 187–193.
- Ivanov, P.C., Bunde, A., Amaral, LAN, Havlin, S., Fritsch-Yelle, J., Baevsky, RM,
Stanley, HE, & Goldberger, AL. 1999. Sleep-wake differences in scaling behavior
of the human heartbeat: Analysis of terrestrial and long-term space flight data.
Europhys. Lett., **48**(5), 594–600.

- 3181 Jaffe, B.E., & Rubin, D.M. 1996. Using nonlinear forecasting to learn the magnitude
3182 and phasing of time-varying sediment suspension in the surf zone. *J. Geophys.*
3183 *Res.*, **101**(C6), 14283–14296.
- 3184 Janicki, A., & Weron, A. 1994. *Simulation and chaotic behavior of alpha-stable*
3185 *stochastic processes*. New York: Marcel Dekker.
- 3186 János, I.M., & Gallas, J.A.C. 1999. Growth of companies and waterlevel fluctuations
3187 of the river Danube. *Physica A*, **271**(3), 448–457.
- 3188 János, I.M., & Müller, R. 2005. Empirical mode decomposition and correlation
3189 properties of long daily ozone records. *Phys. Rev. E*, **71**(5), 56126.
- 3190 Jayesh, C.T., & Warhaft, Z. 1994. On temperature spectra in grid turbulence. *Phys.*
3191 *Fluids*, **6**, 306.
- 3192 Kahalerras, H., Malécot, Y., Gagne, Y., & Castaing, B. 1998. Intermittency and
3193 Reynolds number. *Phys. Fluids*, **10**, 910.
- 3194 Kang, H., & Meneveau, C. 2001. Passive scalar anisotropy in a heated turbulent wake:
3195 new observations and implications for large-eddy simulations. *J. Fluid Mech.*, **442**,
3196 161–170.
- 3197 Kang, H., Chester, S., & Meneveau, C. 2003. Decaying turbulence in an active-grid-
3198 generated flow and comparisons with large-eddy simulation. *J. Fluid Mech.*, **480**,
3199 129–160.
- 3200 Kantelhardt, J.W., Rybski, D., Zschiegner, S.A., Braun, P., Koscielny-Bunde, E.,
3201 Livina, V., Havlin, S., & Bunde, A. 2003. Multifractality of river runoff and pre-
3202 cipitation: comparison of fluctuation analysis and wavelet methods. *Physica A*,
3203 **330**(1-2), 240–245.

- Kantelhardt, J.W., Koscielny-Bunde, E., Rybski, D., Braun, P., Bunde, A., & Havlin, S. 2006. Long-term persistence and multifractality of precipitation and river runoff records. *J. Geophys. Res.*, **111**. 3204–3206
- Kida, S. 1991. Log-stable distribution and intermittency of turbulence. *J. Phys. Soc. Japan*, **60**(5). 3207–3208
- Kolmogorov, A. N. 1941a. Local structure of turbulence in an incompressible fluid at very high Reynolds numbers. *Dokl. Akad. Nauk SSSR*, **30**, 299–303. 3209–3210
- Kolmogorov, A. N. 1941b. On decay of isotropic turbulence in an incompressible viscous fluid. *Dokl. Akad. Nauk SSSR*, **31**, 538–540. 3211–3212
- Kolmogorov, A. N. 1941c. Energy dissipation in locally isotropic turbulence. *Dokl. Akad. Nauk SSSR*, **32**(1), 19–21. 3213–3214
- Kolmogorov, A. N. 1962. A refinement of previous hypotheses concerning the local structure of turbulence in a viscous incompressible fluid at high Reynolds number. *J. Fluid Mech.*, **13**, 82–85. 3215–3217
- Kolmogorov, AN. 1940. The Wiener spiral and some other interesting curves in Hilbert space. *Dokl. Akad. Nauk SSSR*, **26**(2), 115–118. 3218–3219
- Koscielny-Bunde, E., Kantelhardt, J.W., Braun, P., Bunde, A., & Havlin, S. 2006. Long-term persistence and multifractality of river runoff records: Detrended fluctuation studies. *J. Hydrol.*, **322**(1-4), 120–137. 3220–3222
- Kraichnan, R. H. 1991. Turbulent cascade and intermittency growth. *Proc. R. Soc. London, Ser. A*, **434**(1890), 65–78. 3223–3224
- Landau, L.D., & Lifshitz, E.M. 1987. Fluid Mechanics. *New York*. 3225
- Livina, V., Ashkenazy, Y., Kizner, Z., Strygin, V., Bunde, A., & Havlin, S. 2003a. A stochastic model of river discharge fluctuations. *Physica A*, **330**(1-2), 283–290. 3226–3227

- 3228 Livina, V., Kizner, Z., Braun, P., Molnar, T., Bunde, A., & Havlin, S. 2007. Temporal
3229 scaling comparison of real hydrological data and model runoff records. *J. Hydrol.*,
3230 **336**(1-2), 186–198.
- 3231 Livina, V.N., Ashkenazy, Y., Braun, P., Monetti, R., Bunde, A., & Havlin, S. 2003b.
3232 Nonlinear volatility of river flux fluctuations. *Phys. Rev. E*, **67**(4), 42101.
- 3233 Loh, C. H., Wu, T. C., & Huang, N. E. 2001. Application of the Empirical Mode
3234 Decomposition-Hilbert Spectrum Method to Identify Near-Fault Ground-Motion
3235 Characteristics and Structural Responses. *BSSA*, **91**(5), 1339–1357.
- 3236 Long, S. R., Huang, N. E., Tung, C. C., Wu, M. L., Lin, R. Q., Mollo-Christensen,
3237 E., & Yuan, Y. 1995. The Hilbert techniques: an alternate approach for non-steady
3238 time series analysis. *IEEE Geoscience and Remote Sensing Soc. Lett.*, **3**, 6–11.
- 3239 Loutridis, S. J. 2005. Resonance identification in loudspeaker driver units: A com-
3240 parison of techniques. *Appl. Acoust.*, **66**(12), 1399–1426.
- 3241 Lumley, J. L. 1992. Some comments on turbulence. *Phys. Fluids*, **4**(2), 203–211.
- 3242 Lumley, J. L., & Yaglom, A. M. 2001. A Century of Turbulence. *Flow Turbul.*
3243 *Combust.*, **66**(3), 241–286.
- 3244 Lux, T. 2001. Power laws and long memory. *Quant. Finance*, **1**(6), 560–562.
- 3245 L’vov, Victor, & Procaccia, Itamar. 1997. Hydrodynamic Turbulence: a 19th Century
3246 Problem with a challenge for the 21st Century. *Turbulence Modeling and Vortex*
3247 *Dynamics, Lecture Notes in Physics*.
- 3248 Makita, H. 1991. Realization of a large-scale turbulence field in a small wind tunnel.
3249 *Fluid Dynamics Research*, **8**, 53–64.
- 3250 Malik, SC, & Arora, S. 1992. *Mathematical Analysis*. John Wiley & Sons Inc.

- Mandelbrot, B.B. 1974. Intermittent turbulence in self-similar cascades: divergence of high moments and dimension of the carrier. *J. Fluid Mech.*, **62**(02), 331–358.
- Mandelbrot, B.B., & Van Ness, J.W. 1968. Fractional Brownian Motions, Fractional Noises and Applications. *SIAM Review*, **10**, 422.
- Marple Jr, L. 1999. Computing the discrete-time analytic signal via FFT. *IEEE T. Signal. Proces.*, **47**(9), 2600–2603.
- Masselink, Gerhard, & Russell, Paul. 2006. Flow velocities, sediment transport and morphological change in the swash zone of two contrasting beaches. *Mar. Geol.*, **227**(3-4), 227–240.
- Mauas, Pablo J. D., Flamenco, Eduardo, & Buccino, Andrea P. 2008. solar forcing of the stream flow of a continental scale south american river. *Phys. Rev. Lett.*, **101**, 168501.
- Mead, K. S., & Denny, M. W. 1995. The effects of hydrodynamic shear stress on fertilization and early development of the purple sea urchin *Strongylocentrotus purpuratus*. *Biol. Bull*, **188**(1), 46–56.
- Meyer, Y. Lecture notes for the Montréal splines and wavelets conference. *Université de Montréal, Canada, Mars 1996, unpublished.*
- Moisy, F., Willaime, H., Andersen, JS, & Tabeling, P. 2001. Passive Scalar Intermittency in Low Temperature Helium Flows. *Phys. Rev. Lett.*, **86**(21), 4827–4830.
- Molla, Md. Khademul Islam, Rahman, M. Sayedur, Sumi, Akimasa, & Banik, Pabitra. 2006. Empirical mode decomposition analysis of climate changes with special reference to rainfall data. *Discrete Dyn. Nat. Soc.*, **2006**, Article ID 45348, 17 pages. doi:10.1155/DDNS/2006/45348.

- 3274 Monin, A. S., & Yaglom, A. M. 1971. *Statistical fluid mechanics vd II*. MIT Press
3275 Cambridge, Mass.
- 3276 Muzy, J.F., & Bacry, E. 2002. Multifractal stationary random measures and multi-
3277 fractal random walks with log infinitely divisible scaling laws. *Phys. Rev. E*, **66**(5),
3278 056121.
- 3279 Mydlarski, L., & Warhaft, Z. 1996. On the onset of high-Reynolds-number grid-
3280 generated wind tunnel turbulence. *J. Fluid. Mech.*, **320**, 331–368.
- 3281 Mydlarski, L., & Warhaft, Z. 1998. Passive scalar statistics in high-Péclet-number
3282 grid turbulence. *J. Fluid Mech.*, **358**, 135–175.
- 3283 Nelkin, M. 1994. Universality and scaling in fully developed turbulence. *Adv. Phys.*,
3284 **43**(2), 143–181.
- 3285 Nichols Pagel, G.A., Percival, D.B., Reinhall, P.G., & Riley, J.J. 2008. Should struc-
3286 ture functions be used to estimate power laws in turbulence? A comparative study.
3287 *Physica D*, **237**(5), 665–677.
- 3288 Novikov, EA. 1969. Scale similarity for random fields. **14**, 104–107.
- 3289 Obukhov, AM. 1941. Spectral energy distribution in a turbulent flow. *Dokl. Akad.*
3290 *Nauk SSSR*, **32**(1), 22–24.
- 3291 Obukhov, AM. 1949. Structure of the temperature field in a turbulent flow. *Izv.*
3292 *Acad. Nauk SSSR Ser. Geog. Geofiz*, **13**, 58–69.
- 3293 Obukhov, AM. 1962. Some Specific Features of Atmospheric Turbulence. *J. Geophys.*
3294 *Res.*, **67**, 3011–3014.
- 3295 Pandey, G., Lovejoy, S., & Schertzer, D. 1998. Multifractal analysis of daily river
3296 flows including extremes for basins of five to two million square kilometres, one day
3297 to 75 years. *J. Hydrol.*, **208**(1-2), 62–81.

- Parisi, G., & Frisch, U. 1985. On the singularity spectrum of fully developed turbulence. *Turbulence and predictability in geophysical fluid dynamics, North Holland, Proceedings of the International Summer School in Physics Enrico Fermi*, 84–87. 3298
3299
3300
- Percival, D.B., & Walden, A.T. 1993. *Spectral Analysis for Physical Applications: Multitaper and Conventional Univariate Techniques*. Cambridge University Press. 3301
3302
- Peters, O., Hertlein, C., & Christensen, K. 2002. A complexity view of rainfall. *Phys. Rev. Lett.*, **88**(1), 018701. 3303
3304
- Podesta, J. J., Forman, M. A, Smith, C W, Elton, D C, Malecot, Y., & Gagne, Y. 3305
2009. Accurate estimation of third-order moments from turbulence measurements. 3306
Nonlin. Processes Geophys., **16**, 99–110. 3307
- Pond, S., & Stewart, RW. 1965. Measurements of the statistical characteristics of 3308
small-scale turbulent motions. *Izv. Atmos. Oceanic Phys*, **1**, 914–919. 3309
- Ponomarenko, V. I., Prokhorov, M. D., Bespyatov, A. B., Bodrov, M. B., & Gridnev, 3310
V. I. 2005. Deriving main rhythms of the human cardiovascular system from the 3311
heartbeat time series and detecting their synchronization. *Chaos Soliton Fract.*, 3312
23, 1429–1438. 3313
- Pope, S. B. 2000. *Turbulent Flows*. Cambridge University Press. 3314
- Reynolds, O. 1883. An experimental investigation of the circumstances which de- 3315
termine whether the motion of water shall be direct or sinuous, and the law of 3316
resistance in parallel channels. *Proc. R. Soc. London, Ser. A*, **174.**, 935–982. 3317
- Reynolds, O. 1894. On the dynamical theory of turbulent incompressible viscous 3318
fluids and the determination of the criterion. *Proc. R. Soc. London, Ser. A*, **186**, 3319
123–161. 3320

- 3321 Richardson, L.F. 1922. *Weather prediction by numerical process*. Cambridge Univer-
3322 sity Press, Cambridge, England,.
- 3323 Rilling, G., & Flandrin, P. 2006. on the Influence of Sampling on the Empirical Mode
3324 Decomposition. *IEEE International Conference on Acoustics, Speech and Signal
3325 Processing, 2006. ICASSP 2006 Proceedings. 2006*, **3**, 444.
- 3326 Rilling, G., & Flandrin, P. 2008. One or two frequencies? The empirical mode
3327 decomposition answers. *IEEE Trans. Signal Process.*
- 3328 Rilling, G., & Flandrin, P. 2009. Sampling effects on the empirical mode decomposi-
3329 tion. *Adv. Adapt. Data Anal.*, **1**, 43–59.
- 3330 Rilling, G., Flandrin, P., & Gonçalves, P. 2003. On empirical mode decomposition
3331 and its algorithms. *IEEE-EURASIP Workshop on Nonlinear Signal and Image
3332 Processing*.
- 3333 Rilling, G., Flandrin, P., & Gonçalves, P. 2005. Empirical Mode Decomposition,
3334 fractional Gaussian noise and Hurst exponent estimation. *Acoustics, Speech, and
3335 Signal Processing, 2005. Proceedings.(ICASSP'05). IEEE International Conference
3336 on*, **4**.
- 3337 Rogers, L. 1997. Arbitrage with Fractional Brownian Motion. *Math. Finance*, **7**(1),
3338 95–105.
- 3339 Ruiz-Chavarria, G., Baudet, C., & Ciliberto, S. 1996. Scaling laws and dissipation
3340 scale of a passive scalar in fully developed turbulence. *Physica D*, **99**(2-3), 369–380.
- 3341 Samorodnitsky, G., & Taqqu, M.S. 1994. *Stable Non-Gaussian Random Processes:
3342 stochastic models with infinite variance*. Chapman & Hall.
- 3343 Schertzer, D., & Lovejoy, S. 1987. Physical modeling and analysis of rain and clouds
3344 by anisotropic scaling multiplicative processes. *J. Geophys. Res*, **92**(D8), 9693–
3345 9714.

- Schertzer, D., Lovejoy, S., Schmitt, F. G., Chigirinskaya, Y., & Marsan, D. 1997. 3346
Multifractal cascade dynamics and turbulent intermittency. *Fractals*, **5**(3), 427– 3347
471. 3348
- Schmitt, F. G. 2003. A causal multifractal stochastic equation and its statistical 3349
properties. *Eur. Phys. J. B*, **34**(1), 85–98. 3350
- Schmitt, F. G. 2005. Relating Lagrangian passive scalar scaling exponents to Eulerian 3351
scaling exponents in turbulence. *Eur. Phys. J. B*, **48**(1), 129–137. 3352
- Schmitt, F. G. 2006. Linking Eulerian and Lagrangian structure functions? scaling 3353
exponents in turbulence. *Physica A*, **368**(2), 377–386. 3354
- Schmitt, F. G., Lavalley, D., Schertzer, D., & Lovejoy, S. 1992. Empirical determi- 3355
nation of universal multifractal exponents in turbulent velocity fields. *Phys. Rev.* 3356
Lett., **68**(3), 305–308. 3357
- Schmitt, F. G., Vannitsem, S., & Barbosa, A. 1998. Modeling of rainfall time series 3358
using two-state renewal processes and multifractals. *J. Geophys. Res.*, **103**(D18), 3359
23181–23193. 3360
- Schmitt, F. G., Schertzer, D., & Lovejoy, S. 1999. Multifractal analysis of foreign 3361
exchange data. *Appl. Stoch. Models and Data Anal.*, **15**(1), 29–53. 3362
- Schmitt, F. G., Huang, Y., Lu, Z., Zongo, S. B., Molinero, J. C., & Liu, Y. 2007. 3363
Analysis of nonlinear biophysical time series in aquatic environments: scaling prop- 3364
erties and empirical mode decomposition. *Pages 261–280 of: Nonlinear Dynamics* 3365
in Geosciences. edited by A. Tsonis and J. Elsner. Springer. 3366
- Schmitt, F. G., Dur, G., Souissi, S., & Brizard Zongo, S. 2008. Statistical properties of 3367
turbidity, oxygen and pH fluctuations in the Seine river estuary (France). *Physica* 3368
A, **387**(26), 6613–6623. 3369

- 3370 Schmitt, F. G., Huang, Y., Lu, Z., Y., Liu, & Fernandez, N. 2009. Analysis of velocity
3371 fluctuations and their intermittency properties in the surf zone using empirical
3372 mode decomposition. *J. Mar. Sys.*, **77**, 473–481, doi:10.1016/j.jmarsys.2008.11.012.
- 3373 Schumm, S.A. 2005. *River Variability and Complexity*. Cambridge University Press.
- 3374 Sellan, F. 1995. Synthèse de mouvements browniens fractionnaires à l' aide de la
3375 transformation par ondelettes. *C. R. Acad. Sci. Paris Sé r. I Math*, **321**, 351358.
- 3376 She, Z. S., & Lévêque, E. 1994. Universal scaling laws in fully developed turbulence.
3377 *Phys. Rev. Lett.*, **72**(3), 336–339.
- 3378 She, Z.S., & Waymire, E.C. 1995. Quantized Energy Cascade and Log-Poisson Statis-
3379 tics in Fully Developed Turbulence. *Phys. Rev. Lett.*, **74**(2), 262–265.
- 3380 Shraiman, B.I., & Siggia, E.D. 2000. Scalar turbulence. *Nature*, **405**(6787), 639–646.
- 3381 Siefert, M., Peinke, J., & Friedrich, R. 2005. A Simple Relation Between Longitudinal
3382 and Transverse Increments. *Progress in Turbulence*, **101**, 63–66.
- 3383 Solé, J., Turiel, A., & Llebot, JE. 2007. Using empirical mode decomposition to
3384 correlate paleoclimatic time-series. *Nat. Hazard Earth Sys. Sci.*, **7**, 299–307.
- 3385 Sreenivasan, KR. 1991. On Local Isotropy of Passive Scalars in Turbulent Shear
3386 Flows. *Proc. R. Soc. Lond. A*, **434**(1890), 165–182.
- 3387 Sreenivasan, K.R. 1996. The passive scalar spectrum and the Obukhov–Corrsin con-
3388 stant. *Phys. Fluids*, **8**, 189.
- 3389 Sreenivasan, K.R., & Antonia, RA. 1997. The phenomenology of small-scale turbu-
3390 lence. *Annu. Rev. Fluid Mech.*, **29**, 435–472.
- 3391 Staicu, A., & van de Water, W. 2003. Small Scale Velocity Jumps in Shear Turbulence.
3392 *Phys. Rev. Lett.*, **90**(9), 94501.

- Stolovitzky, G., & Sreenivasan, K. R. 1994. Kolmogorov's refined similarity hypothesis for turbulence and general stochastic processes. *Rev. Mod. Phys.*, **66**(1), 229–240. 3393–3395
- Svendsen, I. A. 1987. Analysis of surf zone turbulence. *J. Geophys. Res.*, **92**(C5), 5115–5124. 3396–3397
- Svendsen, I.A. 2005. Introduction to Nearshore Hydrodynamics. *Adv. Series on Ocean Eng.*, **24**. 3398–3399
- Taqqu, M. S., & Samorodnisky, G. 1994. *Stable Non-Gaussian Random Processes*. Chapman & Hall, New York. 3400–3401
- Taylor, G. I. 1935. Statistical Theory of Turbulence. *Proc. R. Soc. London, Ser. A*, **151**(873), 421–444. 3402–3403
- Taylor, G. I. 1938. The Spectrum of Turbulence. *Proc. R. Soc. London, Ser. A*, **164**(919), 476–490. 3404–3405
- Telesca, L., & Macchiato, M. 2004. Time-scaling properties of the Umbria-Marche 1997–1998 seismic crisis, investigated by the detrended fluctuation analysis of interevent time series. *Chaos Soliton Fract.*, **19**(2), 377–385. 3406–3408
- Tessier, Y., Lovejoy, S., Hubert, P., Schertzer, D., & Pecknold, S. 1996. Multifractal analysis and modeling of rainfall and river flows and scaling, causal transfer functions. *J. Geophys. Res.*, **101**, 26427–26440. 3409–3411
- Torres-Freyermuth, A., Losada, I. J., & Lara, J. L. 2007. Modeling of surf zone processes on a natural beach using Reynolds-Averaged Navier-Stokes equations. *J. Geophys. Res.*, **112**, C09014. 3412–3414
- Trowbridge, J., & Elgar, S. 2001. Turbulence Measurements in the Surf Zone. *J. Phys. Oceanogr.*, **31**(8), 2403–2417. 3415–3416

- 3417 Tsinober, A. 2001. *An Informal Introduction to Turbulence*. Kluwer Academic Pub-
3418 lishers, Amsterdam.
- 3419 Tsuji, Y. 2004. Intermittency effect on energy spectrum in high-Reynolds number
3420 turbulence. *Phys. Fluids*, **16**, L43–L46.
- 3421 Vainshtein, SI. 2003. Most singular vortex structures in fully developed turbulence.
3422 *Arxiv preprint physics/0310008*.
- 3423 van de Water, W., & Herwijer, J. A. 1999. High-order structure functions of turbu-
3424 lence. *J. Fluid Mech.*, **387**, 3–37.
- 3425 Veltcheva, A. D., & Soares, C. G. 2004. Identification of the components of wave
3426 spectra by the Hilbert Huang transform method. *Appl. Ocean Res.*, **26**(1-2), 1–12.
- 3427 Venugopal, V., Roux, S. G., Fofoula-Georgiou, E., & Arnéodo, A. 2006. Scaling
3428 behavior of high resolution temporal rainfall: New insights from a wavelet-based
3429 cumulant analysis. *Phys. Lett. A*, **348**(3-6), 335–345.
- 3430 Warhaft, Z. 2000. Passive scalars in turbulent flows. *Annu. Rev. Fluid Mech.*, **32**(1),
3431 203–240.
- 3432 Wood, A.T.A., & Chan, G. 1994. Simulation of stationary Gaussian processes in [0,
3433 1] d. *J Comput. Graph. Stat.*, **3**(4), 409–432.
- 3434 Wu, Z., & Huang, N. E. 2004. A study of the characteristics of white noise using
3435 the empirical mode decomposition method. *Proc. R. Soc. London, Ser. A*, **460**,
3436 1597–1611.
- 3437 Wu, Z., Huang, N.E., Long, S.R., & Peng, C.K. 2007. On the trend, detrending, and
3438 variability of nonlinear and nonstationary time series. *PNAS*, **104**(38), 14889.
- 3439 Xia, H., Punzmann, H., Falkovich, G., & Shats, MG. 2008. Turbulence-condensate
3440 interaction in two dimensions. *Phys. Rev. Lett.*, **101**(19), 194504.

- Yaglom, A. M. 1957. Some classes of random fields in n -dimensional space, related 3441
to stationary random processes. *Theor. Probab. App+*, **2**, 273. 3442
- Yaglom, A. M. 1966. The influence on the fluctuation in energy dissipation on the 3443
shape of turbulent characteristics in the inertial interval. *Sov. Phys. Dokl*, **2**, 26–30. 3444
- Yaglom, A. M. 2001. The century of turbulence theory: The main achievements and 3445
unsolved problems. *New Trends in Turbulence, Springer-Verlag, Berlin, Heidelberg,* 3446
New York, 1–52. 3447
- Zhang, C. 2005. Madden-Julian Oscillation. *Rev. Geophys.*, **43**, 36. 3448
- Zhang, Q., Xu, C., Chen, Y.D., & Yu, Z. 2008. Multifractal detrended fluctuation 3449
analysis of streamflow series of the Yangtze River basin, China. *Hydrol. Process.*, 3450
22, 4997–5003. 3451
- Zhang, Q., Xu, C., Liu, C., & D., Chen Y. 2009. Multifractal analysis of streamflow 3452
records of the East River basin (Pearl River), China. *Physica A*, **388 (6)**, 927–934. 3453